

Abstract

Harnessing Traveling-wave Photon-phonon Interactions in Integrated Waveguides

Eric Andrew Kittlaus

2019

By interfacing chip-based electrical circuits with optical waveguides, the field of integrated photonics seeks to create next-generation technologies for information processing, high-speed communications, and precision sensing. To this end, a considerable body of work over the past two decades has demonstrated high-performance waveguide-integrated modulators, filters, light sources, and detectors with potential advantages in terms of size, power consumption, performance, and cost over conventional benchtop systems.

In this dissertation, we explore interactions between traveling photons and phonons within these integrated photonic circuits. By coupling optical and elastic degrees of freedom, we develop new functionalities not available within all-optical systems. We harness these techniques to demonstrate optical amplifiers, microwave filters, nonreciprocal devices, and signal-processing techniques within integrated silicon waveguides.

Underpinning these interactions is a nonlinear optical effect called stimulated Brillouin scattering (SBS). While Kerr (electronic) and Raman (optical phonon-mediated) nonlinearities are well-known to be enhanced by sub-wavelength confinement in integrated waveguides, Brillouin nonlinearities, which are the strongest nonlinearity in optical fiber, were previously absent in semiconductor integrated photonic circuits. By designing new optomechanical waveguide structures which tightly confine light and sound, these nonlinearities become radically enhanced, making them not only measurable, but exceedingly strong and tailorable.

Utilizing suspended waveguide designs, we describe the development of silicon waveguide-integrated Brillouin amplifiers that permit appreciable (>5 dB) optical amplification through forward SBS (FSBS). This process also enables a novel form of cascaded energy transfer between multiple coupled optical waves. In contrast to prior works, which painted a rel-

atively bleak picture for Brillouin amplification in silicon, these results demonstrate great potential for efficient optomechanical signal processing within silicon waveguides.

Beyond applications in nonlinear optics, we use these robust FSBS couplings to explore new concepts for acousto-optic signal processing through Brillouin-mediated coherent phonon generation. One such technique is realized using structures that couple two distinct optical waveguides to a common phonon mode. In this device, forward SBS is used to convert a microwave signal into an elastic wave, where the signal is filtered through the device's designed phononic transfer function. This signal then phase-modulates light guided in a separate waveguide, converting it back to the optical domain. This operation is used to demonstrate high-fidelity, ultra-narrowband radiofrequency filtering within a microwave-photonic link.

Within multimode optomechanical waveguides, we engineer stimulated inter-modal Brillouin scattering (SIMS) to permit new degrees of control over the dynamics of photon-phonon interactions. SIMS enables flexible optical signal routing by harnessing on-chip mode multiplexing, and intrinsically decouples Stokes and anti-Stokes processes to produce single-sideband optical amplification and energy transfer. These couplings are used to create a new kind of Brillouin laser, which produces Schawlow-Townes-like linewidth narrowing for phonons, despite the absence of an acoustic cavity or feedback mechanism. The dynamics of inter-modal Brillouin scattering also enable the experimental demonstration of optomechanical cooling within a continuous, traveling-wave system. Such operations represent an extension of existing cavity-optomechanical systems to the continuum limit.

Finally, we utilize SIMS to produce nonreciprocal acousto-optic mode conversion within a multi-core optomechanical waveguide by utilizing a nonlocal inter-band Brillouin scattering (NIBS) process. Through this interaction, an optically-driven elastic wave mediates unidirectional light scattering through a nonreciprocal phase-matching condition. In contrast to prior resonant optomechanical structures, the bandwidth of this process is controlled through optical dispersion, permitting nonreciprocal operation over bandwidths as large as 150 GHz (1.2 nm). Depending on the desired operation scheme, the same reconfigurable device can be used to demonstrate unidirectional single-sideband modulation, widely-tunable narrowband microwave filtering, and microwave and optical spectral analysis.

Such advances demonstrate the utility of photon-phonon interactions within a wide array of integrated optical systems. Beyond this work, further refinement of these techniques may enable on-chip Brillouin-based signal processing operations with superb tunability, fidelity, and bandwidth.

Harnessing Traveling-wave Photon-phonon Interactions in Integrated Waveguides

A Dissertation
Presented to the Faculty of the Graduate School
of
Yale University
in Candidacy for the Degree of
Doctor of Philosophy

by
Eric Andrew Kittlaus

Dissertation Director: Prof. Peter Rakich

May 2019

ProQuest Number: 13918044

All rights reserved

INFORMATION TO ALL USERS

The quality of this reproduction is dependent upon the quality of the copy submitted.

In the unlikely event that the author did not send a complete manuscript and there are missing pages, these will be noted. Also, if material had to be removed, a note will indicate the deletion.



ProQuest 13918044

Published by ProQuest LLC (2019). Copyright of the Dissertation is held by the Author.

All rights reserved.

This work is protected against unauthorized copying under Title 17, United States Code
Microform Edition © ProQuest LLC.

ProQuest LLC.
789 East Eisenhower Parkway
P.O. Box 1346
Ann Arbor, MI 48106 – 1346

Copyright © 2019 by Eric Kittlaus

All rights reserved.

Contents

List of Figures	viii
List of Tables	xxxviii
Acknowledgments	xxxix
1 Introduction	1
1.1 First Observations of Brillouin Scattering	1
1.2 Discovery of Stimulated Light Scattering	2
1.3 Stimulated Brillouin Scattering In Optical Fibers	3
1.3.1 First Observations and SBS as a Power-handling Limit	3
1.3.2 Fiber Brillouin Lasers	4
1.3.3 Fiber Brillouin Amplifiers	5
1.3.4 Brillouin-based Sensing	5
1.3.5 Brillouin Dynamic Gratings	6
1.4 Brillouin-based Signal Processing	7
1.5 Forward and Inter-modal Brillouin Scattering in Optical Fibers	8
1.6 Light-sound Coupling at the Nanoscale	10
1.6.1 SBS within Whispering-gallery-mode Resonators	10
1.6.2 SBS in Nanoscale Waveguides	12
1.7 Outlook and Summary of Dissertation	14
2 Theory of Stimulated Brillouin Scattering	17
2.1 Origins of Brillouin Interactions	18

2.1.1	Phenomenological Picture of Backward SBS	20
2.1.2	Scalar Model of Backward SBS	22
2.1.3	SBS in Guided-wave Systems	26
2.2	Types of Brillouin Scattering Processes	30
2.2.1	Dynamics of Backward SBS (BSBS)	30
2.2.2	Dynamics of Forward SBS (FSBS)	35
2.2.3	Dynamics of Forward Stimulated Inter-modal Brillouin Scattering (SIMS)	40
2.3	Modal Picture of BSBS, FSBS, and SIMS	48
3	Forward Brillouin Amplification in Silicon Membrane Waveguides	51
3.1	Introduction	51
3.2	Silicon Membrane Waveguide Design	55
3.3	Nonlinear Absorption in Silicon Waveguides	55
3.4	Characterization of Optical Loss	57
3.5	Measurements of Free-carrier Lifetimes in the Silicon Optomechanical Waveguide	58
3.5.1	Steady-state Free-carrier Absorption	59
3.5.2	Four-wave Mixing Modification by Free-carrier Modulation	59
3.5.3	Passive Reduction of the Free-carrier Lifetime	62
3.6	Forward Brillouin Gain: Coupled-amplitude Equations	63
3.7	Experimental Observation of Forward Brillouin Amplification	64
3.7.1	Cascaded Brillouin Energy Transfer	68
3.7.2	Potential for Further Amplification and Energy Transfer	70
3.7.3	Brillouin Gain and Loss	70
3.8	Coherent Anti-Stokes Brillouin Scattering Measurements and Study of Resonance Broadening	72
3.8.1	Phase-matching for CABS and Four-wave Mixing	72
3.8.2	Theory of CABS in the Presence of Four-wave Mixing	74
3.8.3	CABS Data	77

3.8.4	Dimensional Broadening of Brillouin Resonances	78
3.9	Conclusions and Outlook	80
4	Coupling Optical Waveguides through Extended Phonon Modes for Microwave Signal Processing	83
4.1	Introduction	83
4.2	Operation Scheme	85
4.3	Photon-phonon Emitter-receiver Theory	88
4.3.1	Translational Invariance of the Phonon Field Amplitude	90
4.3.2	Driven Phonon Amplitude for Two- and Three-tone Excitation	92
4.3.3	Modulation Efficiency by a Monochromatic Phonon Field	93
4.3.4	RF-Photonic Filter Response	94
4.3.5	Thermal Brillouin Noise and Spur-free Dynamic Range	97
4.3.6	Noise Figure	98
4.4	Characterization of Device Response	100
4.5	RF-Photonic Link Performance	102
4.5.1	Linear and Nonlinear Response of the PPER Link	102
4.5.2	Modulation Figure of Merit	104
4.5.3	Microwave Filter Response	105
4.5.4	Noise and Dynamic Range	105
4.6	Potential for Improved Performance	106
5	Inter-modal Brillouin Scattering	111
5.1	Introduction	111
5.2	Integrated Mode Multiplexers	113
5.3	Multimode Optomechanical Waveguide Design	117
5.4	Linear and Nonlinear Losses in Multimode Silicon Waveguides	119
5.5	Stimulated Inter-modal Brillouin Scattering	122
5.5.1	Operation Scheme	123
5.5.2	Experimental Demonstration of Inter-modal SBS	126
5.5.3	Single-sideband Brillouin Gain	128

5.5.4	Single-sideband Amplification	128
5.5.5	Pump-probe Gain and Loss Schemes	130
5.6	Single-sideband Energy Transfer	132
5.6.1	SIMS vs. FSBS Cascading and Phonon Dynamics	134
5.7	Design Considerations and Tailorable SIMS Interactions	137
5.7.1	Guided Elastic Waves in the Membrane Waveguide and Phonon Wavevector Tunability	137
5.7.2	Dimensional Tunability of Brillouin Frequency	140
5.7.3	Sensitivity of SIMS to Dimensional Broadening	140
5.8	Inter-modal Silicon Brillouin Laser	142
5.8.1	Silicon Brillouin Laser Design	143
5.8.2	Observation of Laser Oscillation	144
5.8.3	Linewidth-narrowing Dynamics	146
5.8.4	Summary and Future Directions	149
5.9	Spontaneous Brillouin Cooling through SIMS	150
5.9.1	Operation Scheme of Spontaneous Inter-modal Brillouin Scattering	151
5.9.2	Observation of Brillouin Cooling within a Linear Waveguide	153
5.9.3	Wavevector-selective Phonon Spectroscopy	155
5.9.4	Cooling Dynamics	158
5.10	Conclusions and Outlook	160
6	Nonreciprocal, Nonlocal Inter-band Brillouin Modulation	162
6.1	Introduction	162
6.2	NIBS Modulator Device Concept	165
6.3	Light-Sound Phase-matching and Modulator Operation Scheme	167
6.3.1	Relationship between Drive and Modulation Wavelengths	170
6.3.2	Origin of Nonreciprocal Response	170
6.3.3	Modulator Operation Bandwidth	171
6.3.4	Forward/Backward Operation and Essential Condition for Robust Nonreciprocity	172

6.4	Experimental Characterization of the NIBS Modulator	173
6.4.1	Anti-Stokes Modulation Data	176
6.4.2	Phase-mismatched Lineshape	178
6.4.3	Experimental Modulation Efficiency and Device Parameters	180
6.5	Scattering Matrix Model of NIBS	181
6.6	Coupled Amplitude Equations and Dynamics of NIBS Couplings	187
6.6.1	General Coupling Equations Including Nonlinear Loss	187
6.6.2	Approximate Analytic Solution to Coupling Equations	190
6.6.3	Externally-driven Phonon Field	196
6.7	Improving Modulation Bandwidth with Waveguide Dispersion Engineering	198
6.8	Discussion and Summary	200
7	Conclusion	202
A	Methods: Fabrication	204
A.1	Preparation of Alignment Markers and SOI Chips	204
A.2	Ridge Waveguide Fabrication	205
A.3	Membrane and Slot Fabrication	205
B	Methods: Coupling to Integrated Waveguide Devices	208
B.1	Integrated Grating Couplers	208
B.2	Coupling to On-chip Devices using Fiber Arrays	210
	Bibliography	213

Acknowledgments

A successful graduate career relies on many people being really, really generous, and working very, very hard. As such, I owe an immense debt of gratitude to my present and past mentors, colleagues, and friends. I would especially like to acknowledge the following people for their kindness and support over the years:

My PhD advisor, Prof. Peter Rakich, is both a talented scientist, and a genuinely kind-hearted mentor and human being. Peter does a fantastic job of fostering a creative and collaborative research environment, and of ensuring that each lab member has the resources and support they need to thrive. Despite his crazy schedule, Peter constantly made himself available to discuss new ideas or provide feedback. Thank you so much, Peter. I am endlessly grateful for the opportunity to work in your group.

My colleagues at Yale; Heedeuk Shin, Ryan Behunin, Will Renninger, Prash Kharel, Nils Otterstrom, Shai Gertler, Yiwen Chu, Taekwan Yoon, Royce Luo, Yishu Zhou, and others. In particular, Prash, Nils, and Shai have been my closest friends and teammates while at Yale, and we together tackled countless experimental challenges, and spent hours arguing over topics from how optical modulation works to the definition of a ‘corner store.’ You guys are all superheroes. Heedeuk, then a postdoc, took me under his wing when I first joined the lab and we puzzled through many long days of fab together. Ryan and Will were our other two postdocs and older lab siblings, who provided lots of advice about how to be a successful scientist and adult. We’ll always remember how Ryan could sit down with a pen and paper and derive anything, and how Will kept spilling his lunch on himself when he first joined. Thanks for the help and hijinks over the years. I’m sure the three of you are absolutely crushing it as professors.

My committee members, Prof. Hui Cao and Prof. Liang Jiang; thank you for your mentorship and wonderful teaching over the years, and for taking the time out of your ridiculously busy lives to serve on my committee.

The Applied Physics administrative staff; Maria Rao, Terri Evangeliste, Nuch Graves, and Giselle Maillet are the glue that hold the department together and I am very grateful for their hard work and help during my graduate studies. Thank you also for the delightful coffee-time conversations!

The fabrication and facilities experts; Mike Rooks is a wizard at electron beam lithography and a great source of fab expertise, and does a heroic job keeping the YINQE facilities in ship shape. Mike Power, Chris Tillinghast, and Jim Agresta likewise provided immense help with process development, and worked very hard to keep the cleanroom running smoothly.

The funding sources for my graduate research; Yale University, the Defense Advanced Research Projects Agency (DARPA), the Office of Naval Research (ONR), and the David and Lucile Packard foundation. Thank you for paying the bills and funding my science fair projects.

My undergraduate research advisor, Prof. Chris Weber, guided me through my first experiences with optics research. Chris would say that he's a semiconductor physicist, but all I knew when asking to join his lab is that he used lasers. His technical savvy and adept hand for mentorship are in large part responsible for my development as a young scientist. Thank you so much for all of your hard work and generosity.

My family; my parents, Edward and Kathy, have been a constant source of advice over the years. Thanks for raising me to be self-sufficient—it's your own fault I never call to ask questions. My brother, Paul, has always been there for encouragement and late-night video game binges. I'm blessed to have an older sibling as cool as you. Katherine, my fiancée, has been by my side for most of my adult life, including five plus years of graduate school. Thank you for your boundless kindness, love, and support. You're the absolute greatest.

Thanks everyone, I wouldn't have been able to do it without all of your help.

List of Figures

2.1	Stokes and anti-Stokes scattering processes. (a) Through a Stokes process, an incident photon (frequency ω_p) emits a red-shifted photon (frequency $\omega_s = \omega_p - \Omega$) and a phonon (frequency Ω). This process is illustrated through a scattering diagram (top) and energy-level diagram (bottom). (b) Through an anti-Stokes process, an incident photon (frequency ω_p) annihilates a phonon and is blue-shifted to frequency $\omega_{as} = \omega_p + \Omega$. <i>Image credit: Shai Gertler, Eric Kittlaus.</i>	19
2.2	Backward stimulated Brillouin scattering. (a) diagrams a slice of a material in which two counterpropagating optical beams at frequencies ω_1 and ω_2 are incident. These light waves produce a traveling intensity beat note within the medium. (b) This intensity fringe pattern induces a traveling elastic wave through electrostrictive forces, with a time-harmonic frequency Ω at the optical beat frequency. (c) This elastic wave can scatter light between the two fields through photoelastic (acousto-optic) coupling, resulting in nonlinear energy transfer through stimulated Brillouin scattering.	21

2.3 Vectorial picture of optical forces and SBS coupling. (a) diagrams a portion of a translationally-invariant waveguide with a rectangular cross section (left), and a perspective view (right) (b) This structure guides many elastic waves, one of which is plotted in (b). For simplicity, the wavevector q of the simulated mode is set to 0 for the purposes of this diagram. (c) This optomechanical waveguide supports a transverse electric-like (TE-like) optical mode with the x -directed electric field profile shown here. This optical field produces a variety of body and boundary forces within the waveguide, including the x -directed electrostrictive body force in (d), and the boundary radiation pressure shown in (e). Cross-sectional slices of the optical mode and forces are plotted below (c-e). Both these electrostrictive and radiation-pressure forces are well-suited to coupling with elastic waves with the x -displacement profile from (b), since they produce forces with the same symmetry and direction as the elastic-wave motion. 29

2.4 **Phase-matching and dynamics of BSBS.** (a-c) depict the gain dynamics of BSBS. Counterpropagating pump (blue) and signal (red) waves are injected in the same spatial mode of a Brillouin-active waveguide. These waves couple through a longitudinal acoustic phonon (b) to produce energy transfer from pump to signal waves. These dynamics can be understood from the phase-matching requirements for backward Brillouin scattering (d-f): In panel (d), wavevector and frequency (energy) conservation are plotted via the horizontal and vertical coordinates, respectively. A forward-propagating phonon (solid green arrow) lying on the phonon dispersion curve (black) scatters light between a forward-propagating wave at frequency ω_p (initial state represented by an open circle) and a backward-propagating wave at frequency ω_s (final state represented by a filled circle). This phonon has a wavevector q equal to the wavevector difference between initial and final optical states $k_p - k_s$, as diagrammed in (e). Because the anti-Stokes process couples through a phonon which travels in the opposite direction (dashed green arrow in (d) and (f)), anti-Stokes scattering is decoupled from the Stokes scattering process. 32

2.5 **Phase-matching and dynamics of FSBS.** (a-c) depict the gain dynamics of FSBS. Co-propagating pump (blue) and signal (red) waves are guided in the same optical mode of a Brillouin-active waveguide. The same device also guides transverse acoustic waves (b) which produces nonlinear light-sound coupling. While pump light is scattered to the signal wave, producing gain, the same acoustic phonon also scatters light to the blue-detuned (anti-Stokes) sideband. This form of dual-sideband gain is quite distinct from the dynamics of BSBS, and can be understood from the phase-matching conditions for FSBS (d-f) Panel (d) plots the dispersion curve for the optical waveguide mode and the acoustic phonon mode. A forward-propagating phonon (solid green arrow) lying on the phonon dispersion curve (black) scatters light between two points (ω_p, k_p) and (ω_s, k_s) on the optical dispersion curve (dark blue). However, this same phonon can also scatter light through anti-Stokes (blue-shifting of the pump) and cascaded Stokes (red-shifting of signal light) processes, mapping light between successive points along the optical dispersion curve. (e-f) depict phase-matching (wavevector conservation) for Stokes and anti-Stokes scattering. The same phonon participates in both, leading to intrinsic coupling between Stokes and anti-Stokes processes. 36

2.6 **Phase-matching and dynamics of SIMS.** (a-c) depict the dynamics of optical amplification in a SIMS-active waveguide. Co-propagating pump (blue) and signal (red) waves are coupled into separate transverse spatial modes of a multimode optomechanical waveguide. These optical waves couple through an asymmetric traveling-wave phonon (black arrow with gray arcs) to produce gain of the red-detuned signal wave at the expense of the pump. (d-f) plot the phase-matching behavior of this process. In (d), a guided-wave acoustic phonon (solid green arrow) which lies on the acoustic dispersion curve (black) is used to couple light from the pump mode (symmetric mode, blue) to the signal wave (anti-symmetric mode, red). Similar to the types of Brillouin processes discussed in prior sections, Stokes scattering transfers light from a point (ω_p, k_p) denoted by an open circle to a point (ω_s, k_s) (filled circle). However, through SIMS the wavevectors k_p and k_s correspond to distinct optical dispersion branches. The same phonon with wavevector $q = k_p - k_s$ cannot produce cascaded Brillouin scattering processes since no destination optical state is available on other dispersion bands. Furthermore, as in BSBS, the phonons which mediate Stokes scattering (solid green arrow) and anti-Stokes scattering (dashed green arrow) travel in different directions, as denoted in (d-f), so these processes are decoupled. 42

2.7 **Modal picture of stimulated Brillouin scattering processes in a silicon waveguide.** The various component parts of SBS are plotted for three different processes within a 1000×230 nm silicon nanowire. (a) In backward intra-modal SBS, nonlinear coupling occurs between two light waves guided in the same optical mode (with approximate wavenumber k) but traveling in opposite directions. These optical waves drive time-harmonic optical forces through electrostriction and radiation pressure. The relevant component of the electrostrictive force is in the z direction, and is mediated by the photoelastic tensor component p_{12} , while radiation pressure is always normal to the dielectric discontinuities at the waveguide boundaries. These forces couple to a compressive-like elastic wave with wavenumber $2k$. Because this elastic mode also experiences motion in the transverse direction, radiation pressure can play a role in the BSBS interaction in highly-confined systems. (b) Intra-modal forward SBS occurs between two co-propagating light waves guided in the same optical mode. These optical fields excite transverse optical forces through electrostriction (through the p_{11} tensor component) and radiation pressure, which couple to an acoustic breathing-type mode with near-zero wavevector. (c) In inter-modal forward SBS, two optical spatial modes with wavevectors k_1 and k_2 excite traveling optical force distributions through electrostriction and radiation pressure. While coupling through transverse field components (i.e. through p_{11} and boundary forces) is typically dominant, longitudinal-wave couplings can play a significant role. These forces couple to a Lamb-like elastic mode with wavevector $k_1 - k_2$ 49

3.1 **Substrate-induced acoustic dissipation.** (a) diagrams the cross-section of a typical silicon-on-silica waveguide geometry. (b) is a simulation demonstrating how elastic waves driven in the silicon waveguide core rapidly radiate into the substrate. (c) depicts a possible waveguide design for both light and sound where the silica substrate has been removed. *Image credit: Peter Rakich.* Panel (c) is from Ref. [195]. 52

<p>3.2 Suspended membrane waveguide design. (a) shows a schematic of the continuously-suspended optomechanical waveguide, with a cross-section of the active region sketched in (b). (c) diagrams relevant device dimensions. The device guides optical waves in the TE-like mode whose E_x field is plotted in (d). The resulting electrostrictive force from this mode has an x-component whose spatial character is plotted in (e). (f) Plots the normalized displacement of a 4-GHz elastic mode to which this force strongly couples. (g) plots a scanning electron micrograph (SEM) of the device cross-section. (h-i) plot SEMs of the top-down view of the device. Adapted from Ref. [219].</p>	54
<p>3.3 Silicon membrane waveguide propagation loss measurements (a) Total transmission loss of a low-power probe as a function of waveguide length for a series of test waveguides. Red line is a fit corresponding to a linear loss of 0.18 dB/cm. (b) Observation of nonlinear loss as input power is increased. Red line is a fit to Eq. 3.2. All measurements are at an optical wavelength of 1550 nm. Adapted from Ref. [219].</p>	57
<p>3.4 Free-carrier-induced modulation (a) Diagram of the heterodyne four-wave-mixing experiment. The photoexcited free-carrier density is modulated by strong pump fields separated by frequency Ω, resulting in nonlinearly-induced phase changes to the probe beam. An acousto-optic modulator provides a reference field for heterodyne detection. (b) Traces for measured anti-Stokes (blue, upper curve) and Stokes (green, lower curve) signals and corresponding theoretical curves as a function of pump modulation frequency. Several Brillouin resonances, which produce narrowband acousto-optic phase modulation, are also visible. The total input power is around 70 mW. Adapted from Ref. [219].</p>	62

3.5 **Experimental demonstration of Brillouin amplification.** (a) Detailed diagram for the Brillouin gain experiment. Subpanels (i)-(iv) illustrate the spectral content of the different tones present corresponding to positions i-iv along the signal path. In diagrams (ii) and (iv), the $+\Omega$ modulation sideband is removed by a notch filter. Abbreviations: IM Mach-Zehnder intensity modulator; EDFA erbium-doped fiber amplifier; NF notch filter; DUT device under test; ISO optical isolator; PD fast photodetector; RFSA radio-frequency spectrum analyzer/power meter. (b) Panels (i), (ii), and (iii) are gain spectra around the Brillouin frequency obtained for pump powers of 21, 36, and 62 mW, respectively. (c) plots peak gain (red), linear loss (dash) and total loss (green) versus on-chip pump power at 1550 nm wavelengths. (d) shows net amplification as a function of pump power. The threshold for amplification is 5 mW. Adapted from Ref. [219]. 66

3.6 Cascaded forward-SBS energy transfer (a) Diagram for the modified forward-SBS experiment used to demonstrate energy transfer. Incident pump light is split into two paths. In the upper path, light is passed through a null-biased intensity modulator driven at a frequency $\Omega/2$ to produce two tones separated by a frequency Ω that is set to the Brillouin frequency Ω_B . These two tones are amplified and passed through the device. In the bottom path, light is frequency-shifted by 40 MHz using an acousto-optic modulator, which is then combined with the output light from the device on a fast photoreceiver for heterodyne detection. This technique allows the detection of each cascaded frequency component as a unique microwave beat note whose power is measured using a radiofrequency spectrum analyzer.. Abbreviations: IM Mach-Zehnder intensity modulator; EDFA erbium-doped fiber amplifier; DUT device under test; PD fast photodetector; RFSA radio-frequency spectrum analyzer/power meter. (b) Panels (i), (ii), and (iii) are stem plots of the normalized output powers as a function of frequency component order n for total incident powers of 0.1, 26, and 65 mW, respectively. Red arrows denote incident light in orders $n = \{0, 1\}$. These data correspond to the three vertical slices denoted in blue in panel (c), which shows theoretical calculations (lines) and measured amplitudes for pump fields ω_0 and ω_1 (solid black, solid red) and first cascaded fields ω_{-1} and ω_2 (solid red, dashed red) fields. Adapted from Ref. [219]. 69

3.7 Brillouin gain and loss. (a) Plots Brillouin attenuation of a weak probe that is blue-detuned from a strong pump wave by the Brillouin frequency shift. The three panels are for pump powers of 21, 36, and 62 mW, respectively. (b) Plots the peak Brillouin gain (black) or loss (red) with increasing pump power within the same device. Brillouin loss becomes exceedingly strong at high pump powers since the generation of Stokes-scattered light preserves the interaction strength as blue-detuned probe light is depleted. Adapted from [219]. 71

3.8	Coherent anti-Stokes forward Brillouin scattering. (a) Energy level diagram for the CABS process. Pump waves at frequencies $\omega_p^{(1)}$ and $\omega_s^{(1)}$ coherently excite the system to an excited vibrational state (i.e. excite an acoustic phonon). Probe light at frequency $\omega_p^{(2)}$ absorbs this phonon through a Brillouin scattering process and is blue-shifted to frequency $\omega_{as}^{(2)}$. This coupling is mediated through an elastic cutoff mode whose dispersion relation is sketched in (b). For intra-modal forward Brillouin scattering, this mode has near-zero wavevector. (c) plots both energy conservation and phase-matching for this process on top of the optical dispersion curve.	73
3.9	Coherent anti-Stokes Brillouin Scattering data (a) and (b) Plot data (red dots) and fits to Eq. 3.36 for CABS signatures on devices with lengths of 0.5 mm (a) and 29 mm (b). The shorter device displays a narrower intrinsic linewidth since it is experiences less resonance broadening from fabrication variations along the device length. (c) Plots a wideband sweep depicting the 29 mm device's three strongest Brillouin resonances and their simulated frequencies (red dashes). The background shape is due to the free-carrier effect discussed above. Adapted from Ref. [219].	77
3.10	Dimension-induced broadening. (a) depicts the relevant dimensions which define the waveguide cross-section. (b) plots the measured quality factors of the Brillouin resonances of the 4 GHz phonon mode for devices of four different lengths. Adapted from [219].	78

4.1 Photonic-phononic emitter-receiver operation scheme. (a) depicts basic operation of the PPER as a RF filter/modulator. Laser light (blue) is intensity-modulated by an input RF signal and injected into the ‘emit’ waveguide through port 1 of the device. This modulation transduces an acoustic phonon through electrostrictive forces. Light from a second laser (red) is injected into the ‘receive’ waveguide through port 2 of the device, and is phase-modulated by the same acoustic phonon before exiting the device through port 4. (b) depicts example power spectral content of the various signals in this experiment (i) a sample broadband RF input spectrum (ii) intensity-modulated laser light with sidebands encoded by the RF modulation (iii) the resulting acoustic phonon spectrum which filters the original RF signal through the device’s narrowband phononic response (iv) the optical spectrum of the output phase-modulated light. Adapted from Ref. [220]. . . 86

4.2 **Silicon photonic-phononic emitter-receiver device.** (a) depicts the device cross section; a dual-ridge membrane structure fabricated from a single-crystal silicon layer is suspended by a series of tethers on an SOI wafer. (b-c) show cross-sectional and top-down SEMs, respectively, of the fabricated device. (d) plots the cross-sectional dimensions of the PPER structure, while (e-f) plot the fundamental TE-like guided optical mode profiles for the two embedded ridge waveguides. (g) plots the x -component of the elastic displacement field for a ~ 4.3 GHz elastic mode which extends throughout the device. (h) diagrams the experimental characterization apparatus for probing the PPER device response. In the top optical path, pump light is intensity modulated around the zero-bias point and amplified through an erbium-doped fiber amplifier to create two strong pump waves separated by $\Omega \approx \Omega_B$. This light is injected into the emit waveguide through port 1. A separate probe wave is split into two paths—in the middle path, it enters the receive waveguide through device port 2 and exits through port 4, at which point it is recombined with a frequency-shifted local oscillator (bottom path) and incident on a fast photodiode for heterodyne spectral analysis in the microwave domain. (i) Plots the normalized modulation response of the PPER device as a function of drive frequency. (j) Plots the power in each of the two principal phase-modulation sidebands as a function of incident on-chip pump power when the device is driven on resonance $\Omega = \Omega_B$ in this configuration. Adapted from Ref. [220]. 99

4.3	<p>Silicon PPER within an RF-photonic link. (a) diagrams the RF-photonic link experiment: Pump light is intensity modulated by a microwave signal and amplified, and subsequently coupled into the emit waveguide of the PPER device. Probe light is passed through the receive waveguide, where it is modulated through the emit-receive process, and is amplified after being coupled off-chip to offset coupling losses. A fiber Bragg grating filters out one of the modulation sidebands to convert the phase modulation to intensity modulation, and the resulting signal is incident on a high-power photodiode to convert back to the RF domain. (b) shows RF power input/output data for both a monochromatic signal (top) and third-harmonic (bottom) tone through the link. The linear behavior of these curves is extrapolated (dashed grey lines) to find the third-order intercept point OIP_3 (black dot). (c) plots input and output power spectra for a two-tone incident RF signal consisting of equal-amplitude drive tones at Ω_B and $\Omega_B + 2\pi \times 50$ MHz. The out-of-band signal is attenuated by 26 dB relative to the in-band signal via the PPER filter's acoustic response. (d) Characterizes the noise floor around the filter center frequency $\Omega_B/2\pi = 4.33$ GHz as a function of probe power. The inset shows the noise floor due to a combination of spontaneous Brillouin noise and a white background due to amplified spontaneous emission of the EDFA. Adapted from Ref. [220].</p>	103
4.4	<p>Comparison of serial and parallel filter architectures for channelization. (a) Serial cascaded architecture for a PPER channelization filter. Because the same pump light can be used for each device (i.e. because the PPER device makes a copy of a narrowband slice of the input RF spectrum), minimal signal degradation is experienced as the number of channels is increased. (b) Architecture based on parallel RF filters. Note that because the signal must be split equally among the channels, amplification is necessary to preserve signal amplitude.</p>	108

5.1	Mode-selective directional couplers.	(a) Top-down diagram of the directional coupler design showing the relevant device dimensions. Light incident in the fundamental symmetric mode of the wider waveguide remains in the same waveguide mode. By contrast, light injected into the fundamental mode of the narrow coupler waveguide is coupled into the higher-order anti-symmetric mode of the wide waveguide. (b) FDTD simulation showing typical device dimensions and simulated power coupling into the anti-symmetric mode of the wider waveguide. For the parameters of this simulation, 78% of the injected light is coupled into the anti-symmetric spatial mode. Adapted from Ref. [221].	114
5.2	Mode multiplexer characterization	(a) depicts schematics for a crosstalk measurement. In the top panel, light injected into input port 1 with power I_1 is coupled into the symmetric mode with a small amount of light scattered into the anti-symmetric mode. Most of the light is correctly de-multiplexed into output port 1, but some light exits through port 2 due to modal crosstalk in both the input and output couplers. Similarly, in the bottom panel light coupled into input port 2 with power I_2 is converted into the anti-symmetric mode with a small amount of light coupled into in the symmetric mode. This light propagates through the multimode waveguide before being de-multiplexed at the output. (b) Typical power crosstalk spectra as a function of input light wavelength for one device. The total crosstalk is calculated by dividing the output powers of the two ports. Adapted from Ref. [221]. . . .	115

5.3	<p>Multimode optomechanical waveguide. (a) depicts a schematic of the suspended multimode Brillouin-active waveguide. (b) plots a cross-sectional scanning electron micrograph (SEM) of the device as-fabricated, with a scale bar representing 500 nm. (c) plots a top-down SEM of the device showing one suspended segment. The scale bar corresponds to 20 μm in length. (d) depicts a simplified view of the device cross section, with the dashed region highlighted in (e)-(i); (e) Plots the relevant dimensions of the device cross-section, with a variable total width w which is typically around 2.8 μm. (f) and (g) plot the simulated x-directed electric field components for the symmetric and anti-symmetric optical modes of the waveguide. The interference between these modes drives an electrostrictive force distribution plotted in (h). The displacement field of a ~ 6 GHz elastic mode which couples strongly to this optical force is plotted in (i). (j) plots a top-down view of a 14 μm long device segment, with the longitudinal phase-matching condition depicted on-top. This length corresponds to the phonon wavevector q. The elastic displacement for the membrane (dark gray) and ridge (light gray) regions is plotted in (k) over the same scale, showing one longitudinal acoustic wavelength. The intensity beat note between the two optical modes is plotted in (l). This beat note has the same wavelength as the phonon and represents a visual demonstration of the phase-matching condition. (m)i-iii plot the spatial distribution of the optical intensity at three slices of the waveguide. Adapted from Ref. [221].</p>	118
5.4	<p>Linear and nonlinear loss measurements for the multimode waveguide. Panels (a) and (b) plot linear loss vs. ring resonator length for the symmetric and anti-symmetric waveguide modes, respectively. Panels (c) and (d) plot output vs. input power for these two modes. All measurements are at $\lambda \approx 1550$ nm. Adapted from Ref. [221].</p>	121

5.5 Operation scheme for on-chip stimulated inter-modal Brillouin scattering. (a) diagrams the three modes which participate in the SIMS process, including symmetric (blue) and anti-symmetric (red) optical modes and the Brillouin-active elastic mode (gray). (b) depicts operation of the mode multiplexers which are here shown as a two-port “gray box.” Light incident in port 1 is coupled into the symmetric waveguide mode, whereas light incident in port 2 is coupled into the same waveguide’s anti-symmetric spatial mode. (c) depicts stimulated inter-modal Brillouin energy transfer. Pump (blue) and signal (red) waves are coupled into the symmetric and anti-symmetric waveguide modes, respectively, of a Brillouin-active multimode waveguide. As these waves traverse the device, energy transfers from the pump to the signal wave (top). Afterwards, the two waves are demultiplexed through an identical mode-selective coupler and may be routed elsewhere on-chip. (d) and (e) depict phase-matching and energy conservation for Stokes and anti-Stokes scattering processes, respectively. Each couples to a phonon with a different wavevector, but nearly identical frequencies, as plotted in the acoustic dispersion curve of (f). (g) and (h) sketch Feynman-like scattering diagrams for Stokes and anti-Stokes processes. In the Stokes process (g), an incident pump photon is converted to a red-shifted signal photon and a phonon. In the anti-Stokes process (h), an incident pump photon annihilates a phonon and is blue-shifted. Adapted from Ref. [221]. 124

- 5.6 Experimental observation of stimulated inter-modal Brillouin scattering.** (a) Diagram of the experimental apparatus used to study SIMS gain and energy transfer. A pump laser around 1550 nm with frequency ω_p is split into three paths—two are used to synthesize optical pump and probe waves, while the third is used to synthesize a frequency-shifted reference field at $\omega_p + \Delta$ using an acousto-optic modulator. The pump wave (frequency ω_p) is amplified through an erbium-doped fiber amplifier (EDFA), and the probe wave $\omega_p - \Omega$ is optionally passed through a second EDFA (labeled EDFA2) to boost the intensity of the probe wave for the energy transfer experiment. After passing through the active device, the probe wave is coupled off-chip and combined with the reference field for heterodyne detection. (b) Plots a SIMS gain spectrum for pump-probe difference frequencies Ω between 500 MHz and 9.5 GHz, showing several resonant gain features corresponding to Brillouin-active elastic modes. The three highlighted dominant modes, labeled B1, B3, and B6, have gain spectra plotted in more detail in corresponding insets. The simulated frequencies of the Brillouin-active modes are plotted as violet circles along the abscissa. The rightmost inset shows the peak single-sideband SIMS gain (red) for mode B6 as a function of increasing pump power, with no observed anti-Stokes component (purple). The gain spectrum is included diagrammatically between the data curves. Adapted from Ref. [221]. 127
- 5.7 Inter-modal Brillouin amplification.** (a) Inter-modal Brillouin gain spectra for mode B6 around 6 GHz, plotted for three different pump powers, showing a narrowband (13 MHz) Brillouin resonance and 3.5 dB of optical gain at the highest tested pump power. (b) plots peak gain (red) and linear (gray) and total optical losses (green) as a function of pump power for this Brillouin-active phonon, while (c) plots the calculated on-chip amplification, obtained by subtracting total loss from Brillouin gain. The pump power threshold for net amplification is 18 mW. Adapted from Ref. [221]. 129

5.8	Inter-modal gain and loss configurations. Four panels show experimental results of inter-modal gain or attenuation for a probe signal in four-different pump-probe configurations. The top two panels show Brillouin gain of a red-shifted probe in anti-symmetric and symmetric modes, respectively, while the bottom two panels show loss in a probe which is blue-detuned from the pump by the Brillouin frequency. Adapted from Ref. [221].	131
5.9	SIMS energy transfer. (a) plots representations of input and output spectra demonstrating inter-modal energy transfer, showing pump-wave depletion and Stokes-wave growth at the device output relative to their input amplitudes. (b) plots experimentally-measured normalized pump and Stokes output powers as a function of total power incident to a SIMS-active device. Adapted from Ref. [221].	133
5.10	Comparison of SIMS and FSBS energy transfer dynamics. Stem plots showing normalized output power spectra under two-tone driving for a FSBS-active waveguide (a) and a SIMS-active waveguide (b). For both experiments, the total incident power is equally divided by two incident waves separated by the Brillouin frequency of the device (denoted by dark blue arrows). While SIMS produces energy transfer only between fields at the incident optical frequencies, FSBS leads to cascaded energy transfer to additional frequency lines. Adapted from Ref. [221].	135
5.11	Elastic modes of the SIMS-active silicon membrane waveguide. (a) Simulated dispersion curves for the observed Brillouin-active elastic modes, with the dominant modes B1, B3, and B6 highlighted and with their displacement profiles plotted alongside. The vertical line labeled $\Delta k(\Omega)$ corresponds to the phonon wavevector determined through optical phase matching for the Brillouin process. (b) Dispersion relations for all elastic modes over this frequency/wavevector window. These modes are categorized according to their dominant displacement profiles. Examples showing three different categories of motion are plotted in subpanels (i)-(iii). Adapted from Ref. [221].	139

5.12	Lithographic tunability of the SIMS frequency. Measured (green) and simulated (black line) Brillouin frequencies for the two elastic modes with the largest Brillouin gain as device width is varied. Adapted from Ref. [221].	141
5.13	Dimension-induced broadening for SIMS. Diagram of the different device dimensions which may vary due to fabrication variations. The effect of each on the Brillouin frequency shift is tabulated in Table 5.1. Adapted from Ref. [221].	141
5.14	SIMS silicon laser design. (a) Depicts a top-down view of the laser design (not-to-scale). A racetrack resonator is composed of two cm-scale suspended Brillouin-active segments. The laser cavity is accessed via a mode-selective coupler which couples a bus waveguide strongly to the anti-symmetric spatial mode of the resonator and weakly to the symmetric mode. This results in the characteristic transmission spectrum of the multimode optical cavity plotted in (b), where the narrow features result from the symmetric mode and the broad features result from the strongly-coupled anti-symmetric mode. Note that the free spectral ranges of the two modes are not identical, making it relatively simple to find a wavelength where the pump-Stokes cavity mode separation is equal to the Brillouin frequency, a necessary condition for strong resonant enhancement. (c) and (d) plot diagrams of the device in the suspended gain region (c) and around the racetrack resonator bends (d), where no acoustic guidance is supported. Adapted from Ref. [222].	143

5.15 Observation of Brillouin laser oscillation. (a) depicts the experimental apparatus used to measure Brillouin lasing. A continuous-wave pump laser at frequency ω_p is split into two paths; the first is amplified and coupled on-chip, while the second is frequency-shifted using an acousto-optic modulator to $\omega_p + 2\pi \times 44$ MHz. The pump and Stokes signal (Brillouin laser) light at frequency ω_s are coupled off-chip and combined with the frequency-shifted reference tone which acts as a local oscillator for heterodyne detection. The combined waves are incident on a fast photo-receiver and the resulting spectrum analyzed using a RF spectrum analyzer. (b) plots theoretical and experimental output laser power vs. incident on-chip pump power, showing a clear threshold around 11 mW. Intracavity powers are determined by using the measured cavity spectra and measured input and output powers. (c) plots heterodyne spectra comparing the measured bandwidths of spontaneously-scattered Stokes light from a linear waveguide and the output beat-note between reference and silicon Brillouin laser light above threshold. Adapted from Ref. [222]. 145

5.16 Linewidth measurements of the silicon Brillouin laser. (a) depicts a simplified version of the standard heterodyne spectroscopy apparatus used to measure the pump-Stokes excess phase noise—equivalent to the phonon linewidth $\delta\nu_b$ below the lasing threshold. In this situation, the phonon linewidth is given by the FWHM of the measured spectrum. (b) depicts a modified sub-coherence heterodyne measurement used to probe the phonon dynamics above threshold. In this experiment, an additional delay τ_d is added in one arm of the unbalanced interferometer, leading to the characteristic spectral shape shown in blue. Here the phonon linewidth is determined by measuring the contrast of interference fringes in the sub-coherence spectrum. (c) plots experimental measurements and theoretical calculations of the phonon linewidth as a function of peak spectral density. Below threshold, the standard heterodyne experiment is used (red dots), while above threshold the sub-coherence measurement technique is used (blue dots). The error bars on the blue dots represent 95% confidence intervals of fits to measured spectra. Adapted from Ref. [222]. 146

5.17 Spontaneous inter-modal Brillouin scattering. (a) Schematic depicting spontaneous Brillouin scattering on-chip. Pump light (green) at frequency ω_p is coupled through a mode multiplexer (M1) into the symmetric waveguide mode. Through interactions with thermal phonons (gray) as it propagates through the waveguide, light is scattered to anti-Stokes (blue) and Stokes (red) sidebands guided in the anti-symmetric mode at frequencies $\omega_p \pm \Omega_b$, where Ω_b is the Brillouin-active phonon frequency of the device. These waves are de-multiplexed into the two ports of an output mode multiplexer (M2).

(b) (i) Through this process, the Stokes scattering process is mediated by a forward-moving phonon, resulting in light scattering to a red-detuned sideband at frequency $\omega_s = \omega_p - \Omega_b$. The lifetime of these phonons can be determined by measuring the spectral bandwidth of the scattered Stokes light.

(ii) (b) The anti-Stokes scattering process is mediated by a backward-moving phonon, resulting in light scattering to a blue-detuned sideband at frequency $\omega_{as} = \omega_p + \Omega_b$. The lifetime of these backward-propagating phonons can be determined by measuring the spectral bandwidth of the scattered anti-Stokes light. (c) and (d) depict phase-matching and energy conservation requirements for Stokes and anti-Stokes scattering processes, which separately determine the wavevectors q_s and q_{as} of phonons that mediate Stokes and anti-Stokes processes. In these diagrams, these phonons produce scattering between initial (open circle) and final (closed circle) optical states through these processes. As plotted on the acoustic dispersion relation (e), these phonons are nearly equal in frequency, and have wavevectors that are nearly opposite in sign. (f) Because the anti-Stokes process annihilates thermal phonons, it increases the effective damping rate of the phonons with which the pump light interacts, resulting in a decrease in the phonon population $\langle n(q) \rangle$ (cooling) for a narrow wavevector band around q_{as} . By contrast, the Stokes process leads to phonon generation, resulting in effective heating of a narrow wavevector band around q_s . In this way, the incident laser field drives the thermal phonon bath out of equilibrium, producing a net phonon flux.

Adapted from Ref. [223]. 152

5.18 **Experimental observation of spontaneous Brillouin cooling.** (a) Experimental diagram used to observe spontaneous Brillouin scattering. Pump light at frequency ω_p is amplified and split into two paths; the bottom path frequency-shifts the light using an acousto-optic modulator (AOM) to a reference frequency $\omega_p + 2\pi \times 44$ MHz to act as a local oscillator for heterodyne detection. In the top path, the intensity of pump light is controlled by an erbium-doped fiber amplifier (EDFA) and variable attenuator (VOA) before being coupled on-chip. As it propagates through the Brillouin-active waveguide, light scatters to anti-Stokes and Stokes sidebands at frequencies ω_{as} and ω_s , respectively, which are coupled off-chip and combined with the reference path for heterodyne detection in the microwave domain. (b) plots measured Stokes and anti-Stokes spectra for several input pump powers. As the pump power increases, the total scattering amplitude increases for both sidebands, but clear asymmetries in height and linewidth are visible. (c) plots the total integrated scattering efficiency ratio between Stokes and anti-Stokes sidebands as a function of pump power in the waveguide. This corresponds to the ratio in phonon occupation numbers (right side). (d) plots the measured dissipation rates as a function of average pump power, showing good agreement with theory. At the highest pump powers of 40 mW, the temperature of the anti-Stokes phonon is cooled over 30 K below room temperature (right y -axis). (e) plots the peak spectral density of the scattered light for both sidebands as a function of pump power. As the pump powers increase, the measured spectral densities deviate from the values expected in the absence of symmetry-breaking between the two processes typical to intra-modal forward-SBS (Ref. [233]). Adapted from Ref. [223]. 154

5.19 **Wavevector-selective phonon spectroscopy.** (a) diagrams the pump-probe experimental diagram. A strong pump laser (frequency $\omega_p^{(2)}$) and weak probe laser (frequency $\omega_p^{(1)}$) are both incident within the optomechanical silicon waveguide. Both pump and probe lasers scatter light through spontaneous inter-modal Brillouin scattering. The pump laser cools a band of phonon wavevectors, while the tunable probe laser has only a small effect on the thermodynamic properties of the system and is used to probe the phonon population as a function of phonon wavevector. The scattered sidebands from the probe laser are analyzed through heterodyne detection referenced by frequency-shifted probe light at frequency $\omega_p^{(2)} + 2\pi \times 44$ MHz. The left panel of (b) shows the measured dissipation rate difference between Stokes and anti-Stokes processes as a function of phonon wavevector, which is selected by the probe wavelength. Each data point represents this dissipation rate asymmetry normalized to a pump power of 30 mW, as determined by measurements of the dissipation rate over a series of ten different pump powers. The theoretical trend from Eq. 5.12 (solid line) shows good agreement with the measured data. Sub-panels (i)-(ii) on the right show sample spectra corresponding to situations where the pump and probe waves are phase-matched to scattering from the same phonon (i) and different phonon bands (ii). Adapted from Ref. [223]. 157

6.1 **Optomechanical silicon inter-band modulator.** (a) plots an artistic representation of the dual-core suspended waveguide, with the cross sectional dimensions diagrammed in (b) The two optical waveguide cores are designed to be different in width by δ to inhibit optical crosstalk. Each waveguide guides fundamental (symmetric) and higher-order (anti-symmetric) optical spatial modes, with E_x field distributions plotted in (c-f). The entire membrane structure confines elastic waves due to the impedance mismatch between silicon and air. The x -displacement field of one such mode that mediates inter-band Brillouin coupling around a frequency of ~ 5.7 GHz is plotted in (g). (h) diagrams the basic operation of the NIBS process. Two optical waves at frequencies $\omega_p^{(1)}$ and $\omega_s^{(1)}$ guided in separate optical modes of the first ‘drive’ waveguide coherently excite an acoustic phonon at their difference frequency Ω through optical forces. Light injected into a second ‘modulator’ waveguide at frequency $\omega_p^{(2)}$ is frequency-shifted to $\omega_s^{(2)} = \omega_p^{(2)} - \Omega$ and mode-converted by this elastic wave through photoelastic coupling. The energy level diagram for this process is shown in (i). (j-k) depict the propagation of light within the modulator waveguide. In the forward direction, light is mode-converted and frequency-shifted through NIBS. In the backward direction, light passes through the device unaffected. Adapted from Ref. [224]. 166

6.2 Phase-matching and operation scheme of the NIBS modulator. (a) shows the operation of two-port mode multiplexers which couple to the symmetric and anti-symmetric optical waveguide modes. (b) plots the dispersion relation of the NIBS-active acoustic phonon. (c) Two strong optical waves in the drive waveguide generate an acoustic phonon through SIMS. (d) plots phase-matching and energy conservation for this process, where the phonon (green) couples light between initial (open circle) and final (filled circle) states. (e-f) depict the propagation of light in the modulator waveguide. In forward operation, light injected into port p1 of M3 (shorthand M3p1) experiences acousto-optic modulation and mode conversion, exiting through port p2 of M4 (M4p2). Light injected in the backward direction through M4p2 passes through the device unaffected and exits through M3p2. (g) shows the phase-matching diagrams for forward (right) and backward propagation (left). In the forward direction, the phonon is phase-matched to an inter-band photonic transition. However, in the backward direction a nonreciprocal wavevector mismatch Δq_{nr} prohibits inter-band coupling. (h) depicts the effects of optical dispersion. In the forward direction, detuning the probe frequency from its phase-matched value ω_f results in a wavevector walkoff Δq_{pm} due to the differing group velocities of the optical modes, leading to a finite operation bandwidth. However, this effect may also cancel Δq_{nr} to produce phase-matched NIBS in the backward direction at ω_b . The resulting transmission spectra are plotted in (i). Adapted from Ref. [224]. . 168

6.3 Experimental demonstration of nonreciprocal modulation. (a) Experimental setup: two optical drive waves separated by the modulation frequency Ω are synthesized from the same laser using an intensity modulator, and are amplified and injected into distinct modes of the drive waveguide through separate ports of mode multiplexer M1. Probe light from a separate laser is split into two paths; in the first path, light is injected into the modulator waveguide in either propagation direction (forward propagation shown here) and mode-converted light is collected at the output. This light is combined with a frequency-shifted local oscillator and incident on a photodiode for heterodyne spectral analysis. (b) Measured modulation efficiency as a function of Ω for one device, revealing strong NIBS coupling through an elastic wave around a frequency $\Omega_B/2\pi = 5.7$ GHz. Hereafter, Ω is fixed to Ω_B . (c) plots the Stokes modulation efficiency for forward- and backward-propagating probe light as a function of probe wavelength, demonstrating nonreciprocal transmission. (d) Zoomed-in plots for three different devices showing broadband modulation and significant nonreciprocal contrast. The three panels correspond to waveguide width asymmetries of $\delta = 5, 10, 15$ nm, changing the center modulation wavelength relative to the pump wavelength. (e) Spectrum of scattered light, showing single-sideband modulation. The residual anti-Stokes-shifted light at $+\Omega$ is due to a small amount of crosstalk during mode multiplexing. (f) Optical tuning of the nonreciprocal modulation response. The drive wavelength is tuned from 1530 nm to 1565 nm, permitting a corresponding shift in the probe response. Adapted from Ref. [224]. 175

6.4	Anti-Stokes NIBS modulation.	(a-b) depict the device operation scheme and energy level diagram in analogy to Fig. 1 of the main article. (a) shows an illustration of nonlocal interband Brillouin scattering for the anti-Stokes process. While the phonon emission is unchanged from the text, light is incident in the anti-symmetric mode of the modulator waveguide. The phonon blue-shifts and mode converts this light as it traverses the device. (b) plots the energy level diagram for this nonlocal coherent anti-Stokes Brillouin scattering process. (c) shows the anti-Stokes modulation response for light propagating in both directions through the modulator waveguide as a function of probe wavelength. (d) plots the corresponding output spectrum relative to a single optical incident field for a wavelength of 1548.3 nm. (e-f) plot data for the Stokes process in the same device for comparison. (e) plots the forward-backward Stokes modulation response, while (f) plots the output spectrum at a probe wavelength of 1548.3 nm. Adapted from Ref. [224].	177
6.5	Phase-mismatched NIBS response.	Frequency response of one silicon NIBS modulator device four different probe wavelengths, and hence wavevector mismatches. (a) $\lambda_p = 1544.1$ nm, $\Delta q = -1422$ m ⁻¹ (b) $\lambda_p = 1548.4$ nm, $\Delta q = 0$ m ⁻¹ (“phase-matched”) (c) $\lambda_p = 1549.3$ nm, $\Delta q = 297$ m ⁻¹ (d) $\lambda_p = 1549.7$ nm, $\Delta q = 428$ m ⁻¹ . These different lineshape behaviors result from position-dependent changes in device dimensions, and hence optical and acoustic propagation. Adapted from Ref. [224].	179
6.6	Experimental modulation efficiency.	NIBS modulation efficiency for one device as a function of incident drive-waveguide power. Adapted from Ref. [224].	180

6.7	NIBS modulation within the scattering matrix formulation.	(a-d)	show the output wave amplitudes at each port corresponding to light incident in each port of the four-port modulator waveguide. In (a-b), significant mode conversion is achieved in the forward direction ($\eta_f^2 \approx 1$), while in the backward direction light propagates through the device with only a small amount being mode-converted ($\eta_b^2 \ll 1$). (e) shows one potential approach to construct a frequency-neutral acousto-optic isolator based on serial cascading of two NIBS modulators. Adapted from Ref. [224].	184
6.8	Dispersion engineering and the phase-matching bandwidth.	(a)	shows the relevant cross-sectional dimensions of a ridge waveguide used to construct the silicon NIBS modulator, and the simulated x -component of the electric field for the symmetric and anti-symmetric optical modes. (b) Calculated normalized transmission as a function of wavelength shows the expected sinc-squared response in the forward and backward directions. (c) An alternative ridge waveguide design with reduced ridge dimensions and angled sidewalls, resulting in a tenfold reduction in the difference of group indexes. (d) Calculated normalized transmission of a NIBS process using waveguides shown in (c). The reduction of Δn_g increases the bandwidth by a factor of ten. Adapted from Ref. [224].	199

<p>A.1 Suspended silicon membrane waveguide fabrication. (a) Diagram of the SOI wafer cross-section as-received. (b) depicts the wafer after HSQ resist is spun on the surface. (c) e-beam lithography defines the waveguide pattern layer. After development of the exposed layer and etching, these patterns are transferred to the silicon layer through Cl_2 reactive ion etching, shown in (d). (e) shows the cross-section when a second positive resist is spun on top of the processed wafer. (f) A second electron beam lithography and development step defines patterns for the slot features. (g) These features are etched through the silicon top layer through a second Cl_2 dry etch step. (h) depicts the final structure after wet-etching in HF. <i>Image credit: Heedeuk Shin and Eric Kittlaus.</i></p>	206
<p>B.1 Input coupling for SOI waveguides using grating couplers. (a) shows a schematic of an optical fiber aligned to an integrated grating coupler, with relevant grating dimensions: pitch Λ, etch depth d, and filling factor $f(z)$. (b) close-up SEM of a fabricated grating coupler, with an apodized filling factor (c) depicts stitched-together SEMs showing the entire input coupler region of a SOI ridge waveguide (d) and (e) show sample transmission data for waveguides interfaced with two apodized grating couplers (d) or two grating couplers with a constant fill factor (e).</p>	209
<p>B.2 Experimental setup for coupling light into integrated optical waveguides. (a) shows an early two-port setup where optical fibers are aligned to the surface of an SOI chip using mechanical translation and rotation stages. An optical imaging system allows alignment of the fibers to integrated grating couplers with micron-scale position, as shown in (b). (c) pictures an alignment setup for characterizing devices with eight total ports. An inset is expanded in (d), showing the region where light is coupled on- and off-chip using optical fiber arrays.</p>	211

List of Tables

3.1	Simulated Changes in Brillouin Frequency Due to Dimensional Variations .	80
5.1	Simulated Changes in Brillouin Frequency Due to Dimensional Variations for the SIMS-active Waveguide	142
6.1	Measured and Calculated Device Parameters	182

Chapter 1

Introduction

1.1 First Observations of Brillouin Scattering

When light passes through a material, some part of it may be scattered via its interaction with the medium's polarizability. Under typical circumstances, most light is scattered elastically and no energy is exchanged with the material. This elastic scattering process, studied by Lord Rayleigh in the late 19th century, is now commonly referred to as *Rayleigh scattering* [1–3]. Such processes are responsible to phenomena ranging from the blue color of the daytime sky [1] to the dominant source of scattering losses from local density variations in glass optical fibers [4, 5].

Light may also scatter inelastically, exchanging energy with a material's internal motional degrees of freedom. It was predicted as early as 1919 that light should be Doppler-shifted by the thermal motion of particles within a medium [6–8]. In other words, even a perfect material is neither homogeneous nor in equilibrium due to the presence thermal vibrations, and interactions with its moving component particles could lead to small spectral shifts of the scattered light. This effect was reported by C.V. Raman in a 1922 letter [9], and possibly explained results of earlier experiments by Rayleigh [10]. Subsequent experiments by Raman and others revealed the inelastic scattering of light due to molecular vibrations in the late 1920s [11–16], leading to the discovery of the eponymous *Raman effect*.

That light could also scatter from traveling elastic waves was first suggested by Brillouin [17] and Mandelstam [18] in the 1920s, and this theory expanded upon by Debye [19]. Due

to the much smaller (\sim GHz) Doppler shift associated with these waves as compared to intramolecular vibrations (\sim THz), experimental observation of this effect was very difficult. The first evidence of light scattering from elastic waves was published in 1930 [20], with more definitive experiments showing photographically-resolved Brillouin scattering in 1932 [21] and thereafter [22, 23]. Subsequent experiments with more sophisticated measurement techniques used the detection of Brillouin scattering components to measure the elastic properties of liquids [24] and crystals [25]. However, the flexibility of these measurements as a spectroscopy tool was limited due to the lack of bright, narrowband light sources.

1.2 Discovery of Stimulated Light Scattering

The invention of the maser [26, 27] and laser [28, 29] allowed the creation of narrowband, highly-coherent electromagnetic radiation. These new devices became the enabling technology for nonlinear optics and revolutionized spectroscopy by providing intense, highly-customizable light sources.

These advances also led to the observation of ‘stimulated’ light scattering for the first time: Rather than simply acting as a passive, linear process, inelastic light scattering could be used to mediate nonlinear optical energy transfer. The first manifestation of stimulated light scattering occurred in 1962, when a strong frequency-shifted signal was seen from a Q -switched ruby laser [30]. It was observed that this frequency shift matched the Raman shift of the nitrobenzene Kerr cell used to mediate Q -switching. Further analysis revealed that the Raman effect in this material was creating optical gain, an effect later reported in many other organic liquids [31], and studied theoretically [32].

Observations of cascaded Stokes and anti-Stokes Raman scattering [33] led to the understanding of SRS as a process which drives coherent molecular vibrations (optical phonons) [34], and the realization that the same should be possible with scattering from acoustic phonons [35]. These conclusions resulted in the experimental demonstration of stimulated Brillouin scattering (SBS) from maser sources in crystals [36] and by laser light in liquids [37–39].

Subsequent theoretical and experimental work explored the photoelastic coupling mech-

anism, temporal dynamics, and spectroscopic applications of SBS [40–55]. Brillouin lasing was also demonstrated in liquids [40, 56–58] shortly after the initial demonstration of SBS, and later in gas cells [59]. Much of this work seems to be overlooked in the modern literature, which tends to focus on later fiber-optic-based Brillouin lasers.

An interesting application of Brillouin lasing within bulk geometries that was immediately identified was the ability to tune the Brillouin frequency shift as a function of angle between pump light and the laser cavity [40]. This results from the phase-matching condition for SBS, and may be used to fine-tune the frequency of the Brillouin laser output relative to that of the pump.

In 1972, it was observed that backward SBS is a phase-conjugate process, so that the back-reflected light retraces the path of the incident light [60]. This effect was later studied theoretically [61, 62], and used for applications including the correction of wavefront aberrations [63, 64], phase-conjugate mirrors [65–67], and beam combining [68–70].

1.3 Stimulated Brillouin Scattering In Optical Fibers

The development of low-loss optical fiber in the 1970s [71–74] revolutionized not only the field of optical communications, but also brought about the new field of nonlinear fiber optics [75]. In contrast to bulk nonlinear optical experiments, where light either interacts only over several diffraction lengths, or must be confined within an optical cavity, optical waveguiding by total internal reflection permitted low-loss guidance of light within a microscale fiber core over kilometer lengths. These long interaction lengths make optical fiber one of the most nonlinear optical devices available to this day.

1.3.1 First Observations and SBS as a Power-handling Limit

Optical fiber also became a natural place to study Raman and Brillouin interactions. However, rather than being viewed as a potential tool for creating amplifiers and lasers, SBS was understood to represent a fundamental power handling limit [76]; assuming that strong Brillouin scattering occurred over sufficient interaction lengths, spontaneously-scattered light could initiate stimulated Brillouin scattering as it traversed the fiber, leading to depletion of

input signal light. This prediction was especially troubling since narrow-linewidth sources, which do not suffer from excessive chromatic dispersion and are therefore useful for optical communications, have spectral bandwidths narrower than that of the Brillouin response, and as a result have very low power thresholds for SBS to occur.

The first demonstration of SBS in fiber optics was reported in 1972 by Ippen and Stolen [77] using a pulsed xenon laser source with a bandwidth of ≈ 100 MHz, comparable to the spontaneous Brillouin linewidth in bulk quartz [54]. This research revealed a Brillouin threshold around 1 W at visible wavelengths, corresponding to threshold powers on the order of 40 mW at near-IR wavelengths, representing a limit to optical power capacity. Further research showed that the SBS threshold could be as low as a few mW for coherent laser excitation in long, low-loss fibers [78, 79].

Suppression of SBS in optical fibers subsequently became an active area of research. Early experiments explored suppression using phase- and amplitude-modulation schemes [80, 81] and straining of the fiber within cables to broaden the Brillouin resonance [82]. Further work investigated varying the fiber core radius along its length [83], nonuniform doping of the fiber core [84], and the use of optical isolators to eliminate back-scattered light [85]. Research on SBS suppression continues to this day [86–90].

1.3.2 Fiber Brillouin Lasers

Simultaneously, research also examined how SBS could be harnessed for useful operations within this new system. The long interaction lengths and low losses of fiber optics make them a natural platform for nonlinear optics, and in particular Brillouin lasers.

The first continuous-wave Brillouin laser utilizing optical fiber within a ring cavity was reported in 1976 using a visible argon-ion laser as a pump [91]. The development of low-loss fiber-optic directional couplers [92, 93] allowed the creation of ultrahigh- Q fiber ring resonators suitable for low-threshold lasers [94]. Such an all-fiber Brillouin ring laser was demonstrated in 1982 with a 0.5 mW pump threshold at 632 nm [94].

One potential application of low-threshold Brillouin lasers was the use of cascaded Brillouin lasing within a high- Q ring cavity for inertial sensing [95], by initiating lasing in counter-propagating directions within a Sagnac loop. This capability is possible because, in

contrast to conventional gain media which provide equal amplification in both propagation direction, backward SBS gain is mediated by traveling-wave phonons which couple to single pairs of counterpropagating pump and signal waves without gain competition. However, at the time low polarization stability and relatively low- Q ring cavities prevented the observation of the gyro effect. This effect was finally demonstrated using bidirectional Brillouin lasing in 1991 [96].

Brillouin lasers are notable for producing highly-coherent laser oscillation as compared to the input pump light. Optimization of fiber Brillouin lasers with active stabilization demonstrated linewidths below 100 kHz [97] in 1981. Further improvements in stabilization schemes allowed sub-kHz operation limited by only by environmental control [98].

1.3.3 Fiber Brillouin Amplifiers

While the potential of SBS for stimulated amplification was studied as early as 1968 [53], practical use of this effect was challenging due to the difficulties of precisely measuring the Brillouin gain spectrum and synthesizing suitable pumps. One early application of stimulated backward light scattering was for pulse compression [99]. In the 1980s, SBS in gas cells was used for subnanosecond pulse generation [100] and pulse amplification [101].

The first fiber Brillouin amplifier was demonstrated in 1986, achieving net gain in a 37.5-km fiber [102]. This application of SBS was particularly interesting since Raman and Brillouin amplification provide a potential means to increase signal propagation lengths without expensive repeater systems. A potential limitation of SBS amplification is its relatively narrow bandwidth (10-100 MHz in fibers), which limits signal bandwidth. By utilizing a modulated pump laser, it was demonstrated that the Brillouin bandwidth can be controllably increased, at the expense of the overall optical gain strength [103].

1.3.4 Brillouin-based Sensing

Beyond applications for optical amplification and lasing, Brillouin scattering in optical fibers enables distributed sensing of strain and temperature. This technique results from the fact that the Brillouin frequency shift is very sensitive to changes in these parameters—therefore, if the temperature or strain gradient changes along the length of a fiber, this

leads to a position-dependent Brillouin frequency shift. Because BSBS scatters light in the backward direction, time-of-flight resolution between incident and back-scattered light permits localization of the scattered signal.

This approach was first experimentally demonstrated in 1989 [104]. Since then, a tremendous amount of work has been carried out on this topic [105–137], demonstrating capabilities such as dynamic operation, simultaneous strain and temperature measurement, 100 km sensing range, and km-range sensing with sub-cm resolution.

These approaches generally fall into one of three groups. Brillouin optical time-domain reflectometry (BOTDR) uses unidirectional access to a fiber and measures spontaneous back-scattering along its length. Brillouin optical time-domain analysis (BOTDA) uses counterpropagating pump and probe waves to measure the Brillouin response of the fiber. BOTDA is limited to ~ 1 meter resolutions by the acoustic lifetime, since shorter pulses necessary for greater signal localization broaden the Brillouin gain spectrum, reducing the scattered signal and decreasing sensitivity to Brillouin line shifts. Brillouin optical correlation domain analysis (BOCDA) utilizes counterpropagating waves which are relatively coherent (and thus couple through SBS) only at a scannable point (or set of points) along the fiber. This approach achieves considerably better spatial resolution than BOTDA. However, these correlation-domain techniques have a lower signal-to-noise ratio (and equivalently require much longer integration times) resulting from necessary post-processing and wide modulation bandwidths (which broaden the effective gain spectrum) that are used to achieve high spatial resolution.

1.3.5 Brillouin Dynamic Gratings

In the backward-SBS process, counterpropagating pump and Stokes waves coherently drive a longitudinal traveling elastic wave. This acoustic phonon acts as a Bragg grating that back-reflects pump light into the Stokes wave, while Stokes light passes through unaffected due to the relative phase between elastic and Stokes waves. In this sense, SBS provides a method to create dynamically reconfigurable Bragg reflectors within optical fiber. This technique, commonly referred to as a Brillouin dynamic grating (BDG or DBG), has been studied over the past decade [138, 139] with applications including tunable filters [140, 141],

distributed sensing [142], tunable time delay [143], and optical signal processing [144, 145].

Typically, a BDG is written with pump and Stokes waves propagating along one axis of a polarization maintaining fiber (PMF). This grating is then used to reflect signal light guided in the other polarization, avoiding crosstalk between drive and signal waves. As the fiber length, and hence grating length increases, the peak reflectivity increases while the grating bandwidth decreases, as would be expected from a traditional Bragg reflector. Beyond PMF, work has also been done to demonstrate a BDG in conventional single-mode fiber [146], although much lower scattering efficiency is observed than is theoretically predicted. Some work has also been done to adapt these concepts to chip-scale architectures [147].

1.4 Brillouin-based Signal Processing

Because SBS allows for highly-selective gain and loss, as well as dynamic tunability and reconfigurability of the gain spectrum, it is a natural tool for optical and microwave signal processing. As early as the early 1990s, SBS was recognized as a powerful method for microwave frequency synthesis [148] and signal processing [149–151]. In 1991, Culverhouse et al. demonstrated that by combining pump and Brillouin laser light on a photodiode, the resulting microwave beat note at the Brillouin frequency is driven with high efficiency [148]. Later work on frequency synthesis explored Brillouin-based optoelectronic oscillators [152, 153], fiber-based synthesizers [154, 155] including tunable microwave sources at frequencies greater than 100 GHz [156], and microchip-based technologies [157, 158].

Beyond its utility for microwave synthesis, SBS has also been used for creating tunable optical and microwave photonic filters [159–163]. In contrast to all-optical filters, SBS is particularly useful because it allows narrowband (kHz-MHz) filtering without the use of optical resonators that experience signal distortion at moderate powers, and is also bandwidth-tunable through pump modulation [160, 161]. Recent work has demonstrated potential for high-performance chip-based Brillouin filtering of microwave signals [164–166] for use within integrated systems.

The narrow bandwidth and strong gain of SBS allows for a strong dispersive response about the Brillouin frequency. This effect was harnessed to demonstrate slow light and time

delay within an optical fiber [167], representing a practical advance over previous schemes for slow light which utilized ultracold atoms [168] or gain crystals [169,170]. However, while SBS is strong compared to other optical nonlinearities, it is still a relatively weak effect in most fibers, so the optical group index changes demonstrated via SBS are much smaller than those possible with coherent electronic effects. Nonetheless, since it can be achieved with commercial telecommunications equipment, SBS-based slow light remains a technologically-relevant operation for all-optical time delay [171–173]. Alternately, optical pulse storage can be achieved by converting light to and from the phononic domain, provided the storage time is smaller than the lifetime of the elastic wave [174].

1.5 Forward and Inter-modal Brillouin Scattering in Optical Fibers

Because elastic dispersion bands are much flatter than those of optical waves (i.e. sound travels more slowly than light), in bulk systems sound cannot phase-match to a Brillouin scattering process between two optical frequencies on the same dispersion branch. As a result, SBS was traditionally studied in backward scattering or off-axis geometries to satisfy phase-matching between optical and elastic waves. However, within systems which possess either multiple optical modes or transverse acoustic guidance, Brillouin scattering in the forward direction becomes possible.

Forward Brillouin scattering was first reported in 1985 by Shelby et al. [175,176]. In this process, the radial ‘breathing’ elastic modes of an optical fiber with near-zero wavevector produce spontaneous light scattering from a bright pump in the form of additional optical phase noise [177]. At the time, this process was seen as a source of noise in quantum experiments [178].

Inter-modal forward Brillouin scattering was first observed within a dual-mode optical fiber by Russell et al. in 1990 [179]. In this forward-scattering process, the elastic mode now has a finite wavevector (and substantial group velocity) to satisfy phase-matching for light scattering between two optical modes with different wavevectors. Although the overlap between photonic and phononic modes was weak within the fiber optic waveguide,

the thresholds for backward SBS and inter-modal SBS were nearly identical. This can be understood as resulting from the very low Brillouin frequency for inter-modal scattering (17 MHz) and resulting larger elastic wave compliance and lifetimes, which directly increase the Brillouin coupling. Further increases in phononic lifetimes were predicted to permit new regimes of Brillouin dynamics where energy could coherently transfer between optical and elastic fields [180].

The development of microstructured photonic crystal fibers (PCF) [181, 182] allowed for new degrees of control over Brillouin scattering through tailoring of the overlap between light and sound waves [183–185]. Such systems permitted considerable increases in the coupling strength of forward intra- and inter-modal Brillouin scattering by providing tight lateral confinement of elastic waves. In the context of intra-modal forward SBS (FSBS), this allowed strong energy transfer from injected pump and Stokes waves to many cascaded Stokes and anti-Stokes orders [186]. These dynamics are possible since, in contrast to other forms of SBS, in FSBS both Stokes (red-shifting) and anti-Stokes (blue-shifting) scattering processes are mediated through coupling to the same phonon mode and hence have an intrinsic symmetry. Through these experiments, when 500 mW of light was injected into two tones separated by the FSBS frequency, 14 optical frequency lines spaced in increments of 1.83 GHz were observed through 10 m of PCF [186].

By contrast, inter-band Brillouin interactions, like BSBS (which scatters light between forward- and backward- propagating dispersion bands), couple only two optical waves. Within photonic crystal fibers, stimulated inter-polarization Brillouin scattering (SIPS), which is a form of inter-modal coupling, was used to demonstrate near-complete optical energy transfer between two optical fields separated by 1.5 GHz [187]. For this experiment, a total of 300 mW of guided-wave input power was incident in a PCF 15 m in length. Because SIPS couples co-propagating optical waves to produce stimulated energy transfer, it is intrinsically nonreciprocal—in the presence of one strong wave, a second frequency-matched wave experiences optical energy transfer only when it travels in the same direction. This technique was used to produce a switchable opto-acoustic isolator in PCF by driving unidirectional depletion of incident light at the Brillouin frequency [188]. While the bandwidth of this isolator was limited to that of the Brillouin gain (7 MHz), utilizing separate waves

to drive the acoustic wave would allow dramatic improvement of the operating bandwidth for isolator technologies of this type.

1.6 Light-sound Coupling at the Nanoscale

The realization of tailorable Brillouin scattering within microstructured fibers marked the beginning of a revolution of SBS applications within microscale systems such as whispering-gallery-mode (WGM) resonators [189] microspheres [190] and wedge resonators [191], suspended-core fibers [192, 193], and nanoscale waveguides [165, 194–197]. Within these systems, the strength and character of Brillouin interactions can be shaped through device geometry allowing radical enhancement [195] or complete self-cancellation [198] of these effects. By controlling interactions between phononic and photonic waves at the mesoscale, a variety of technologies including ultralow-noise Brillouin lasers [189, 199, 200], microwave synthesizers [157, 158] and signal processing technologies [164, 165, 201–203], and novel optomechanical systems [190, 204–211] become available.

1.6.1 SBS within Whispering-gallery-mode Resonators

Fiber ring resonators proved very useful as a platform for creating Brillouin lasers [94] due to their ability to provide large interaction lengths with low intrinsic losses. These lasers admitted a variety of applications including narrow-linewidth laser oscillation [97, 98], inertial sensing [95, 96], and microwave frequency synthesis [148]. The ultimate performance of Brillouin laser systems is limited by environmental stability, which is difficult to precisely control in meter-scale fiber optic systems.

The development of high quality factor (Q) optical microresonators presents an alternative paradigm to achieving low-threshold Brillouin laser oscillation within stable microfabricated systems [212]. Brillouin lasing with only a 3 μW threshold was observed in micromachined, highly-multimode calcium fluoride resonators [189]. Within these single-crystal resonators, the Brillouin frequency is direction-dependent, although this effect was weakest for the longitudinal phonon mode used to mediate Brillouin lasing. Within amorphous material systems, microcavity Brillouin lasers have been used to produce ultra-stable

oscillators [213] and Hz-absolute linewidth laser operation [214] ultimately limited by thermorefractive noise within the resonator itself.

An alternate approach to producing high- Q microresonators is based on lithographically-defined silica-on-silicon wedge resonators [191]. In contrast to micromachined WGM devices, these structures are fabricated on-chip, allowing for inexpensive and scalable fabrication, and may be designed from millimeter to centimeter scales. This last point is especially important since, at the time, fabrication of large microcavity resonators with free-spectral ranges small enough to match the Brillouin frequency shift (a necessary condition for Brillouin lasing) was very difficult. (While Brillouin lasing had been observed in highly-multimode resonators [189], the presence of many mode families may be undesirable.) In the largest tested wedge resonator devices, Q -factors nearing 1 billion were achieved, and controllable single-transverse-mode Brillouin lasing was achieved at thresholds below 200 μW . These resonators were subsequently used for applications including narrow-linewidth lasing, microwave frequency synthesis [157], and gyroscopes [215]. In other words, these resonators provide a powerful platform which has adapted many previously-studied applications of Brillouin fiber lasers to on-chip implementations. The recent demonstration of these high- Q resonators fabricated with silicon nitride bus waveguides may allow these technologies to be adapted within integrated photonic circuits [216].

In addition to the considerable work being done to adapt BSBS-based lasers to millimeter-scale resonators, concurrent work sought to explore optomechanical coupling through SBS within smaller microscale resonator devices which laterally confine both light and sound waves [204]. In contrast to radiation-pressure-based cavity-optomechanical systems [217], these devices utilize electrostrictively-mediated coupling between distinct optical modes. Through forward inter-modal SBS, silica microsphere and microtoroid resonators have demonstrated optomechanical self-oscillation [204], cooling and heating of phonon modes [205], and SBS-based optomechanically-induced transparency and nonreciprocal light transmission [207–211].

1.6.2 SBS in Nanoscale Waveguides

Photonic crystal fibers and other microscale systems demonstrated the capability to enhance SBS by shrinking optical and acoustic mode sizes. However, even within small-core fiber systems, interaction lengths of many meters are necessary for appreciable Brillouin coupling to occur. Nonetheless, these inventions showed the potential for strong Brillouin interactions, which may be adapted to integrated waveguide systems. This prospect is especially intriguing since, ultimately, the impact of many Brillouin-based signal-processing technologies is contingent on scalability, and their ability to be economically integrated within complex photonic microsystems.

Interestingly, it turns out that, as optomechanical waveguide core sizes are shrunk to wavelength-scale dimensions, Brillouin coupling strengths become enhanced beyond what is predicted from traditional SBS theory [195]. The reasons for this increase are twofold. First, due to the decreased modal areas of both light and sound waves, their combined interaction strength is greatly enhanced, particularly in the case of forward-SBS interactions. Second, within many waveguide systems, Brillouin coupling due to boundary-induced radiation pressure becomes significant (comparable to or exceeding that due to electrostriction) and may coherently add to the electrostrictive interaction. These effects were predicted to create both forward- and backward-SBS couplings within suspended silicon nanowires that were many orders of magnitude (10^4 - 10^5 times) greater than those in optical fibers [195]. The potential for strong SBS within silicon waveguides is particularly intriguing due to silicon's mature fabrication infrastructure, and the potential integration of electronic and optical/optomechanical devices on the same chip. Furthermore, SBS offers a path to create strong and tailorable optical nonlinearities in silicon, despite its relatively limited active optical properties (e.g. silicon lacks a χ_2 nonlinearity). More generally, strong Brillouin interactions within integrated photonic waveguides open the door to an array of on-chip SBS-based signal processing and nonlinear optical applications.

Stimulated Brillouin scattering in integrated waveguides was first demonstrated in 2011 within micron-scale As_2S_3 ridge waveguides [194]. This work utilized both the large photoelastic coupling of chalcogenide glasses and the elastic-wave guidance of these waveguides

within silica claddings to achieve backward-SBS gain coefficients in excess of $200 \text{ W}^{-1}\text{m}^{-1}$; these numbers are roughly three orders of magnitude greater than those for silica fibers. Net optical amplification of around 10 dB was demonstrated, even with relatively high waveguide losses of around 6 dB.

Despite significant work toward developing silicon as an integrated photonic platform, SBS in silicon waveguides was not previously observed. This absence of SBS in traditional silicon-on-insulator waveguides results from silicon’s relatively weak photoelastic response in the longitudinal direction (i.e. BSBS is intrinsically weak in silicon). Furthermore, in silicon-on-insulator waveguides, elastic waves are not guided in the silicon core, stifling SBS interactions.

In order to observe strong SBS in integrated silicon waveguides, it was necessary to remove the silica substrate to facilitate the guidance of phonons. This technique was used in 2013 to observe SBS in silicon waveguides for the first time [196]. In this study, nanoscale silicon optical waveguide cores were embedded within a silicon nitride membrane, with phononic slot mirrors patterned in the membrane to provide transverse acoustic confinement. Within this structure, Brillouin gains $G_B > 2000 \text{ W}^{-1}\text{m}^{-1}$ were demonstrated through forward-SBS (FSBS) interactions. Subsequent works demonstrated silicon nanopillar [197] and suspended nanowire [218] waveguides with increased nonlinearities up to $G_B = 10^4 \text{ W}^{-1}\text{m}^{-1}$.

However, despite the realization of record-high nonlinearities in silicon, modest optical power handling, combined with high linear and nonlinear losses in these structures, prevented the demonstration of appreciable Brillouin amplification in these structures. As such, it remained unclear whether these interactions could be used to create silicon-based Brillouin amplifiers and lasers.

Furthermore, FSBS produces dynamics that differ from those of the traditionally-studied backward-SBS process, necessitating further effort to design and implement new FSBS-based signal processing operations. In particular, while BSBS couples only two counter-propagating optical waves, FSBS can couple to many optical tones through interactions with the same acoustic phonon. As a result, FSBS does not produce single-sideband gain, but rather an unusual form of dual-sideband gain, making it nontrivial to adapt the wide ar-

ray of established BSBS-based technologies for Brillouin-enabled signal processing to silicon photonic systems.

As the field explores possibilities for harnessing FSBS, one avenue which has shown early promise for silicon Brillouin photonics is the creation of chip-based microwave-photonic filters [165, 166, 202]. In particular, because FSBS interacts through transversely-confined phonons, by coupling multiple optical waveguides to the same phonon mode, new hybrid photonic/phononic signal processing architectures become available. In a 2015 paper by Shin et al. [165], band-pass filter responses with ultra-narrow 3 MHz-bandwidths were demonstrated through this method, with steep rolloffs and >60 dB out-of-band rejection. Future work may implement these filter functions within fully-integrated signal processing circuits.

1.7 Outlook and Summary of Dissertation

Building on the recent demonstration of strong Brillouin nonlinearities in chalcogenide (Pant et al., 2011 [194]) and silicon waveguides (Shin et al., 2013 [196]), we are only beginning to explore and understand the possibilities for integrated Brillouin photonics. Nonetheless, these and other advances paint a promising picture for the potential impact of Brillouin-based signal processing technologies within integrated optical waveguides. Coupled with rapidly-advancing technologies for on-chip optical circuits, light sources, modulators, detectors, and other components, SBS may enable a wide array of new chip-based optical and optomechanical technologies.

In this dissertation, we report several recent advances which further expand the toolkit of chip-based optics through Brillouin interactions. These new capabilities represent a significant step toward the realization of flexible photonic-phononic devices within integrated optical circuits.

This dissertation is structured as follows:

- In Chapter 2, we describe the origins and theoretical behavior of stimulated Brillouin scattering, with a focus on guided-wave systems. We begin by studying the coupling mechanisms necessary for SBS, and the essential conditions for strong SBS to occur.

Next, we derive the dynamics for three different SBS processes in optomechanical waveguides: backward SBS, forward-SBS, and inter-modal SBS. Finally, we compare the spatial character of these couplings.

- In Chapter 3, we develop a new optomechanical ‘suspended membrane waveguide’ structure which permits robust Brillouin amplification in silicon. Through passive reduction of both linear and nonlinear losses which hindered performance in prior devices, this device supports net optical amplification through FSBS at just ~ 5 mW optical pump powers, demonstrating impressive potential for silicon-based Brillouin devices. This work is based on Ref. [219].

[219] E.A. Kittlaus, H. Shin, and P.T. Rakich, “Large Brillouin Amplification in Silicon.” *Nature Photonics* **10**, 463-467 (2016).

- In Chapter 4, we use these strong FSBS interactions in silicon to produce high-fidelity microwave filters using hybrid photonic-phononic signal processing. Through this process, an RF signal is encoded on intensity-modulated light incident in a suspended silicon waveguide; through FSBS, this optical signal transduces this information onto an acoustic phonon, which is filtered through the device’s intrinsic elastic response before being encoded on light guided in a spatially separate waveguide. This form of nonlocal emit-and-receive coupling produces tunable, narrow-bandwidth filtering, while avoiding nonlinear distortion associated with optical ring resonator filters, and does not experience additive noise commonly associated with filters based on Brillouin gain. This work is based on Ref. [220].

[220] E.A. Kittlaus, P. Kharel, N.T. Otterstrom, Z. Wang, and P.T. Rakich, “RF-Photonic Filters via On-Chip Photonic–Phononic Emit–Receive Operations.” *Journal of Lightwave Technology* **36**, 13, 2803-2809 (2018).

- In Chapter 5, we demonstrate stimulated inter-modal Brillouin scattering (SIMS) on-chip. This interaction produces strong Brillouin coupling between two distinct spatial optical modes of a silicon waveguide. In contrast to intra-modal FSBS, SIMS produces two-field couplings reminiscent of traditional BSBS, providing a platform to adapt

many existing schemes for BSBS-based signal processing in fiber to silicon photonic circuits. Moreover, this process utilizes on-chip mode multiplexing to route pump and signal waves without the use of circulators as is necessary in BSBS-based systems. We use this interaction to produce optical amplification and single-sideband energy transfer in Ref. [221]. Subsequently, this interaction was used to realize two advances in Brillouin photonics: the first Brillouin laser in a silicon waveguide [222], and the first demonstration of optomechanical cooling within a continuous system [223].

[221] E.A. Kittlaus, N.T. Otterstrom, and P.T. Rakich, “On-chip inter-modal Brillouin Scattering.” *Nature Communications* **8**, 15819 (2017).

[222] N.T. Otterstrom, R.O. Behunin, E.A. Kittlaus, Z. Wang, and P.T. Rakich, “A silicon Brillouin laser.” *Science* **360**, 6393, 1113-1116 (2018).

[223] N.T. Otterstrom, R.O. Behunin, E.A. Kittlaus, and P.T. Rakich, “Optomechanical cooling in a continuous system.” *Physical Review X* **8**, 041034 (2018).

- Finally, in Chapter 6 we present a multi-core device which produces an interaction termed nonlocal inter-band Brillouin scattering (NIBS). Through this process, an optically-driven phonon spatiotemporally modulates light in a multimode waveguide to produce nonreciprocal acousto-optic modulation and mode conversion. This traveling-wave interaction produces wideband (>1 nm) nonreciprocity in a low-loss integrated waveguide for the first time, representing a significant step toward the creation of practical waveguide-integrated optical isolators and circulators. These results are based on Ref. [224].

[224] E.A. Kittlaus, N.T. Otterstrom, P. Kharel, S. Gertler, and P.T. Rakich, “Nonreciprocal interband Brillouin modulation.” *Nature Photonics* **12**, 613-619 (2018).

Chapter 2

Theory of Stimulated Brillouin Scattering

In this chapter, we categorize the various types of Brillouin interactions within guided-wave systems, and explore the necessary conditions for efficient light-sound couplings to occur. In contrast to bulk systems, where SBS occurs between optical waves traveling in different directions, we will find that within microscale optomechanical waveguides both inter- and intra-modal Brillouin couplings are possible between co-propagating light waves. Furthermore, due to the traveling-wave nature of SBS, these differing geometries produce a variety of distinct dynamical behaviors.

We begin by discussing the physical mechanisms behind light-sound couplings within dielectric media, and derive the bulk Brillouin interaction strength. Next, we explore backward- and forward-SBS within one-dimensional optomechanical waveguides which laterally confine both light and sound waves. Through analysis of the phase-matching requirements for each scattering process, we determine what forms of Brillouin couplings are allowed, and solve the coupled amplitude equations for each to determine the corresponding spatial dynamics.

2.1 Origins of Brillouin Interactions

The interaction between light and elastic waves in matter was theorized by Brillouin [17] and Mandelstam [18] in the 1920s, and was first experimentally studied in the early 1930s [20, 21, 225]. These interactions result from changes of the material dielectric tensor ε in response to an applied elastic strain field S [226]:

$$\Delta\varepsilon_{il} = \varepsilon_{ij}p_{jkmn}\varepsilon_{kl}S_{mn}, \quad (2.1)$$

where p_{ijkl} are the components of the photoelastic (also called elasto-optic) tensor, typically determined through empirical measurements [226, 227]. Practically every dielectric material exhibits a nonzero photoelastic response, though the magnitude and behavior of acousto-optic (Brillouin) couplings depend directly on the form of the photoelastic tensor.

Through the photoelastic effect, elastic waves create time-dependent refractive index variations, which may scatter incident light to a different optical frequency and wavevector. Inelastic acousto-optic scattering interactions can be classified as either Stokes (red-shifting) or anti-Stokes (blue-shifting) processes. In the former process, a phonon is excited, and in the latter process, a phonon is annihilated and its energy transferred to the optical field. These two processes are diagrammed in Fig. 2.1.

Photoelastic couplings are typically termed according to the source of incident phonons, despite having similar underlying physics: light scattering from externally-driven elastic waves (e.g. ultrasound driven through the piezoelectric effect) is commonly referred to as acousto-optic light scattering. Light may also scatter from incoherent thermal phonons within a material through spontaneous Brillouin scattering (also called Brillouin light scattering). Finally, multiple light fields may couple through nonlinear interactions with elastic waves in a material, which is termed stimulated Brillouin scattering. These types of Brillouin interactions permit control of both light and sound waves within dielectric media.

For stimulated Brillouin scattering to occur, the sound waves that scatter light through photoelasticity must be driven by optical waves within the medium. This optical driving of acoustic waves is achieved through electrostrictive forces, which result in mechanical

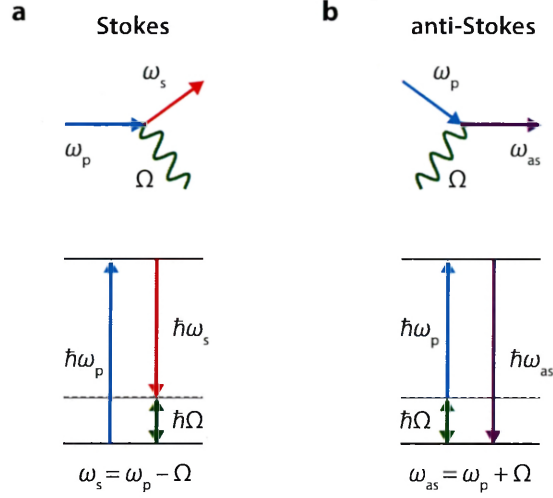


Figure 2.1: **Stokes and anti-Stokes scattering processes.** (a) Through a Stokes process, an incident photon (frequency ω_p) emits a red-shifted photon (frequency $\omega_s = \omega_p - \Omega$) and a phonon (frequency Ω). This process is illustrated through a scattering diagram (top) and energy-level diagram (bottom). (b) Through an anti-Stokes process, an incident photon (frequency ω_p) annihilates a phonon and is blue-shifted to frequency $\omega_{as} = \omega_p + \Omega$. *Image credit: Shai Gertler, Eric Kittlaus.*

stresses¹ and material deformation that are quadratic in the applied electric field. Through energy conservation (virtual work), the electrostrictive effect is thermodynamically linked to the same strain dependence of the material dielectric tensor [228–230], resulting in a stress whose magnitude is proportional to the photoelastic tensor magnitude [229, 230]:

$$\langle \sigma_{ij} \rangle = -\frac{1}{2} \varepsilon_0 \varepsilon_{ij} p_{jkmn} \varepsilon_{kl} \langle E_i E_j \rangle. \quad (2.2)$$

Here the stress, and the electric field product $E_i E_j$, are time-averaged since the mechanics (at GHz frequencies) respond much slower than the optical frequency ($\sim 10^2 - 10^3$ THz). For cubic and isotropic materials, the dielectric tensor is diagonal with $\varepsilon_{ij} = n^2 \delta_{ij}$, and this expression simplifies to

$$\langle \sigma_{kl} \rangle = -\frac{1}{2} \varepsilon_0 n^4 p_{ijkl} \langle E_i E_j \rangle, \quad (2.3)$$

where n is the material refractive index. In these material systems, there are only three

¹ Note that, in equilibrium, the mechanical stresses σ_{kl} and body forces f_l are directly related as $f_l = -\partial_k \sigma_{kl}$.

independent photoelastic coefficients, which can be written using contracted notation where $11 \rightarrow 1, 22 \rightarrow 2, 33 \rightarrow 3$, and $23, 32 \rightarrow 4$, and $p_{13} = p_{12}$ by symmetry. In this notation, p_{11} produces stress with the same polarization as the electric field, p_{12} produces stress at orthogonal polarizations to the electric field, and p_{44} produces shear stresses. For isotropic media, p_{44} is further constrained to $p_{44} = (p_{11} - p_{12})/2$.

When optical fields are present in a material, electrostriction induces a strain S related to the total stress through the elastic stiffness tensor $\sigma_{ij} = C_{ijkl}S_{kl}$, which in turn modifies the material refractive index through photoelasticity (Eq. 2.1). When this induced refractive index modulation couples the same optical fields that generated it, nonlinear optical coupling via stimulated Brillouin scattering can occur. Here, we briefly discuss how the interplay between these effects can lead to nonlinear optical interactions through backward stimulated Brillouin scattering (BSBS), which couples counter-propagating optical waves through a longitudinal elastic wave.

2.1.1 Phenomenological Picture of Backward SBS

Within bulk media, stimulated Brillouin scattering may occur between overlapping optical waves through interactions with longitudinal acoustic phonons. As an introductory example, we consider the commonly-studied case of SBS between counter-propagating optical waves.

Within this geometry, backward SBS (BSBS) may be understood according to the diagrams in Fig. 2.2. Two counter-propagating optical waves with frequencies ω_1 and ω_2 (wavevectors k_1 and k_2) are incident within a dielectric medium (Fig. 2.2a), and produce a traveling interference beat-note at their difference frequency Ω :

$$\Omega = \omega_1 - \omega_2, \tag{2.4}$$

where we have assumed $\omega_1 > \omega_2$ for simplicity. This intensity fringe pattern excites a traveling strain wave within the material via electrostrictive forces (Fig. 2.2b). Through a form of dynamical Bragg scattering, this elastic deformation then acts as a moving mirror that scatters light between the two optical waves (Fig. 2.2c), with a Doppler shift that couples light from high- to low-frequency through a stimulated Stokes process.

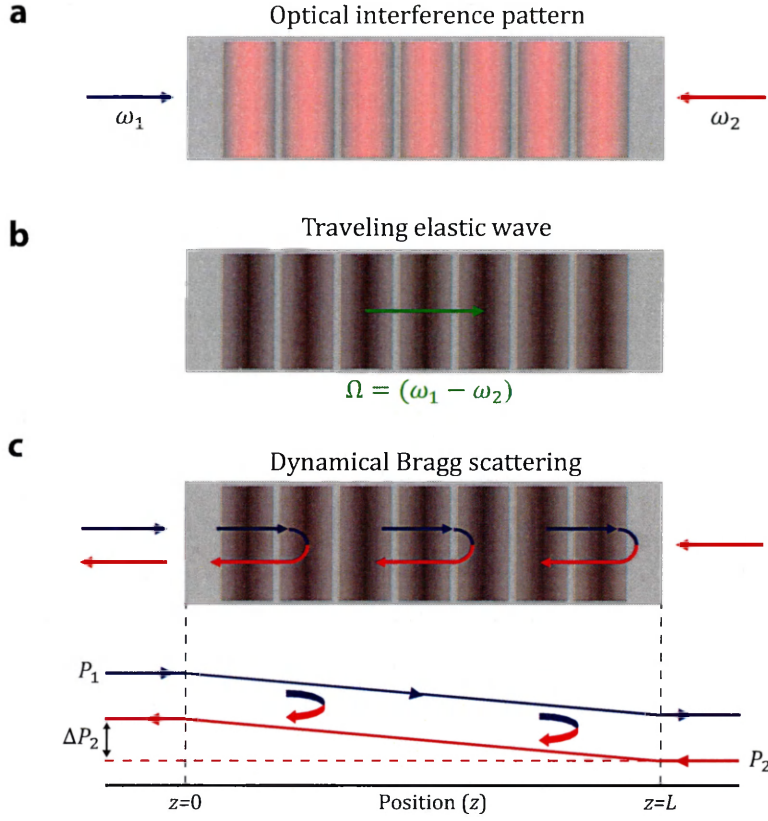


Figure 2.2: **Backward stimulated Brillouin scattering.** (a) diagrams a slice of a material in which two counterpropagating optical beams at frequencies ω_1 and ω_2 are incident. These light waves produce a traveling intensity beat note within the medium. (b) This intensity fringe pattern induces a traveling elastic wave through electrostrictive forces, with a time-harmonic frequency Ω at the optical beat frequency. (c) This elastic wave can scatter light between the two fields through photoelastic (acousto-optic) coupling, resulting in nonlinear energy transfer through stimulated Brillouin scattering.

When the velocity of the driven strain wave matches the longitudinal speed of sound v in the material, this process becomes dramatically enhanced. This condition occurs when the frequency and wavevector of the driven elastic wave satisfy the dispersion relation of the fundamental longitudinal acoustic phonon [70]:

$$\Omega_B = |q| v, \quad (2.5)$$

where Ω_B is the so-called ‘Brillouin frequency’ at which efficient optical energy transfer

occurs, and q is the wavevector of the optically driven phonon. This wavevector is equal to the wavevector of the optical interference pattern (beat note) between the two optical waves

$$q = k_1 - k_2 = \frac{n}{c} (\omega_1 + \omega_2). \quad (2.6)$$

Combining Eqs. 2.4-2.6, we find a Brillouin frequency of

$$\Omega_B = \frac{\omega_1 \frac{2v}{c/n}}{1 + \frac{v}{c/n}} \approx \frac{2v}{c/n} \omega_1. \quad (2.7)$$

For BSBS, the Brillouin frequency is proportional to the optical drive frequency and the speed of sound in the material. Typical values for crystalline media at optical wavelengths are in the 10-100 GHz range. Efficient Brillouin coupling occurs within a narrow bandwidth Γ about Ω_B , which is set by the acoustic phonon lifetime. In bulk materials at room temperature, Γ is typically in the 10-100 MHz range, corresponding to an acoustic quality factor $Q \equiv \Omega_B/\Gamma \sim 100-1000$ for these acoustic phonons. Here, Q can be understood as the number of cycles before a phonon decays. These typical values correspond to propagation lengths in the $\sim 100 \mu\text{m}$ range.

2.1.2 Scalar Model of Backward SBS

Following the treatment of Ref. [70] and others, we now briefly describe a scalar model for BSBS coupling between three waves—two optical, and one acoustic. The two counterpropagating optical plane waves of frequencies ω_1 and ω_2 are represented in complex notation

$$E_1(z, t) = a_1(z, t)e^{i(k_1z - \omega_1t)} + \text{c.c.} \quad (2.8)$$

$$E_2(z, t) = a_2(z, t)e^{i(-k_2z - \omega_2t)} + \text{c.c.} \quad (2.9)$$

The acoustic field is represented as a longitudinal plane wave with the material displacement distribution

$$u_z(z, t) = b(z, t)e^{i(qz - \Omega t)} + \text{c.c.}, \quad (2.10)$$

where we will henceforth drop the subscript z for simplicity. Note that we have decomposed the longitudinal acoustic displacement into its oscillating component $e^{i(qz-\Omega t)}$ and an envelope $b(z, t)$. The displacement must satisfy the driven-damped acoustic wave equation:

$$\frac{\partial^2 u}{\partial t^2} - \gamma \frac{\partial^2 u}{\partial z^2} - v^2 \frac{\partial^2 u}{\partial z^2} = \frac{f_z}{\rho_0}. \quad (2.11)$$

Here γ is the material acoustic damping parameter, ρ_0 is the material mass density, and the driving term f_z is the longitudinal body force, which is given by Eq. 2.3:

$$f = \nabla \sigma; \quad \sigma = -\frac{1}{2} \varepsilon_0 n^4 p_{12} \langle E^2 \rangle. \quad (2.12)$$

The resulting acoustic drive term from the incident optical fields is:

$$f_z = \frac{iq}{2} \varepsilon_0 n^4 p_{12} \left[a_1 a_2^* e^{i(qz-\Omega t)} + \text{c.c.} \right]. \quad (2.13)$$

Substituting Eqs. 2.10 and 2.13 into Eq. 2.11 and making the approximation that the acoustic amplitude b varies slowly in time and space, the equation for the acoustic envelope becomes

$$-2i\Omega \frac{\partial b}{\partial t} + (\Omega_B^2 - \Omega^2 - i\Omega\Gamma_B) b - 2iqv^2 \frac{\partial b}{\partial z} = \frac{iq}{2\rho_0} \varepsilon_0 n^4 p_{12} a_1 a_2^*. \quad (2.14)$$

Here the Brillouin frequency term comes from the relationship $\Omega_B^2 = v^2 q^2$, and we have defined the Brillouin linewidth $\Gamma_B \equiv q^2 \gamma$, where $1/\Gamma_B$ is the phonon lifetime. Equation 2.14 can be simplified by making two approximations. First, we assume that the system is at a steady state in time, so that $\frac{\partial b}{\partial t} = 0$. Second, we assume that the phonon envelope does not change dramatically over the acoustic decay length, so that we can set the term $v^2 \frac{\partial b}{\partial z} = 0$. While in the case of extremely strong Brillouin couplings this condition can break down, for the vast majority of experimental systems it is an excellent approximation. Under these assumptions, the acoustic envelope directly follows the product of the optical field amplitudes

$$b(z, t) = \frac{iq}{2\rho_0} \varepsilon_0 n^4 p_{12} \frac{a_1 a_2^*}{\Omega_B^2 - \Omega^2 - i\Omega\Gamma_B}. \quad (2.15)$$

The evolution of the optical fields is described by the wave equation

$$\frac{\partial^2 E_i}{\partial z^2} - \left(\frac{n}{c}\right)^2 \frac{\partial^2 E_i}{\partial t^2} = \frac{1}{\varepsilon_0 c^2} \frac{\partial^2 P_i}{\partial t^2}, \quad (2.16)$$

where $i = 1, 2$ indexes the optical field, and P_i is the nonlinear polarization component which sources each optical field. The total nonlinear polarization is given by

$$P = \varepsilon_0 \Delta \chi E = \varepsilon_0 \Delta \varepsilon E = -2iq\varepsilon_0 n^4 p_{12} u E, \quad (2.17)$$

with the relevant source terms given by

$$P_1 = -2iq\varepsilon_0 n^4 p_{12} b a_2 e^{i(k_1 z - \omega_1 t)} + \text{c.c.}, \quad P_2 = -2iq\varepsilon_0 n^4 p_{12} b^* a_1 e^{i(k_2 z - \omega_2 t)} + \text{c.c.} \quad (2.18)$$

Substituting these terms into the optical wave equation and again making the slowly-varying amplitude approximation leads to two coupled equations for the optical amplitudes

$$\frac{\partial a_1}{\partial z} + \frac{n}{c} \frac{\partial a_1}{\partial t} = \frac{\omega n^3 p_{12} q}{c} b a_2 \quad (2.19)$$

$$\frac{\partial a_2}{\partial z} + \frac{n}{c} \frac{\partial a_2}{\partial t} = \frac{\omega n^3 p_{12} q}{c} b^* a_1, \quad (2.20)$$

where b is given by Eq. 2.15, and we have made the approximation $\omega_1 \approx \omega_2 \equiv \omega$. In the steady-state, these equations become

$$\frac{\partial a_1}{\partial z} = \frac{i\varepsilon_0 \omega q^2 (n^4 p_{12})^2}{2nc\rho_0} \frac{|a_2|^2 a_1}{\Omega_B^2 - \Omega^2 - i\Omega\Gamma_B} \quad (2.21)$$

$$\frac{\partial a_2}{\partial z} = \frac{-i\varepsilon_0 \omega q^2 (n^4 p_{12})^2}{2nc\rho_0} \frac{|a_1|^2 a_2}{\Omega_B^2 - \Omega^2 - i\Omega\Gamma_B}. \quad (2.22)$$

These expressions can be recast in terms of the optical power intensities with the normalization $I_i = 2n\varepsilon_0 c a_i^* a_i$:

$$\frac{\partial I_1}{\partial z} = -G_B(\Omega) I_1 I_2 \quad (2.23)$$

$$\frac{\partial I_2}{\partial z} = -G_B(\Omega) I_1 I_2, \quad (2.24)$$

where $G_B(\Omega)$ is the frequency-dependent Brillouin gain coefficient

$$G_B = \frac{(n^4 p_{12})^2 \omega^2}{nc^3 v \rho_0 \Gamma_B} \frac{(\Gamma_B/2)^2}{(\Omega_B - \Omega)^2 + (\Gamma_B/2)^2}. \quad (2.25)$$

Here we see that the peak backward-SBS coupling scales strongly with refractive index $\propto n^7$, and is proportional to p_{12}^2 . Furthermore, the Brillouin gain coefficient is inversely proportional to the acoustic dissipation rate Γ_B . Therefore, when elastic waves live longer in a medium, they lead to increased Brillouin couplings since they can interact over greater lengths. Conversely, excess acoustic dissipation may stifle Brillouin interactions. Values of the SBS gain coefficient in terms of optical intensity are typically in the $10^{-1} - 10^2$ cm/GW range.

In the presence of a strong pump, a weak, red-detuned signal wave experiences exponential gain as it propagates through a Brillouin-active medium. In an optical waveguide, where mode areas, and hence the intensity of an undepleted pump, is constant with z , the total backward-SBS gain factor after a length L is

$$\frac{I_2(z=0)}{I_2(z=L)} = e^{G_B(\Omega) I_1 L}. \quad (2.26)$$

This analysis is remarkably successful at capturing the behavior of BSBS across a wide variety of systems. However, the treatment of SBS as a bulk interaction falls short when considering micro- and nano-scale devices, where geometry plays a large role in shaping the character of Brillouin interactions. For example, within nanoscale waveguide systems, geometric forces due to radiation pressure and boundary electrostriction can dramatically enhance or suppress the Brillouin interaction strength [195–198, 230, 231]. Furthermore, wavelength-scale confinement of optical and elastic waves leads to nontrivial field profiles, and the full-vectorial nature of the propagating modes must be taken into account. In this case, the electric field profile of the optical modes is no longer entirely transverse, and the full anisotropic mechanical properties of the waveguide material are relevant. As a result, Brillouin gain calculations which account for the complete interaction between confined elastic and optical waves are necessary [195, 231–233]. These analyses predict a va-

riety of phenomena within nanoscale waveguides, including giant Brillouin gain coefficients ($>10^2$ - 10^4 times larger than bulk), coherent addition or cancellation of electrostrictive and boundary forces, and efficient Brillouin coupling through forward-SBS (FSBS) interactions.

2.1.3 SBS in Guided-wave Systems

Within translationally-invariant waveguide systems, we consider Brillouin interactions between pump and Stokes waves with field profiles

$$\mathbf{E}_p(\mathbf{r}, t) = \mathbf{E}_p(\mathbf{r}_\perp) e^{i(k_p z - \omega_p t)}, \quad (2.27)$$

$$\mathbf{E}_s(\mathbf{r}, t) = \mathbf{E}_s(\mathbf{r}_\perp) e^{i(k_s z - \omega_s t)}, \quad (2.28)$$

where the electric field for each can be decomposed into a field vector that depends on the transverse dimension, and a wave-propagating term. According to Ref. [195], the Brillouin gain in such a system can generally be calculated via the spatial overlap between the time-harmonic optical force \mathbf{f} and the elastic-wave velocity distribution $\dot{\mathbf{u}}$ driven by these forces. Both the elastic wave and the optical force propagate with wavevector $q = k_p - k_s$ and have frequency $\Omega = \omega_p - \omega_s$ determined by the pump-Stokes interference beat-note.

In this picture, the Brillouin gain coefficient can be found using a particle conservation argument: Through SBS, each scattered pump photon (frequency ω_p) is converted to a Stokes photon (ω_s) and a phonon (Ω). Because of this correspondence, we can directly calculate the Stokes scattering rate from the phonon generation rate, which is related to the total amount of mechanical work performed to transduce these phonons². Through energy conservation, this is directly related to the driven elastic wave power density $\mathbf{f} \cdot \dot{\mathbf{u}}$, leading to [195]:

$$G_B(\Omega) = \frac{\omega_s}{2\Omega P_p P_s} \text{Re}\langle \mathbf{f}, \dot{\mathbf{u}} \rangle, \quad (2.29)$$

where P_p and P_s are the optical powers in the pump and Stokes waves, and the inner

2. Specifically, in terms of particle fluxes we can recast the typical Stokes gain equation $\partial P_s / \partial z = G_B P_p P_s - \alpha P_s$ in terms of a semiclassical Stokes particle flux Φ_s , and particle generation rates γ_s , γ_p , and γ_b , so that $\partial \Phi_s / \partial z = \gamma_s - \alpha \Phi_s$ with $\gamma_s = G_B P_p P_s / \hbar \omega_s$. Particle conservation gives $\gamma_s = \gamma_b = -\gamma_p$, and the phonon generation rate can be related to the classical elastic-wave power as $\gamma_b = (\partial P_b / \partial z)(1 / \hbar \Omega)$. We can determine the elastic power through direct integration of the cross-sectional overlap integral $\langle \mathbf{f}, \dot{\mathbf{u}} \rangle$.

product between vector fields is defined as the cross-sectional overlap integral

$$\langle \mathbf{A}, \mathbf{B} \rangle \equiv \int \mathbf{A}^* \cdot \mathbf{B} dA. \quad (2.30)$$

For delta function forces (e.g. along waveguide boundaries), this area integral becomes a line integral. This approach is particularly convenient since Equation 2.29 captures both body and boundary interactions, and avoids calculating nontrivial polarization currents along discontinuous boundaries and fields. Instead, we have expressed the Brillouin gain simply as a product between the optical force and driven elastic wave vectors.

Since the optical power in a waveguide is given by $v_g \langle \mathbf{E}, \varepsilon \mathbf{E} \rangle$, where v_g is the optical group velocity, we can write this expression in normalized form as³

$$G_B(\Omega) = \frac{2\omega_s}{v_{g,p} v_{g,s}} \frac{\text{Im} \langle \mathbf{f}, \mathbf{u} \rangle}{\langle \mathbf{E}_p, \varepsilon \mathbf{E}_p \rangle \langle \mathbf{E}_s, \varepsilon \mathbf{E}_s \rangle}, \quad (2.31)$$

Note that the Brillouin gain coefficient in this model should not depend on the optical field strength. Both the force \mathbf{f} and displacement \mathbf{u} fields depend quadratically on electric field in this model, so the field amplitude terms ultimately cancel.

To calculate $G_B(\Omega)$ using Eq. 2.31, we must first solve for the driven elastic wave as a function of force and, consequently, the incident field profiles. To avoid this complexity, we can instead simplify this calculation using a modal expansion approach. Starting with the elastic wave equation in the presence of a time-harmonic force at Ω [234]:

$$\rho_0 \Omega^2 u_i = \frac{\partial}{\partial x_j} c_{ijkl} \frac{\partial u_l}{\partial x_k} + f_i. \quad (2.32)$$

Here ρ_0 is the mass density, and c_{ijkl} is the material elastic tensor. Due to the symmetry properties of the elastic tensor, in the absence of driving forces this equation represents a Hermitian eigenvalue equation, and we can decompose our total elastic field profile \mathbf{u} into a summation over eigenmodes $\mathbf{u}_m e^{-i\Omega_m t}$ that satisfy an orthogonality condition $\langle \mathbf{u}_m, \rho \mathbf{u}_n \rangle = \delta_{mn} \langle \mathbf{u}_m, \rho \mathbf{u}_m \rangle$. If we write the elastic displacement field as $\mathbf{u} = \sum_m b_m \mathbf{u}_m$, in the presence

3. Alternately, we may begin by normalizing the optical fields such that $v_g \langle \mathbf{E}, \varepsilon \mathbf{E} \rangle = 1$ and working in natural units.

of force profile \mathbf{f} this condition leads to the expansion coefficients [231]:

$$b_m = \frac{\langle \mathbf{u}_m, \mathbf{f} \rangle}{\langle \mathbf{u}_m, \rho \mathbf{u}_m \rangle} \frac{1}{\Omega_m^2 - \Omega^2} \quad (2.33)$$

In the absence of loss, when $\Omega = \Omega_m$, the mode amplitude diverges. Within a realistic system, there are many elastic loss mechanisms which will lead to a finite dissipation rate Γ_m for each mode. We can pencil in this loss as an imaginary frequency $\Omega_m \rightarrow \Omega_m - i\Gamma_m/2$, provided that the acoustic mode quality factor $Q_m \equiv \Omega_m/\Gamma_m \gg 1$. In this case, the mode amplitude becomes

$$b_m = \frac{\langle \mathbf{u}_m, \mathbf{f} \rangle}{\langle \mathbf{u}_m, \rho \mathbf{u}_m \rangle} \frac{1}{\Gamma_m \Omega_m} \frac{\Gamma_m/2}{\Omega_m - \Omega^2 - i\Gamma_m/2}. \quad (2.34)$$

Substituting Eq. 2.34 and the modal expansion into Eq. 2.31, and using the fact that $\Omega \ll \omega_p, \omega_s$ we find that the total Brillouin gain coefficient can be written as a sum of SBS gains of each elastic eigenmode as

$$G_B(\Omega) = \sum_m G_{B,m} \frac{(\Gamma_m/2)^2}{(\Omega - \Omega_m)^2 + (\Gamma_m/2)^2}, \quad (2.35)$$

so that the gain of each mode has a Lorentzian lineshape, with a peak gain of

$$G_{B,m} = \frac{2\omega_s Q_m}{\Omega_m^2 v_{g,p} v_{g,s}} \frac{|\langle \mathbf{f}, \mathbf{u} \rangle|^2}{\langle \mathbf{E}_p, \varepsilon \mathbf{E}_p \rangle \langle \mathbf{E}_s, \varepsilon \mathbf{E}_s \rangle \langle \mathbf{u}_m, \rho \mathbf{u}_m \rangle}. \quad (2.36)$$

Eq. 2.36 allows calculation of the Brillouin gain as a function of elastic mode profile, and allows for solving the elastic wave equation and optical force profiles separately. As before, the inner products in the denominator represent normalization of the field quantities that participate in the SBS process.

Through the relation $G_{B,m} \propto |\langle \mathbf{f}, \mathbf{u} \rangle|^2$, it is clear the efficient Brillouin coupling requires strong overlap between optical forces and elastic waveguide modes. In nanoscale waveguide systems, the total optical force contains contributions from both electrostriction (which produces body and boundary forces), and radiation pressure, which produces forces normal to dielectric boundaries:

$$\mathbf{f}(\mathbf{r}, t) = \mathbf{f}_{rp}(\mathbf{r}, t) + \mathbf{f}_{es}(\mathbf{r}, t). \quad (2.37)$$

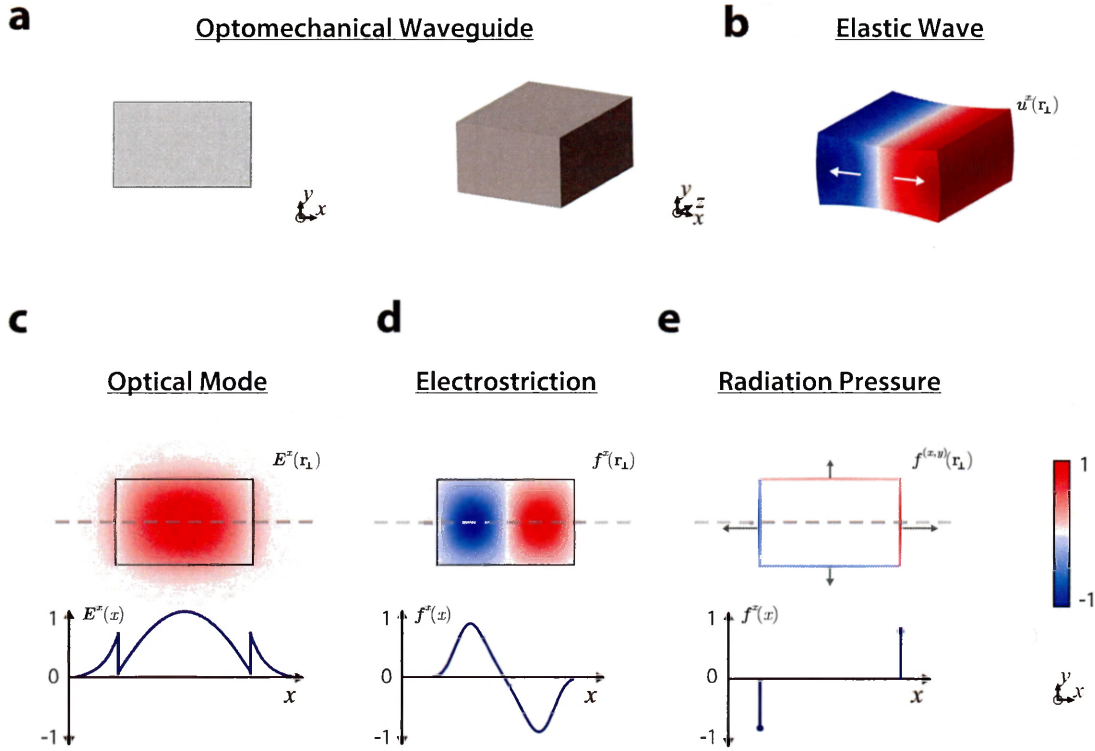


Figure 2.3: **Vectorial picture of optical forces and SBS coupling.** (a) diagrams a portion of a translationally-invariant waveguide with a rectangular cross section (left), and a perspective view (right) (b) This structure guides many elastic waves, one of which is plotted in (b). For simplicity, the wavevector q of the simulated mode is set to 0 for the purposes of this diagram. (c) This optomechanical waveguide supports a transverse electric-like (TE-like) optical mode with the x -directed electric field profile shown here. This optical field produces a variety of body and boundary forces within the waveguide, including the x -directed electrostrictive body force in (d), and the boundary radiation pressure shown in (e). Cross-sectional slices of the optical mode and forces are plotted below (c-e). Both these electrostrictive and radiation-pressure forces are well-suited to coupling with elastic waves with the x -displacement profile from (b), since they produce forces with the same symmetry and direction as the elastic-wave motion.

Within a translationally-invariant waveguide, the optical force and elastic wave may be decomposed into transverse and longitudinal components as $\mathbf{f}(\mathbf{r}, t) = \mathbf{f}(\mathbf{r}_\perp)e^{i(qz - \Omega t)}$ and $\mathbf{u}(\mathbf{r}, t) = \mathbf{u}(\mathbf{r}_\perp)e^{i(qz - \Omega t)}$, where $\mathbf{r}_\perp = (x, y)$. As a result, the overlap integral $\langle \mathbf{f}, \mathbf{u} \rangle$ can be seen as resulting from the overlaps of each of the vector components of the cross-sectional field profiles, as depicted in Fig. 2.3; the interference of optical fields (Fig. 2.3c) leads to body and surface forces (Fig. 2.3d-e). In this specific example, the x -components of boundary radiation pressure and body electrostriction forces add together constructively. This force profile leads to a strong overlap with an x -directed elastic breathing mode, pictured in Fig. 2.3b, since $\mathbf{u}_x(\mathbf{r}_\perp)$ and $\mathbf{f}_x(\mathbf{r}_\perp)$ have the same spatial symmetry.

We consider the modal picture of SBS for various types of Brillouin scattering processes in Section 2.3. First, however, we investigate the spatial dynamics of each Brillouin process, and explore how traveling-wave phase-matching dictates the coupled-wave behavior of Brillouin interactions within such guided-wave systems.

2.2 Types of Brillouin Scattering Processes

Thus far, we have examined SBS in bulk materials based on a back-scattering (BSBS) process. However, within waveguide systems which confine both light and sound, a variety of SBS processes are possible. In this section, we compare and contrast the different types of Brillouin interactions supported by nanoscale waveguide systems. We begin with BSBS and discuss how its traveling-wave dynamics result from the phase-matching conditions for Stokes and anti-Stokes scattering processes. Thereafter, we consider intra- and inter-modal forward SBS, which produce dynamics quite distinct from those of BSBS couplings.

2.2.1 Dynamics of Backward SBS (BSBS)

As derived in Section 2.1.2, BSBS produces two-tone couplings, and single-sideband amplification of a weak signal in the presence of a strong blue-detuned optical pump. This behavior is diagrammed in Fig. 2.4a-c. Counter-propagating pump and signal waves are guided in the same spatial optical mode of a BSBS-active waveguide. Through interactions with a longitudinal acoustic phonon, energy is transferred from the pump to the signal wave,

resulting in single-sideband gain through a stimulated Stokes scattering process.

Phase-matching and energy conservation for this process are both captured using the diagrammatic representation in Fig. 2.4d. Through a Brillouin scattering process, a phonon scatters an optical photon between distinct points that lie on the optical dispersion curve. In this representation, an optical state is represented by coordinates (wavevector, frequency) $= (k_i, \omega_i)$, where the superscript i is used to label the specific optical wave. Thus, Stokes scattering couples light from a pump wave at a point (k_p, ω_p) denoted by an open circle to a Stokes wave at a point (k_s, ω_s) represented by a filled circle. This process is mediated by a phonon (solid green arrow) with frequency Ω_B and wavevector q_s . Energy conservation for the Stokes process states that $\omega_p = \omega_s + \Omega_B$, whereas phase-matching requires that the sum of the wavevectors of the initial particle states equals the sum of the wavevectors of the final particle states. This condition can be written $k_p = k_s + q_s$, and is diagrammed in Fig. 2.4e. Because the frequencies, and hence wavenumbers, of the pump and signal waves are very close, this phase-matching condition is often written as $q_s = 2|k_p|$.

For BSBS, Stokes and anti-Stokes processes are mediated by different phonons. This can be seen from Fig. 2.4d, where a blue-shifting process is mediated by a phonon (dashed green line) which is backward-traveling, whereas a red-shifting process is mediated by a forward-moving phonon. This symmetry-breaking between these two processes arises from the wavevector conservation condition, where an anti-Stokes process annihilates an existing phonon with wavevector $q_{as} \approx -2|k_p|$ and scatters a pump photon from (k_p, ω_p) to (k_{as}, ω_{as}) . Wavevector conservation for this process is plotted in Fig. 2.4f.

In BSBS, Stokes and anti-Stokes scattering lead to fundamentally different dynamics. Through a Stokes process, a Stokes phonon is emitted, enhancing the Stokes scattering rate by increasing the phonon population. This self-reinforcing effect leads to stimulated (nonlinear) light scattering. By contrast, during an anti-Stokes process, an anti-Stokes-active phonon is annihilated. Because this blue-shifting process annihilates a phonon, rather than producing phonon emission, it is not self-reinforcing and cannot become a stimulated process. As a result, only thermally-populated (or otherwise driven) phonons may mediate anti-Stokes processes.

As discussed earlier, BSBS couples energy unidirectionally between two optical waves.

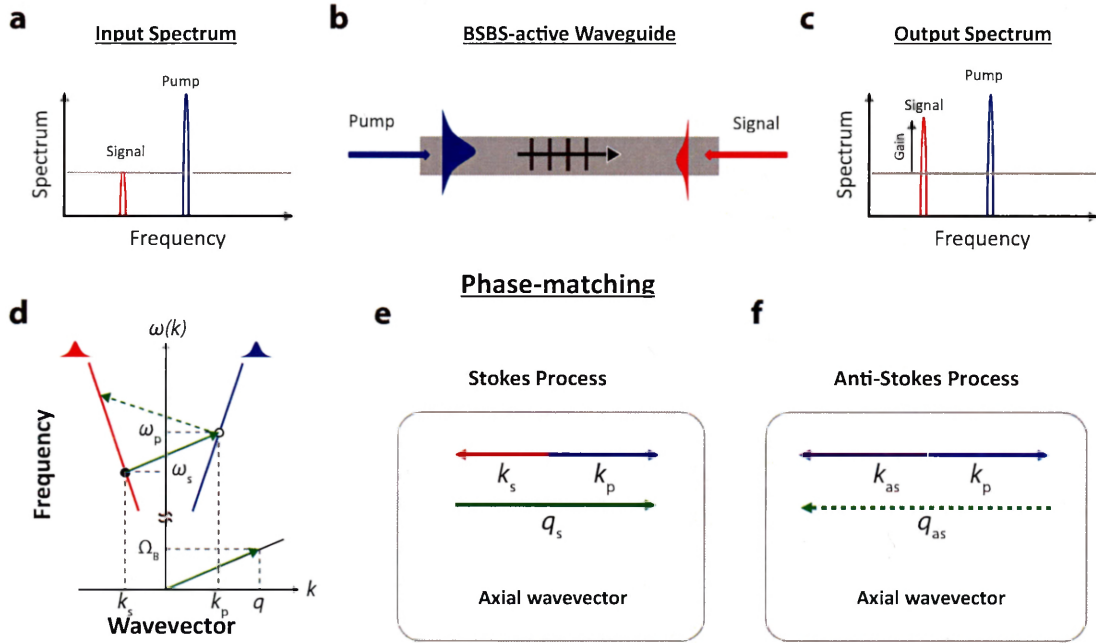


Figure 2.4: **Phase-matching and dynamics of BSBS.** (a-c) depict the gain dynamics of BSBS. Counterpropagating pump (blue) and signal (red) waves are injected in the same spatial mode of a Brillouin-active waveguide. These waves couple through a longitudinal acoustic phonon (b) to produce energy transfer from pump to signal waves. These dynamics can be understood from the phase-matching requirements for backward Brillouin scattering (d-f): In panel (d), wavevector and frequency (energy) conservation are plotted via the horizontal and vertical coordinates, respectively. A forward-propagating phonon (solid green arrow) lying on the phonon dispersion curve (black) scatters light between a forward-propagating wave at frequency ω_p (initial state represented by an open circle) and a backward-propagating wave at frequency ω_s (final state represented by a filled circle). This phonon has a wavevector q equal to the wavevector difference between initial and final optical states $k_p - k_s$, as diagrammed in (e). Because the anti-Stokes process couples through a phonon which travels in the opposite direction (dashed green arrow in (d) and (f)), anti-Stokes scattering is decoupled from the Stokes scattering process.

The spatial evolution of the powers in each field can be determined according to the coupled differential equations:

$$\frac{\partial P_p}{\partial z} = -G_B P_p P_s - \alpha P_p \quad (2.38)$$

$$\frac{\partial P_s}{\partial z} = -G_B P_p P_s + \alpha P_s. \quad (2.39)$$

Here P_p and P_s are the guided-wave powers in the pump (blue) and Stokes/signal (red) fields, and α is a linear propagation loss parameter assumed to be the same for both waves. As usual, G_B is the (frequency-detuning-dependent) Brillouin gain coefficient. Note that because the signal wave is traveling backward with respect to the pump ($-z$ direction), the sign on the loss term is positive with respect to $+\partial z$.

Neglecting pump depletion, these equations produce exponential gain for the signal wave. We briefly consider the case where pump light with total power P_p^0 is injected into a BSBS-active waveguide at position $z = -L$, and a signal wave with power P_s^0 is injected into the same waveguide at $z = 0$. Assuming that $P_s^0 \ll P_p^0$ and $|\alpha L| \ll 1$, the pump and signal powers at any point z within the waveguide are given by

$$P_p(z) = P_p^0 e^{-\alpha(z+L)} \quad (2.40)$$

$$P_s(z) = P_s^0 e^{(G_B P_p^0 - \alpha)(-z)}. \quad (2.41)$$

The signal-wave amplification exiting the waveguide at $z = -L$ is

$$\frac{P_s(-L)}{P_s^0} = e^{(G_B P_p^0 - \alpha)L}. \quad (2.42)$$

Thus the waveguide acts as a linear Brillouin amplifier with an exponential gain factor $e^{(G_B P_p^0 - \alpha)L}$. As the signal power grows to a comparable level to that of the pump wave, this behavior changes due to pump depletion. As an illustrative example, we solve for the

BSBS wave dynamics in the absence of loss:

$$\frac{\partial P_p}{\partial z} = -G_B P_p P_s \quad (2.43)$$

$$\frac{\partial P_s}{\partial z} = -G_B P_p P_s. \quad (2.44)$$

Direct integration shows that at any point, $P_p(z) - P_s(z) = c$, where c is a constant. The equations thus become decoupled and we can write

$$\frac{\partial P_s}{\partial z} = -G_B P_s (c + P_s). \quad (2.45)$$

This equation can be solved by direct integration to find

$$P_s(z) = \frac{ck}{e^{G_B cz} - k}, \quad (2.46)$$

where $k = P_s(0)/P_p(0) = P_s(0)/(c + P_s(0))$, and the constant c is given by the solution to the transcendental equation

$$e^{G_B c L} = \frac{(P_p(-L) - c)(P_s(0) + c)}{P_p(-L)P_s(0)}. \quad (2.47)$$

These equations permit near-complete optical power transfer between pump and signal waves, provided that the gain-power-length product⁴ $G_B P_p^0 L \gg 1$. In this case, the signal power initially grows as $P_s(-z)/P_s(0) = (1 - G_B P_s(0)z)^{-1}$ before eventually saturating at $P_s(-L) = P_p^0$. BSBS energy transfer occurs at the strongest rate at the beginning ($z = 0$) position in the waveguide where the pump wave is injected, since this is where both the pump and Stokes waves, and hence the mediating phonon field, are maximized. This energy transfer always occurs from the blue-detuned to the red-detuned wave.

4. More accurately, the power term should be replaced by a term like $\sqrt{P_p^0 P_s^0}$ in the case of small input signal waves to capture the necessary condition for pump depletion

2.2.2 Dynamics of Forward SBS (FSBS)

Next, we investigate intra-modal forward SBS (FSBS) within guided-wave systems. FSBS, which couples optical waves traveling in the same direction, requires the existence of elastic waves that are confined in the transverse dimension. Through interactions with these ‘breathing’ modes, FSBS produces physics that are very distinct from BSBS, leading to multi-sideband couplings that scatter light to numerous frequency components. This behavior is diagrammed in Fig. 2.5a-c. Co-propagating pump and signal waves detuned by the Brillouin frequency Ω_B are injected into a FSBS-active optomechanical waveguide, where they couple through a transverse acoustic phonon. As these waves propagate through the device, energy is transferred both from the pump to the signal wave, and to an additional optical tone blue-detuned from the pump by Ω_B through anti-Stokes scattering.

This multi-sideband energy transfer occurs because both Stokes and anti-Stokes processes couple to the same acoustic phonon mode, as shown in Fig. 2.5d-f. In the dispersion diagram of Fig. 2.5d, a forward-propagating (wavevector q) acoustic phonon mode scatters light between a pump wave at point (k_p, ω_p) on the optical dispersion curve (open circle), to (k_s, ω_s) (filled circle). The wavevector of this phonon is very close to zero (corresponding to a cutoff mode with very low group velocity), and is given by $q = k_p - k_s \approx \Omega_B/v_g$, where v_g is the optical group velocity. Because light is coupled between points on the same optical dispersion curve, this same phonon also couples pump light to a blue-detuned sideband at $(k_{as}, \omega_{as} = \omega_p + \Omega_B)$. From the wavevector conservation (phase-matching) condition, which states that the total wavevector sum must be conserved through a scattering process, both Stokes and anti-Stokes processes couple through the same phonon with wavevector $q = q_s = q_{as}$, as diagrammed in Fig. 2.5. Furthermore, since v_g (the slope of the optical dispersion curve) is practically constant over the range of several Brillouin frequency shifts, Stokes- and anti-Stokes-shifted light waves may experience cascaded FSBS, permitting energy transfer to successive frequency tones spaced by Ω_B .

Because Stokes and anti-Stokes processes couple to the same phonon mode through FSBS, phonon generation and annihilation are intrinsically balanced. As a result, FSBS does not produce stimulated phonon gain, instead driving a phonon field which is constant in

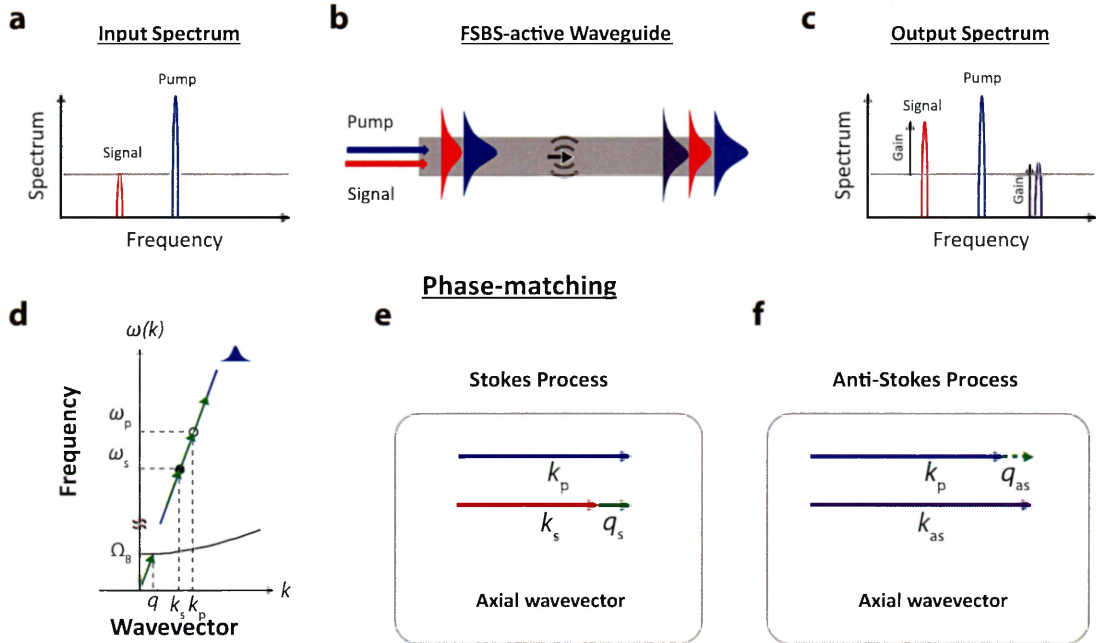


Figure 2.5: **Phase-matching and dynamics of FSBS.** (a-c) depict the gain dynamics of FSBS. Co-propagating pump (blue) and signal (red) waves are guided in the same optical mode of a Brillouin-active waveguide. The same device also guides transverse acoustic waves (b) which produces nonlinear light-sound coupling. While pump light is scattered to the signal wave, producing gain, the same acoustic phonon also scatters light to the blue-detuned (anti-Stokes) sideband. This form of dual-sideband gain is quite distinct from the dynamics of BSBS, and can be understood from the phase-matching conditions for FSBS (d-f) Panel (d) plots the dispersion curve for the optical waveguide mode and the acoustic phonon mode. A forward-propagating phonon (solid green arrow) lying on the phonon dispersion curve (black) scatters light between two points (ω_p, k_p) and (ω_s, k_s) on the optical dispersion curve (dark blue). However, this same phonon can also scatter light through anti-Stokes (blue-shifting of the pump) and cascaded Stokes (red-shifting of signal light) processes, mapping light between successive points along the optical dispersion curve. (e-f) depict phase-matching (wavevector conservation) for Stokes and anti-Stokes scattering. The same phonon participates in both, leading to intrinsic coupling between Stokes and anti-Stokes processes.

space (in the absence of external losses). These dynamics also have important consequences for spontaneous forward Brillouin scattering and Brillouin lasing. Because FSBS does not modify the phonon population in a self-reinforcing way, it cannot be initiated from thermal noise, in contrast to BSBS. Consequently, FSBS may not generally be used to create a Brillouin laser without some external mechanism that breaks Stokes/anti-Stokes symmetry.

To explore the dynamics of FSBS couplings, we write down the coupled power amplitude equations between a set of optical tones a_n indexed by integer n . As in the case of BSBS, we assume that the phonon field is heavily spatially damped compared to the length over which the optical amplitudes change appreciably, and that we are in the steady state (time derivatives of envelopes are zero). In this case, optical power transfer is governed by the equation [233]:

$$\frac{\partial a_n}{\partial z} = \frac{G_B}{2} (a_{n-1}b - a_{n+1}b^*). \quad (2.48)$$

Here G_B is the Brillouin gain coefficient, which we have assumed is the same for each nearest-neighbor coupling. We have also assumed that each optical tone with power amplitude a_n is separated from its neighbors by the Brillouin-active phonon frequency Ω_B (i.e. that the coupling is on-resonance). The optical power in each tone is $P_n = |a_n|^2$, and the phonon field amplitude is calculated as the sum of optical beat-notes by [186, 233]

$$b = \sum_n a_{n-1}^* a_n. \quad (2.49)$$

Differentiating Eq. 2.49 with respect to position z and substituting in Eq. 2.48, we find that $\frac{\partial b}{\partial z} = 0$, indicating that the phonon field created through FSBS is constant in space.

Using this fact, we investigate the case of small-signal FSBS gain, where we consider the spatial evolution of three tones $a_n = a_{-1}, a_0$, and a_1 at frequencies $\omega_p + n \cdot \Omega_B$ within a Brillouin-active waveguide. a_{-1} and a_0 are have incident values a_{-1}^{inc} and a_0^{inc} , respectively, where $|a_{-1}^{\text{inc}}| \ll |a_0^{\text{inc}}|$. We assume that $a_1(z=0) = 0$, and that $a_0(z) = a_0^{\text{inc}}$, in other words that the pump is undepleted. The equations for the spatial evolution of the Stokes and

anti-Stokes fields are

$$\frac{\partial a_{-1}}{\partial z} = \frac{G_B}{2} a_0 b^* \quad (2.50)$$

$$\frac{\partial a_1}{\partial z} = \frac{G_B}{2} a_0 b. \quad (2.51)$$

Because $b = (a_{-1}^{\text{inc}})^* a_0^{\text{inc}}$ is a constant, these equations can be directly integrated:

$$a_{-1}(z) = \frac{G_B}{2} a_0 b^* z + a_{-1}^{\text{inc}} = a_{-1}^{\text{inc}} \left(1 + \frac{G_B}{2} |a_0|^2 z\right) \quad (2.52)$$

$$a_1(z) = \frac{G_B}{2} a_0 b z = \frac{G_B}{2} a_0^2 a_{-1}^{\text{inc}} z. \quad (2.53)$$

The optical power evolution of these fields is then given by

$$P_{-1}(z) = P_{-1}^{\text{inc}} \left(1 + \frac{G_B P_0^{\text{inc}} z}{2}\right)^2 \quad (2.54)$$

$$P_1(z) = \left(\frac{G_B P_0^{\text{inc}} z}{2}\right)^2 P_{-1}^{\text{inc}}. \quad (2.55)$$

In the small-signal limit, both the Stokes and anti-Stokes fields experience energy transfer from the pump wave. Interestingly, the gain of the Stokes wave is directly proportional to $1 + G_B P_0 z + (G_B P_0 z)^2/4$. Note that this expression deviates from the exponential amplification observed through BSBS, representing only the first three terms in the series expansion of $e^{G_B P_0 z}$. This sub-exponential Stokes gain results from the back-action on the phonon field from anti-Stokes scattering.

Eq. 2.48 can be solved exactly if we write the phonon field from Eq. 2.49 as $b = b_0 e^{i\phi}$, where ϕ is an overall phase factor. In this case, the coupled-amplitude equations become

$$\frac{\partial a_n}{\partial z} = \frac{G_B b_0}{2} \left(a_{n-1} e^{i\phi} - a_{n+1} e^{-i\phi}\right). \quad (2.56)$$

The solutions to this differential equation are Bessel functions, with a trial solution of the form

$$a_n(z) = \sum_m c_{m,n} J_m(G_B b_0 z). \quad (2.57)$$

Plugging in to Eq. 2.56 leads to the condition on the coefficients $c_{m,n}$

$$c_{m+1,n} - c_{m-1,n} = e^{i\phi} c_{m,n-1} - e^{-i\phi} c_{m,n+1}, \quad (2.58)$$

which leads to the constraint

$$c_{m,n} = c_{n-m} e^{im\phi}. \quad (2.59)$$

Further inspection of boundary conditions reveals that [186]:

$$c_{m,n} = a_{n-m}(0) e^{im(\phi-\pi)}, \quad (2.60)$$

so that the full solution for the FSBS coupled-amplitudes is

$$a_n(z) = \sum_m a_{m-n}(0) e^{im(\phi-\pi)} J_m(G_B b_0 z). \quad (2.61)$$

In the presence of just two incident optical fields $a_0(0)$ and $a_1(0)$, this expression simplifies to

$$a_n(z) = a_0(0) e^{in(\phi-\pi)} J_n(G_B b_0 z) + a_1(0) e^{i(n-1)(\phi-\pi)} J_{n-1}(G_B b_0 z), \quad (2.62)$$

where $b_0 = \sqrt{P_0^{\text{inc}} P_1^{\text{inc}}}$. These equations predict cascaded Brillouin energy transfer to an increasing number of tones as the total Brillouin interaction length $G_B b_0 z$ is increased. We can compare this result to the small-signal Stokes gain by expanding to first order in the argument

$$\begin{aligned} a_n(z) &= a_0(0) J_0(G_B b_0 z) + a_1(0) e^{i\phi} J_1(G_B b_0 z) \\ &\approx a_0(0) + a_1(0) \frac{G_B b_0 e^{i\phi} z}{2} \\ &= a_0(0) + a_1(0) \frac{G_B b z}{2} \\ &= a_0(0) \left(1 + \frac{G_B |a_1(0)|^2 z}{2} \right), \end{aligned} \quad (2.63)$$

which is identical to Eq. 2.52.

This analysis shows that FSBS produces very different couplings from those of BSBS.

Instead of producing two-field couplings and exponential amplification, FSBS behaves as a form of traveling-wave phase-modulation, resulting in Bessel-like evolution of the optical amplitudes, and cascaded energy transfer to successive modulation orders as the total coupling strength is increased. These physics can be understood from the fact that FSBS couples optical fields along a single branch of an optical dispersion curve that is linear over the frequency range of interest. This form of coupling may also seem intuitive based on the type of acoustic phonons which mediate FSBS—in the diagram of Fig. 2.5b, it seems plausible that the transverse breathing-mode elastic wave would treat each traveling optical wave on equal footing (produce scattering of each wave), since the optical fields have nearly identical mode shapes and frequencies.

2.2.3 Dynamics of Forward Stimulated Inter-modal Brillouin Scattering (SIMS)

Thus far, we have examined the dynamics of both intra-modal forward- and backward-SBS, and have seen that these two processes produce very different coupled-wave dynamics. In this section, we examine a third form of Brillouin coupling between forward-propagating waves guided in distinct spatial optical modes. This interaction, termed stimulated inter-modal Brillouin scattering (SIMS), produces two-tone couplings similar to BSBS through a forward-scattering process. These types of interactions may be technologically important within integrated silicon optomechanical waveguides, as we discuss later in this dissertation.

The behavior of SIMS amplification is depicted in Fig. 2.6a-c. Co-propagating pump and signal waves are injected into different spatial optical modes of a multimode Brillouin-active waveguide (sketched here with a symmetric (pump) and anti-symmetric (signal) field profile). The signal wave is red-detuned from the pump wave by the Brillouin frequency Ω_B , and their interference beat-note drives a traveling antisymmetric (Lamb-wave-like) acoustic phonon through optical forces. This phonon couples these optical tones through stimulated inter-modal Stokes scattering to produce nonlinear energy transfer from the pump to the signal.

In contrast to the multi-sideband couplings of FSBS, this process restores the single-sideband energy transfer of BSBS, except that it uses a forward-scattering geometry. This

behavior results from the fact that, similar to BSBS, SIMS couples light between two optical dispersion branches (Fig. 2.6d). In contrast to BSBS, where Brillouin coupling occurs between the forward and backward branches of the same optical mode, in SIMS this coupling occurs between forward-propagating branches of different spatial modes. In the configuration sketched in Fig. 2.6d, light is scattered from the fundamental (symmetric) optical mode at (k_p, ω_p) to a higher-order (anti-symmetric) optical mode at (k_s, ω_s) through a Stokes process. Because these two optical modes may have different optical phase velocities resulting from geometric dispersion, k_p and k_s may have disparate values. These optical waves couple through a phonon with wavevector $q_s = k_p - k_s$ (solid green arrow). Because the Brillouin-active phonon wavevector is directly set by the difference in optical mode wavevectors, it may be varied through changes in waveguide design, opening the door to additional degrees of tunability in SBS processes.

Since coupling is mediated between optical waves lying on distinct dispersion curves, Stokes and anti-Stokes processes are again mediated by phonons with different wavevectors. As diagrammed in Fig. 2.6d-f, the Stokes-active phonon (solid green) and anti-Stokes-active phonon (dashed green) travel in opposite directions. From the phase-matching condition, $q_{as} = k_{as} - k_p$, under typical circumstances where the optical modes propagate at different phase velocities, $q_{as} \approx -q_s$.

As a result, SIMS restores the intrinsic dispersive symmetry-breaking between Stokes and anti-Stokes processes necessary for stimulated phonon gain and Brillouin lasers. Furthermore, in contrast to intra-modal FSBS, cascaded scattering is not possible since there are no available destination optical states. Thus SIMS produces nonlinear coupling between only two optical waves, with similar power evolution equations as those for BSBS (Eqs. 2.38-2.39):

$$\frac{\partial P_p}{\partial z} = -G_B P_p P_s - \alpha P_p, \quad (2.64)$$

$$\frac{\partial P_s}{\partial z} = G_B P_p P_s - \alpha P_s. \quad (2.65)$$

These equations differ from those for BSBS only in the propagation of the signal wave, where we have taken $-\partial z \rightarrow \partial z$. For simplicity, we have assumed a single linear propagation loss

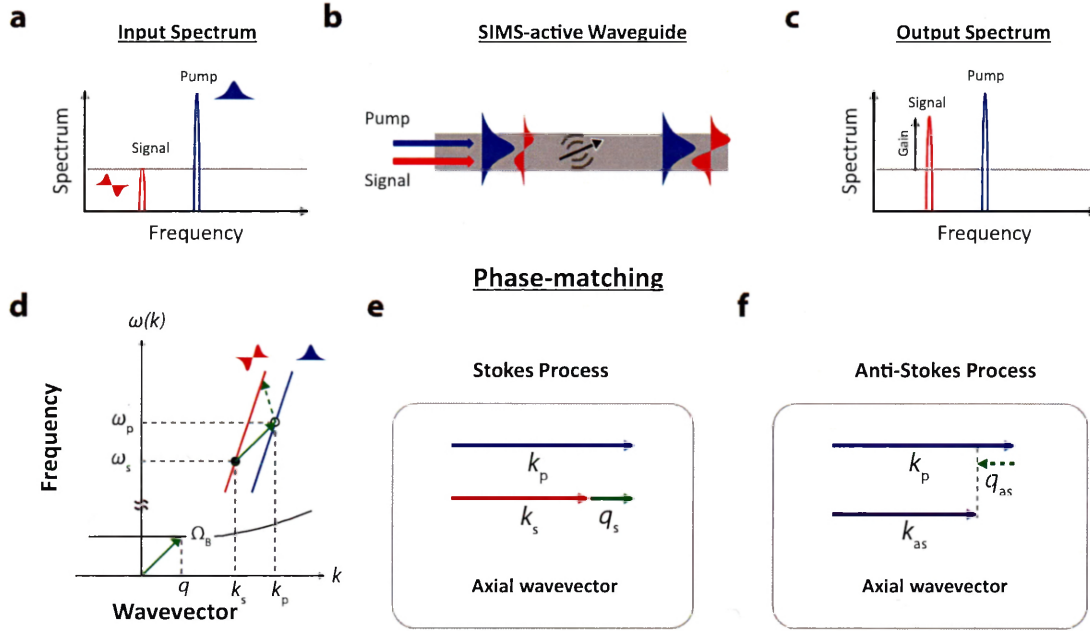


Figure 2.6: **Phase-matching and dynamics of SIMS.** (a-c) depict the dynamics of optical amplification in a SIMS-active waveguide. Co-propagating pump (blue) and signal (red) waves are coupled into separate transverse spatial modes of a multimode optomechanical waveguide. These optical waves couple through an asymmetric traveling-wave phonon (black arrow with gray arcs) to produce gain of the red-detuned signal wave at the expense of the pump. (d-f) plot the phase-matching behavior of this process. In (d), a guided-wave acoustic phonon (solid green arrow) which lies on the acoustic dispersion curve (black) is used to couple light from the pump mode (symmetric mode, blue) to the signal wave (anti-symmetric mode, red). Similar to the types of Brillouin processes discussed in prior sections, Stokes scattering transfers light from a point (ω_p, k_p) denoted by an open circle to a point (ω_s, k_s) (filled circle). However, through SIMS the wavevectors k_p and k_s correspond to distinct optical dispersion branches. The same phonon with wavevector $q = k_p - k_s$ cannot produce cascaded Brillouin scattering processes since no destination optical state is available on other dispersion bands. Furthermore, as in BSBS, the phonons which mediate Stokes scattering (solid green arrow) and anti-Stokes scattering (dashed green arrow) travel in different directions, as denoted in (d-f), so these processes are decoupled.

α for both waves. Within integrated waveguides, optical modes may have very different loss parameters, though in the case of low losses, this is typically a reasonable approximation. As in the case of BSBS, if we neglect pump depletion, these equations for two-tone Brillouin couplings produce exponential gain of the signal wave.

We consider a pump wave with incident power P_p^0 and signal wave with power P_s^0 injected into the same SIMS-active waveguide at $z = 0$. Assuming that $P_s^0 \ll P_p^0$ and $|\alpha L| \ll 1$, the pump and signal powers at any point z within the waveguide are given by

$$P_p(z) = P_p^0 e^{-\alpha(z+L)}, \quad (2.66)$$

$$P_s(z) = P_s^0 e^{(G_B P_p^0 - \alpha)(z)}. \quad (2.67)$$

The signal-wave amplification exiting the waveguide at $z = L$ is

$$\frac{P_s(L)}{P_s^0} = e^{(G_B P_p^0 - \alpha)L}. \quad (2.68)$$

These equations represent linear optical amplification of the signal wave with an exponential gain factor $e^{(G_B P_p^0 - \alpha)L}$ identical to the BSBS case. In contrast to BSBS, however, the large-signal spatial dynamics are modified. While Eqs. 2.64-2.65 can produce near-complete unidirectional energy transfer from the pump to signal wave as in BSBS, these equations can be solved exactly for closed-form solutions without the use of a transcendental equation as in Eq. 2.47.

We begin solving Eqs. 2.64-2.65 with a change of variables $P_p = e^{-\alpha z} Q_p$, $P_s = e^{-\alpha z} Q_s$. This substitution results in the equations

$$\frac{\partial Q_p}{\partial z} = -G_B Q_p Q_s e^{-\alpha z}, \quad (2.69)$$

$$\frac{\partial Q_s}{\partial z} = G_B Q_p Q_s e^{-\alpha z}. \quad (2.70)$$

These coupled equations satisfy the conservation relation $\frac{\partial Q_p}{\partial z} + \frac{\partial Q_s}{\partial z} = 0$, so that $Q_p + Q_s = P^{\text{in}}$, where $P^{\text{in}} = P_p(0) + P_s(0)$ is the total incident power. As a result Eqs. 2.69-2.70 can

be decoupled:

$$\frac{\partial Q_p}{\partial z} = -G_B Q_p (P^{\text{in}} - Q_p) e^{-\alpha z}, \quad (2.71)$$

$$\frac{\partial Q_s}{\partial z} = G_B Q_s (P^{\text{in}} - Q_s) e^{-\alpha z}. \quad (2.72)$$

These equations are separable, and lead to the final solution

$$P_p(z) = \frac{P^{\text{in}} e^{-\alpha z}}{1 + \frac{P_s(0)}{P_p(0)} e^{-\frac{G_B P^{\text{in}}}{\alpha} (e^{-\alpha z} - 1)}}, \quad (2.73)$$

$$P_s(z) = \frac{P^{\text{in}} e^{-\alpha z}}{1 + \frac{P_p(0)}{P_s(0)} e^{-\frac{G_B P^{\text{in}}}{\alpha} (e^{-\alpha z} - 1)}}. \quad (2.74)$$

In the absence of loss, these expressions simplify to the form

$$P_p(z) = \frac{P^{\text{in}}}{1 + \frac{P_s(0)}{P_p(0)} e^{G_B P^{\text{in}} z}}, \quad (2.75)$$

$$P_s(z) = \frac{P^{\text{in}}}{1 + \frac{P_p(0)}{P_s(0)} e^{-G_B P^{\text{in}} z}}. \quad (2.76)$$

These equations describe unidirectional energy transfer from the pump to the signal wave. In the case of equal incident powers for the two waves, a gain-power-length product of $G_B P^{\text{in}} z > \ln(3) \approx 1.1$ is necessary for 50% energy transfer from pump to signal, and $G_B P^{\text{in}} z > 5.3$ is necessary for 99% energy transfer.

SIMS Ring Laser Theory

Because SIMS produces single-sideband Brillouin couplings, and hence stimulated phonon gain, it can be used to create Brillouin ring lasers, provided that Brillouin gain is greater than linear loss in the system. A ring laser of this type is investigated experimentally in Chapter 5.8. Here, we briefly study the dynamics of Eqs. 2.64-2.65 within a ring cavity, and derive the steady-state laser output power from boundary conditions. Due to the role of interference when considering the cavity couplings, we rewrite these equations in terms

of the complex power amplitudes:

$$\frac{\partial a_p}{\partial z} = -g a_p |a_s|^2 - \beta_p a_p, \quad (2.77)$$

$$\frac{\partial a_s}{\partial z} = g |a_p|^2 a_s - \beta_s a_s. \quad (2.78)$$

Here $g = G_B/2$ is the amplitude Brillouin gain coefficient, and β_s and β_p are the linear amplitude losses for the pump and Stokes waves. Optical powers are normalized such that $P_i = |a_i|^2$. These waves are assumed to propagate in a ring geometry of circumference L , with a point coupler setting the boundary conditions between $z = L$ and $z = 0$ as follows:

$$a_s(0) = r_s(1 - \gamma_s)e^{i\delta_s} a_s(L), \quad (2.79)$$

$$a_p(0) = \mu + r_p(1 - \gamma_p)e^{i\delta_p} a_p(L). \quad (2.80)$$

Here r_s and r_p are the fractions of a_p and a_s which are re-injected into the ring. γ_s and γ_p are coupler losses for each field, and μ is the pump field injected into the cavity. $\delta_s = (n_s L/c)(\Delta_s)$ and $\delta_p = (n_p L/c)(\Delta_p)$ are the round-trip accumulated phase differences due to frequency detunings Δ_s and Δ_p from the respective cavity modes in terms of the pump and Stokes-wave phase indices n_p and n_s .

We can solve analytically for the steady-state solution to these equations when linear losses are the same rate β for both fields, and both are on-resonance with their respective passive cavity modes. In this case, $\mu = \sqrt{1 - r_p^2} a^{\text{inc}}$, where a^{inc} is the pump field incident on the coupler. Above threshold, lasing can initiate from thermal noise through resonant amplification of a_s , which is seeded through thermal Brillouin scattering. The spatial coupled-amplitude equations and boundary conditions become:

$$\frac{\partial a_p}{\partial z} = -g a_p a_s^2 - \beta a_p, \quad (2.81)$$

$$\frac{\partial a_s}{\partial z} = g a_p^2 a_s - \beta a_s, \quad (2.82)$$

$$a_s(0) = r_s(1 - \gamma_s)a_s(L), \quad (2.83)$$

$$a_p(0) = \mu + r_p(1 - \gamma_p)a_p(L). \quad (2.84)$$

For simplicity of notation, we have neglected an overall phase factor for the optical waves, i.e. $|a_i|^2 = a_i^2$. Dividing by a_p and a_s in equations 2.81 and 2.82, respectively, we have:

$$\frac{1}{a_p} \frac{\partial a_p}{\partial z} = -ga_s^2 - \beta, \quad (2.85)$$

$$\frac{1}{a_s} \frac{\partial a_s}{\partial z} = ga_p^2 - \beta. \quad (2.86)$$

Dividing 2.86 by 2.85 and cross-multiplying, we find

$$\left(-ga_s - \frac{\beta}{a_s}\right)\partial a_s = \left(-ga_p - \frac{\beta}{a_p}\right)\partial a_p. \quad (2.87)$$

Integrating both sides leads to the expression

$$\frac{a_p}{a_s} e^{-\frac{G}{2\beta}(a_p^2 + a_s^2)} = c. \quad (2.88)$$

Equation 2.88 specifies a constant c that describes the evolution of a_p and a_s in phase-space. This will be one of two equations used to determine the steady-state values of a_p and a_s . Summing equations 2.81 and 2.82 leads to an energy conservation condition:

$$a_p \frac{\partial a_p}{\partial z} + a_s \frac{\partial a_s}{\partial z} = -\beta(a_p^2 + a_s^2), \quad (2.89)$$

$$\frac{1}{2} \frac{\partial(a_p^2 + a_s^2)}{\partial z} = \beta \partial z \quad (2.90)$$

Integrating both sides,

$$a_p^2(L) + a_s^2(L) = e^{-2\beta L}(a_p^2(0) + a_s^2(0)). \quad (2.91)$$

This equation relates the wave amplitudes before and after the point coupler and results

from the fact that energy is only lost due to propagation loss in this system. Another equation relating the waves at this boundary can be written from equation 2.88:

$$\frac{a_p(L)}{a_s(L)} e^{-\frac{G}{2\beta}(a_p^2(L)+a_s^2(L))} = \frac{a_p(0)}{a_s(0)} e^{-\frac{G}{2\beta}(a_p^2(0)+a_s^2(0))}. \quad (2.92)$$

This expression can be simplified by inserting Eq. 2.91 into the exponential term and substituting boundary equations for the two waves from Eqs. 2.83-2.84:

$$\frac{a_p(L)r_s(1-\gamma_s)}{\mu+r_p(1-\gamma_p)a_p(L)} = e^{\frac{G}{2\beta}((1-e^{2\beta L})(a_p^2(L)+a_s^2(L)))}. \quad (2.93)$$

We eliminate a_s from this equation by substituting the boundary conditions from Eqs. 2.83-2.84 into Eq. 2.91:

$$a_s^2(L) = \frac{e^{-2\beta L}(\mu+r_p(1-\gamma_p)^2 a_p(L))^2 - a_p^2(L)}{1-r_s^2(1-\gamma_s)^2 e^{-2\beta L}}. \quad (2.94)$$

Finally, substituting Eq. 2.94 into Eq. 2.93 leads to a single equality in terms of $(a_p(L))$.

$$\frac{a_p(L)r_s(1-\gamma_s)}{\mu+r_p(1-\gamma_p)a_p(L)} = e^{\frac{G}{2\beta}\left((1-e^{2\beta L})\left(a_p^2(L)+\left(\frac{e^{-2\beta L}(\mu+r_p(1-\gamma_p)^2 a_p(L))^2 - a_p^2(L)}{1-r_s^2(1-\gamma_s)^2 e^{-2\beta L}}\right)\right)\right)}. \quad (2.95)$$

This expression can be solved numerically to find $a_p(L)$, which then defines $P_s(L) = a_s^2(L)$ through Eq. 2.94. Output pump and signal powers are related to these quantities as

$$P_s^{\text{out}} = a_s^2(L)(1-r_s^2)(1-\gamma_s)^2, \quad (2.96)$$

$$P_p^{\text{out}} = a_p^2(L)(1-r_p^2)(1-\gamma_p)^2. \quad (2.97)$$

These equations describe the steady-state input-output response of the Brillouin ring laser. One interesting result of this analysis is that the slope efficiency of the SIMS ring laser is highest just above threshold. Far above threshold, pump depletion due to strong Brillouin coupling around the ring cavity reduces the effective slope efficiency. Eqs. 2.94-2.97 can be used to choose cavity parameters and designs that optimize laser performance.

2.3 Modal Picture of BSBS, FSBS, and SIMS

In this chapter, we have explored three types of SBS processes within optomechanical waveguides, and seen how they offer distinct (and complementary) dynamics based on their respective traveling-wave phase-matching conditions. In summary, we now examine how these various interactions occur within a sample system. This illustrative example is shown in Fig. 2.7, where we consider the interacting modes and optical forces for SBS couplings within a rectangular silicon nanowire with cross-sectional dimensions 1000×230 nm. This optomechanical waveguide supports multiple optical and elastic modes, which may interact through bulk- and boundary-induced optical forces.

Firstly, the BSBS interaction is diagrammed in Fig. 2.7a. Counter-propagating pump and Stokes waves (approximate wavevectors k and $-k$, respectively) frequency-detuned by the Brillouin frequency Ω_B are guided in the fundamental spatial waveguide mode. These waves interfere to produce a time-harmonic electrostrictive body force. While in general this force has components in all spatial directions, the longitudinal component, mediated by the p_{12} photoelastic tensor coefficient, typically plays the dominant role. Additionally, radiation pressure exerts forces perpendicular to the waveguide boundaries, which may play a role within tightly-confined geometries. BSBS couples through traveling elastic waves with wavevector $2k$. Once such acoustic phonon mode, with a primary strain field in the longitudinal direction, is plotted in the bottom row of Fig. 2.7a.

Intra-modal FSBS, diagrammed in Fig. 2.7b, couples two frequency-detuned optical waves guided within the same spatial mode. These modes excite transverse optical force profiles through electrostriction (mediated by the p_{11} photoelastic tensor component) and radiation pressure, which couple to transverse elastic ‘breathing’ modes (acoustic wavevector near zero). Note that these acoustic modes only exist within systems that possess transverse acoustic confinement (i.e. waveguiding). As we saw in Section 2.2.2, FSBS interactions produce coupled-wave dynamics that are quite different from the exponential gain behavior of BSBS, leading to energy transfer between multiple coupled optical fields.

Within multimode optomechanical waveguides, such as the micron-wide silicon nanowire, inter-modal Brillouin couplings may also occur. Fig. 2.7c diagrams the components of

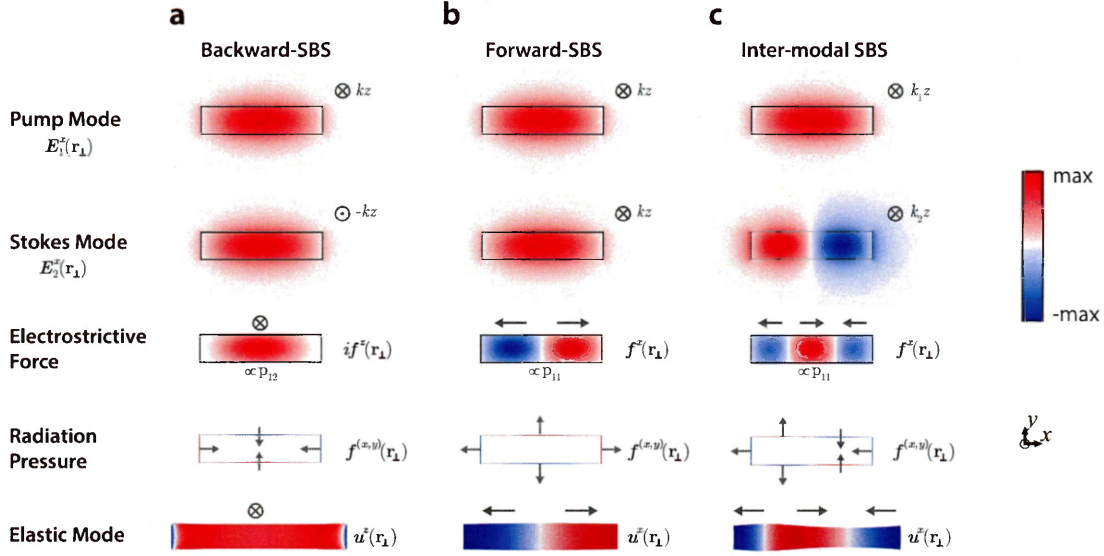


Figure 2.7: **Modal picture of stimulated Brillouin scattering processes in a silicon waveguide.** The various component parts of SBS are plotted for three different processes within a 1000×230 nm silicon nanowire. (a) In backward intra-modal SBS, non-linear coupling occurs between two light waves guided in the same optical mode (with approximate wavenumber k) but traveling in opposite directions. These optical waves drive time-harmonic optical forces through electrostriction and radiation pressure. The relevant component of the electrostrictive force is in the z direction, and is mediated by the photoelastic tensor component p_{12} , while radiation pressure is always normal to the dielectric discontinuities at the waveguide boundaries. These forces couple to a compressive-like elastic wave with wavenumber $2k$. Because this elastic mode also experiences motion in the transverse direction, radiation pressure can play a role in the BSBS interaction in highly-confined systems. (b) Intra-modal forward SBS occurs between two co-propagating light waves guided in the same optical mode. These optical fields excite transverse optical forces through electrostriction (through the p_{11} tensor component) and radiation pressure, which couple to an acoustic breathing-type mode with near-zero wavevector. (c) In inter-modal forward SBS, two optical spatial modes with wavevectors k_1 and k_2 excite traveling optical force distributions through electrostriction and radiation pressure. While coupling through transverse field components (i.e. through p_{11} and boundary forces) is typically dominant, longitudinal-wave couplings can play a significant role. These forces couple to a Lamb-like elastic mode with wavevector $k_1 - k_2$.

forward inter-modal SBS (SIMS); co-propagating pump and Stokes waves are guided in distinct waveguide modes. Because these two optical modes have different effective indices, they have distinct wavevectors k_1 and k_2 . These light waves couple to propagating elastic waves with wavevector $k_1 - k_2$. The SIMS interaction has aspects of both forward and backward SBS. For example, electrostrictive coupling may be mediated through a combination of p_{11} (transverse) and p_{12} (longitudinal) photoelastic interactions. SIMS-active elastic modes may experience displacement in either of these directions. As derived in Section 2.2.3, SIMS produces two-tone couplings reminiscent of BSBS. However, because these waves co-propagate, they lead to distinct spatial dynamics in the case of large Brillouin couplings.

In addition to examining the role that geometry plays in SBS, the results of this chapter also highlight the importance of material properties in shaping Brillouin couplings. Beyond controlling the shape and confinement of Brillouin-active elastic modes, the choice of Brillouin-active medium, and in particular the material dielectric and photoelastic response, directly impacts the SBS interaction strength. In the coming chapters, we explore experimental demonstrations of SBS in silicon, where $|p_{11}|$ is more than five times larger than $|p_{12}|$. As a result, Eq. 2.25 suggests that FSBS should be more than an order of magnitude stronger than BSBS in silicon. With further study, new techniques may allow direct tailoring of a material's photoelastic response, enabling further degrees of control over a variety of Brillouin- and Brillouin-like interactions.

Chapter 3

Forward Brillouin Amplification in Silicon Membrane Waveguides

3.1 Introduction

Silicon has gained considerable attention as the leading material for integrated photonics due to its compatibility with existing semiconductor fabrication infrastructure and good transparency in the near- and mid-infrared [235]. Furthermore, silicon's high refractive index permits light to be confined and routed using compact optical waveguides that support tight bends. However, silicon lacks a χ_2 nonlinearity, precluding direct electro-optic modulation in silicon. Furthermore, silicon has an indirect bandgap, forbidding light emission. As a result, the use of innovative strategies is necessary to produce useful nonlinear optical devices in silicon. Typical approaches include hybrid integration with other materials or using the Kerr effect.

An alternate approach is to utilize nonlinearities based on photon-phonon couplings. Such nonlinearities can be classified as either Raman or Brillouin interactions, which couple light to optical or acoustic phonons, respectively. While silicon-based Raman amplifiers and lasers have been demonstrated, the large Raman frequency shift (15.6 THz) is not amenable to many signal-processing applications. Furthermore, linear and nonlinear propagation losses limit effect sizes for these types of nonlinearities or necessitate electrical removal of

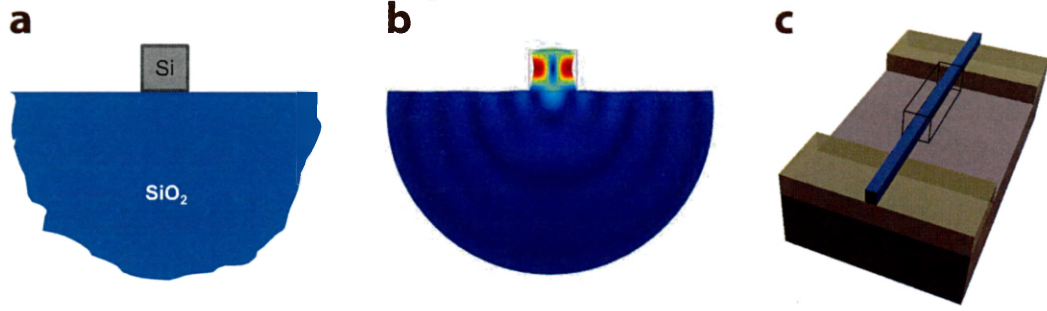


Figure 3.1: **Substrate-induced acoustic dissipation.** (a) diagrams the cross-section of a typical silicon-on-silica waveguide geometry. (b) is a simulation demonstrating how elastic waves driven in the silicon waveguide core rapidly radiate into the substrate. (c) depicts a possible waveguide design for both light and sound where the silica substrate has been removed. *Image credit: Peter Rakich.* Panel (c) is from Ref. [195].

optically-generated free carriers [236].

Brillouin nonlinearities provide an attractive platform for optical gain [194, 237], signal processing and filtering [150, 151, 159–161, 163, 238], nonreciprocal processes [157, 188, 207, 239], frequency synthesis [148, 152–156, 186, 240], and metrology [96, 98]. Furthermore, stimulated Brillouin scattering (SBS) interactions couple optical waves separated by technologically-relevant frequency shifts in the MHz-100 GHz range. However, despite more than a decade of research in silicon photonics, SBS was until recently considered absent in silicon waveguides [195, 241]. This contrasts sharply with glass-based fibers, where Brillouin scattering is orders of magnitude stronger than Kerr and Raman interactions [75].

The absence of SBS in traditional silicon-on-insulator waveguides (Fig. 3.1a) can be understood from two reasons. First, the p_{12} component of silicon’s photoelastic tensor, which mediates backward SBS interactions, is much smaller in silicon than in most materials, resulting in a weak electrostrictive and photoelastic effect. Furthermore, due to the slower speed of sound in silica as compared with silicon, sound waves generated through SBS immediately radiate from the active waveguide into the substrate, preventing the creation of strong elastic fields necessary for efficient SBS (Fig. 3.1b) [195].

As a result, two innovations were necessary to observe strong Brillouin nonlinearities in silicon. The first is the removal of the insulator around the waveguide to confine sound to the silicon core (Fig. 3.1c). The second is the use of a forward SBS interaction, which

had previously only been observed in optical fibers [175, 176, 186]. This effect couples co-propagating optical waves to cutoff acoustic phonon modes and relies on a different photoelastic tensor element from BSBS, p_{11} . In silicon, p_{11} is more than five times larger than p_{12} , resulting in a thirty-fold comparative enhancement in Brillouin coupling [70, 227].

Forward SBS was first observed in silicon in Ref. [196] using silicon optical waveguides embedded within a silicon nitride membrane. In this suspended structure, the nitride membrane is patterned with slots which act as phononic mirrors. Using this design, nonlinear gain coefficients $G_B > 2000 \text{ W}^{-1}\text{m}^{-1}$ were demonstrated. Subsequent works demonstrated nanopillar [197] and suspended nanowire [218] waveguides with increased nonlinearities up to $G_B \approx 10^4 \text{ W}^{-1}\text{m}^{-1}$. However, despite the realization of record-high nonlinearities in silicon, linear and nonlinear losses hindered the demonstration of optical amplification in these structures. Only Ref. [218] demonstrated gain that could balance optical loss, achieving 0.5 dB of amplification at $\sim 40 \text{ mW}$ pump powers. Furthermore, in nanoscale waveguides, Brillouin amplification diminishes with longer interaction lengths due to issues of dimensionally-induced inhomogeneous broadening [242]. These experimental and theoretical analyses suggested that large net amplification is fundamentally difficult to achieve in silicon waveguides at near-infrared wavelengths [243], posing a challenge to the creation of practical Brillouin-based amplifiers and lasers in silicon.

In this section, we describe the development of a new optomechanical silicon waveguide which supports significant ($>5 \text{ dB}$) net Brillouin amplification, with a low ($<5 \text{ mW}$) threshold for net gain [219]. This performance is possible due to the low linear ($<0.2 \text{ dB/cm}$) and nonlinear losses and large nonlinear coefficient ($G_B > 10^3 \text{ W}^{-1}\text{m}^{-1}$) of this structure. This device is fabricated from pristine crystalline silicon with no doping or active removal of loss-producing free carriers¹, as is commonly necessary for Raman amplifiers and lasers [236, 244]. This demonstration of strong Brillouin couplings in an ultralow-loss silicon waveguide opens the door to high-performance Brillouin amplifiers and signal processing technologies within silicon photonic circuits.

1. Doping of silicon may be used to shorten free-carrier lifetimes, at the expense of increased linear optical absorption. Likewise, active sweeping of free carriers from the waveguide cross-section may be accomplished by an external electric field. However, this increases power consumption and fabrication complexity.

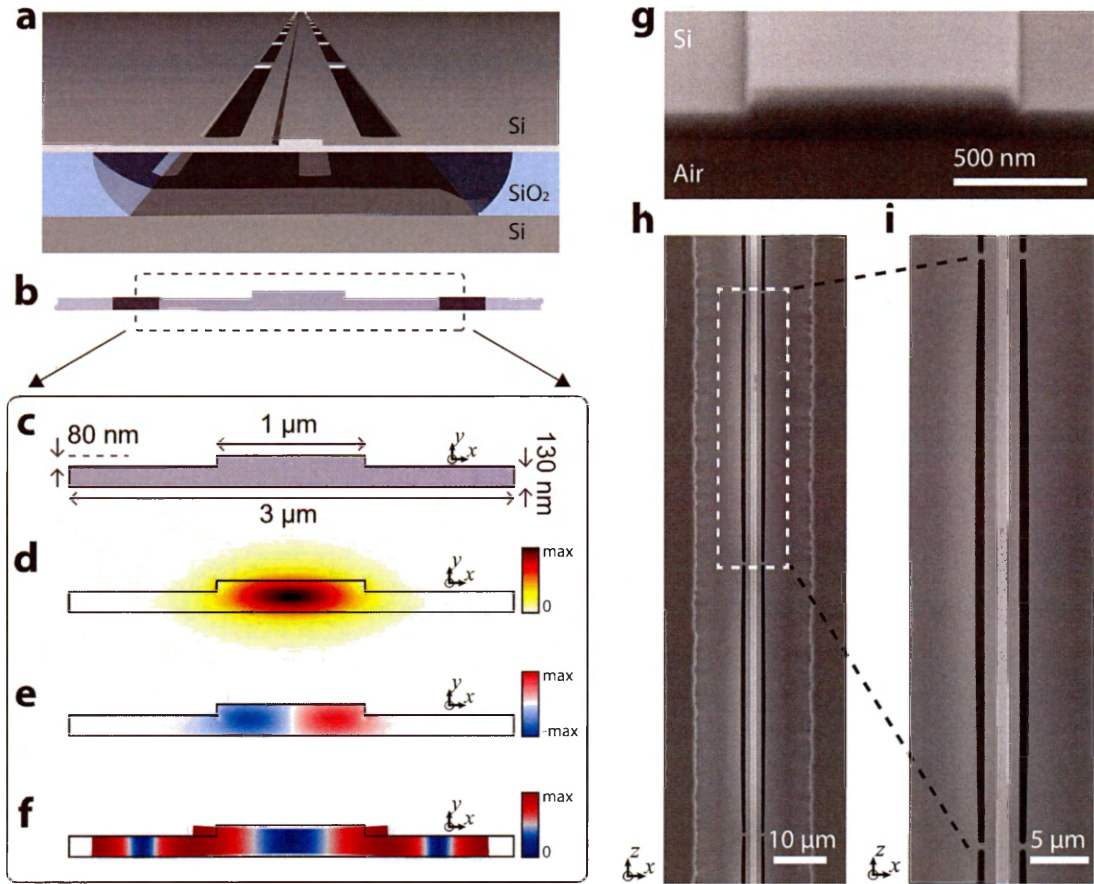


Figure 3.2: **Suspended membrane waveguide design.** (a) shows a schematic of the continuously-suspended optomechanical waveguide, with a cross-section of the active region sketched in (b). (c) diagrams relevant device dimensions. The device guides optical waves in the TE-like mode whose E_x field is plotted in (d). The resulting electrostrictive force from this mode has an x -component whose spatial character is plotted in (e). (f) Plots the normalized displacement of a 4-GHz elastic mode to which this force strongly couples. (g) plots a scanning electron micrograph (SEM) of the device cross-section. (h-i) plot SEMs of the top-down view of the device. Adapted from Ref. [219].

3.2 Silicon Membrane Waveguide Design

In order to support low-loss propagation of light and tight confinement of sound, we use an optomechanical waveguide geometry which permits separate control of light and sound waves. The device concept is similar to that of Ref. [196]; however, instead of using a silicon core inside a silicon nitride membrane, the entire device is fabricated from a single-crystal silicon layer using a standard SOI fabrication process. The design of this optomechanical silicon waveguide is plotted in Fig. 3.2a-c. The structure consists of a suspended silicon membrane with a ridge waveguide in the center. This structure permits tailorable guidance of light and sound waves to optimize and tailor their interaction—while light is confined to the 1- μm -wide ridge waveguide core, elastic waves extend throughout the 3- μm -wide membrane. The low-loss TE-like (transverse electric-like) guided optical mode at $\lambda = 1550$ nm has the x -directed electric field profile plotted in Fig. 3.2d. Figure 3.2e plots the corresponding electrostrictive optical force generated by this mode; these optical forces mediate efficient coupling to a guided phonon mode at ~ 4 GHz frequencies whose displacement amplitude is plotted in Fig. 3.2f.

Scanning electron micrographs of the device as-fabricated are plotted in Fig. 3.2d-i. Each suspended region (as seen in Fig. 3.2i) is supported by periodic nanoscale (500 nm) tethers placed every 50 μm along the waveguide length; this design enables robust fabrication of cm-long suspended waveguides. For more details on the device fabrication process, see Appendix A.

3.3 Nonlinear Absorption in Silicon Waveguides

Within silicon waveguides, several forms of nonlinear optical losses are possible, which can hinder device performance at high guided-wave powers. At telecommunications wavelengths (around 1550 nm), the dominant effects are two-photon absorption (TPA) and free-carrier absorption. The former results from two photons being absorbed to excite an electron from the valence band to the conduction band through a phonon-assisted transition, resulting in a nonlinear effect that is third-order in electric field amplitude (i.e. is a $\chi^{(3)}$ process). Excited free carriers can then absorb light through intraband optical absorption called

TPA-induced free-carrier absorption (FCA), resulting in a fifth-order nonlinear loss. At high power levels, this absorption often dominates over the third order nonlinear loss.

Two-photon absorption is related to the Kerr nonlinearity through the Kramers-Kronig relations and can be described by a material parameter which is the imaginary part of the nonlinear refractive index n_2 . In silicon, this value is around $\beta_{\text{TPA}} = 1 \text{ cm GW}^{-1}$ at 1550 nm [245, 246]. The effective absorption coefficient (in units of inverse length times inverse guided-wave power) for a propagating optical mode can be estimated as $\beta_{\text{TPA}}/A_{\text{eff}}$, where A_{eff} is the effective mode area. A detailed calculation which takes into account the full-vectorial nature of tightly-confined electromagnetic modes is presented in Refs. [241, 247].

The strength of the free-carrier nonlinearity depends on the steady-state free-carrier population, which is a function of the free-carrier generation rate and excited carrier lifetime [248]. The free-carrier density can be found from the rate equation

$$\frac{dN(t)}{dt} = \frac{\beta_{\text{TPA}}}{2\hbar\omega} I^2(t) - \frac{N(t)}{\tau}, \quad (3.1)$$

where ω is the photon frequency and τ is the effective free-carrier lifetime [248]. This free-carrier population changes the real and imaginary parts of the material refractive index, the latter of which results in an excess optical absorption. Methods to calculate the strength of this absorption are studied using a Drude-Lorentz model in Refs. [248, 249], or a Drude-Sommerfeld model in Ref. [250].

The propagating power evolution for a single pump field in a silicon waveguide can be described by the differential equation

$$\frac{dP_p}{dz} = -\alpha P_p - \beta P_p^2 - \gamma P_p^3 \quad (3.2)$$

where α is the linear loss and γ is the guided-wave free-carrier absorption coefficient. In the presence of a strong pump field within a single-mode waveguide, induced cross-field nonlinear absorption results in a power evolution for a weak probe or signal field of

$$\frac{dP_s}{dz} = -\alpha P_s - 2\beta P_p P_s - \gamma P_p^2 P_s. \quad (3.3)$$

3.4 Characterization of Optical Loss

In order to achieve robust Brillouin amplification, low linear and nonlinear losses are necessary. We first quantified the linear propagation losses of the suspended membrane waveguide through modified cutback measurements—several waveguides of different lengths were fabricated on the same chip, and their total transmission was measured. The resulting loss measurements are plotted in Fig. 3.3a. These measurements correspond to a linear propagation loss of 0.18 ± 0.02 dB/cm (linear loss coefficient $\alpha = 4.1 \pm 0.5$ m⁻¹), with insertion losses of 6.5 dB/facet from integrated grating couplers used to couple light on-chip.

These low linear losses are possible due to the relatively wide ridge waveguide design and separate geometric confinement of light and sound waves. The relatively shallow 80 nm ridge structure minimizes interactions between the optical mode and rough sidewalls [251]. Furthermore, the nanoscale tethers which suspend the structure are spatially separated from the optical mode area and do not contribute to scattering loss.

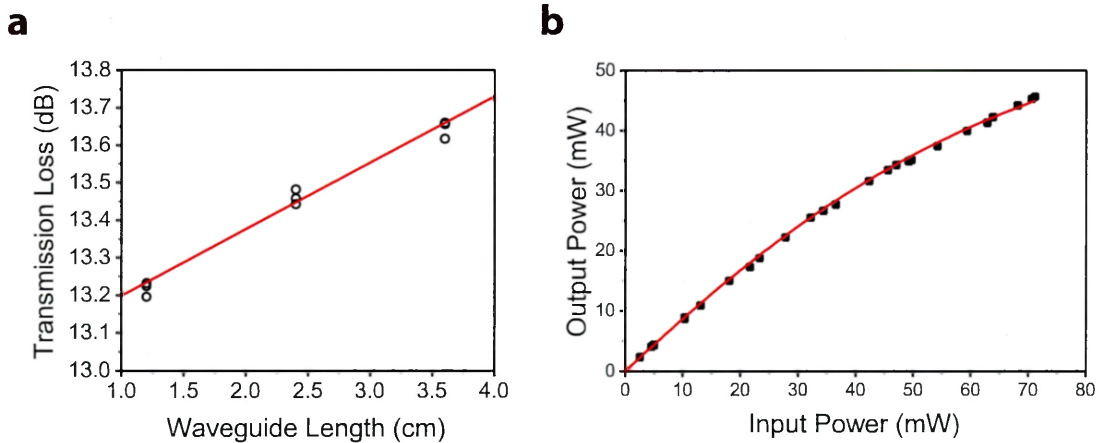


Figure 3.3: **Silicon membrane waveguide propagation loss measurements** (a) Total transmission loss of a low-power probe as a function of waveguide length for a series of test waveguides. Red line is a fit corresponding to a linear loss of 0.18 dB/cm. (b) Observation of nonlinear loss as input power is increased. Red line is a fit to Eq. 3.2. All measurements are at an optical wavelength of 1550 nm. Adapted from Ref. [219].

In order to characterize the nonlinear absorption in the optomechanical silicon waveguide, power-dependent transmission measurements were carried out within the device. These measurements, showing output optical power as a function of input power, are plot-

ted in Fig. 3.3b for incident on-chip powers up to 72 mW. To extract the corresponding nonlinear FCA coefficient, we first begin by theoretically calculating the nonlinear absorption due to TPA using the full-vectorial method of Ref. [247]. Assuming bulk nonlinearity values of $n_2 = 4.5 \times 10^{-18} \text{ m W}^{-1}$ and $\beta_{\text{TPA}} = 7.9 \times 10^{-12} \text{ m W}^{-1}$ [245] along with finite element simulations of the optical mode field profiles using the commercially-available package COMSOL, we found a guided-wave nonlinear Kerr coefficient $\gamma_k = 110 \pm 17 \text{ m}^{-1}\text{W}^{-1}$ and two-photon absorption coefficient $\beta = 48 \pm 14 \text{ m}^{-1}\text{W}^{-1}$.

The measured value of the linear loss α and calculated value of two photon absorption β are used along with the model in Eq. 3.2 to fit the data in Fig. 3.3b and determine the value for the fifth-order FCA loss coefficient γ . The corresponding fit is plotted as the red line, showing good agreement with measured data. These data correspond to a free-carrier absorption coefficient $\gamma = 2550 \pm 450 \text{ m}^{-1}\text{W}^{-2}$. This value is more than an order of magnitude smaller than that reported for Brillouin-active nanowires in [197], where such losses were a fundamental limit to Brillouin amplification. In the following section, we will see that this dramatically improved fifth-order loss is due in part to passive reductions in the effective free-carrier lifetime.

3.5 Measurements of Free-carrier Lifetimes in the Silicon Optomechanical Waveguide

In this section, we estimate the effective lifetime of excited free carriers within the silicon waveguide through two different combinations of experimental and theoretical analyses. The first is using the measured value of γ and calculated and measured experimental parameters along with a steady-state model. The second method is by using dynamic frequency-dependent modulation of the free-carrier density and measuring its effect on nonlinear four-wave mixing. These measurements show that the ridge waveguide structure allows for dramatic reduction of the free-carrier lifetime compared to bulk values through the effects of surface recombination and in-plane carrier diffusion [249]. These reduced nonlinear interactions permit low-loss propagation of light even at high guided-wave powers, which ultimately allow robust Brillouin amplification to occur in this device.

3.5.1 Steady-state Free-carrier Absorption

Under the condition of continuous-wave (cw) illumination, the steady-state free-carrier population density from Eq. 3.1 is

$$\Delta N = \frac{\beta_{\text{TPA}}\tau}{2\hbar\omega} \left(\frac{P_{\text{p}}}{A_{\text{eff}}} \right)^2. \quad (3.4)$$

As before, P_{p} is the optical pump power and A_{eff} is the optical mode effective area. This free-carrier concentration induces an electro-optic absorption $\alpha_{\text{FCA}} = \gamma P_{\text{p}}^2$ with units of inverse length approximately given by: [252]

$$\alpha_{\text{FCA}} = 1.45 \times 10^{-17} \left(\frac{\lambda}{1.55} \right)^2 \Delta N \quad (3.5)$$

where λ is the optical wavelength in microns and ΔN is the density of electron-hole pairs from Eq. 3.4. Comparing this expression with the measured value for the free-carrier absorption coefficient and known parameters of the system leads to an estimated carrier lifetime $\tau = 2.2$ ns, a large reduction relative to bulk values of >10 ns. We next corroborate this measurement through a dynamic modulation measurement of the free-carrier density.

3.5.2 Four-wave Mixing Modification by Free-carrier Modulation

In addition to acting as a source of nonlinear absorption, the free-carrier nonlinearity modifies the real part of the material refractive index. However, in contrast to the Kerr nonlinearity which is practically instantaneous, the free-carrier nonlinearity responds at a rate limited by the relatively long free-carrier lifetime. We exploit this effect to measure the frequency-dependence of the index modulation strength due to this nonlinearity, and thereby provide an additional estimation of the free-carrier lifetime.

The experimental approach is as follows: Two bright pump fields with power amplitudes A_1 and A_2 of equal magnitude and separated by a difference frequency Ω are incident in the silicon waveguide. These waves produce free carriers through two-photon absorption with a time-harmonic modulation at this same frequency. A third probe field with amplitude A_4 at a frequency far detuned from the pump waves is injected into the waveguide simultane-

ously, and experiences phase modulation due to the time-dependent free-carrier population, transferring light to red-detuned (Stokes) and blue-detuned (anti-Stokes) sidebands with amplitudes A_3 and A_5 , respectively, with relative frequencies of $\pm\Omega$.

The TPA-induced free-carrier population creates refractive index and absorption modifications proportional to the change in carrier density [252]:

$$\Delta n = -\frac{e^2 \lambda^2}{8 \pi^2 c^2 \epsilon_0 n} \left[\frac{\Delta N_e}{m_e} + \frac{\Delta N_h}{m_h} \right] \approx -\frac{e^2 \lambda^2}{8 \pi^2 c^2 \epsilon_0 n} \left[\frac{1}{m_e} + \frac{1}{m_h} \right] \cdot \Delta N \equiv Q \cdot \Delta N, \quad (3.6)$$

$$\Delta \alpha = \frac{e^3 \lambda^2}{4 \pi^2 c^3 \epsilon_0 n} \left[\frac{\Delta N_e}{m_e^2 \mu_e} + \frac{\Delta N_h}{m_h^2 \mu_h} \right] \approx \frac{e^3 \lambda^2}{4 \pi^2 c^3 \epsilon_0 n} \left[\frac{1}{m_e^2 \mu_e} + \frac{1}{m_h^2 \mu_h} \right] \cdot \Delta N \equiv V \cdot \Delta N. \quad (3.7)$$

Here e is the fundamental charge, ΔN_e and ΔN_h are the modifications in electron and hole densities, m_e and m_h are the effective electron and hole masses, and μ_e and μ_h are their mobilities.

The time-harmonic free-carrier generation at frequency Ω is written as

$$\Delta N(t) = \text{Re}\{\tilde{N}(\Omega) e^{-i\Omega t}\}, \quad (3.8)$$

where the complex-valued carrier modulation is

$$\tilde{N}(\Omega) = \frac{4\beta_{\text{TPA}}|A_1|^2|A_2|^2}{\hbar\omega A_{\text{eff}}} \cdot [1/\tau - i\Omega]^{-1}. \quad (3.9)$$

With these equations, the five-field coupled-amplitude equations can be written as:

$$\frac{dA_1}{dz} = i\gamma_k \left[|A_1|^2 + 2|A_2|^2 + 2|A_4|^2 \right] \cdot A_1 \quad (3.10)$$

$$\frac{dA_2}{dz} = i\gamma_k \left[|A_2|^2 + 2|A_1|^2 + 2|A_4|^2 \right] \cdot A_2 \quad (3.11)$$

$$\frac{dA_3}{dz} = i(2\gamma_{\text{FWM}}^*) A_1 A_2^* A_4 + \left[i\frac{\omega}{c} \cdot \frac{Q}{2} + \frac{V}{4} \right] \cdot \tilde{N}^*(\Omega) \cdot A_4 \quad (3.12)$$

$$\frac{dA_4}{dz} = i\gamma_k \left[|A_4|^2 + 2|A_1|^2 + 2|A_2|^2 \right] \cdot A_4 \quad (3.13)$$

$$\frac{dA_5}{dz} = i(2\gamma_{\text{FWM}}) A_1^* A_2 A_4 + \left[i\frac{\omega}{c} \cdot \frac{Q}{2} + \frac{V}{4} \right] \cdot \tilde{N}(\Omega) \cdot A_4 \quad (3.14)$$

Here γ_k is the complex third order nonlinear coefficient, including both Kerr and associated TPA. $\gamma_{\text{FWM}} = \text{Re}\{\gamma_k\}$ is the nonlinear coefficient for third-order four-wave mixing. These equations include the effects of self- and cross-phase modulation for incident pump and probe waves A_1 , A_2 , and A_4 , and the four-wave mixing and free-carrier nonlinearities for the generated sidebands.

Experimental characterization of these effects is carried out using the apparatus diagrammed in Fig. 3.4a. Two strong pump waves around 1550 nm and separated in frequency by Ω are generated from the same laser using a null-biased intensity modulator driven at $\Omega/2$ by a microwave frequency synthesizer. These waves are combined with probe light at 1535 nm in a fiber wavelength-division multiplexer and coupled on-chip, where nonlinear energy transfer occurs. The resulting signal is routed off-chip and passed through an interference filter which rejects light at the pump wavelength, and passes only modulated probe light. This signal is combined with a frequency-shifted local oscillator synthesized from the probe laser using an acousto-optic modulator and combined on a fast photoreceiver to perform heterodyne spectral analysis in the microwave domain.

Fig. 3.4b plots the power in each of the nonlinearly-generated probe sidebands (with relative frequencies of $\pm\Omega$) as a function of modulation frequency. While the sidebands exhibit an asymmetry in their frequency response due to the relative phases of competing nonlinear effects, both are enhanced at low modulation frequencies where the free-carrier

population responds strongly. These data are fit to the model of Eqs. 3.5.2 with reasonable values used for the various electronic parameters in the model, and a best-fit free-carrier lifetime of 2.3 ns.

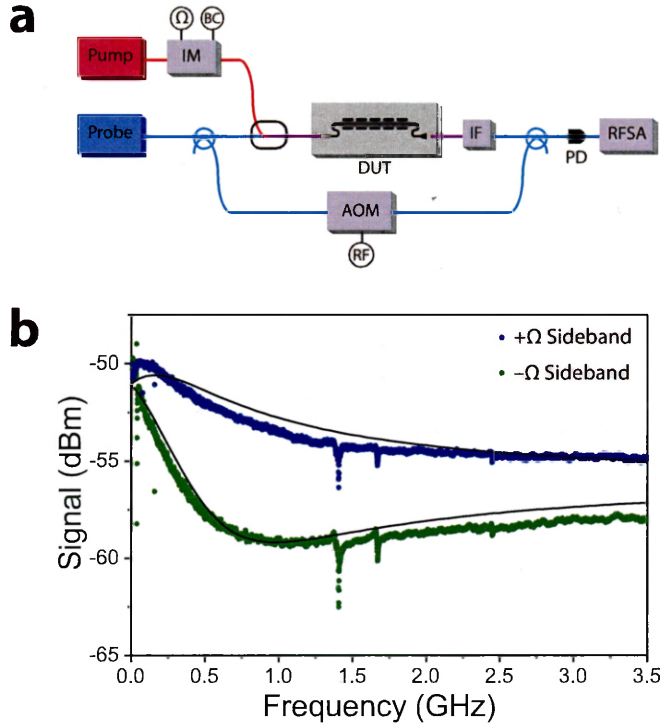


Figure 3.4: **Free-carrier-induced modulation** (a) Diagram of the heterodyne four-wave-mixing experiment. The photoexcited free-carrier density is modulated by strong pump fields separated by frequency Ω , resulting in nonlinearly-induced phase changes to the probe beam. An acousto-optic modulator provides a reference field for heterodyne detection. (b) Traces for measured anti-Stokes (blue, upper curve) and Stokes (green, lower curve) signals and corresponding theoretical curves as a function of pump modulation frequency. Several Brillouin resonances, which produce narrowband acousto-optic phase modulation, are also visible. The total input power is around 70 mW. Adapted from Ref. [219].

3.5.3 Passive Reduction of the Free-carrier Lifetime

These measured free-carrier lifetimes are orders of magnitude smaller than values for lightly-doped bulk silicon, which are typically ≈ 100 s of ns. This reduction can be attributed to at least two effects: First, due to the small thickness of the silicon ridge waveguide, surface recombination at the boundaries leads to a reduction in the effective carrier lifetime [253]. However, this effect is more dramatic if surfaces are of poor quality, which is not necessarily

the case in our low-loss ridge waveguides. A more dramatic benefit is likely supplied by the ridge waveguide geometry; while high carrier densities are generated in the waveguide core, these excited free carriers rapidly diffuse into the membrane. This in-plane diffusion permits dramatic passive reduction of the effective free-carrier lifetime, which decreases of the effective free-carrier loss [249, 253]. Further optimizations of the waveguide cross-sectional design may further reduce the free-carrier lifetimes.

An alternate (or complementary) approach to mediate free-carrier losses, which we did not utilize in this structure, is the active removal of free carriers by placing an electric field across the device. This is commonly done by placing a reverse-biased p-i-n junction across the waveguide core to achieve high field intensities. While this approach has been extensively used in Raman lasers and amplifiers [236, 244, 254], it leads to high electrical power dissipation and so is not suitable for all applications.

3.6 Forward Brillouin Gain: Coupled-amplitude Equations

To model the coupled-wave dynamics of FSBS in the silicon membrane waveguide, we leverage the coupled-amplitude formalism of Section 2.2.2 and Ref. [233], and include the effects of linear and nonlinear absorption from Eqs. 3.2-3.3. Through FSBS, Stokes (red-shifting) and anti-Stokes (blue-shifting) processes are intrinsically linked since they couple through the same phonon. The resulting coupled power-amplitude equations, including the effects of nonlinear loss from a strong pump wave, are:

$$\frac{\partial a_s}{\partial z} = \frac{-G_B}{2} (a_p b^*) - \frac{1}{2} (\alpha + 2\beta |a_p|^2 + \gamma |a_p|^4) a_s, \quad (3.15)$$

$$\frac{\partial a_p}{\partial z} = \frac{G_B}{2} (a_s b - a_{as} b^*) - \frac{1}{2} (\alpha + \beta |a_p|^2 + \gamma |a_p|^4) a_p, \quad (3.16)$$

$$\frac{\partial a_{as}}{\partial z} = \frac{G_B}{2} (a_p b) - \frac{1}{2} (\alpha + 2\beta |a_p|^2 + \gamma |a_p|^4) a_{as}, \quad (3.17)$$

$$b = a_s^* a_p + a_p^* a_{as}. \quad (3.18)$$

Here the optical powers are normalized such that $P_i = |a_i|^2$, and G_B is the Brillouin gain coefficient. These equations predict small-signal Stokes gain factor of $P_s(z)/P_s(0) = 1 + G_B P_p z + (G_B P_p z)^2/4$ according to Eq. 2.54, but this gain is expected to saturate at moderate

powers due to nonlinear absorption.

3.7 Experimental Observation of Forward Brillouin Amplification

In order to determine the net optical amplification supported by the silicon membrane waveguide, we first experimentally examine the small-signal Brillouin gain to quantify the intrinsic Brillouin coupling strength. Combining these gain measurements with the prior studies of linear and nonlinear loss, we then calculate the total on-chip amplification.

The experimental apparatus used to perform direct gain measurements is diagrammed in Fig. 3.5a. Light at frequency ω_p from a tunable narrow-linewidth semiconductor laser is passed through an intensity modulator driven by a microwave frequency synthesizer at frequency Ω to produce frequency-detuned sidebands at $\omega_p \pm \Omega$. An erbium doped fiber amplifier is used to boost the intensity of these waves and the unwanted $+\Omega$ sideband is filtered out using a fiber Bragg grating (FBG) notch filter. As a result, what remains is a strong pump at frequency ω_p and weak signal wave at frequency $\omega_s = \omega_p - \Omega$ synthesized from the same laser. Throughout these small-signal gain experiments, the signal wave power is 30 dB smaller than that of the pump wave.

Light is coupled on chip using integrated grating couplers, and passed through a narrow tapered bend region to eliminate any higher-order modal content. This coupling method ensures that only the fundamental TE-like optical mode is present on-chip. After light passes through the active device region, it is coupled off-chip, passed through an optical isolator, and any light scattered to the blue side of the pump wave is rejected by a notch filter identical to the first FBG. This is used because the forward-SBS process produces a form dual-sideband gain where pump energy is transferred to both red- and blue-shifted sidebands; the additional filter removes the output anti-Stokes light. To measure the power of the transmitted signal, pump and signal waves are both incident on a fast photoreceiver. These two fields interfere to create a microwave signal at their difference frequency. In this way, we can characterize the transmitted signal power as a function of pump-probe frequency detuning Ω with sub-Hz resolution, which is otherwise not possible with optical

spectral analysis.

The total power of the RF beat note between pump and Stokes waves is proportional to $P_p P_s$, the product of pump and signal wave powers. As Ω is swept through the Brillouin frequency Ω_B of the device, the intensity of the beat note grows proportionally to the Stokes gain of the device.

In the presence of pump and signal fields at the detector, the total electric field amplitude is

$$E(t) = E_p \cos(\omega_p t) + E_s \cos(\omega_s t + \phi). \quad (3.19)$$

Where E_p and E_s are the pump and signal field intensities, and ϕ is an arbitrary phase term. The resulting photocurrent is

$$i(t) \propto \langle E^2(t) \rangle = \frac{1}{2} E_p^2 + \frac{1}{2} E_s^2 + E_p E_s \cos((\omega_p - \omega_s)t - \phi). \quad (3.20)$$

Here time averaging has been applied for sum-frequency terms that are much faster than the detector bandwidth. The corresponding RF power at frequency $\Omega = \omega_p - \omega_s$ is proportional to the square of the photocurrent:

$$P_{\text{RF}} = \eta P_p P_s \quad (3.21)$$

where η is a coefficient of proportionality that takes into account the detector responsivity and gain and coupling losses between waveguide and detector.

As the signal is swept through the Brillouin resonance, it increases in power:

$$P_{\text{RF}}(\Omega) = \eta P_p (P_s^0 + \Delta P_s(\Omega)). \quad (3.22)$$

This change in signal intensity is referred to as the Brillouin gain. To determine this gain, the signal is normalized as

$$\frac{P_{\text{RF}}(\Omega)}{\eta P_p P_s^0} = 1 + \frac{\Delta P_s(\Omega)}{P_s^0}. \quad (3.23)$$

This is equivalent to the case of a traditional power gain measurement, where $P_s = P_s^0 + \Delta P_s(\Omega)$ is measured and $P_s/P_s^0 = 1 + \Delta P_s(\Omega)/P_s^0$. This experiment allows the measurement of small-signal gain as a function of pump power, which, along with the linear and

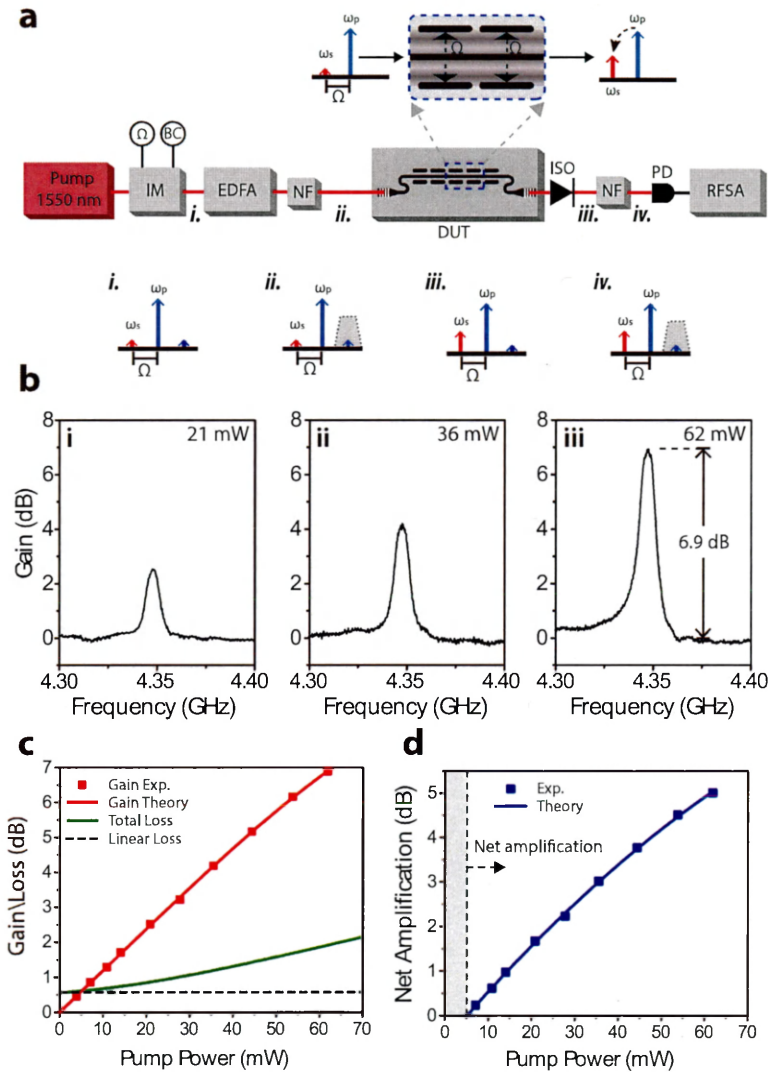


Figure 3.5: **Experimental demonstration of Brillouin amplification.** (a) Detailed diagram for the Brillouin gain experiment. Subpanels (i)-(iv) illustrate the spectral content of the different tones present corresponding to positions i-iv along the signal path. In diagrams (ii) and (iv), the $+\Omega$ modulation sideband is removed by a notch filter. Abbreviations: IM Mach-Zehnder intensity modulator; EDFA erbium-doped fiber amplifier; NF notch filter; DUT device under test; ISO optical isolator; PD fast photodetector; RFSA radio-frequency spectrum analyzer/power meter. (b) Panels (i), (ii), and (iii) are gain spectra around the Brillouin frequency obtained for pump powers of 21, 36, and 62 mW, respectively. (c) plots peak gain (red), linear loss (dash) and total loss (green) versus on-chip pump power at 1550 nm wavelengths. (d) shows net amplification as a function of pump power. The threshold for amplification is 5 mW. Adapted from Ref. [219].

nonlinear loss measurements, is used to determine net amplification in the optomechanical silicon waveguide.

Figures 3.5b.i-iii plot the measured forward-SBS gain spectra for incident on-chip pump powers of 21, 36, and 62 mW, respectively, around the Brillouin frequency $\Omega_B = 4.35$ GHz that corresponds to the resonance frequency of the acoustic phonon plotted in Fig. 3.2f. These data reveal a high quality factor ($Q = 680$) acoustic resonance with up to 6.9 dB of optical gain at the highest tested pump powers. Repeated measurements of the the peak Brillouin gain as a function of pump power are plotted atop net optical loss in Fig. 3.5c. The optical gain is fit to a model that includes Brillouin coupling and optical losses (red theory line) to determine a Brillouin gain coefficient of $G_B = 1150 \pm 60 \text{ W}^{-1}\text{m}^{-1}$ for this phonon mode, in good agreement with simulated Brillouin gain of $1020 \pm 190 \text{ W}^{-1}\text{m}^{-1}$ at a frequency of 4.41 GHz obtained from finite element simulations.

Net Brillouin amplification, plotted in Fig. 3.5d, is calculated by subtracting the total propagation loss (green) from the peak Brillouin gain (red) in Fig. 3.5c. These data reveal net optical amplification at on-chip pump powers above a threshold of 5 mW, and up to 5.2 dB of amplification at the highest tested pump power (62 mW). This amplification was limited only by the available pump power from the EDFA and the power handling of the narrow input mode filters. Amplification continues to increase as pump power is increased through the tested pump power range, suggesting that further amplification is possible at higher pump powers in devices with alternate integrated mode filter designs.

These results, made possible by the low linear and nonlinear losses of this 2.9 cm-long optomechanical waveguide, enable a dramatic improvement in nonlinear performance over prior designs, including a 30-fold improvement in net amplification over prior systems [218], and a 40-fold improvement in total Brillouin coupling over Ref. [196]. The linear and/or nonlinear losses of the suspended silicon membrane are an order of magnitude improved over prior systems while maintaining strong ($G_B > 10^3 \text{ W}^{-1}\text{m}^{-1}$) Brillouin gain, due to the ability to separately engineer the optical and elastic modes of this system.

3.7.1 Cascaded Brillouin Energy Transfer

The strong Brillouin couplings and high power handling of the membrane-suspended silicon waveguide also permit a unique form of cascaded Brillouin energy transfer, as predicted in Section 2.2.2. Because both Stokes- and anti-Stokes-shifted waves which participate in the forward-SBS process couple to the same acoustic phonon mode, when strong energy transfer occurs this same phonon can scatter light to successive cascaded orders through a Brillouin cross-phase modulation process. These physics were previously observed in highly-nonlinear microstructured fibers [186].

To observe this phenomenon in our silicon waveguide, we modify the gain experiment (see Fig. 3.6) by removing the notch filters and null-biasing the intensity modulator with a drive frequency $\Omega/2$ to produce two strong frequency tones (at optical frequencies $\omega_p \pm \Omega/2$) separated by Ω , which is fixed to the Brillouin frequency shift Ω_B . After exiting the device, the output light signal is combined with a frequency-shifted local oscillator with a relative frequency offset of $\Delta/2\pi = 40$ MHz, so that each cascaded order can be identified as a unique frequency beat-note in the microwave domain using a radiofrequency spectrum analyzer.

Fig. 3.6b.i-iii shows stem plots of the power amplitude of the optical tones at frequencies of $\omega_p \pm (2n-1)\Omega/2$ for $n = \{-2, -1, 0, 1, 2, 3\}$ at three different total input powers, revealing cascaded energy transfer from the input tones to higher-order frequency components. The evolution of these powers as a function of total incident power is plotted in Fig. 3.6c. As the input power is increased to a maximum of 65 mW, significant cascaded energy transfer is observed from the input tones, including more than 60% power transfer from the $n = 1$ order to other comb lines.

To quantify the strength of this cascaded energy transfer process, we define a relevant figure of merit which is the gain-power-length product $\xi \equiv G_B \sqrt{(P_0 P_1)} L_{\text{eff}}$, where P_0 and P_1 are the incident powers in fields $n = \{0, 1\}$, respectively, and L_{eff} is the effective interaction length taking into account linear and nonlinear losses. This figure of merit is relevant since, in the absence of such losses, the amplitudes a_n of the output fields can be expressed exactly as

$$a_n(\xi) = a_0(0)e^{i(n-2)(\phi-\pi)} J_{n-2}(\xi) + a_1(0)e^{i(n-3)(\phi-\pi)} J_{n-3}(\xi) \quad (3.24)$$

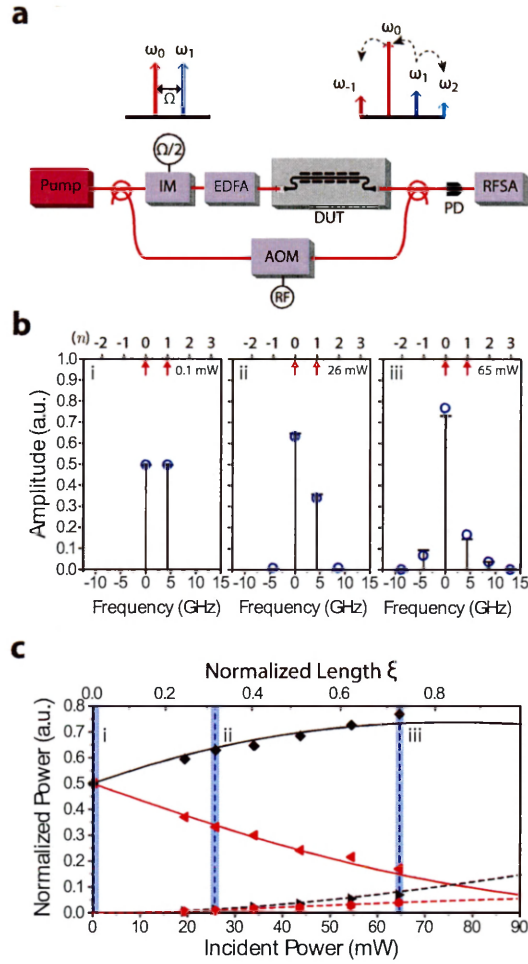


Figure 3.6: **Cascaded forward-SBS energy transfer** (a) Diagram for the modified forward-SBS experiment used to demonstrate energy transfer. Incident pump light is split into two paths. In the upper path, light is passed through a null-biased intensity modulator driven at a frequency $\Omega/2$ to produce two tones separated by a frequency Ω that is set to the Brillouin frequency Ω_B . These two tones are amplified and passed through the device. In the bottom path, light is frequency-shifted by 40 MHz using an acousto-optic modulator, which is then combined with the output light from the device on a fast photoreceiver for heterodyne detection. This technique allows the detection of each cascaded frequency component as a unique microwave beat note whose power is measured using a radiofrequency spectrum analyzer. Abbreviations: IM Mach-Zehnder intensity modulator; EDFA erbium-doped fiber amplifier; DUT device under test; PD fast photodetector; RFSA radio-frequency spectrum analyzer/power meter. (b) Panels (i), (ii), and (iii) are stem plots of the normalized output powers as a function of frequency component order n for total incident powers of 0.1, 26, and 65 mW, respectively. Red arrows denote incident light in orders $n = \{0, 1\}$. These data correspond to the three vertical slices denoted in blue in panel (c), which shows theoretical calculations (lines) and measured amplitudes for pump fields ω_0 and ω_1 (solid black, solid red) and first cascaded fields ω_{-1} and ω_2 (solid red, dashed red) fields. Adapted from Ref. [219].

where ψ is the phase difference between the two incident fields at the device input [186]. For our experimental parameters, $\xi = 0.71$, corresponding to near-saturation of the $n = 1$ field at its maximum value. As this value is increased further, for example by increasing pump powers or device length, more cascaded frequency lines of comparable amplitude would appear. Such processes may be used for wideband energy transfer and frequency/waveform synthesis within integrated waveguides.

3.7.2 Potential for Further Amplification and Energy Transfer

In the experiments presented here, input powers were limited to a number of factors, including input taper damage, the optical power available from external amplifiers, and input coupling losses. Furthermore, fabricated device lengths were limited to < 3 cm in early designs. However, waveguides of the geometry used here can easily support guided-wave powers > 150 mW [165, 221]. Furthermore, low linear and nonlinear propagation losses permit propagation lengths > 10 cm even at relatively high input powers. As a result, the same waveguide parameters studied here could enable as much as 30 dB of net amplification for devices 20 cm in length with improved input power handling. These same conditions permit a figure of merit for cascaded energy transfer $\xi \cong 3.8$, corresponding to energy transfer to more than 10 orders of comparable strength.

Critically, scaling the performance of this device to longer interaction lengths is only possible if dimensional broadening of the phononic resonance does not continue to diminish the Brillouin gain for increasing device lengths [196, 197, 218, 242]. In Section 3.8, we use an alternate experimental technique to corroborate the results presented here and to characterize the Brillouin response of devices of various lengths to study these effects in the suspended silicon optomechanical waveguide design.

3.7.3 Brillouin Gain and Loss

Within the same device, it is also possible to produce Brillouin loss of a blue-detuned probe. In this configuration, the same experiment as Fig. 3.5a is used with a strong pump wave at ω_p and an incident probe wave at the anti-Stokes frequency $\omega_{as} = \omega_p + \Omega$. At low powers, energy is transferred from this frequency component back to the pump wave, and also to

a Stokes-detuned sideband at $\omega_s = \omega_p - \Omega$ through concurrent Stokes scattering processes. The resulting attenuation of the probe wave is plotted in Fig. 3.7a for pump powers of 21, 36, and 62 mW, respectively, reaching a maximum of almost -12 dB at the highest tested pump powers. The strength of Brillouin gain and loss within the same device is plotted as a function of pump power in 3.7b.

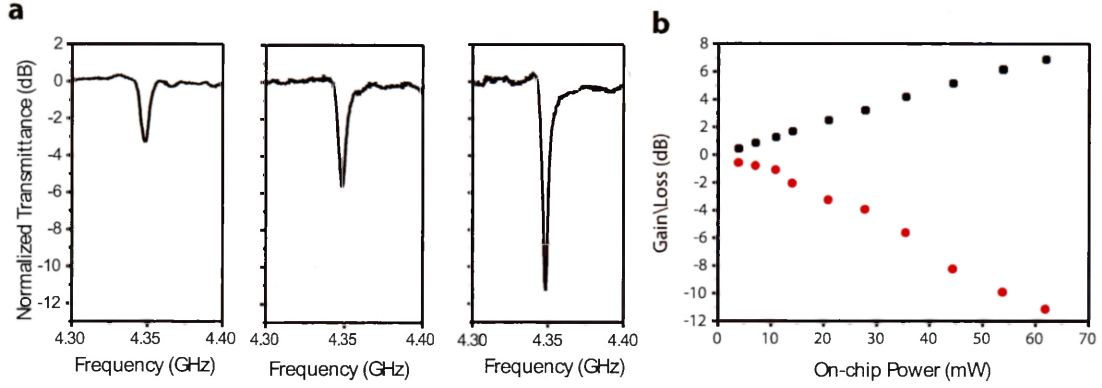


Figure 3.7: **Brillouin gain and loss.** (a) Plots Brillouin attenuation of a weak probe that is blue-detuned from a strong pump wave by the Brillouin frequency shift. The three panels are for pump powers of 21, 36, and 62 mW, respectively. (b) Plots the peak Brillouin gain (black) or loss (red) with increasing pump power within the same device. Brillouin loss becomes exceedingly strong at high pump powers since the generation of Stokes-scattered light preserves the interaction strength as blue-detuned probe light is depleted. Adapted from [219].

The increased strength of this Brillouin loss relative to the gain process is due to the fact that FSBS energy transfer is intrinsically non-exponential since the driven phonon strength is conserved through FSBS couplings. Thus, in contrast to BSBS-based loss, the rate of energy transfer does not decrease as the probe wave propagates. If the pump power were turned up further through these experiments, complete extinction of the blue-detuned probe wave would be observed, after which the direction of energy transfer would reverse, scattering light from ω_p back to ω_{as} through anti-Stokes scattering.

3.8 Coherent Anti-Stokes Brillouin Scattering Measurements and Study of Resonance Broadening

Thus far, we have studied the Brillouin response of the silicon membrane waveguide through direct optical gain and energy transfer measurements. In this section, we present an alternate approach to characterize the Brillouin response of devices using a coherent anti-Stokes Brillouin scattering (CABS) process. In analogy to coherent anti-Stokes Raman scattering (CARS), CABS in principle provides a background-free measurement of the Brillouin nonlinearity. In practice, within highly nonlinear waveguides, other nonlinearities such as the Kerr effect contribute to the measured signal. However, as we will discuss, this can provide a useful benchmark to compare the strength of the Brillouin nonlinearity to a known reference.

The energy level diagram for the CABS process is plotted in Fig. 3.8a. Parametric generation of a Brillouin-active phonon at frequency Ω is mediated by two waves with frequencies $\omega_p^{(1)}$ and $\omega_s^{(1)} = \omega_p^{(1)} - \Omega$ through a FSBS process. Incident probe light at a disparate optical frequency $\omega_p^{(2)}$ can then spontaneously scatter from this excited phonon and become blue-shifted through an anti-Stokes process to $\omega_{as}^{(2)} = \omega_p^{(2)} + \Omega$. This results in the generation of light at a new frequency, and unwanted light signals at the incident frequency can be removed using a fixed-wavelength optical filter if desired.

3.8.1 Phase-matching for CABS and Four-wave Mixing

Phase-matching for CABS is plotted in Fig. 3.8c, with the acoustic dispersion relation of the near-zero wavevector phonon which mediates this process plotted in Fig. 3.8b. The optical dispersion relation is assumed to be linear over the range of frequencies used in this experiment. The phase-matching requirement for the anti-Stokes process is:

$$k(\omega_p^{(2)} + \Omega) = k(\omega_p^{(2)}) + q(\Omega) \quad (3.25)$$

where $q(\Omega)$ is the wavevector of the parametrically-generated acoustic phonon. While this phase-matching requirement is structurally identical to that of traditional SBS, $q(\Omega)$ is

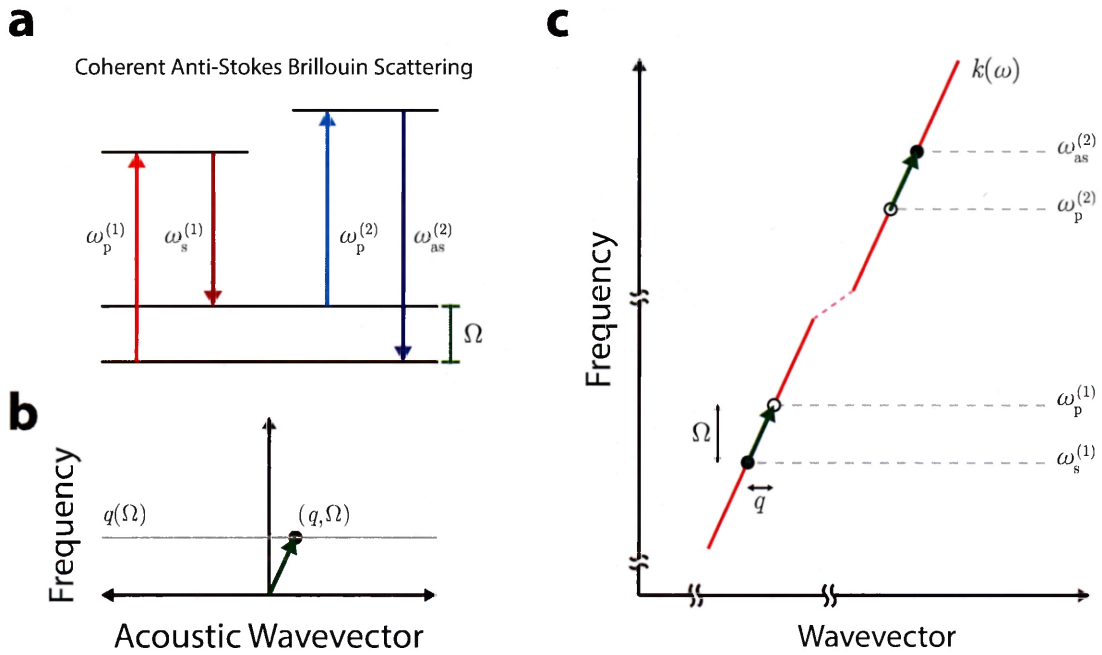


Figure 3.8: **Coherent anti-Stokes forward Brillouin scattering.** (a) Energy level diagram for the CABS process. Pump waves at frequencies $\omega_p^{(1)}$ and $\omega_s^{(1)}$ coherently excite the system to an excited vibrational state (i.e. excite an acoustic phonon). Probe light at frequency $\omega_p^{(2)}$ absorbs this phonon through a Brillouin scattering process and is blue-shifted to frequency $\omega_{as}^{(2)}$. This coupling is mediated through an elastic cutoff mode whose dispersion relation is sketched in (b). For intra-modal forward Brillouin scattering, this mode has near-zero wavevector. (c) plots both energy conservation and phase-matching for this process on top of the optical dispersion curve.

fixed by the wavevectors of the optical drive waves:

$$q(\Omega) = k(\omega_p^{(1)}) - k(\omega_p^{(1)} - \Omega). \quad (3.26)$$

However, as a result, the phase-matching requirements for this process are exactly the same as for Kerr-induced four-wave mixing. The latter can be expressed as

$$k(\omega_p^{(1)}) + k(\omega_p^{(2)}) = k(\omega_p^{(1)} - \Omega) + k(\omega_p^{(2)} + \Omega) \quad (3.27)$$

where the phase-matching requirement states that the net wavevectors of the input and output particle states must be equal. The right-hand side can be rewritten to first order as:

$$k(\omega_p^{(1)}) + k(\omega_p^{(2)}) = k(\omega_p^{(1)}) - \Omega \frac{dk}{d\omega}(\omega_p^{(1)}) + k(\omega_p^{(2)}) + \Omega \frac{dk}{d\omega}(\omega_p^{(2)}) \quad (3.28)$$

In other words, so long as $\frac{dk}{d\omega}(\omega_p^{(2)}) \approx \frac{dk}{d\omega}(\omega_p^{(1)})$, which is required for CABS, four-wave mixing will also be phase-matched. This result is general even when different optical modes are introduced, i.e. in the case of inter-band CABS and inter-band four-wave mixing.

3.8.2 Theory of CABS in the Presence of Four-wave Mixing

We briefly outline the coupled amplitude equations which describe the dynamics of CABS in the presence of Kerr-induced self- and cross-phase modulation and four-wave mixing. This treatment is similar to the treatment for free-carrier induced four-wave mixing in Section 3.5.2, except that we assume that optical powers are small enough that free-carrier-induced fifth-order nonlinearities are negligible, and we now include the effects of Brillouin couplings in the coupled equations of motion.

The CABS process is driven by two bright pump fields with power amplitudes A_1 and A_2 separated by difference frequency Ω . These waves drive a coherent phonon field whose spatial evolution is determined by their intensity-beat note. This is equivalent to the approximation that the phonon field decays rapidly in space as compared to the length scale over which significant optical energy transfer occurs.

In order to probe the dynamics of the driven phonon field through CABS, a probe field

with amplitude A_4 is simultaneously injected into the waveguide, and experiences phase modulation due to the driven phonon field, transferring light to red-detuned (Stokes) and blue-detuned (anti-Stokes) sidebands with amplitudes A_3 and A_5 , respectively, with relative frequencies of $\pm\Omega$. In the following equations we have included the effects of pump depletion due to Brillouin scattering, but not due to four-wave mixing—this is equivalent to the condition that $|A_4A_5| \ll |A_1A_2|$ and $|A_4A_3| \ll |A_1A_2|$, in other words that the probe and generated four-wave mixing tones are small as compared to the pump fields. The full four-wave mixing dynamical equations are derived in [75]. In practical spectroscopy measurements, pump depletion from both processes is negligible. With these approximations, the coupled amplitude equations of the five coupled waves can be written as [75, 196, 219]:

$$\frac{dA_1}{dz} = i\gamma_k \left[|A_1|^2 + 2|A_2|^2 + 2|A_4|^2 \right] \cdot A_1 + i\gamma_B^*(\Omega) |A_2|^2 A_1 \quad (3.29)$$

$$\frac{dA_2}{dz} = i\gamma_k \left[|A_2|^2 + 2|A_1|^2 + 2|A_4|^2 \right] \cdot A_2 + i\gamma_B(\Omega) |A_1|^2 A_2 \quad (3.30)$$

$$\frac{dA_3}{dz} = i(2\gamma_{\text{FWM}}^* + \gamma_B^*(\Omega)) A_1 A_2^* A_4 \quad (3.31)$$

$$\frac{dA_4}{dz} = i\gamma_k \left[|A_4|^2 + 2|A_1|^2 + 2|A_2|^2 \right] \cdot A_4 \quad (3.32)$$

$$\frac{dA_5}{dz} = i(2\gamma_{\text{FWM}} + \gamma_B(\Omega)) A_1^* A_2 A_4 \quad (3.33)$$

When the Brillouin nonlinearity is mediated by coupling to a single phonon mode, its frequency dependence can be approximated as:

$$\gamma_B(\Omega) = \frac{G_B}{2} \frac{\Omega_B/2Q}{\Omega_B - \Omega - i\Omega_B/2Q} \quad (3.34)$$

where Ω_B is the Brillouin frequency corresponding to the acoustic phonon resonance, Q is the quality factor of this mechanical resonance, and G_B is the peak Brillouin gain coefficient.

In the small-signal approximation, the optical power in the anti-Stokes field is given by

$$|A_{3,\text{out}}|^2 = w |\gamma_B (\Omega) + 2\gamma_{\text{FWM}}|^2 P_1 P_2 P_4 L^2 \quad (3.35)$$

where P_i is the incident power in field A_i , L is the device length, and w is a constant determined by normalization of the optical fields. Note that here we have assumed that the Brillouin-active and Kerr-active lengths of the device are the same. In the case of structures that do not experience Brillouin coupling along their entire length, the effective Brillouin gain should be normalized by a factor which is the ratio between Brillouin-active and total device lengths [196, 219].

While the Brillouin nonlinearity is sharply resonant, the Kerr nonlinearity is frequency-independent over similar bandwidths. As a result, output spectra can be fit as normalized relative to the constant FWM background as

$$\frac{|A_{3,\text{out}}|^2}{|A_{3,\text{out}}^{\Omega \neq \Omega_B}|^2} = \left| e^{i\phi_r} + \frac{G_B}{4\gamma_{\text{FWM}}} \frac{\Omega_B/2Q}{\Omega_B - \Omega - i\Omega_B/2Q} \right|^2. \quad (3.36)$$

Here, ϕ_r is the relative phase between Kerr and background nonlinearities. The corresponding response has a Fano-like lineshape typical of interference between resonant and background scattering processes [255]. This lineshape can be fit to determine the Brillouin resonance frequency, quality factor Q , and the relative strength of Brillouin and four-wave mixing nonlinearities $\frac{G_B}{4\gamma_{\text{FWM}}}$.

This technique has previously been used to characterize forward Brillouin coupling in several studies [196, 197, 218], where it was also referred to as a “heterodyne four-wave mixing measurement” or “Brillouin cross-phase modulation.” Because the output signal of the CABS process is directly proportional to the input powers and interaction length, rather than appearing as gain on top of an optical input field, this technique allows measurement of the Brillouin response with great sensitivity even when $G_B PL \ll 1$, i.e. for small gain-power-length products.

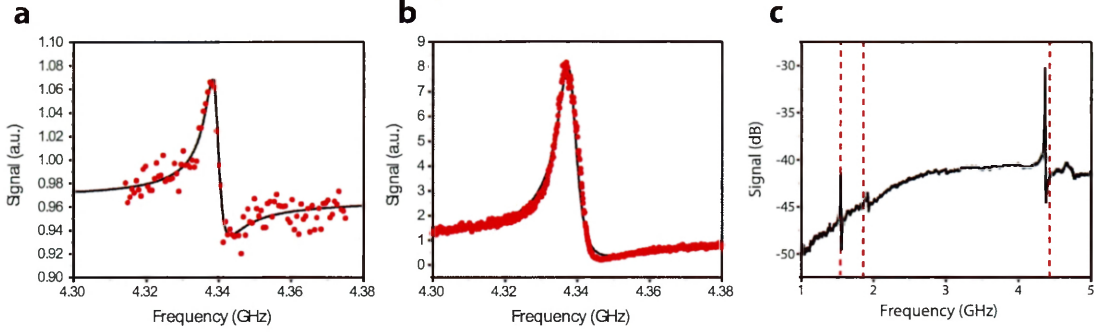


Figure 3.9: **Coherent anti-Stokes Brillouin Scattering data** (a) and (b) Plot data (red dots) and fits to Eq. 3.36 for CABS signatures on devices with lengths of 0.5 mm (a) and 29 mm (b). The shorter device displays a narrower intrinsic linewidth since it experiences less resonance broadening from fabrication variations along the device length. (c) Plots a wideband sweep depicting the 29 mm device’s three strongest Brillouin resonances and their simulated frequencies (red dashes). The background shape is due to the free-carrier effect discussed above. Adapted from Ref. [219].

3.8.3 CABS Data

To further corroborate our experimental measurements of Brillouin gain, and to study the effects of dimensionally-induced broadening as device lengths are changed, we perform CABS spectroscopy of several Brillouin-active waveguides of different suspended lengths. Experimental data on two such devices are plotted in Fig. 3.9. The first device, whose dominant Brillouin response is plotted in Fig. 3.9a, has only 500 μm of its total length suspended by tethers, and shows an intrinsic quality factor $Q \approx 1000$ for the phonon resonance based on a fit to Eq. 3.36. Fig. 3.9b plots the experimental response of the device whose net optical amplification was characterized earlier. This fit gives a quality factor $Q = 680$, and $\frac{G_B}{4\gamma_{\text{FWM}}} \approx 2.55$. For this device, with simulated value of the Kerr nonlinearity $\gamma_k = 110 \text{ W}^{-1}\text{m}^{-1}$, this corresponds to a Brillouin gain $G_B = 1120 \pm 180 \text{ W}^{-1}\text{m}^{-1}$. Both of these numbers are in good agreement with those determined from direct gain measurements. Fig. 3.9c plots a wideband scan showing the three strongest Brillouin resonances in this device—the measured frequencies of these Brillouin-active phonons agree well with computed frequencies from finite-element elastic simulations.

One word of caution is necessary when fitting experimental data to Eq. 3.36—especially when signal-to-noise is poor. In practice, the Fano fitting function seems to be under-

constrained without fixing one or several of the fit parameters to a known value. For example, fits with different values of ϕ_r , Ω_B , Q , and $\frac{G_B}{\gamma_{\text{FWM}}}$ can give lineshapes which are qualitatively or even quantitatively similar. In one related test case where we numerically simulated the dynamics of a system with fixed input values of all parameters except for the phase ϕ_r and an additional phase mismatch term, fits to the numerical data which appeared near-ideal gave parameter values for Q and G_B which differed from their input values from as much as 10%.

3.8.4 Dimensional Broadening of Brillouin Resonances

With the creation of the first Brillouin-active silicon waveguides, it was immediately realized that fabrication variations along the waveguide can lead to effective broadening of the resonant Brillouin response [196,242]. This effect leads to a decrease in the effective phononic quality factor, and hence the Brillouin gain. This form of inhomogeneous broadening was studied as a function of device length and dimension for silicon nanowires in Refs. [197, 218]. Due to variations in wafer thickness and fabrication (e.g. etch depth) over large length scales, this effect is compounded as device length increases. As a result, Brillouin amplification measured in micron- or millimeter-scale devices does not necessarily scale to longer interaction lengths.

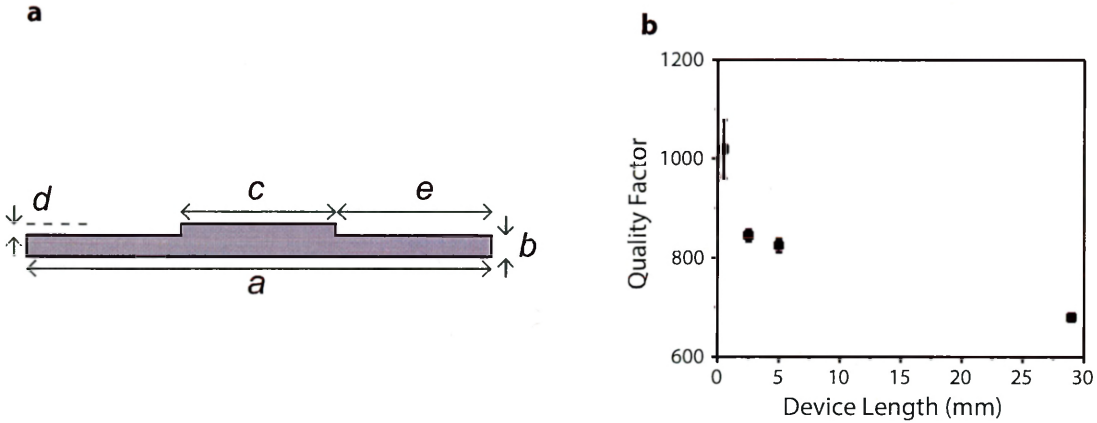


Figure 3.10: **Dimension-induced broadening.** (a) depicts the relevant dimensions which define the waveguide cross-section. (b) plots the measured quality factors of the Brillouin resonances of the 4 GHz phonon mode for devices of four different lengths. Adapted from [219].

One advantage of the membrane waveguide structure which we have mentioned prior is that it separately confines light and sound. As a result, the transverse acoustic waveguide can be made much wider than the optical waveguide—in the designs studied here, the acoustic waveguide width is $3\times$ that of the optical waveguide. While this reduces the effective Brillouin gain due to the reduced acousto-optic overlap—in this case by a factor of $\frac{1}{3}$ over a dual-guiding design—this design dramatically reduces linear and nonlinear optical losses by reducing scattering and free-carrier lifetimes. Furthermore, this design reduces the sensitivity to fabrication imperfections since dimensional tolerances in the membrane fabrication represent a smaller fractional variation in the device width. This can be also understood from a simple Fabry-Perot model of the transverse-like elastic mode, whose frequency Ω is inversely proportional to device width w :

$$\Omega = \frac{v_s}{w} \quad (3.37)$$

where v_s is the speed of sound in silicon. As a result, the change in resonance frequency due to a small change in dimension is:

$$\Delta\Omega = \frac{\Delta w v_s}{w^2}. \quad (3.38)$$

For a fixed fabrication tolerance Δw , the dimensional-broadening-limited quality factor is then equal to

$$Q \equiv \frac{\Omega}{\Delta\Omega} = \frac{w}{\Delta w} \quad (3.39)$$

so that quality factor of FSBS-active phonons is directly proportional to device width in the case where inhomogeneous broadening dominates over intrinsic phonon loss mechanisms.

Fig. 3.10a diagrams the five transverse dimensions which define the suspended optomechanical waveguide design. The sensitivity of the Brillouin resonance frequency to small changes in these dimensions, calculated using finite element simulations, is plotted in Table 3.1. The most sensitive parameter to variations in dimension is the total device width, through the width of the optical ridge the and membrane thickness also play a role. These dimensional sensitivities are roughly an order of magnitude smaller than those for nanowire

Table 3.1: Simulated Changes in Brillouin Frequency Due to Dimensional Variations

Dimension	Description	Sensitivity to Dimension Error
a	Total membrane width	1.4×10^6 Hz/nm
b	Membrane thickness	8.3×10^5 Hz/nm
c	Ridge waveguide width	7.5×10^5 Hz/nm
d	Ridge waveguide height	7×10^3 Hz/nm
e	Ridge offset from center	5×10^3 Hz/nm

designs [197]. Interestingly, small variations in ridge height and offset from center do not affect the center frequency, although significant (~ 100 nm) variations can dramatically alter the resonance frequency beyond these perturbative calculations. This is due in part to the fact that the ridge is assumed to be symmetrically placed in the center of the structure, which causes $\frac{\partial \Omega_B}{\partial d_i}$, the fractional Brillouin frequency change per change in dimension i , to be nearly zero for these dimensions.

Quality factors obtained using CABS spectroscopy are plotted for four devices of different lengths (0.5 mm, 2.5 mm, 5 mm, and 29 mm) in Fig. 3.10b. These data reveal quality factors around $Q = 1000$ for the shortest tested devices, and modest decreases in quality factor from ~ 850 to ~ 650 as the device length is increased from 2.5 mm to 29 mm. These data suggest that quality factors should not decrease much further as device length is further increased, boding well for increased net amplification in longer devices.

The measured quality factors correspond to ~ 4.5 nm inhomogeneities in device width along the 29 mm-long device according to either Eq. 3.39 or the calculations of Table 3.1. In fact, we hypothesize that fabrication-induced phonon linewidth increases are already saturated in the few mm-scale devices, and that the further decrease is due to variations in silicon layer thickness as-received in the silicon-on-insulator (SOI) wafers used for device fabrication.

3.9 Conclusions and Outlook

These results show that strong Brillouin amplification is in fact possible in silicon waveguides at near-IR wavelengths—a feat which was considered fundamentally difficult upon

prior experimental [218] and theoretical [243] analyses. Importantly, we find that even for long interaction lengths, dimensional broadening does not pose a fundamental roadblock to robust integrated photonic-phononic devices based on forward-SBS.

This level of performance is enabled by passive reductions of linear and nonlinear propagation losses, strong Brillouin coupling enabled through independent photonic and phononic control, and increased robustness to dimensional variations of the membrane waveguide design. By enabling robust Brillouin couplings in a low loss silicon waveguide, the suspended membrane structure opens the door to the adaptation of a wide array of Brillouin-based signal processing technologies to chip-based silicon photonics.

In light of these advances, however, we are also left with a conundrum. The vast array of traditional fiber-based Brillouin light sources and signal processing technologies are based on backward SBS, which produces two-wave couplings between counter-propagating optical fields through interactions with longitudinal phonon modes. The type of Brillouin interactions heretofore realized in silicon waveguides are based on forward SBS, which couples many optical waves, and produces dual-sideband gain, with dynamics that permit cascaded comb line generation. These couplings also not produce stimulated amplification [233] due to balancing between Stokes and anti-Stokes processes, forbidding laser oscillation in simple cavity designs. Due to these differences, it is nontrivial in many cases to adapt existing strategies for signal processing [150,151,237], slow light [167], and filtering [159–161,163,238] based on BSBS in fiber to FSBS-based integrated photonics.

At the same time, these forward Brillouin couplings have great potential for new types of signal processing applications. In particular, as we will discuss in Chapter 4, these interactions are uniquely suited to CABS-like emit-and-receive operations which utilize FSBS-based phonon generation and readout [165,220]. These device concepts may be applied to the creation of elegant, ultra-narrowband microwave-photonic filters with favorable noise characteristics as compared to BSBS-based technologies; because FSBS does not amplify thermal noise, it may have utility for a variety of new low-noise signal-processing implementations. Furthermore, because FSBS can couple to extended phonon modes, it is uniquely suited to nonlocal sensing applications [256]. FSBS may also be used to create low-noise Brillouin lasers, provided that the symmetry between Stokes and anti-Stokes processes is

broken, for example through the use of coupled optical cavities [257]. Thus, while FSBS may at first seem to be a new and complex phenomenon, the potential applications are numerous, and certainly with further study will lead to many new on-chip operations.

While backward-SBS produces single sideband gain, prospects for BSBS-based lasers in silicon at near-IR wavelengths seem slim, since BSBS is predicted to be orders of magnitude weaker than FSBS in silicon. This results from the weaker p_{12} photoelastic response, destructive interference between radiation pressure and electrostrictive forces in nanowire geometries, and higher phonon frequencies necessary for BSBS-active phonons. BSBS has only been measured in silicon in Ref. [197], where 0.2 dB of Brillouin gain was produced in 2-cm-long devices through this process.

The demonstration of strong FSBS in silicon also opens the door for another intriguing form of Brillouin coupling, called stimulated inter-modal Brillouin scattering (SIMS). This process, which couples light waves guided in distinct optical spatial modes, can occur between both forward- and backward-propagating waves. In the former case, this process offers many of the potential advantages of FSBS in silicon (large gain, tailorable light-sound overlap, control over extended phonon modes), while also restoring the single-sideband coupling of BSBS necessary for many traditional signal processing applications. Beyond these, however, SIMS also has the potential to enable new types of broadband nonreciprocal operations [187, 188, 258], new forms of multimode couplings, and the leveraging of powerful on-chip mode multiplexing and signal routing techniques. In Chapter 5, we detail our efforts to realize forward-SIMS on-chip, enabling new dynamics which are powerful and complementary to those offered by forward Brillouin scattering in silicon. Together, these advances open the door to a wide variety of Brillouin-based interactions on chip, with tailorable dynamics suitable for the next generation of phonon-enabled devices in silicon photonics.

Chapter 4

Coupling Optical Waveguides through Extended Phonon Modes for Microwave Signal Processing

4.1 Introduction

The realization of strong forward-SBS interactions in integrated silicon waveguides opens the door to high-performance Brillouin-based signal processing within silicon photonics. However, the unique dynamics of FSBS make it nontrivial to adapting many existing technologies based on backward-SBS to FSBS-based devices. In Chapter 5, we will explore the use of inter-modal interactions to create single-sideband Brillouin gain in silicon as a basis for amplifiers and lasers. We will see that these multi-mode couplings provide one promising path toward creating flexible and useful traveling-wave optomechanical devices on-chip.

In this chapter, however, we explore a different approach by harnessing the unique properties of FSBS for new coherent information processing technologies. Through an emit-receive process, we use FSBS to produce distributed phonon transduction for integrated opto-acoustic filtering operations, based on two unique aspects of FSBS not available within traditional BSBS-based waveguide systems.

Firstly, FSBS couples to phonons which are confined by the transverse waveguide ge-

ometry, allowing traveling-wave optomechanical couplings involving elastic waves which are extended in space. For example, within optical fibers, which have ~ 10 micron-scale optical waveguide cores, FSBS couples through phonons which are guided throughout the mm-scale fiber cross-section. Within nanoscale membrane waveguides of the type studied in Chapter 3 and Ref. [196], the transverse confinement can be precisely controlled through device lithography. As a result, these phonons, generated through FSBS within one optical waveguide core may couple to light guided in distinct waveguides embedded at different locations throughout the extended optomechanical device. This geometry allows nonlocal opto-acoustic modulation while prohibiting optical cross-talk.

Second, because the dynamics of FSBS do not produce stimulated phonon emission or absorption, but rather a form of traveling-wave phase modulation, the phonon field driven through FSBS remains constant in intensity as the waves propagate. As a result, coherent phonon generation is possible over meter-scale lengths (or greater), limited only by propagation losses of the optical drive waves. This behavior is quite distinct from the self-limiting dynamics of BSBS, where a strong elastic field is driven only in the vicinity of significant optical energy transfer.

Building on existing implementations of SBS for radiofrequency (RF) signal processing [149–151, 157, 158], filtering [159–164], and frequency synthesis [148, 152–158], a natural application of on-chip SBS is for the creation of new tools for optical processing of microwave signals. In contrast to traditional RF systems based on electronic components, encoding information on light enables both low-loss signal transmission and intrinsically tunable, reconfigurable filtering operations. Furthermore, the use of Brillouin-based techniques permits narrowband filtering and control within the context of wideband microwave photonic systems. Hybrid photonic-phononic platforms thus offer the potential for both flexible microwave signal processing schemes, and economical integration into sophisticated chip-based photonic circuits [259–261].

Here, we use FSBS interactions within an optomechanical silicon device to produce narrowband, high-fidelity microwave filtering. This filtering operation is enabled by phonon-mediated emit-and-receive interactions between a pair of nanophotonic waveguides. Through this emit-receive process, an optical field in one waveguide which is intensity-modulated by

a microwave signal transduces a coherent phonon through FSBS. This phonon then phase-modulates light in a separate waveguide, transferring a copy of the modulated signal back to the optical domain, with a frequency response set by the engineered phononic response of the device [165]. Building on the robust FSBS-active waveguide designs demonstrated in Chapter 3, this all-silicon device produces a narrowband (5 MHz) acoustic response with large Brillouin couplings and high optical power handling (>100 mW) necessary to enable low-loss RF-photonic filtering. As a result, this device supports near-unity RF link gain $G = -2.3$ dB without the use of microwave amplifiers, and offers high linearity. In comparison with many prior SBS-based filter architectures, this system eliminates the need for complicated signal encoding schemes by allowing direct filtering of intensity-modulated signals. This work demonstrates the utility of FSBS interactions for high-performance microwave signal processing, with the potential for monolithic integration within complex silicon photonic circuits.

4.2 Operation Scheme

A schematic showing the basic operation of the photonic-phononic emitter-receiver (PPER) device is depicted in Fig. 4.1a. The device consists of distinct ‘emit’ and ‘receive’ optical waveguides which are coupled through a common acoustic phonon mode. During operation, an intensity-modulated optical pump is incident in the emit waveguide through port 1 as diagrammed in Fig. 4.1a. When the modulation frequency Ω of this light is close to the acoustic resonance (Brillouin) frequency Ω_B of the device, efficient transduction of the acoustic phonon at frequency Ω is produced. This phonon temporally modulates the effective index of probe light coupled into the receive waveguide through port 2 to produce optical phase modulation. Pump and probe waves are coupled off-chip through device ports 3 and 4, respectively.

Through this operation, the PPER device maps intensity modulation in one optical channel onto phase modulation in another. At the same time, the device’s phononic response can be used as an acoustic-domain RF filter; this behavior is depicted in Fig. 4.1b. A broadband RF signal (example spectral content plotted in Fig. 4.1b.i) is encoded as

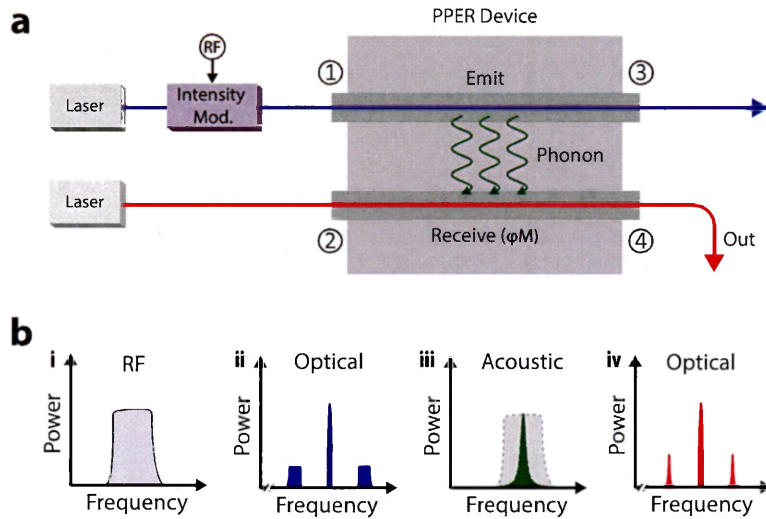


Figure 4.1: **Photonic-phononic emitter-receiver operation scheme.** (a) depicts basic operation of the PPER as a RF filter/modulator. Laser light (blue) is intensity-modulated by an input RF signal and injected into the ‘emit’ waveguide through port 1 of the device. This modulation transduces an acoustic phonon through electrostrictive forces. Light from a second laser (red) is injected into the ‘receive’ waveguide through port 2 of the device, and is phase-modulated by the same acoustic phonon before exiting the device through port 4. (b) depicts example power spectral content of the various signals in this experiment (i) a sample broadband RF input spectrum (ii) intensity-modulated laser light with sidebands encoded by the RF modulation (iii) the resulting acoustic phonon spectrum which filters the original RF signal through the device’s narrowband phononic response (iv) the optical spectrum of the output phase-modulated light. Adapted from Ref. [220].

intensity modulation on an optical carrier (Fig. 4.1b.ii). Because the bandwidth of the acoustic phonon resonance of the PPER device is much narrower than that of the RF signal, only a portion of this signal is transduced into the phononic domain (Fig. 4.1b.iii). This signal, which has now been filtered through the device's engineered elastic response, phase-modulates light in the receive waveguide to produce narrow modulation sidebands (Fig. 4.1b.iv). This optical signal may then be transmitted over long distances by coupling an optical fiber to port 4, or converted back to the microwave domain through use of a frequency discriminator and photodiode.

Two interesting technological aspects of the PPER process are its tailorable acoustic response and ultra-wide optical phase-matching bandwidth. The frequency response of the acoustic phonon is set directly through device geometry and design, and may be optimized to have application-specific parameters. For example, this phonon can be designed to be non-resonant, singly-resonant, or multi-resonant through a collection of acoustic cavities to produce different filter shapes [165]. Once this phonon is excited, regardless of generation scheme, phase-matching permits modulation of light over a very wide range of wavelengths. This can be understood from the phase-matching conditions for light scattering to either red- or blue-detuned sidebands:

$$k(\omega_p - \Omega) + q_s = k(\omega_p) \quad (4.1)$$

$$k(\omega_p + \Omega) = k(\omega_p) + q_{as}. \quad (4.2)$$

Here $k(\omega)$ is the optical wavevector at frequency ω , ω_p is the frequency of incident probe light, Ω is the modulation frequency, and q_s and q_{as} are the wavevectors of phonons which mediate Stokes (red-shifting) and anti-Stokes (blue-shifting) processes, respectively. Assuming that optical dispersion is linear over a small frequency shift Ω , an excellent approximation for modulation frequencies in the GHz range, we can Taylor expand $k(\omega)$ to first order to find that

$$q(\omega_p) \equiv q_s = q_{as} = \Omega \frac{dk}{d\omega}(\omega_p) = \frac{\Omega}{c} n_g(\omega_p). \quad (4.3)$$

This is the condition for a phonon with wavevector q to be phase-matched to Brillouin modulation of light at optical frequency ω_p . If this same phonon is used to modulate light at a different frequency ω'_p , the resulting wavevector mismatch is

$$\Delta q \equiv q(\omega'_p) - q(\omega_p) = \frac{\Omega}{c} (n_g(\omega'_p) - n_g(\omega_p)). \quad (4.4)$$

Provided that the accumulated phase mismatch $\Delta q L/2$ over a device length L is ~ 1 or less, phase matching still permits relatively efficient modulation. This condition can be written as

$$|n_g(\omega'_p) - n_g(\omega_p)| < \frac{2c}{\Omega L}. \quad (4.5)$$

For a typical silicon device with $\Omega = 2\pi \times 5$ GHz and $L = 0.02$ m, this condition becomes $|n_g(\omega'_p) - n_g(\omega_p)| < 1$, so that a group index change of more than one refractive index unit is necessary to produce phase-mismatched coupling. As a result, with careful design, the same phonon could be used to modulate light over more than an entire octave of optical frequencies within a PPER device.

In the next section, we theoretically study the dynamics of the PPER device and its operation as an RF filter as diagrammed in Fig. 4.1. Thereafter, we investigate the performance of a real device and discuss the potential for further refinements of this technology.

4.3 Photon-phonon Emitter-receiver Theory

In this section, we write the coupled-amplitude equations which govern the dynamics of emit-receive coupling through FSBS, and develop closed-form expressions for parameter values relevant to PPER device performance, particularly for RF filtering applications.

We begin by considering the fields within the emit waveguide (indexed with the superscript ⁽¹⁾) that may couple through FSBS. We make the approximations according to Ref. [233] that the phonon field is heavily spatially damped relative to the length over which significant optical energy transfer occurs, and solve for the spatial dynamics of the system in the steady state.

In this case, a Brillouin active phonon with amplitude b and frequency Ω may couple a series of optical fields $a_n^{(1)}$ with frequencies $\omega_n = \omega_p^{(1)} + n\Omega$ through the coupled-amplitude equation

$$\frac{\partial a_n^{(1)}}{\partial z} = \frac{i}{v_n} \left(g_n a_{n-1}^{(1)} b + g_{n+1}^* a_{n+1}^{(1)} b^* \right), \quad (4.6)$$

where g_n is the nearest-neighbor coupling rate, and v_n is the optical group velocity of field n . Provided that these do not vary strongly over the frequency range of the coupled optical fields¹, we can drop the subscripts on these terms and rewrite Eq. 4.6 as

$$\frac{\partial a_n^{(1)}}{\partial z} = \frac{i}{v} \left(g a_{n-1}^{(1)} b + g^* a_{n+1}^{(1)} b^* \right). \quad (4.7)$$

The coupled amplitude equations for the receive waveguide (optical fields indexed with the superscript ⁽²⁾) are structurally identical, with the exception that in a practical system the optical group velocity and Brillouin couplings may be different; to include this possibility we also label these terms with the superscript ⁽²⁾:

$$\frac{\partial a_n^{(2)}}{\partial z} = \frac{i}{v^{(2)}} \left(g^{(2)} a_{n-1}^{(2)} b + g^{(2)*} a_{n+1}^{(2)} b^* \right). \quad (4.8)$$

The phonon amplitude at Ω is directly related to the summation of nearest-neighbor optical beat notes through [233]:

$$b = \left(\frac{1}{\Omega - \Omega_B + i\Gamma/2} \right) \sum_n g^* a_n^{(1)} a_{n-1}^{(1)*} + g^{(2)*} a_n^{(2)} a_{n-1}^{(2)*} \quad (4.9)$$

where Γ is the lifetime of the acoustic phonon mode, which we have assumed has a Lorentzian frequency response due to this finite lifetime. The field amplitudes are related to the optical and acoustic power flows in the waveguide by²

1. In most systems, the optical propagation constants and mode shapes are nearly constant over \sim GHz frequency ranges, so this is an excellent approximation.

2. These equalities are exact for monochromatic fields.

$$P_b \simeq \hbar\Omega v_b b^* b, \quad (4.10)$$

$$P_a \simeq \hbar\omega v a^* a, \quad (4.11)$$

and the Brillouin coupling rate is related to the frequency-dependent Brillouin gain in either waveguide through the relationship [233]

$$G_B^{(1,2)} = \frac{4|g^{(1,2)}|^2}{v^2\Gamma\hbar\omega_p^{(1,2)}} \frac{(\Gamma/2)^2}{(\Omega - \Omega_B)^2 + (\Gamma/2)^2}. \quad (4.12)$$

4.3.1 Translational Invariance of the Phonon Field Amplitude

Through FSBS coupling, and in the absence of external optical loss, the phonon field amplitude is constant along the device length. Here, we show this directly by computing the derivative of the phonon amplitude with respect to position.

$$\begin{aligned} \frac{\partial b}{\partial z} = & \left(\frac{1}{\Omega - \Omega_B + i\Gamma/2} \right) \sum_n g^* \frac{\partial a_n^{(1)}}{\partial z} a_{n-1}^{(1)*} + g^* a_n^{(1)} \frac{\partial a_{n-1}^{(1)*}}{\partial z} + \\ & g^{(2)*} \frac{\partial a_n^{(2)}}{\partial z} a_{n-1}^{(2)*} + g^{(2)*} a_n^{(2)} \frac{\partial a_{n-1}^{(2)*}}{\partial z}. \end{aligned} \quad (4.13)$$

Substituting in Eqs. 4.7-4.8 for the differential terms, this expression becomes

$$\begin{aligned} \frac{\partial b}{\partial z} = & \left(\frac{1}{\Omega - \Omega_B + i\Gamma/2} \right) \sum_n \frac{g^* i}{v} \left[gb \left(|a_{n-1}^{(1)}|^2 - |a_n^{(1)}|^2 \right) + g^* b^* \left(a_{n+1}^{(1)} a_{n-1}^{(1)*} - a_n^{(1)} a_{n-2}^{(1)*} \right) \right] \\ & + \left(\frac{1}{\Omega - \Omega_B + i\Gamma/2} \right) \sum_n \frac{g^{(2)*} i}{v^{(2)}} \left[g^{(2)} b \left(|a_{n-1}^{(2)}|^2 - |a_n^{(2)}|^2 \right) + g^{(2)*} b^* \left(a_{n+1}^{(2)} a_{n-1}^{(2)*} - a_n^{(2)} a_{n-2}^{(2)*} \right) \right] \\ = & 0. \end{aligned} \quad (4.14)$$

When the sums are taken over all possible values of n , (or at least all those for which the field amplitudes are nonzero), each term is exactly canceled. As a result, we see that couplings of the form in Eqs. 4.7-4.8 produce a phonon amplitude that is translationally invariant (constant in space). Thus for any position z along the waveguide length, we can write $b(z) = b(0)$, so that the total phonon amplitude may be calculated by considering the input

optical waves at $z = 0$ with Eq. 4.9. One of several useful consequences of this fact is that the PPER process can be used to drive a strong, coherent phonon field over arbitrary lengths³. Furthermore, the same optical signal that is used to drive the phonon field in one PPER device propagates without a change in optical intensity modulation character, and may subsequently be injected into another PPER device with a different resonant frequency Ω_B . In this case, the driven phonon intensity is changed according to the Lorentzian prefactor $(\Omega - \Omega_B + i\Gamma/2)^{-1}$. Hence, a cascaded bank of narrowband PPER devices may be used to separately sample the modulation spectrum of a single optical signal into many channels. (For further details, see the technical note in Section 4.6).

While we have so far considered a monochromatic phonon field, the same physics hold true for fields with arbitrary spectral content. For simplicity, we consider a single optical waveguide which contains an optical wave with a continuous complex-valued spectral distribution $A(\omega)$. Given appropriate normalization, we can write the driven acoustic phonon spectrum according to Eq. 4.9 as:

$$b(\Omega) = \left(\frac{g^*}{\Omega - \Omega_B + i\Gamma/2} \right) \int d\omega A(\omega) A^*(\omega - \Omega). \quad (4.15)$$

The optical fields in a single Brillouin-active waveguide core couple through this phonon field analogously to Eq. 4.6 as

$$\frac{\partial A(\omega)}{\partial z} = \frac{i}{v} \left(g \int A(\omega - \Omega) b(\Omega) d\Omega + g^* \int A(\omega + \Omega) b^*(\Omega) d\Omega \right). \quad (4.16)$$

As before, we have neglected optical and acoustic dispersion over the relevant frequency ranges. Taking the derivative of Eq. 4.15 with respect to position and substituting in Eq.

³ Note that throughout this discussion we have neglected optical dispersion, which can lead to amplitude modulation and more complex dynamics. For this approximation to be valid, group velocity dispersion should be negligible over the frequency range of the optical tones involved in FSBS coupling.

4.16, we find

$$\begin{aligned}
\frac{\partial b(\Omega)}{\partial z} &= \left(\frac{g^*}{\Omega - \Omega_B + i\Gamma/2} \right) \int d\omega \left(\frac{\partial A(\omega)}{\partial z} A^*(\omega - \Omega) + A(\omega) \frac{\partial A^*(\omega - \Omega)}{\partial z} \right) \\
&= \left(\frac{g^* g}{\Omega - \Omega_B + i\Gamma/2} \right) \int \int d\Omega d\omega b(\Omega) (|A(\omega - \Omega)|^2 - |A(\omega)|^2) \\
&\quad + \left(\frac{g^* g^*}{\Omega - \Omega_B + i\Gamma/2} \right) \int \int d\Omega d\omega b^*(\Omega) (A(\omega + \Omega) A^*(\omega - \Omega) - A(\omega) A^*(\omega - 2\Omega)) \\
&= 0.
\end{aligned} \tag{4.17}$$

Therefore even in the presence of nontrivial optical fields, the driven phonon intensity due to FSBS (and hence the optical modulation intensity) does not change with propagation relative to its initial value.

4.3.2 Driven Phonon Amplitude for Two- and Three-tone Excitation

In the previous section, we found that, in the absence of external optical loss, the phonon amplitude driven through FSBS is constant. Here, we briefly consider two useful configurations for the drive fields and determine the resulting phonon amplitude from these incident light signals. Thereafter, we will determine the resulting modulation strength in the spatially-separate receive waveguide of the PPER device.

First, we consider the case of two monochromatic optical pump waves with powers P_0 and P_1 which are at frequencies $\omega_p^{(1)}$ and $\omega_p^{(1)} + \Omega$, respectively. Using Eq. 4.9 with the normalization condition $P_a = \hbar\omega v a^* a$, we can write the resulting phonon amplitude as:

$$b = \left(\frac{g^* e^{i\phi_b}}{\Omega - \Omega_B + i\Gamma/2} \right) \frac{1}{\hbar\omega_p^{(1)} v} \sqrt{P_0 P_1}, \tag{4.18}$$

where we have made the approximation that $\sqrt{\omega_p^{(1)}(\omega_p^{(1)} + \Omega)} \approx \omega_p^{(1)}$, and $e^{i\phi_b}$ is an overall phase factor related to the relative phases of the two optical drive fields.

Second, we consider the case of three monochromatic optical pump waves resulting from the output of an optical intensity modulator. This case is particularly relevant for the use of the PPER device in RF photonics, where optical signals are often encoded as intensity modulation.

Optical intensity modulation is commonly produced by placing an optical phase modulator in one arm of a Mach-Zehnder interferometer. While the phase-modulation arm does not produce an optical intensity beat-note, the interference of this light with a suitably phase-shifted carrier tone from the other arm produces a beat note at each harmonic of the modulation frequency. The combined incident field for a balanced and quadrature-biased Mach-Zehnder intensity modulator can be written as

$$E_{\text{inc}}^{(1)}(t) = a_{\text{inc}}^{(1)} \left(\frac{i}{\sqrt{2}} e^{i\omega_p^{(1)}t} + \frac{1}{\sqrt{2}} \sum_n J_n \left(\frac{\pi V_0}{V_\pi} \right) e^{i(\omega_p^{(1)} + n\Omega)t} \right) \quad (4.19)$$

where $a_{\text{inc}}^{(1)}$ is the total incident power amplitude, V_0 is the modulator driving voltage, and V_π is the modulator half-wave voltage. Intensity modulation at harmonics $n\Omega$ is driven by the interference between the out-of-phase carrier component at $\omega_p^{(1)}$ and the $\omega_p^{(1)} \pm n\Omega$ optical sidebands. While in most cases only the first-order modulation sidebands are desired, the harmonics occur as a by-product of cascaded phase modulation, and are relatively small when the modulation strength is weak.

Assuming a drive frequency Ω , the phonon field is driven at harmonic frequencies $n\Omega$ by each pair of optical tones at $\omega_p^{(1)} \pm \Omega$. If the PPER device responds only around Ω , the phonon is driven by three optical tones—the carrier at $\omega_p^{(1)}$ and the two closest modulation sidebands. The resulting driven phonon intensity from Eq. 4.9 is given by

$$b = \left(\frac{ig^*}{\Omega - \Omega_B + i\Gamma/2} \right) \frac{1}{\hbar\omega_p^{(1)}v} P_0 J_1 \left(\frac{\pi V_0}{V_\pi} \right), \quad (4.20)$$

where P_0 is the total incident power.

4.3.3 Modulation Efficiency by a Monochromatic Phonon Field

We now derive the output spectrum in the receive waveguide ⁽²⁾ given a monochromatic input at frequency $\omega_p^{(2)}$, an input driven phonon field at frequency Ω with amplitude $b = b_0 e^{i\phi_1}$, and Brillouin coupling coefficient $g^{(2)} = g_0 e^{i\phi_g}$. For simplicity we have written both the phonon amplitude and receive waveguide Brillouin coupling as a real amplitude times

an arbitrary phase. The expression governing the field evolution from Eq. 4.8 is

$$\frac{\partial a_n^{(2)}}{\partial z} = \frac{i}{v^{(2)}} \left(g_0 b_0 e^{i(\phi_1 + \phi_g)} a_{n-1}^{(2)} + g_0 b_0 e^{-i(\phi_1 + \phi_g)} a_{n+1}^{(2)} \right). \quad (4.21)$$

which has the solution

$$a_n^{(2)}(z) = a_0 e^{in(\phi_1 + \phi_g + \pi/2)} J_n \left(\frac{2g_0 b_0 z}{v^{(2)}} \right). \quad (4.22)$$

Here a_0 is the amplitude of the monochromatic input field. This solution is equivalent to phase modulation with a total phase shift:

$$\beta^{(2)} = \frac{2g_0 b_0 z}{v^{(2)}}. \quad (4.23)$$

The total optical power in each optical tone is

$$P_n^{(2)}(z) = P_0^{(2)} J_n^2 \left(\frac{2g_0 b_0 z}{v^{(2)}} \right) = P_0^{(2)} J_n^2 \left(\beta^{(2)} \right) \quad (4.24)$$

where $P_0^{(2)}$ is the injected power.

For the case of incident modulation by two optical tones with powers P_0 and P_1 with driving on resonance with the phonon intensity given by Eq. 4.18, the modulation phase shift is:

$$\beta^{(2)} = z \sqrt{G_B^{(1)} G_B^{(2)} P_0 P_1}. \quad (4.25)$$

For the case where the input modulation is driven by an intensity modulator as described above, the phase shift is

$$\beta^{(2)} = z \sqrt{G_B^{(1)} G_B^{(2)} P_0} J_1 \left(\frac{\pi V_0}{V_\pi} \right). \quad (4.26)$$

4.3.4 RF-Photonic Filter Response

Here we consider the performance of the PPER device within an RF-photonic link similar to that depicted in Fig. 4.1. A microwave signal is encoded on the input pump wave in the emit waveguide through optical intensity modulation, and this signal is transferred onto the probe wave propagating within the receive waveguide through phase modulation. This

signal is then demodulated and converted back to the microwave domain.

Link Gain and First-order response

To characterize the performance of this system, we consider a monochromatic microwave signal at frequency Ω , with RF power $P_{\text{RF}}^{\text{in}}$ corresponding to a peak voltage of $V_0 = \sqrt{2R_i P_{\text{RF}}^{\text{in}}}$, where R_i is the input resistance (typically 50 Ω). At the output of the system, this results in a phase modulation strength from Eq. 4.26 of $\beta^{(2)} = L\sqrt{G_{\text{B}}^{(1)}G_{\text{B}}^{(2)}}P_0J_1\left(\frac{\pi\sqrt{2R_iP_{\text{RF}}^{\text{in}}}}{V_\pi}\right)$, where L is the propagation length of the signal through the PPER device.

To convert the phase modulated signal back into the RF domain, we optically filter out either of the principal modulation sidebands (± 1 order), and inject the light onto a photodiode. The resulting optical power beat note at Ω is $2\sqrt{P_0^{(2)}P_1^{(2)}} = 2P_0^{(2)}J_0(\beta^{(2)})J_1(\beta^{(2)})$. This time-harmonic power beat-note results in a photocurrent

$$I_\Omega = 2\eta P_0^{(2)}J_0(\beta^{(2)})J_1(\beta^{(2)})\sin(\Omega t + \phi), \quad (4.27)$$

where t and ϕ are time coordinates and a phase shift, and η is the detector efficiency in units of A/W. The average RF output power at Ω is

$$P_\Omega = \langle I_\Omega^2 \rangle R_o |H_{\text{pd}}|^2, \quad (4.28)$$

where H_{pd} is the photodiode circuit efficiency and R_o is the output resistance. For our experiments, $R_o = 50 \Omega$ and $H_{\text{pd}} = 1/2$ due to current splitting between the photodiode termination and the load. Combining Eqs. 4.27-4.28, the output RF power is

$$P_\Omega^{\text{out}} = 2\left(\eta P_0^{(2)}J_0(\beta^{(2)})J_1(\beta^{(2)})\right)^2 R_o |H_{\text{pd}}|^2. \quad (4.29)$$

In the small signal limit, $J_0(\beta^{(2)}) \approx 1$ and $J_1(\beta^{(2)}) \approx \beta^{(2)}/2$. The resulting output RF power is

$$P_\Omega^{\text{out}} = P_{\text{RF}}^{\text{in}} \left(\frac{\pi\eta P_0^{(1)}P_0^{(2)}L\sqrt{G_{\text{B}}^{(1)}G_{\text{B}}^{(2)}}}{2V_\pi} \right)^2 R_i R_o |H_{\text{pd}}|^2. \quad (4.30)$$

This expression can be used to find the link gain g , which is defined in dB by $g \equiv$

$$10 \log_{10} (P_{\Omega}^{\text{out}} / P_{\text{RF}}^{\text{in}}).$$

Propagation of Third-order Spurious Tones

An important consideration in RF-photonic link design is the generation of third-order spurious tones, which can lead to distortion around the carrier frequency (i.e. through a third-order mixing process $\Omega_1 + \Omega_2 - \Omega_{1,2}$). Since the PPER acts as a narrowband filter, such spurious tones can occur at the link output through two primary means—either from (1) distortion in the input intensity modulation process, or from (2) cascaded Brillouin phase modulation in the receive waveguide. For most device parameters, (1) is the primary source of distortion, whereby mixing between out-of-band frequency components can result in new frequencies around Ω_{B} that can pass through the PPER filter. To quantify the strength of this effect, we consider driving the intensity modulator at $\Omega/3$ and transmitting the third-order modulation at Ω through the phononic filter. The resulting phase modulation strength is

$$\beta_{3\Omega/3}^{(2)} = z \sqrt{G_{\text{B}}^{(1)} G_{\text{B}}^{(2)}} P_0 J_3 \left(\frac{\pi V_0}{V_{\pi}} \right), \quad (4.31)$$

corresponding to an output power

$$P_{3\Omega/3}^{\text{out}} = \frac{1}{2} \left(\eta P_0^{(2)} J_0 \left(z \sqrt{G_{\text{B}}^{(1)} G_{\text{B}}^{(2)}} P_0 J_3 \left(\frac{\pi V_0}{V_{\pi}} \right) \right) J_1 \left(z \sqrt{G_{\text{B}}^{(1)} G_{\text{B}}^{(2)}} P_0 J_3 \left(\frac{\pi V_0}{V_{\pi}} \right) \right) \right)^2 R_{\text{o}} |H_{\text{pd}}|^2. \quad (4.32)$$

In the small-modulation limit, this expression becomes

$$P_{3\Omega/3}^{\text{out}} = (P_{\text{RF}}^{\text{in}})^3 \frac{\pi^6}{576} \left(\eta P_0^{(1)} P_0^{(2)} L \sqrt{G_{\text{B}}^{(1)} G_{\text{B}}^{(2)}} \right)^2 R_{\text{o}} \left(\frac{R_{\text{i}}}{V_{\pi}^2} \right)^3 |H_{\text{pd}}|^2. \quad (4.33)$$

The extrapolated third-order intercept point OIP_3 is found by requiring that Eq. 4.33 and Eq. 4.30 are equal, which occurs at an input RF power of $P_{\text{RF}}^{\text{in}} = (12/\pi^2)(V_{\pi}^2/R_{\text{i}})$ and is equal to

$$\text{OIP}_3 = 3 \left(\eta P_0^{(1)} P_0^{(2)} L \sqrt{G_{\text{B}}^{(1)} G_{\text{B}}^{(2)}} \right)^2 R_{\text{o}} |H_{\text{pd}}|^2. \quad (4.34)$$

Together with the noise floor, this determines the PPER's third-order spur-free dynamic range.

4.3.5 Thermal Brillouin Noise and Spur-free Dynamic Range

As probe light traverses the receive waveguide, spontaneous Brillouin scattering from thermal phonons results in optical energy transfer to frequency-detuned sidebands through Stokes and anti-Stokes processes. Through the demodulation process described above (filtering out either sideband), this thermal Brillouin scattering can represent a fundamental RF noise source within the PPER filter. After propagating a length L , the total scattered optical power spectral density is [233]:

$$S(\omega) = \hbar\omega_p^{(2)} G_B^{(2)} P_0^{(2)} L n_{\text{th}} \frac{(\Gamma/2)^2}{\omega^2 + (\Gamma/2)^2}, \quad (4.35)$$

where ω is the detuning relative to the center frequency of scattered light, and n_{th} is the thermal phonon population according to the Bose-Einstein distribution $n_{\text{th}} = 1/(e^{(\hbar\Omega_B/k_B T)} - 1)$, with T being the temperature in Kelvin. Note that the expression here is exactly valid for the anti-Stokes sideband; for the Stokes scattering process, the thermal population term should be replaced with $n_{\text{th}} + 1$; however, at room temperature where $n_{\text{th}} \approx 10^3$, this difference is negligible. The total spontaneously scattered power can be calculated by $P = 1/(2\pi) \int d\omega S(\omega)$. If we consider a narrow bandwidth around the center of scattered light, the peak noise power spectral density (in units of W/Hz) is simply

$$S = \hbar\omega_p^{(2)} G_B^{(2)} P_0^{(2)} L n_{\text{th}}. \quad (4.36)$$

The resulting time-averaged RF noise power within a bandwidth Δ around the Brillouin center frequency from Eq. 4.28 is given by:

$$P_N = 2 |H_{\text{pd}}|^2 \eta^2 P_0^{(2)} S R_o \Delta = 2 |H_{\text{pd}}|^2 \eta^2 \hbar\omega_p^{(2)} G_B^{(2)} \left(P_0^{(2)}\right)^2 L n_{\text{th}} R_o \Delta. \quad (4.37)$$

The third-order spur-free dynamic range for the RF-photonic link is related to the third-order intercept point OIP_3 and the noise floor power spectral density as $\text{SFDR}_3 = (\text{OIP}_3/P_N)^{2/3}$

which is calculated from Eqs. 4.34 and 4.37 to be⁴

$$\text{SFDR}_3 = \left(\frac{3G_B^{(1)} \left(P_0^{(1)}\right)^2 L}{2\hbar\omega_p^{(2)} n_{\text{th}} \Delta} \right)^{\frac{2}{3}}. \quad (4.38)$$

This equation is valid so long as thermal Brillouin noise is the dominant source of RF noise in the system (as compared to shot noise, for example), and the operating bandwidth is much narrower than the linewidth of the Brillouin resonance. If the operating bandwidth is wider, this number will be an underestimate. The SFDR_3 represents a fundamental performance characteristic of the filter within an RF-photonics link.

4.3.6 Noise Figure

The noise figure for a system is typically defined as:

$$\text{NF} \equiv \frac{\text{Noise PSD Out}}{(\text{Noise PSD In}) \times (\text{Gain})}. \quad (4.39)$$

In terms of the input noise power spectral density N_{in} , and using Eqs. 4.30 and 4.37 (assuming that the output noise is dominated by thermal Brillouin scattering), this is

$$\text{NF} = \frac{8\hbar\omega_p^{(2)} n_{\text{th}}}{\pi^2 G_B^{(1)} \left(P_0^{(1)}\right)^2 L} \frac{V_\pi^2}{R_i} \frac{1}{N_{\text{in}}}. \quad (4.40)$$

The value of the noise figure depends directly on the input noise source. This input noise may be due to thermal Johnson-Nyquist charge noise, where from the fluctuation-dissipation theorem $N_{\text{in}} = k_B T$, but is more typically limited by shot noise or non-fundamental detector noise.

4. In the expression for the spur-free dynamic range, the power of $^{2/3}$ is due to the fact that the output signal is linear with respect the input, while the third-order spur is cubic with respect to input power. The range over which a signal is measurable but third-order spurs are not (the ‘spur-free’ dynamic range) picks up the resulting exponent of $^{2/3}$. For further details see Ref. [262].

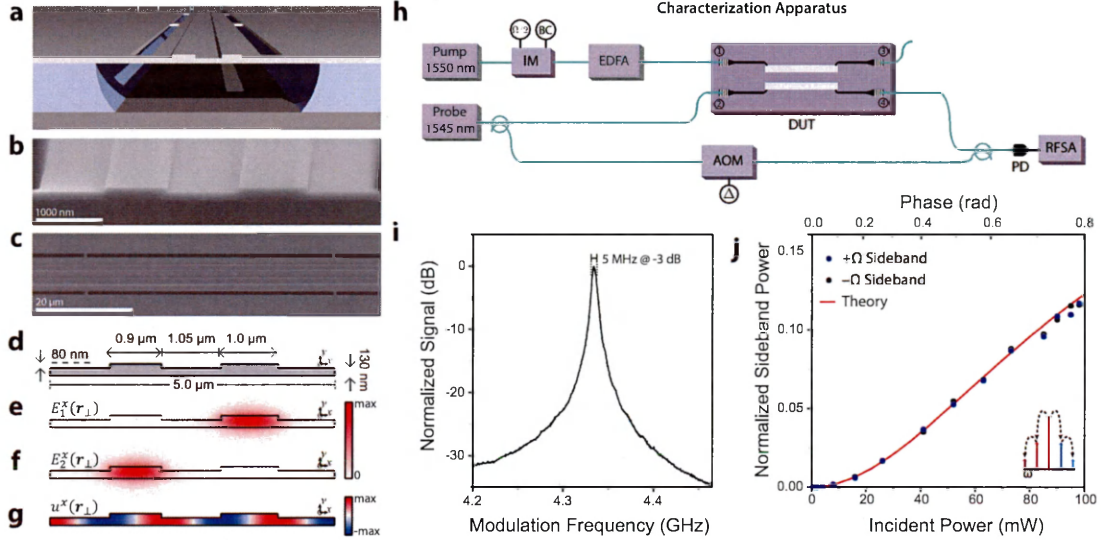


Figure 4.2: **Silicon photonic-phononic emitter-receiver device.** (a) depicts the device cross section; a dual-ridge membrane structure fabricated from a single-crystal silicon layer is suspended by a series of tethers on an SOI wafer. (b-c) show cross-sectional and top-down SEMs, respectively, of the fabricated device. (d) plots the cross-sectional dimensions of the PPER structure, while (e-f) plot the fundamental TE-like guided optical mode profiles for the two embedded ridge waveguides. (g) plots the x -component of the elastic displacement field for a ~ 4.3 GHz elastic mode which extends throughout the device. (h) diagrams the experimental characterization apparatus for probing the PPER device response. In the top optical path, pump light is intensity modulated around the zero-bias point and amplified through an erbium-doped fiber amplifier to create two strong pump waves separated by $\Omega \approx \Omega_B$. This light is injected into the emit waveguide through port 1. A separate probe wave is split into two paths—in the middle path, it enters the receive waveguide through device port 2 and exits through port 4, at which point it is recombined with a frequency-shifted local oscillator (bottom path) and incident on a fast photodiode for heterodyne spectral analysis in the microwave domain. (i) Plots the normalized modulation response of the PPER device as a function of drive frequency. (j) Plots the power in each of the two principal phase-modulation sidebands as a function of incident on-chip pump power when the device is driven on resonance $\Omega = \Omega_B$ in this configuration. Adapted from Ref. [220].

4.4 Characterization of Device Response

Having established the theoretical behavior of the PPER system as an RF filter, we now experimentally characterize a fabricated device with the design shown in Fig. 4.2a-g. The PPER device is based on the FSBS-active suspended membrane design of Ref. [219] (Chapter 3) and consists of two optical ridge waveguides embedded within the same suspended silicon membrane. Each ridge waveguide supports low-loss guidance of a fundamental TE-like optical mode (Fig. 4.2e-f), and the ridges are designed to differ in width by 100 nm to inhibit optical crosstalk via evanescent coupling. Both optical modes may interact with the same Lamb-like elastic mode (Fig. 4.2g) that extends throughout the membrane through a PPER process. In this process, modulated optical waves in the emit waveguide drive the elastic wave through forward-SBS. This optically-driven elastic wave then produces time modulation of the optical waveguide modes, producing linear time-harmonic phase modulation on light in the receive waveguide.

To characterize the strength of modulation produced through the PPER process in this device, we first perform measurements of the modulation response and efficiency using a two-tone drive measurement (Fig. 4.2h). In this experiment, two equal-intensity drive tones separated by a frequency Ω are synthesized from the same pump laser (frequency ω_p) using a null-biased intensity modulator driven at $\Omega/2$ (top path of Fig. 4.2h). These waves at optical frequencies $\omega_p \pm \Omega/2$ are injected into the emit waveguide and drive elastic waves within the PPER device via optical forces at frequency Ω . The total power of these waves is controlled using an erbium-doped fiber amplifier and variable attenuator. Light from a separate probe laser (frequency ω_{pr}) is split into the two paths. In the top path, light is coupled into the receive waveguide, while in the bottom path probe light is frequency-shifted using an acousto-optic modulator to produce a local oscillator at optical frequency $\omega_{pr} + \Delta = \omega_{pr} + 2\pi \times 44$ MHz. On-chip probe light experiences phase-modulation at Ω due to the driven elastic wave, resulting in energy transfer to frequency detuned sidebands at $\omega_{pr} \pm \Omega$; this modulated light is coupled off-chip and combined with the local oscillator arm, after which the signal incident on a fast photodiode, producing unique microwave beat-notes at $\{\Omega + \Delta, \Delta, \Omega - \Delta\}$ corresponding to the optical frequency components at

$\{\omega_{\text{pr}} - \Omega, \omega_{\text{pr}}, \omega_{\text{pr}} + \Omega\}$. These signals are then measured using a radiofrequency spectrum analyzer.

The modulation efficiency of the PPER process is quantified by measuring the output power in the frequency-shifted sidebands at $\omega_{\text{pr}} \pm \Omega$ relative to the unshifted input probe power. As the modulation frequency Ω is swept through the Brillouin frequency Ω_{B} of the device, a dramatic increase in modulation is observed, as plotted in Fig. 4.2i. This narrowband ($Q = 820$) feature at $\Omega_{\text{B}} = 4.33$ GHz corresponds to the resonant Brillouin-active phonon in Fig. 4.2g. This 5-MHz-wide Lorentzian response represents the acoustic transfer function of the PPER device. To evaluate the absolute strength of the PPER modulation, the frequency is fixed to $\Omega = \Omega_{\text{B}}$ and the total on-chip pump power is varied. As the incident power is increased to a maximum of 100 mW, the resulting scattered sideband power normalized to the input power increases to $\eta \equiv \frac{P^{\text{out}}(\omega_{\text{pr}} \pm \Omega)}{P^{\text{in}}(\omega_{\text{pr}})} = 12\%$, as plotted in Fig. 4.2j. This modulation strength corresponds to a phase shift of 0.8 rad, a key performance metric for both the acousto-optic efficiency of the device as well as the potential RF-photonics link gain of the system, as these figures of merit scale with phase-shift squared for small driving powers. At high powers, the scattering efficiency in Fig. 4.2j begins to saturate due to a combination of the Bessel-squared phase modulation response (Eq. 4.24) and nonlinear absorption due to TPA and TPA-induced FCA (Section 3.3).

These results demonstrate that the silicon membrane PPER is capable of producing efficient phase modulation, owing to a combination of robust Brillouin couplings, high power handling, and low propagation losses. Based on linear and nonlinear transmission measurements, this device has a total linear insertion loss of $\alpha L = 0.5$ dB over a length of $L = 2.53$ cm, and a nonlinear free-carrier absorption coefficient $\gamma^{\text{FCA}} \approx 2400 \text{ W}^{-2}\text{m}^{-1}$. The effective Brillouin coupling coefficient is $G_{\text{B}} \equiv \sqrt{G_{\text{B}}^{(1)}G_{\text{B}}^{(2)}} = 820 \pm 20 \text{ W}^{-1}\text{m}^{-1}$ from the data in Fig. 4.2j. The single-waveguide Brillouin gain coefficients were found through Brillouin gain measurements [219] to be $G_{\text{B}}^{(1)} = 880 \pm 50 \text{ W}^{-1}\text{m}^{-1}$ for the emit waveguide and $G_{\text{B}}^{(2)} = 740 \pm 50 \text{ W}^{-1}\text{m}^{-1}$ for the receive waveguide, which agree well with simulated values of $G_{\text{B}} = 860 \pm 130 \text{ W}^{-1}\text{m}^{-1}$ and $G_{\text{B}} = 790 \pm 120 \text{ W}^{-1}\text{m}^{-1}$, respectively. The robust performance of the silicon PPER device enables a tenfold increase in modulation efficiency over earlier PPER designs [165] as a basis for high-performance RF filtering applications. In

the next section, we characterize the response of the same silicon membrane PPER device within an RF-photonic link. Afterwards, we discuss the potential for further performance improvements and use cases of the PPER architecture.

4.5 RF-Photonic Link Performance

In this section, we explore the performance of the silicon PPER device within a RF-photonic link, and show that it permits high-fidelity narrowband filtering operations. We begin by characterizing the input/output response of the system, and then investigate additional noise induced through the PPER process.

The RF-photonic performance of the silicon PPER device is characterized within the link experiment diagrammed in Fig. 4.3a, mirroring the conceptual design of Fig. 4.1a. In this experiment, an input RF signal is encoded onto pump light using a commercial intensity modulator (Optilab IM-1550-20, RF V_π at 4.33 GHz = 9.9 V) biased at the quadrature point. This modulated light signal is amplified through an erbium-doped fiber amplifier (labeled EDFA1) and is coupled into the emit waveguide via an integrated grating coupler. The modulation of this signal is encoded on a transverse acoustic phonon with frequency content filtered by the device’s acoustic transfer function. Probe light is injected into the receive waveguide, where it is phase-modulated by the spectral content of the driven phonon field. This modulated light signal is then coupled off-chip and amplified through an output erbium-doped fiber amplifier (labeled EDFA2) to offset the fiber-chip coupling losses, and is converted to an intensity-modulated signal by filtering out one of the $\pm\Omega$ phase modulation sidebands. This signal is then incident on a commercial high-power photodiode (Discovery Semiconductors, Inc. DSC100S, responsivity $R = 0.75$ A/W, bias voltage $V_b = 7$ V), which converts the modulated optical signal back to a microwave signal.

4.5.1 Linear and Nonlinear Response of the PPER Link

We first measure the link gain of the compound system using a single RF drive tone at $\Omega = \Omega_B = 2\pi \times 4.33$ GHz, with an incident on-chip pump power $P_p = 105$ mW and probe power at detector of $P_{pr} = 75$ mW. As the input RF power increases, the output RF power

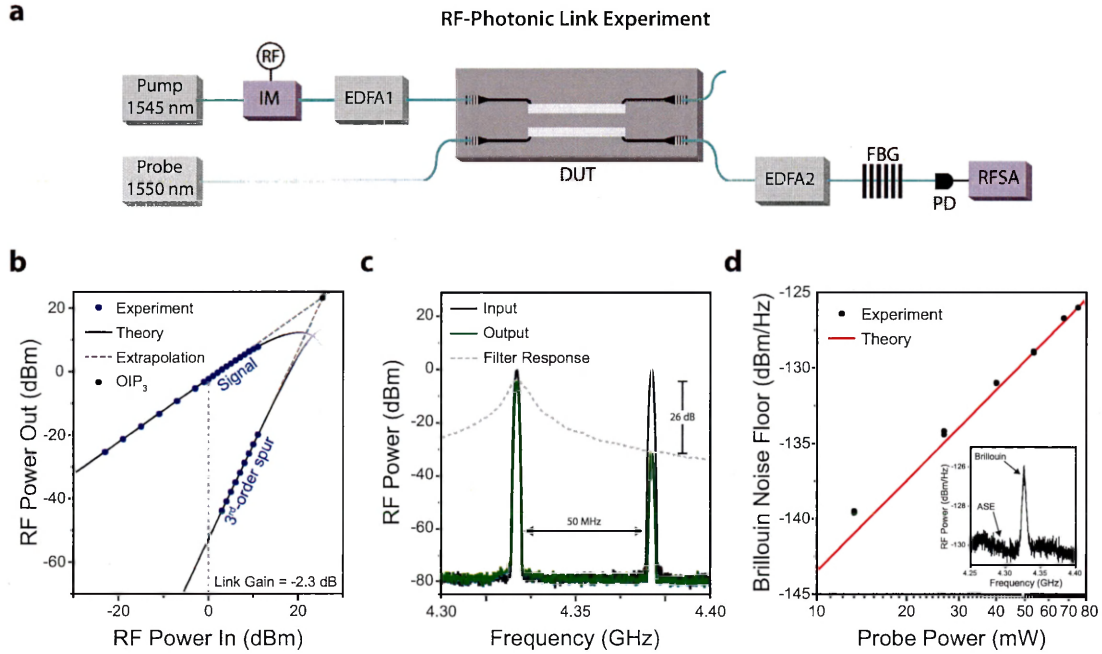


Figure 4.3: **Silicon PPER within an RF-photonic link.** (a) diagrams the RF-photonic link experiment: Pump light is intensity modulated by a microwave signal and amplified, and subsequently coupled into the emit waveguide of the PPER device. Probe light is passed through the receive waveguide, where it is modulated through the emit-receive process, and is amplified after being coupled off-chip to offset coupling losses. A fiber Bragg grating filters out one of the modulation sidebands to convert the phase modulation to intensity modulation, and the resulting signal is incident on a high-power photodiode to convert back to the RF domain. (b) shows RF power input/output data for both a monochromatic signal (top) and third-harmonic (bottom) tone through the link. The linear behavior of these curves is extrapolated (dashed grey lines) to find the third-order intercept point OIP₃ (black dot). (c) plots input and output power spectra for a two-tone incident RF signal consisting of equal-amplitude drive tones at Ω_B and $\Omega_B + 2\pi \times 50$ MHz. The out-of-band signal is attenuated by 26 dB relative to the in-band signal via the PPER filter's acoustic response. (d) Characterizes the noise floor around the filter center frequency $\Omega_B/2\pi = 4.33$ GHz as a function of probe power. The inset shows the noise floor due to a combination of spontaneous Brillouin noise and a white background due to amplified spontaneous emission of the EDFA. Adapted from Ref. [220].

increases commensurately, until some signal compression is observed at the highest input powers (top curve of Fig. 4.3b). Through this system, the net RF-photonics link gain is -2.3 dB. The observed compression represents the first of two fundamental forms of distortion in RF-photonics links, as a deviation from the ideal linear response of a filter. This compression is characterized by measuring the RF output power at 1 dB compression from the linear response, which is $P_{1\text{dB}} = 7.7$ dBm through the PPER filter. The second form of distortion that we consider is the creation of spurious frequency tones. In a traditional RF-photonics link experiment, the most important of these is those generated through third-order mixing, since this process can produce spurs around the original carrier frequency (e.g. through a $\Omega_1 + \Omega_2 - \Omega_2$ process). Within the PPER system, most spurs are rejected by the narrowband acoustic response. Therefore, to consider the potential strength of such effects, we consider spurious tones that are either (1) generated at harmonics of Ω_B through cascaded Brillouin phase modulation, or (2) unwanted frequency components around Ω_B which are created at the frontend of the link and are passed through the modulator. The latter of these are created within the input intensity modulator, and are typically the dominant source of spurious tones in terms of potential magnitude. This is consistent with traditional RF-photonics links where distortion is typically limited by the input modulation scheme. To quantify the magnitude of this effect, we drive the system at $\Omega = \Omega_B/3$ and measure the strength of the third-order spur that passes through the filter at Ω_B , as plotted in the bottom curve in Fig. 4.3b. The third order intercept point OIP_3 , which estimates the input power at which spurs would overtake the transmitted signal⁵, is calculated to be $\text{OIP}_3 = 23$ dBm through extrapolating the curves in Fig. 4.3b.

4.5.2 Modulation Figure of Merit

The ultimate performance of the PPER link as shown in Fig. 4.3a is limited by components external to the silicon membrane PPER device. However, we can characterize the internal efficiency of the PPER device through a unitless figure of merit by comparing the output phase modulation magnitude to that of the input intensity modulation. Through the link

⁵. Note that this point is simply a mathematical construct, as signal compression will alter the system dynamics at such large input powers.

gain experiment, the small-signal phase modulation angle produced through the PPER device is $\phi_{\text{PM}}^{\text{out}} = 0.56 \text{ rad/V}$, compared to an input intensity modulation angle of $\phi_{\text{IM}}^{\text{in}} = 0.32 \text{ rad/V}$. These modulation strengths were measured as a function of the input RF voltage at 4.33 GHz. A natural figure of merit is the ratio between these two modulation strengths, $\phi_{\text{PM}}^{\text{out}}/\phi_{\text{IM}}^{\text{in}}$, which can be calculated for any modulation-conversion operation such as the PPER process. When this quantity is ≥ 1 , the modulation strength is preserved or enhanced through PPER operation. In the silicon membrane PPER, $\phi_{\text{PM}}^{\text{out}}/\phi_{\text{IM}}^{\text{in}} = 1.76$, indicating net enhancement of the incident modulation strength.

4.5.3 Microwave Filter Response

Narrowband microwave filtering through the PPER link is demonstrated in Fig. 4.3c, using a sample dual-tone RF signal consisting of equal-amplitude drive tones at Ω_{B} and $\Omega_{\text{B}} + 2\pi \times 50 \text{ MHz}$. When this signal is passed through the PPER filter, the out-of-band signal is attenuated by the device's single-pole acoustic transfer function (dashed gray line in Fig. 4.3c corresponds to the curve measured in Fig. 4.2i), resulting in 26 dB relative rejection of this tone as compared to the in-band signal. Through the engineering of more complex device structures, the filter rolloff and out-of-band rejection can be greatly improved [165].

4.5.4 Noise and Dynamic Range

To quantify the net dynamic range of the PPER link, we carry out noise measurements through the PPER device. For the set of parameters used in this experiment, the noise floor is dominated by spontaneous Brillouin scattering from thermal phonons (as opposed to coherent driven phonons generated through the PPER process). The resulting peak noise power spectral density is plotted as a function of optical probe power P_{pr} in Fig. 4.3d, showing the expected linear trend corresponding to a room temperature thermal phonon population of $k_{\text{B}}T/\hbar\Omega_{\text{B}} \approx 1390$ [233, 263]. For this experiment, the out-of-band noise floor is dominated by amplified spontaneous emission from EDFA2 (inset of Fig. 4.3d), and would otherwise be limited by detector noise. For the probe power at detector $P_{\text{pr}} = 75 \text{ mW}$ used for the experiment in Fig. 4.3b, the Brillouin noise floor is $N = -126$

dBm Hz⁻¹. These measurements correspond to a receive waveguide Brillouin coefficient $G_B = 730 \pm 40 \text{ W}^{-1}\text{m}^{-1}$, which agrees with the numbers obtained above from stimulated scattering experiments. Together with the prior measurements of RF distortion, these noise measurements set the dynamic range parameters for this RF-photonics link. The calculated third-order spur-free dynamic range SFDR₃, which corresponds to the dynamic range over which a signal is detectable while spurs or not, is $\text{SFDR}_3 = 2(\text{OIP}_3 - N)/3 = 99.3 \text{ dB Hz}^{2/3}$. The linear dynamic range is $\text{CDR}_{1\text{dB}} = P_{1\text{dB}} - N = 135 \text{ dB Hz}$. These measured dynamic ranges agree well with the calculated expressions in the previous section. For example, from Eq. 4.38,

$$\begin{aligned} \text{SFDR}_3 &= \left(\frac{3G_B^{(1)} \left(P_0^{(1)}\right)^2 L}{2\hbar\omega_p^{(2)} n_{\text{th}}\Delta} \right)^{\frac{2}{3}} = \left(\frac{3 \times 880 \text{ W}^{-1}\text{m}^{-1} \times (76 \text{ mW})^2 \times 2.53 \text{ cm}}{2\hbar 2\pi \times 194 \text{ THz} \times 1390} \right)^{\frac{2}{3}} \\ &= 100.2 \text{ dB Hz}^{2/3} \quad (4.41) \end{aligned}$$

where the average on-chip pump power $P_0^{(1)} = 76 \text{ mW}$ has been used.

To calculate the effective noise figure added by the PPER device, we must compare to an input noise power. As a result, this metric depends greatly on the external components of the RF link without the PPER device. In an absolute ‘worst case’ scenario where the fundamental limiting noise prior to filtering was Johnson-Nyquist noise (see Section 4.3.6), with a room temperature noise power of $N_{\text{in}} = -174 \text{ dBm Hz}^{-1}$, the noise figure of this link would be $\text{NF} = -N_{\text{in}} + N - G = 50 \text{ dB}$. Compared to practical experiments, the additive noise would likely be one or more orders of magnitude smaller.

4.6 Potential for Improved Performance

In the previous section, we showed that the silicon waveguide-based PPER device permits robust optical and RF-photonics performance, as a promising platform for narrowband microwave filtering applications. Beyond this first demonstration, to increase the dynamic range and fidelity of the PPER filter, many changes to the device design and link components may be useful.

External to the device itself, the performance of the PPER filter system may be enhanced by improving the modulation and detection schemes. In particular, decreasing the half-wave voltage of the intensity modulator used to encode RF signals onto pump light increases total link gain as $1/V_\pi^2$, resulting in lower RF losses through the filter. Conversely, by decreasing V_π as well as the receive waveguide power or device length, the system noise floor can be decreased with little or no penalty to gain and dynamic range, enabling filtering of low-power signals as would likely be desirable in practical applications. While the modulator used in the photonic link tested here has a relatively high $V_\pi = 9.9$ V, commercial modulators are available with $V_\pi < 4$ V, and integrated modulator technologies have already been demonstrated in silicon with $V_\pi < 1$ V [264,265], so this approach seems feasible. Beyond the link frontend, the current method for phase-to-intensity demodulation could be improved. Currently, one of the two modulation sidebands is filtered out as a simple method to characterize the system response; however, this approach discards half of the signal power. Alternately, the link gain of this system could be improved by replacing this demodulation scheme with a phase-shifting element or coherent detection using an integrated Mach-Zehnder interferometer and balanced photodetectors [266]. Furthermore, through active control of modulation distortion, the dynamic range of the PPER link could be improved. For example, linearized modulation schemes have been shown to permit large increases in dynamic range for certain RF-photonics applications [267–269].

Significant improvements in link performance can also be realized by increasing the internal efficiency of the PPER process, in particular within the emit waveguide. This results from the fact that noise is only created within the receive waveguide. So, while increasing the probe power in the receive waveguide enhances the output signal strength, it also increases the noise floor by the same amount. By contrast, increasing the Brillouin interaction strength in the emit waveguide directly improves the dynamic range (related to the factor $\left(G_B^{(1)} \left(P_0^{(1)}\right)^2 L\right)^{2/3}$ in the spur-free dynamic range). In practice, increasing the device length is not desirable since it increases footprint. Therefore the most direct way to improve the PPER performance is by improving the pump power handling. While in the current device pump powers were limited to ~ 100 mW due to TPA-related nonlinear free-carrier absorption, this effect can be mitigated by either external free-carrier removal with

electric fields [236] or by moving the pump wavelength above the TPA threshold in silicon ($\lambda_p > 2.2 \mu\text{m}$). The latter is theoretically made possible by the wideband response of the intra-modal PPER process (Section 4.2) and the availability of silicon-based modulators at these wavelengths [265], and would enable pump powers $\sim 2 \text{ W}$ to propagate through the emit waveguide with negligible nonlinear absorption. In this case, improvements in SFDR_3 of more than 10 dB should be possible. For example, increasing the pump power to 1 W within the current design should enable a spur-free dynamic range of $\text{SFDR}_3 = 115 \text{ dB Hz}^{2/3}$. Alternately, higher pump powers will allow efficient operation with much smaller device footprints. An additional advantage to shortening device lengths is that this would reduce inhomogeneous broadening (Section 3.8.4) [219, 242], leading to smaller filter widths and increased Brillouin couplings. As an example, an optimized and fully-integrated silicon PPER system with parameters ($P_p = 2 \text{ W}$, $\lambda_p = 2.75 \mu\text{m}$, $P_{pr} = 10 \text{ mW}$, $\lambda_{pr} = 1.55 \mu\text{m}$, $V_\pi = 1 \text{ V}$, $Q = 1500$, $L = 200 \mu\text{m}$) would enable enhanced linearity and noise performance (link gain $G = 0 \text{ dB}$, $\text{SFDR}_3 = 107 \text{ dB Hz}^{-2/3}$, $\text{CDR}_{1\text{dB}} = 148 \text{ dB Hz}^{-1}$, $N = -152 \text{ dBm Hz}^{-1}$, $\text{NF} = 21 \text{ dB}$) in a small footprint.

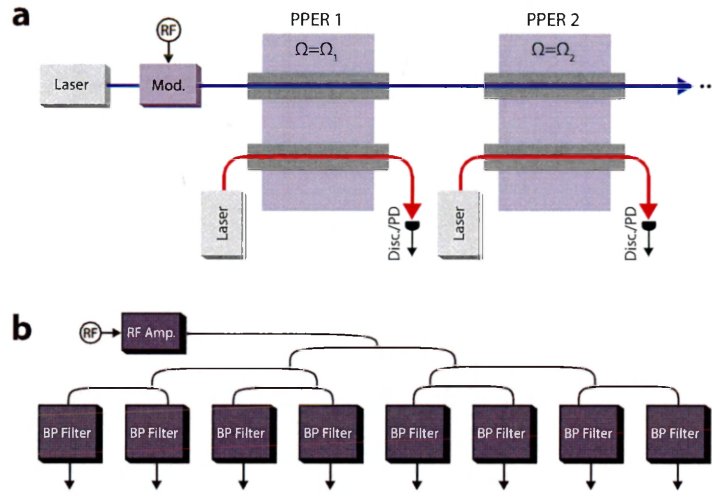


Figure 4.4: Comparison of serial and parallel filter architectures for channelization. (a) Serial cascaded architecture for a PPER channelization filter. Because the same pump light can be used for each device (i.e. because the PPER device makes a copy of a narrowband slice of the input RF spectrum), minimal signal degradation is experienced as the number of channels is increased. (b) Architecture based on parallel RF filters. Note that because the signal must be split equally among the channels, amplification is necessary to preserve signal amplitude.

Such size reductions and performance increases open the door to cascaded filter banks, which utilize some of the unique benefits of the PPER process. In particular, as pump light propagates through the emit waveguide, its intensity modulation is unchanged (Section 4.3.1); therefore, if optical insertion losses are small, this same pump light can be injected into other PPER filters. Through a serial cascaded process, an RF signal encoded on the pump wave can pass through many successive PPER devices, each selecting out a distinct spectral channel without impacting the fidelity of the original signal; this process is diagrammed in Fig. 4.4a. Using the parameters above, a cascaded array of 200 PPER devices 0.2 mm each in length could span a 0.5 GHz frequency bandwidth with 2.5 MHz bandwidth per channel, while maintaining excellent dynamic range and sensitivity. By contrast, a parallel channelizing filter based on a bank of fixed microwave band-pass filters (Fig. 4.4b) requires power to be split between each channel, resulting in decreases to signal-to-noise ratio that increase with the number of channels. Thus for certain applications, the PPER architecture may enable performance metrics that compare favorably even with established RF technologies.

Ultimately, the silicon-based PPER presented here would be implemented within complex, fully-integrated silicon photonic circuits. For example, this device can be readily interfaced with existing silicon-based modulators [270, 271] and integrated photodetectors [272–274]. Combining these technologies would enable low-cost realization of PPER operations within integrated microwave photonics. Furthermore, like other RF-photonic filters, the PPER concept can be adapted to frequency-agile operation by modifying the modulation scheme [164, 165, 202, 259]. More complex types of emit-receive filters are also possible through the use of inter-modal interactions [221], for example using the modulator design presented in Chapter 6.

More generally, emit-receive processes can be created in a variety of physical systems where multiple optical fields couple through a common phonon mode. The key requirement in these systems is that the emit and receive channels must be optically isolated from each other. Potential systems for studying PPER interactions include optomechanical waveguides coupled to acoustic cavity supermodes [165], multi-core optical fibers [275], and optical waveguides which guide light fields in disparate wavelengths [196, 197] or spatial

modes [221] within the same device. PPER interactions in these systems may enable optical and RF signal processing and spectral analysis with platform flexibility complementary to the silicon membrane device.

In summary, we have demonstrated efficient photon-phonon couplings within a dual-core optomechanical silicon waveguide, and utilized emit-receive processes to create an RF-photonic filter. This device supports robust Brillouin-based modulation and high-fidelity filtering, which we studied within an RF-photonic link. Future work may explore large-scale integration of such devices into a wide array of complex integrated photonic systems for applications in communications, sensing, and microwave and optical signal analysis.

Chapter 5

Inter-modal Brillouin Scattering

5.1 Introduction

The creation of strong forward-SBS interactions in silicon waveguides demonstrated that flexible Brillouin-based signal processing is possible in silicon photonics. These results represent a significant milestone—Brillouin nonlinearities, which were previously absent in silicon waveguides, have been transformed into the strongest nonlinear interaction in silicon, with nonlinear coefficients in excess of 10^3 - 10^4 $\text{W}^{-1}\text{m}^{-1}$. Furthermore, Brillouin interactions offer interesting degrees of tailorability not possible with bulk nonlinearities, including the ability to separately access and control optical and mechanical degrees of freedom, or to engineer couplings between multiple optical and/or elastic modes. These powerful dynamics, which offer intriguing opportunities for new signal-processing operations and physical phenomena, have been realized using intra-modal forward SBS. While FSBS offers potential advantages over traditional fiber-based BSBS for certain applications, it does not produce single-sideband gain. As a result, it is potentially difficult to adapt existing BSBS-based technologies for signal processing, slow light, and filtering to silicon photonic circuits using FSBS. In this section, we describe the development of on-chip stimulated inter-modal Brillouin scattering (SIMS), which offers complementary dynamics to FSBS while restoring single-sideband couplings reminiscent of BSBS.

Stimulated inter-modal and inter-polarization Brillouin scattering have previously been observed in multi-mode [179] and microstructured fibers to demonstrate single-sideband

gain and energy transfer [187], optical self-oscillation [276], and optical isolation [188]. Inter-modal Brillouin scattering in optomechanical microsphere resonators has been used to create attractive schemes for optomechanical cooling [205], Brillouin scattering-induced transparency [207, 208] (an opto-acoustic analogue to electromagnetically-induced transparency), and nonreciprocal light propagation [211]. Beyond these exciting experimental results, theoretical investigations have shown that these processes can permit broadband optical isolation by harnessing the unique dispersion-tailorability of multimode interactions [239, 258]. These processes, in addition to many existing BSBS-based technologies, should be achievable on-chip using SIMS.

The unique properties of SIMS result from the phase-matching requirements for inter-modal scattering processes. In contrast to FSBS, where Stokes and anti-Stokes processes couple to the same phonon mode, SIMS decouples these processes, requiring that phonons which mediate Stokes and anti-Stokes scattering travel in opposite directions (see Section 2.2.3). As a result, stimulated Stokes amplification, as well as an array of nonreciprocal operations, become possible through a forward-scattering process. The key to practical implementations of SIMS is the development of integrated mode multiplexers, which enable the separation and routing of pump and signal waves without the use of narrowband filters or optical circulators, as is necessary for typical BSBS-based signal processing technologies. These attributes make SIMS particularly enticing for flexible chip-based device architectures.

We begin by describing the design of mode multiplexers that allow coupling to and interrogation of individual optical spatial modes of an integrated multimode waveguide. Next, we design a multimode suspended optomechanical waveguide and investigate its linear and nonlinear optical properties. Thereafter, we carefully characterize the Brillouin response of this device to demonstrate single-sideband gain, net optical amplification, and significant ($> 50\%$) optical energy transfer. [221] This process is harnessed to create the first Brillouin laser in a silicon waveguide [222], and to demonstrate optomechanical cooling of a band of phonons within a linear waveguide [223]. These highly-customizable SIMS interactions within silicon waveguides demonstrate new techniques for controlling and tailoring Brillouin interactions in integrated photonic circuits.

5.2 Integrated Mode Multiplexers

In order to perform on-chip inter-modal nonlinear optics, we first developed integrated mode multiplexers that we use to address separate spatial modes of a silicon ridge waveguide. We investigated two designs that have previously been studied in silicon-on-insulator optical circuits: asymmetric Y-junction couplers [277] and mode-selective directional couplers [278]. It was necessary to adapt designs previously implemented using nanowire couplers in Refs. [277,278] using ridge waveguides that are easily compatible with our Brillouin-active waveguide structures ¹. Through our experiments, we found that the Y-junction structures, which involved adiabatically combining two waveguides of different widths, were very sensitive to proximity effects around the junction region during e-beam lithography, which made them less robust for broadband operation. As a result, the majority of our fabricated devices employ the mode-selective directional coupler design.

The basic structure of the mode-selective coupler is diagrammed in Fig. 5.1a. Note that this mode multiplexer is written in the same layer as the 80-nm-deep ridge waveguide, permitting simple fabrication. A wide multimode waveguide guides two optical modes—a fundamental (symmetric) and a first-excited (anti-symmetric) optical mode. Light in the symmetric optical mode does not couple to the narrow coupler waveguide as it passes through the coupling region of length L_c due to the different waveguide widths. However, light guided in the fundamental mode of the coupler waveguide strongly couples to the anti-symmetric spatial mode of the wide waveguide since the effective indices of these two modes are approximately matched, permitting phase-matched evanescent coupling to occur. From a coupled-mode treatment, the fraction of guided-wave power C that is converted from the coupler waveguide to the anti-symmetric mode is given by the equations [279]:

$$C = \frac{\kappa_{12}}{\beta_0} \sin(\beta_0 L_c), \quad (5.1)$$

1. A practical consequence of this is that the ridge waveguide couplers can have increased modal crosstalk due to the reduced effective index differences between optical modes.

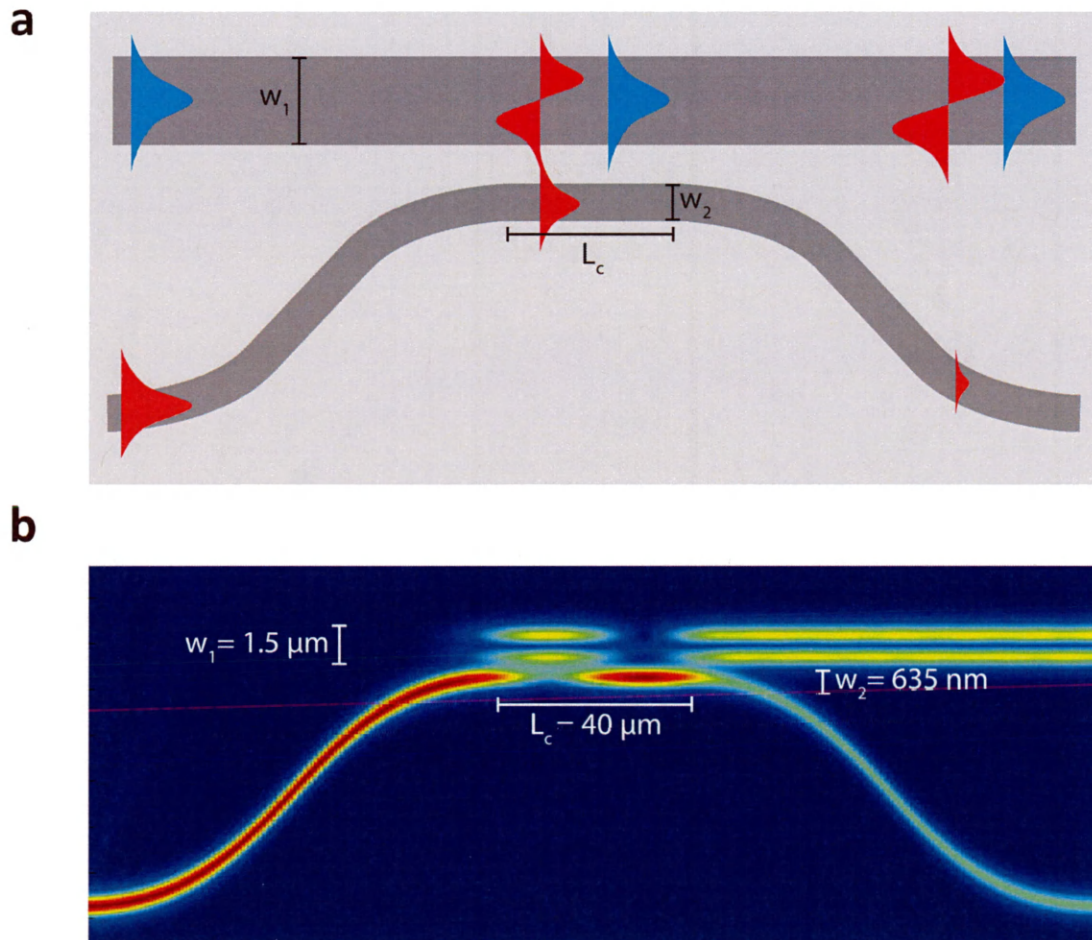


Figure 5.1: **Mode-selective directional couplers.** (a) Top-down diagram of the directional coupler design showing the relevant device dimensions. Light incident in the fundamental symmetric mode of the wider waveguide remains in the same waveguide mode. By contrast, light injected into the fundamental mode of the narrow coupler waveguide is coupled into the higher-order anti-symmetric mode of the wide waveguide. (b) FDTD simulation showing typical device dimensions and simulated power coupling into the anti-symmetric mode of the wider waveguide. For the parameters of this simulation, 78% of the injected light is coupled into the anti-symmetric spatial mode. Adapted from Ref. [221].

$$\beta_0 = \sqrt{\kappa_{21}\kappa_{12} + \frac{(\beta_1 - \beta_2)^2}{2}}. \quad (5.2)$$

Here β_1 and β_2 are the propagation constants of the anti-symmetric waveguide mode and the fundamental mode of the coupler waveguide within their respective waveguide cores, and κ_{12} and κ_{21} are the one-way coupling coefficients of the two modes. This equation shows that near-unity power transfer is possible when the effective indices of the two modes are well-matched. Note also that both the magnitude and phase of the coupling change dramatically with changes in propagation constant mismatch, permitting efficient coupling into the desired mode with relatively little crosstalk to other waveguide modes.

To optimize the coupler design for our SOI ridge waveguide platform, we performed parameter sweeps of FDTD simulations using Lumerical (see Fig. 5.1b) and fabricated device splits to optimize designs. The as-fabricated directional couplers achieved 60-95% coupling from the fundamental mode of the coupler waveguide to the anti-symmetric mode of the wider waveguide depending on design parameters.

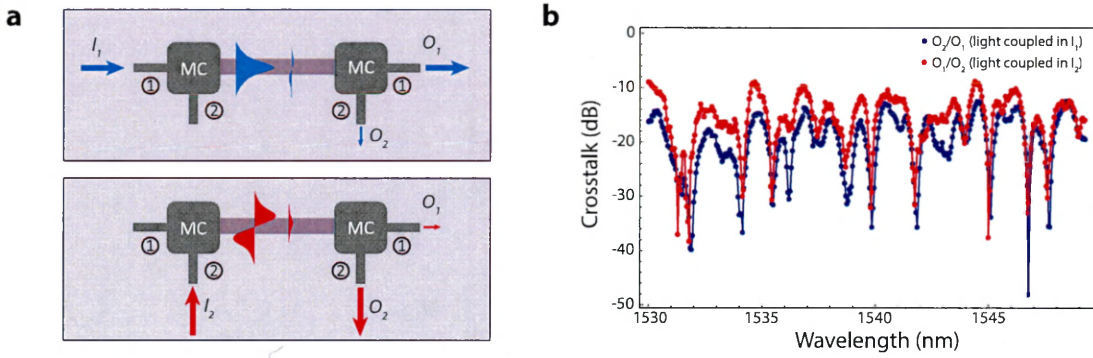


Figure 5.2: Mode multiplexer characterization (a) depicts schematics for a crosstalk measurement. In the top panel, light injected into input port 1 with power I_1 is coupled into the symmetric mode with a small amount of light scattered into the anti-symmetric mode. Most of the light is correctly de-multiplexed into output port 1, but some light exits through port 2 due to modal crosstalk in both the input and output couplers. Similarly, in the bottom panel light coupled into input port 2 with power I_2 is converted into the anti-symmetric mode with a small amount of light coupled into in the symmetric mode. This light propagates through the multimode waveguide before being de-multiplexed at the output. (b) Typical power crosstalk spectra as a function of input light wavelength for one device. The total crosstalk is calculated by dividing the output powers of the two ports. Adapted from Ref. [221].

In practice, some small amount of light is (de)multiplexed into the incorrect mode or port due to the intrinsic coupling of the device, or scattering from surface roughness in the coupler or throughout the intermediary waveguide, resulting in modal crosstalk. We investigated the crosstalk performance of the mode multiplexers by placing two nominally identical couplers in series and measuring the transmitted power between each set of input ports—this experiment is diagrammed in Fig. 5.2a. The two ports of each coupler refer to (1) light incident into the wide multimode waveguide in the symmetric mode or (2) light incident into the narrow coupler waveguide which is ideally coupled into the anti-symmetric mode of the multimode waveguide. Note that crosstalk can happen in both input and output multiplexers—for example, in the top panel of 5.2a, most of the input light in port (1) is correctly multiplexed into the symmetric mode, but a small amount is coupled into the anti-symmetric mode (crosstalk). At the output, the majority of the light in the anti-symmetric mode will couple out of port 2. However, additional crosstalk from light in the symmetric mode can lead to additional power coupled out of port 2. As such, assuming identical crosstalk in both (de)multiplexers, the addition of a second multiplexer in series leads to an additional 3 dB of crosstalk—in practice this effect is likely even more dramatic since the two multiplexers are not identical due to dimensional variations across the cm-scale silicon chip.

Fig. 5.2b plots the corresponding crosstalk through the two (de)multiplexers in series as a function of wavelength for one typical device. Median crosstalk values for this configuration are typically -15 to -20 dB, but at certain wavelengths have net crosstalk well below -30 dB. These crosstalk numbers may be improved through further design optimization and by using multimode waveguide designs with larger effective index splitting between symmetric and anti-symmetric modes. Throughout this chapter, all experiments performed on multimode waveguides are carried out in regions with total crosstalk less than -20 dB (-30 dB typical).

5.3 Multimode Optomechanical Waveguide Design

The design of the multimode Brillouin-active waveguide is based on the same design strategies for optical and elastic-wave guidance developed in Chapter 3.2, except we utilize a wider ridge waveguide to support low-loss guidance of two optical modes. A schematic of the multimode membrane-suspended waveguide is plotted in Fig. 5.3a. As before, the optomechanical waveguide consists of a silicon ridge waveguide on a suspended membrane. Scanning electron micrographs (SEM) show the cross-section of a fabricated device (Fig. 5.3b) and a top-down view of one suspended segment (Fig. 5.3c) 50 μm in length. The active device region consists of a 80 nm \times 1.5 μm wide ridge on a 135 nm thick silicon membrane of variable width w , with a typical value of $w = 2.85 \mu\text{m}$ (Fig. 5.3e).

This optomechanical waveguide supports low-loss guidance of a fundamental (symmetric) and a first-excited (anti-symmetric) transverse electric-like optical mode through total internal reflection. These modes are plotted in Fig. 5.3f-g, respectively, at $\lambda = 1550 \text{ nm}$. While, in principle, several higher-order modes are also guided by this structure, they do not support low-loss guidance due to interactions with the tether structures and are not excited through the experiments in this chapter.

This system also supports guidance of numerous elastic waves, which are confined to the membrane structure due to the large silicon-air acoustic impedance mismatch. However, only a small number of these elastic modes possess the correct symmetry and modal overlap to mediate strong Brillouin coupling. One such $\sim 6 \text{ GHz}$ elastic mode that couples strongly to the electrostriction-mediated optical force resulting from interference of the two optical modes (5.3h) is plotted in 5.3i. Phase-matching for the light-sound coupling can be understood from the top-down device diagrams in Fig. 5.3j-l; Fig. 5.3j depicts a 14- μm -long device segment with the membrane shown in dark gray and the ridge highlighted in light gray. The displacement of these features due to the guided elastic mode is plotted in Fig. 5.3k. For comparison, the intensity beat-note of the two optical modes is plotted on the same scale in Fig. 5.3l. Both vary over the same longitudinal period, indicating that coupling between these fields is phase-matched.

In the next section, we characterize the linear and nonlinear optical propagation losses

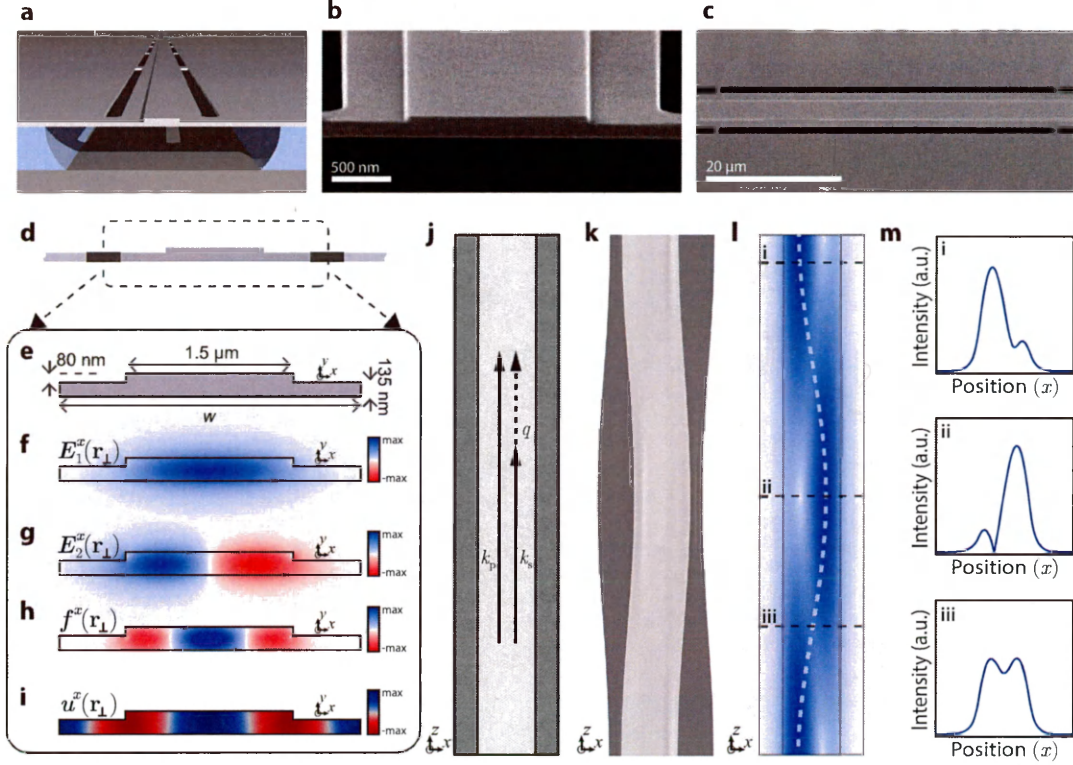


Figure 5.3: **Multimode optomechanical waveguide.** (a) depicts a schematic of the suspended multimode Brillouin-active waveguide. (b) plots a cross-sectional scanning electron micrograph (SEM) of the device as-fabricated, with a scale bar representing 500 nm. (c) plots a top-down SEM of the device showing one suspended segment. The scale bar corresponds to 20 μm in length. (d) depicts a simplified view of the device cross section, with the dashed region highlighted in (e)-(i); (e) Plots the relevant dimensions of the device cross-section, with a variable total width w which is typically around 2.8 μm . (f) and (g) plot the simulated x -directed electric field components for the symmetric and anti-symmetric optical modes of the waveguide. The interference between these modes drives an electrostrictive force distribution plotted in (h). The displacement field of a ~ 6 GHz elastic mode which couples strongly to this optical force is plotted in (i). (j) plots a top-down view of a 14 μm long device segment, with the longitudinal phase-matching condition depicted on-top. This length corresponds to the phonon wavevector q . The elastic displacement for the membrane (dark gray) and ridge (light gray) regions is plotted in (k) over the same scale, showing one longitudinal acoustic wavelength. The intensity beat note between the two optical modes is plotted in (l). This beat note has the same wavelength as the phonon and represents a visual demonstration of the phase-matching condition. (m)i-iii plot the spatial distribution of the optical intensity at three slices of the waveguide. Adapted from Ref. [221].

of this structure. We will find that both symmetric and anti-symmetric optical modes propagate with low linear loss. Furthermore, due to the large optical mode areas and reduced modal overlaps for inter-modal interactions, nonlinear losses are also suppressed in this same structure. Thereafter we will characterize inter-modal Brillouin coupling in this device.

5.4 Linear and Nonlinear Losses in Multimode Silicon Waveguides

In analogy to Chapter 3.3-3.4, where we characterized the linear and nonlinear propagation characteristics of the FSBS-active optomechanical silicon waveguide, here we study the linear and nonlinear propagation coefficients of the new multimode optomechanical waveguide structure. In particular, we find that the reduced modal overlap leads to a reduction in inter-modal nonlinear losses as compared to intra-modal waveguides.

We first calculate the effective third-order nonlinear coefficients using a FEM simulation. As in the single-mode case, these nonlinearities are slightly increased from their bulk material values due to the nontrivial vectorial nature of the highly-confined propagating optical modes [247]. We again assume bulk nonlinearity values of $n_2 = 4.5 \times 10^{-18} \text{ m}^2\text{W}^{-1}$ and $\beta_{\text{TPA}} = 7.9 \times 10^{-12} \text{ m}^2\text{W}^{-1}$ [245] for the Kerr effect and two-photon absorption, respectively. From our simulations, we calculate guided-wave Kerr coefficients of $\gamma_k^{11} = 74 \pm 11 \text{ m}^{-1}\text{W}^{-1}$, $\gamma_k^{22} = 71 \pm 11 \text{ m}^{-1}\text{W}^{-1}$, and $\gamma_k^{12} = \gamma_k^{21} = 44 \pm 7 \text{ m}^{-1}\text{W}^{-1}$. Here we have used the superscripts of γ^{ij} to label the optical modes participating in the nonlinear coupling, where superscript 1 (2) refers to the symmetric (anti-symmetric) waveguide mode. Similarly, we calculate two-photon absorption coefficients of $\beta^{11} = 34 \pm 10 \text{ m}^{-1}\text{W}^{-1}$, $\beta^{22} = 30 \pm 9 \text{ m}^{-1}\text{W}^{-1}$, and $\beta^{12} = \beta^{21} = 20 \pm 6 \text{ m}^{-1}\text{W}^{-1}$. For all of these coefficients, we use units of guided wave power instead of optical intensity for simplicity, i.e. $\gamma_k \approx n_2\omega/(c \cdot A_{\text{eff}})$ and $\beta \approx \beta_{\text{TPA}}/A_{\text{eff}}$, where A_{eff} is the effective nonlinear mode area. These two-photon coefficients are difficult to separate from higher-order free carrier losses through nonlinear transmission measurements. Since the TPA coefficient of silicon is relatively well-known, we assume that the guided-wave TPA coefficients are equal to the calculated values. Along

with linear and nonlinear transmission measurements, these values are used to estimate the inter- and intra- modal free-carrier absorption coefficients, γ^{ijk} .

We first characterize the linear propagation losses α^i of each mode by measuring the intrinsic Q -factors of racetrack resonators fabricated from suspended multimode silicon waveguides of varying lengths. The results of these measurements are plotted in Fig. 5.4a-b and correspond to linear propagation losses of 0.24 ± 0.02 dB/cm ($\alpha^1 = 5.5 \pm .5$ m⁻¹) for the symmetric mode and 0.30 ± 0.12 dB/cm ($\alpha^2 = 6.8 \pm 2.7$ m⁻¹) for the anti-symmetric mode. The increased losses for the anti-symmetric mode are likely due to increased interactions with rough sidewalls (and potentially with the periodic tethers) which cause scattering losses to occur. Further reduction of linear losses for both modes is likely possible by expanding the membrane width to reduce these scattering losses.

Next, we characterize the intra-modal nonlinear transmission of our waveguide. The intra-modal power evolution in the presence of linear and nonlinear loss in a single-mode silicon waveguide is modeled by the differential equation

$$\frac{dP_i}{dz} = -\alpha^i P_i - \beta^{ii} P_i^2 - \gamma^{iii} P_i^3, \quad (5.3)$$

where α^i is the linear propagation loss coefficient for the i^{th} waveguide mode and γ^{iii} is the intra-modal fifth-order nonlinear loss coefficient due to FCA. Fitting measured nonlinear transmission measurements (Fig. 5.4c-d) to this model allows the calculation of γ^{iii} .

To determine these free-carrier losses, power-dependent transmission data for each optical mode are fit to Eq. 5.3 using Mathematica. In these fits, α^1 and α^2 are fixed to their measured values and β^{11} , β^{12} , and β^{22} are fixed to their calculated values. Intra-modal transmission data for each mode are plotted in Supplementary Figure 1c-d as a function of input power, and are best fit with free-carrier absorption coefficients $\gamma^{111} = 900 \pm 400$ m⁻¹W⁻² and $\gamma^{222} = 720 \pm 430$ m⁻¹W⁻².

As in the case of the intra-modal optomechanical waveguide, significant reduction of the effective free-carrier lifetime is observed compared to bulk values due to in-plane carrier diffusion [249]. The estimated fifth-order absorption coefficients are consistent with a free-carrier lifetime of 1.5 ns according to a Drude-Lorentz model [248, 249] or a lifetime of 1.2

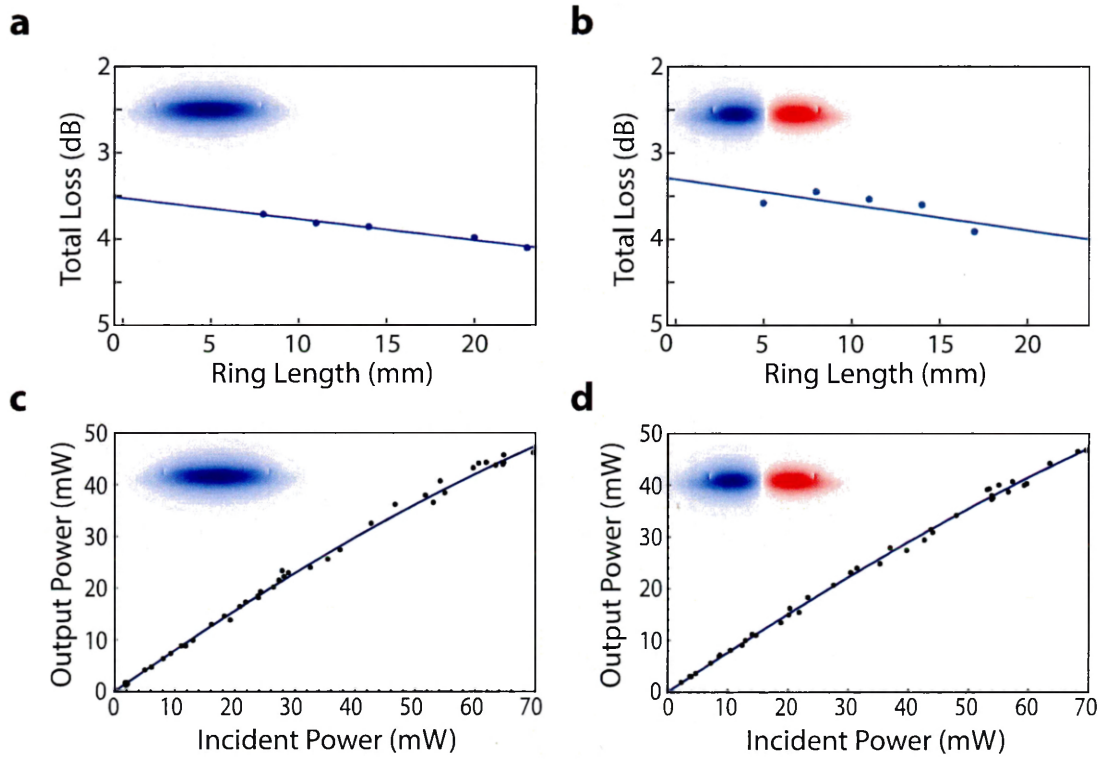


Figure 5.4: **Linear and nonlinear loss measurements for the multimode waveguide.** Panels (a) and (b) plot linear loss vs. ring resonator length for the symmetric and anti-symmetric waveguide modes, respectively. Panels (c) and (d) plot output vs. input power for these two modes. All measurements are at $\lambda \approx 1550$ nm. Adapted from Ref. [221].

ns according to a Drude-Sommerfeld model of free-carrier absorption [250].

In the presence of a bright pump P_i , the inter-modal nonlinear loss experienced by a weak signal field P_j guided in a different optical mode is given by the additional differential equation

$$\frac{dP_j}{dz} = -\alpha^j P_j - 2\beta^{ji} P_i P_j - \gamma^{jii} P_i^2 P_j. \quad (5.4)$$

Comparing this equation to measured cross-modal nonlinear loss while using the measured value of α^i and calculated value for β^{ji} allows estimation of γ^{jii} . Measurements of small signal inter-modal nonlinear loss of 0.45 dB are observed at 76 mW symmetric-mode pump powers, consistent with $\gamma^{211} \approx \gamma^{122} = 310 \pm 200 \text{ m}^{-1}\text{W}^{-2}$, around 34% of γ^{111} . According to the overlap integral method for calculating inter-modal free-carrier losses from Ref. [250], γ^{211} is expected to be 41% of γ^{111} in magnitude, which agrees well with the measured value. Note that the measured inter-modal free-carrier loss is very uncertain—this results from a variety of factors. First, at the tested input powers this effect is very weak. Second, it depends on the calculated values for TPA, which are somewhat uncertain. Finally, heating of the mode-converter structures can lead to variations in mode coupling and transmission due to the thermo-optic effect.

It is worth noting that these nonlinear losses are greatly reduced from the intra-modal FSBS-active waveguide. This results from a combination of increased mode volumes, further-decreased free-carrier lifetimes, and reduced modal overlaps for inter-modal interactions. These reduced nonlinear losses bode well for optical amplification and robust operation at high optical pump powers, necessary for low-noise laser designs.

5.5 Stimulated Inter-modal Brillouin Scattering

In this section, we describe the experimental observation of stimulated inter-modal Brillouin scattering within the silicon optomechanical waveguide. We first discuss the operation scheme of the waveguide and the phase-matching requirements for SIMS. Next, we characterize Brillouin coupling within this device and demonstrate single-sideband gain and optical amplification. Finally, we demonstrate strong stimulated energy transfer between

two optical fields and discuss further experiments.

5.5.1 Operation Scheme

Through SIMS, we consider the interaction of symmetric and anti-symmetric optical modes (labeled mode 1 and mode 2, respectively) with a guided elastic wave. These three waves, depicted pictorially in Fig. 5.5a, propagate within the optomechanical waveguide described in Section 5.3. We interface this multimode silicon waveguide with mode multiplexers based on the directional coupler design detailed in Section 5.2, which we diagram in 5.5b; light incident in port 1 of the mode multiplexer is coupled into the symmetric waveguide mode, while light incident in port 2 is coupled into the anti-symmetric spatial mode. These couplers may also be operated in reverse to de-multiplex these modes into their respective ports.

The operation scheme of the SIMS-active waveguide is depicted in 5.5c. A strong pump wave at frequency ω_p is injected into port 1 of the input multiplexer and coupled into the symmetric optical mode. A red-detuned signal wave with frequency ω_s is coupled through port 2 into the anti-symmetric mode. The difference frequency between these waves $\Omega = \omega_p - \omega_s$ is set equal to the resonance frequency of the Brillouin-active phonon Ω_B . As these optical waves propagate through the active device region, they experience strong inter-modal Brillouin coupling through the phonon at frequency Ω_B to produce stimulated Stokes energy transfer from pump to signal waves (this power evolution is sketched in the top panel of 5.5c). Afterwards, pump and signal waves are demultiplexed through a second mode multiplexer into two output waveguides, permitting separate routing of these waves on-chip.

In contrast to intra-modal forward SBS, this process produces single-sideband optical gain. This two-wave coupling is possible through SIMS because the Stokes and anti-Stokes scattering processes are mediated by different phonon modes. This distinction can be understood from the phase-matching conditions for these two processes.

Through a Stokes process, diagrammed in Fig. 5.5g, a pump photon ($\omega_p, k_1(\omega_p)$) guided in the symmetric optical mode is scattered to a red-shifted signal photon ($\omega_s, k_2(\omega_s)$) in the anti-symmetric mode, and a Stokes phonon with (frequency, wavevector) = (Ω_s, q_s) .

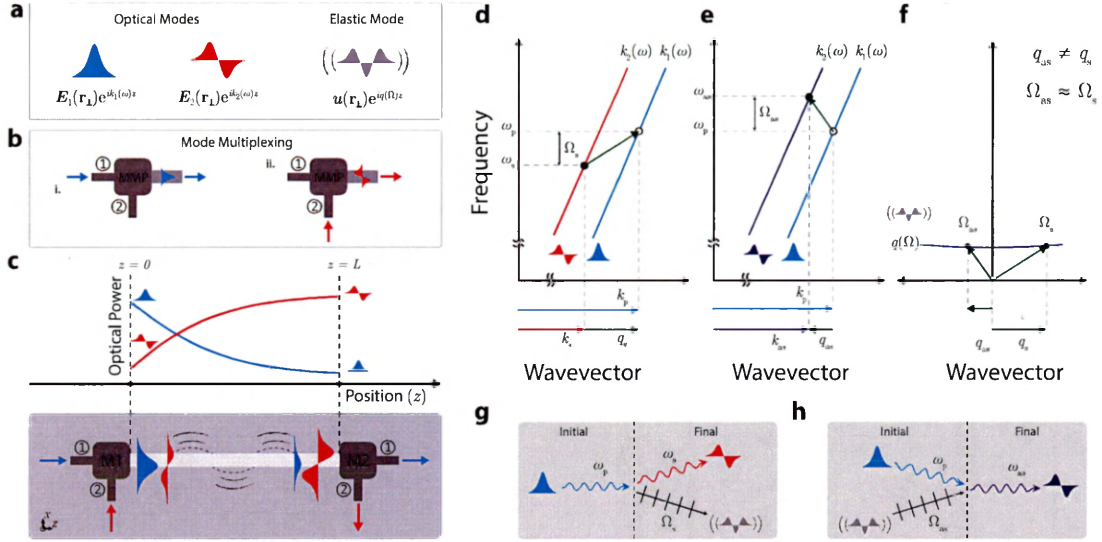


Figure 5.5: **Operation scheme for on-chip stimulated inter-modal Brillouin scattering.** (a) diagrams the three modes which participate in the SIMS process, including symmetric (blue) and anti-symmetric (red) optical modes and the Brillouin-active elastic mode (gray). (b) depicts operation of the mode multiplexers which are here shown as a two-port “gray box.” Light incident in port 1 is coupled into the symmetric waveguide mode, whereas light incident in port 2 is coupled into the same waveguide’s anti-symmetric spatial mode. (c) depicts stimulated inter-modal Brillouin energy transfer. Pump (blue) and signal (red) waves are coupled into the symmetric and anti-symmetric waveguide modes, respectively, of a Brillouin-active multimode waveguide. As these waves traverse the device, energy transfers from the pump to the signal wave (top). Afterwards, the two waves are demultiplexed through an identical mode-selective coupler and may be routed elsewhere on-chip. (d) and (e) depict phase-matching and energy conservation for Stokes and anti-Stokes scattering processes, respectively. Each couples to a phonon with a different wavevector, but nearly identical frequencies, as plotted in the acoustic dispersion curve of (f). (g) and (h) sketch Feynman-like scattering diagrams for Stokes and anti-Stokes processes. In the Stokes process (g), an incident pump photon is converted to a red-shifted signal photon and a phonon. In the anti-Stokes process (h), an incident pump photon annihilates a phonon and is blue-shifted. Adapted from Ref. [221].

For this process to efficiently occur, both energy conservation ($\Omega_s = \omega_p - \omega_s$) and phase-matching conditions ($q_s = k(\omega_p) - k(\omega_s)$) must be satisfied. Combined, these require that $q_s = k_1(\omega_p) - k_2(\omega_p - \Omega_s)$. This condition is represented through the diagram in Fig. 5.5d, which plots phase-matching (energy conservation) on the horizontal (vertical) axis. A phonon that satisfies the SIMS condition lies on the $q(\Omega)$ sketched in Fig. 5.5f and maps light between initial (open circle) and final optical states (solid circle) on the two dispersion branches of Fig. 5.5d. In this configuration, the phonon that mediates a Stokes process is forward-moving.

By contrast, through the anti-Stokes process, diagrammed in Fig. 5.5h, a pump photon ($\omega_p, k_1(\omega_p)$) combines with an existing guided phonon (Ω_{as}, q_{as}) to produce a blue-shifted photon ($\omega_{as}, k_2(\omega_{as})$). For this process, phase matching and energy conservation require $q_{as} = k_2(\omega_p + \Omega_{as}) - k_1(\omega_p)$. This process is diagrammed in Fig. 5.5e. In this configuration, the anti-Stokes phonon that scatters light between initial (open circle) and final optical states (solid circle) is backward-moving.

Because the Stokes and anti-Stokes processes are mediated by phonons with distinct wavevectors ($q_s \neq q_{as}$), the two processes are decoupled, resulting in separate single-sideband couplings for Stokes and anti-Stokes processes. These dynamics contrast sharply with those of intra-modal FSBS, where the same phonon couples to both Stokes and anti-Stokes scattering processes, meaning that the two always co-exist in the absence of an external symmetry-breaking mechanism. The dynamics of FSBS also permit cascaded Brillouin scattering processes, which are not possible through two-mode SIMS.

By breaking the symmetry between Stokes and anti-Stokes processes, SIMS also decouples phonon generation and annihilation to permit stimulated phonon gain. As a result, SIMS produces stimulated Stokes amplification for both signal and phonon waves, making it readily amenable to laser designs that initiate laser oscillation from thermal mechanical noise. At the same time, since anti-Stokes processes can only occur from thermal (or otherwise externally-driven) phonons, this spontaneous scattering process provides a potential way to damp (cool) phonons within a linear waveguide and without the external optical and acoustic cavities typically employed within cavity-optomechanical systems. We explore these physics in Section 5.9.

5.5.2 Experimental Demonstration of Inter-modal SBS

Next, we quantify SIMS gain and amplification within the silicon optomechanical waveguide. All experiments are performed using the setup diagrammed in Fig. 5.6a. Pump, signal, and reference local oscillator waves are synthesized from the same continuous-wave laser by splitting it into three paths: The top path is used to create a strong pump by amplifying laser light at frequency ω_p through an erbium-doped fiber amplifier. This light is then coupled on-chip and into the symmetric waveguide mode through use of an integrated grating coupler and a mode multiplexer. A weak probe wave at frequency $\omega_p - \Omega$ is synthesized in the middle path using a null-biased intensity modulator driven by a microwave frequency synthesizer which scatters light to symmetric sidebands at $\omega_p \pm \Omega$, and a notch filter to filter out the unwanted sideband. This light is then coupled into the anti-symmetric waveguide mode of the Brillouin-active waveguide. After passing through the active device region, this probe wave is coupled off chip and combined with a frequency-shifted local oscillator at frequency $\omega_p + \Delta_{\text{AOM}}$ which is produced in the bottom path by passing laser light through an acousto-optic modulator. These two tones are then incident on a fast photodetector where their beat note produces a microwave signal at $\Omega + \Delta_{\text{AOM}}$ with a power proportional to the transmitted probe power.

To observe the frequency-dependent Brillouin coupling of the suspended optomechanical waveguide, the transmitted probe power is measured as a function of the pump-probe detuning Ω ; when Ω is equal to the frequency of a Brillouin-active phonon, optical Brillouin gain is observed. The experimentally-measured Brillouin gain spectrum for a pump power of 70 mW is plotted for pump-probe detunings from 0.5-9.5 GHz in Fig. 5.6b. In this spectrum, several Brillouin-active phonon modes (labeled B1-B9) are visible, including dominant resonances B1, B3, and B6. The frequencies of these phonon modes show good agreement with those predicted from multi-physics finite element simulations (plotted as violet circles along the abscissa).

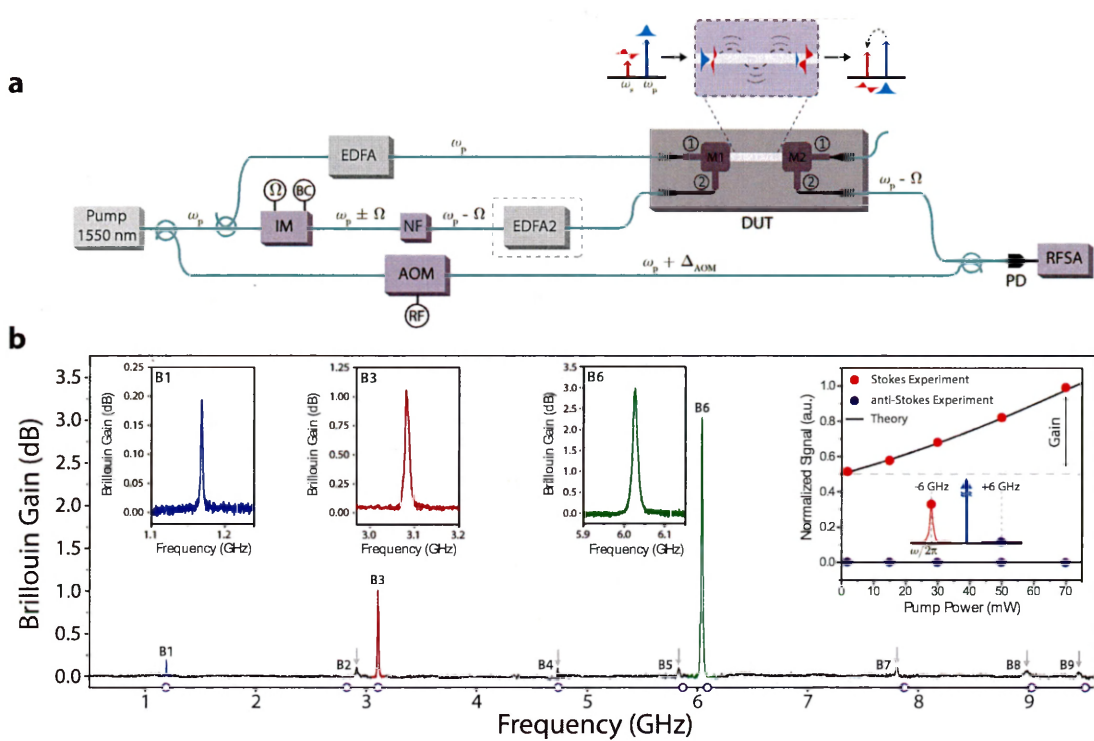


Figure 5.6: **Experimental observation of stimulated inter-modal Brillouin scattering.** (a) Diagram of the experimental apparatus used to study SIMS gain and energy transfer. A pump laser around 1550 nm with frequency ω_p is split into three paths—two are used to synthesize optical pump and probe waves, while the third is used to synthesize a frequency-shifted reference field at $\omega_p + \Delta$ using an acousto-optic modulator. The pump wave (frequency ω_p) is amplified through an erbium-doped fiber amplifier (EDFA), and the probe wave $\omega_p - \Omega$ is optionally passed through a second EDFA (labeled EDFA2) to boost the intensity of the probe wave for the energy transfer experiment. After passing through the active device, the probe wave is coupled off-chip and combined with the reference field for heterodyne detection. (b) Plots a SIMS gain spectrum for pump-probe difference frequencies Ω between 500 MHz and 9.5 GHz, showing several resonant gain features corresponding to Brillouin-active elastic modes. The three highlighted dominant modes, labeled B1, B3, and B6, have gain spectra plotted in more detail in corresponding insets. The simulated frequencies of the Brillouin-active modes are plotted as violet circles along the abscissa. The rightmost inset shows the peak single-sideband SIMS gain (red) for mode B6 as a function of increasing pump power, with no observed anti-Stokes component (purple). The gain spectrum is included diagrammatically between the data curves. Adapted from Ref. [221].

5.5.3 Single-sideband Brillouin Gain

As discussed earlier, in contrast to FSBS, which produces multi-field couplings, SIMS dynamics lead to single-sideband couplings as a result of phase-matched symmetry-breaking between Stokes and anti-Stokes processes. To experimentally study this behavior, we focus on the Brillouin resonance B6 at a frequency of 6.03 GHz, which is engineered to have the strongest Brillouin coupling; this mode is studied from a design perspective in Fig. 5.3.

To study single-sideband gain, we fix the pump-probe frequency detuning to $\Omega = 2\pi \times 6.03$ GHz and observe the output optical spectrum as the pump power is increased. As plotted in the rightmost inset of 5.6b, as the pump power increases to a maximum of 70 mW, 3 dB of optical gain for the signal tone is observed (red dots) through a stimulated Stokes scattering process. In contrast to FSBS, no light is scattered to the anti-Stokes order (purple dots) as pump power is increased. This result verifies the expected symmetry-breaking from the inter-modal phase matching requirements (Fig. 5.5d-e).

5.5.4 Single-sideband Amplification

We next quantify the strength of this single-sideband SIMS gain and show that it is sufficient to permit optical amplification. Within the silicon waveguide, net amplification requires that the Brillouin gain be greater than the probe-wave linear and nonlinear losses, which were previously characterized in Section 5.4. To quantify the strength of the Brillouin gain, we use the experiment diagrammed in Fig. 5.6a to tune the pump-probe detuning through $\Omega = 2\pi \times 6.03$ GHz, the Brillouin frequency of mode B6, at different pump powers. Three gain spectra for on-chip pump-wave powers of 13, 43, and 88 mW are depicted in Fig. 5.7b.i-iii, showing both the intrinsic narrow linewidth (13 MHz) for the high quality-factor ($Q = \Omega_B/\Delta\Omega = 460$) phonon mode, and a maximum of 3.5 dB of optical gain at the highest tested pump power. The peak gain as a function of pump power is plotted in Fig. 5.7b, along with optical losses. A red theory curve is plotted atop the measured data and is fit to a model capturing the linear and nonlinear optical properties of the membrane waveguide to determine a Brillouin gain coefficient of $G_B = 470 \pm 30 \text{ W}^{-1}\text{m}^{-1}$. Both the measured gain as well as the Brillouin frequency agree well with values from finite element simulations,

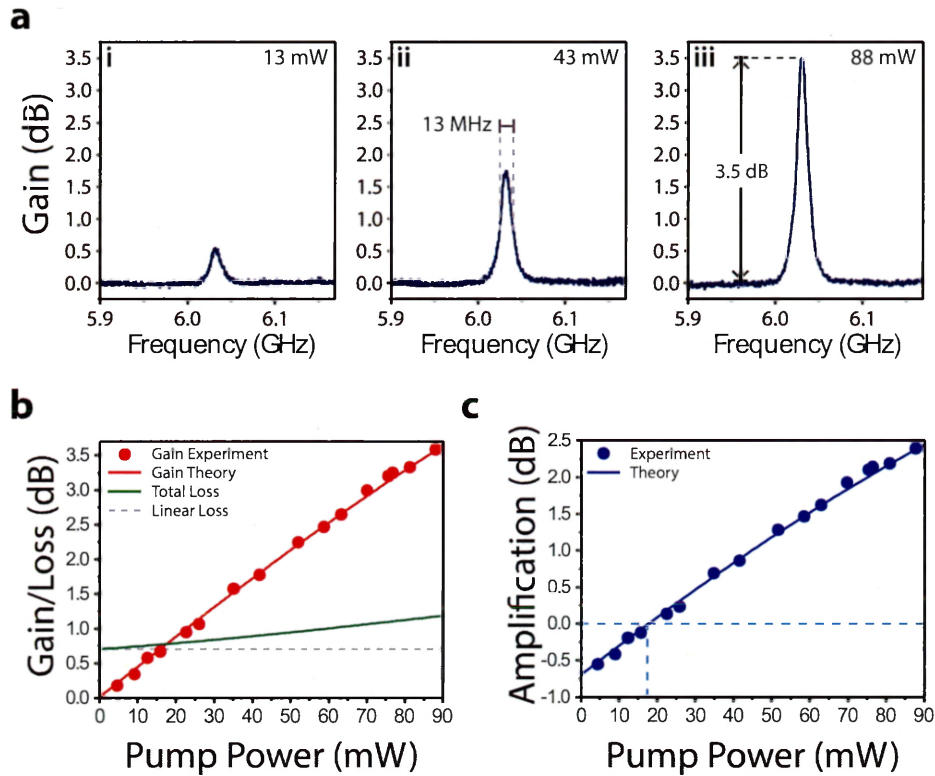


Figure 5.7: **Inter-modal Brillouin amplification.** (a) Inter-modal Brillouin gain spectra for mode B6 around 6 GHz, plotted for three different pump powers, showing a narrowband (13 MHz) Brillouin resonance and 3.5 dB of optical gain at the highest tested pump power. (b) plots peak gain (red) and linear (gray) and total optical losses (green) as a function of pump power for this Brillouin-active phonon, while (c) plots the calculated on-chip amplification, obtained by subtracting total loss from Brillouin gain. The pump power threshold for net amplification is 18 mW. Adapted from Ref. [221].

which give a Brillouin gain $G_B = 430 \pm 70 \text{ W}^{-1}\text{m}^{-1}$ and frequency $\Omega_B = 2\pi \times 6.07 \text{ GHz}$ for this device with width $w = 2.85 \text{ }\mu\text{m}$.

From Fig. 5.7b, it is apparent that total gain exceeds loss for on-chip powers greater than $\sim 18 \text{ mW}$. The total net amplification, calculated by subtracting linear and nonlinear losses from the Brillouin gain, is plotted as a function of pump power in Fig. 5.7c, reaching a maximum value of 2.3 dB at the highest tested pump powers. Through these experiments, the total on-chip power was limited only by the pump power supplied by the EDFA; therefore additional amplification should be possible at higher pump powers.

5.5.5 Pump-probe Gain and Loss Schemes

Thus far, we have focused on inter-modal Stokes amplification where pump light is in the symmetric optical mode and red-shifted probe light is in the anti-symmetric optical mode. It is also possible to inject pump light into the anti-symmetric mode to amplify probe light in the symmetric mode. Furthermore, when the probe is blue-detuned from the pump by the Brillouin frequency, it experiences Brillouin attenuation through optical energy transfer into the pump wave. All of these processes are forms of stimulated inter-modal Stokes scattering, which transfers energy to red-shifted frequencies. Experimental data for four different pump-probe configurations are plotted in Fig. 5.8a. These data were obtained using a Brillouin-active waveguide of width $w = 2.77 \text{ }\mu\text{m}$, having a Brillouin frequency $\Omega_B/2\pi = 6.16 \text{ GHz}$ and gain $G_B = 404 \pm 20 \text{ W}^{-1}\text{m}^{-1}$. This specific experiment utilized the asymmetric Y-junction mode converter design that allows near-unity coupling into each optical mode [277]. Net amplification is achieved for probe light in both modes around pump powers of 20 mW. Furthermore, 3 dB of Brillouin loss is also possible for probe waves in either mode. Because this probe wave experiences attenuation only when it is co-propagating with the optical pump, this can be seen as a form of nonreciprocal transmission (optical isolation), though the nonreciprocal effect bandwidth in this scheme is limited to the linewidth of the phononic response [188].

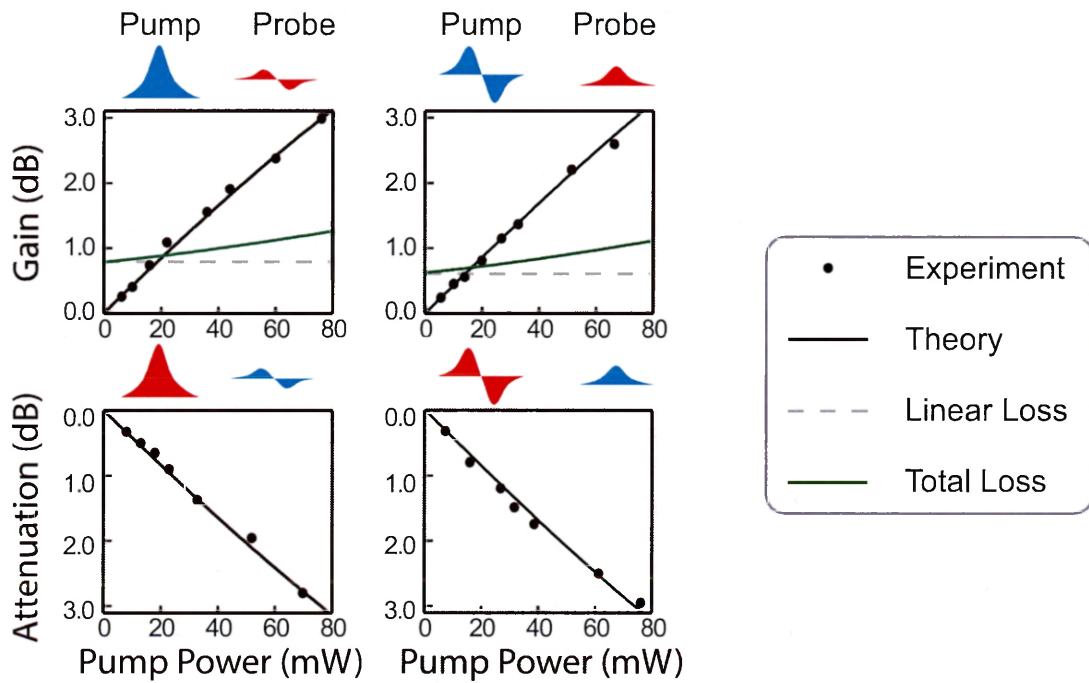


Figure 5.8: **Inter-modal gain and loss configurations.** Four panels show experimental results of inter-modal gain or attenuation for a probe signal in four-different pump-probe configurations. The top two panels show Brillouin gain of a red-shifted probe in anti-symmetric and symmetric modes, respectively, while the bottom two panels show loss in a probe which is blue-detuned from the pump by the Brillouin frequency. Adapted from Ref. [221].

5.6 Single-sideband Energy Transfer

We have shown that, through the use of a multimode optomechanical waveguide, strong inter-modal Brillouin scattering can be used to create single-sideband amplification in silicon. In addition to producing single-sideband gain, a key element of the dynamics of SIMS is the ability to support significant energy transfer between two optical fields—In fact, in the limit of large couplings over long length scales, near-unity power transfer from pump to signal waves is supported through SIMS coupling. These dynamics have previously been studied in highly-nonlinear fiber optics [187,188], but not in integrated waveguide systems, despite their potential to produce strong mode conversion, optical switching, and broadband optical nonreciprocity [258,280]. These dynamics also contrast sharply with the behavior of intra-modal FSBS, which, in the limit of strong energy transfer, instead produces cascaded comb-line generation, as studied in Chapter 3.7.1 and Ref. [186].

The dynamics of this process are governed by the coupled amplitude equations [233,250]:

$$\frac{\partial P_p}{\partial z} = -(\alpha_p + \beta_{pp}P_p + \gamma_{ppp}P_p^2)P_p - (G + 2\beta_{ps} + 4\gamma_{pps}P_p + \gamma_{pss}P_s)P_sP_p, \quad (5.5)$$

$$\frac{\partial P_s}{\partial z} = -(\alpha_s + \beta_{ss}P_s + \gamma_{sss}P_s^2)P_s - (-G + 2\beta_{sp} + 4\gamma_{ssp}P_s + \gamma_{spp}P_p)P_pP_s. \quad (5.6)$$

Here P_p and P_s are the powers in the pump and Stokes (red-detuned signal) fields, α_i is their corresponding linear loss coefficients, and β_{ij} and γ_{ijk} are the intra- and inter-modal nonlinear loss coefficients, where $i, j, k \in p, s$ are shorthand for the fields participating in the corresponding absorption process. Note that enhanced nonlinear losses are experienced in the presence of multiple strong optical fields—these combinatorial factors can be thought of as resulting from the interference of the pump and probe waves.

To quantify the strength of SIMS energy transfer within the silicon membrane waveguide, we use a second EDFA (labeled EDFA2 in Fig. 5.6a) to boost the total power of the probe wave (frequency $\omega_p - \Omega$) so that its on-chip power is equal to that of the pump wave. Here the pump-probe detuning Ω is fixed to the Brillouin resonance frequency so that strong inter-modal Brillouin coupling occurs. As pump and probe waves propagate through the waveguide, energy is transferred from pump to probe with a fractional efficiency which

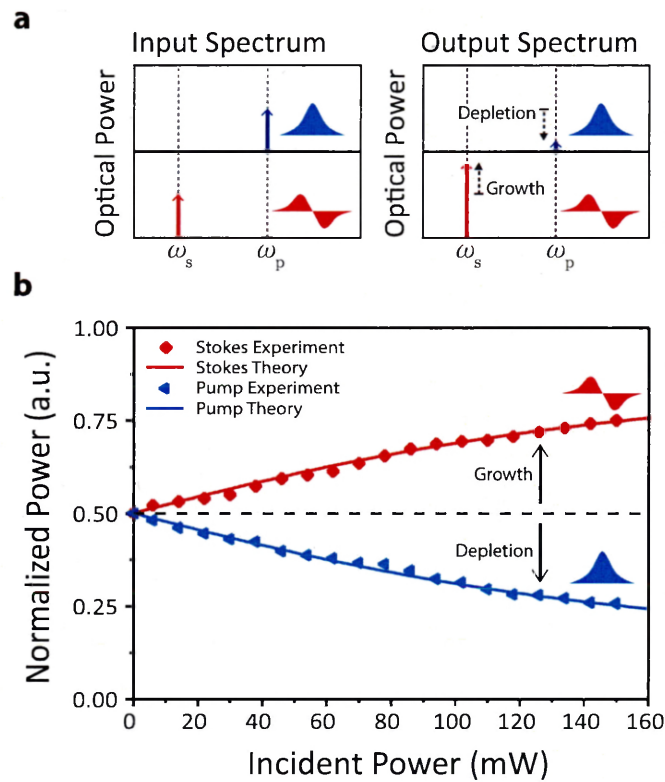


Figure 5.9: **SIMS energy transfer.** (a) plots representations of input and output spectra demonstrating inter-modal energy transfer, showing pump-wave depletion and Stokes-wave growth at the device output relative to their input amplitudes. (b) plots experimentally-measured normalized pump and Stokes output powers as a function of total power incident to a SIMS-active device. Adapted from Ref. [221].

increases with the total combined power. As in the gain experiment, these waves are demultiplexed at the output of the device and the power of each is measured at the output ports. For these experiments, we use a device with width $w = 2.77 \mu\text{m}$ and Brillouin gain $G_B = 420 \pm 20 \text{ W}^{-1}\text{m}^{-1}$.

The net energy transfer is plotted as a function of total incident power in Fig. 5.9b, showing a maximum of 50% fractional energy transfer at the highest combined input power of 150 mW. These results demonstrate significant power conversion—many 10s of mW—from the fundamental to higher-order waveguide mode, demonstrating the potential for efficient SIMS mode conversion in silicon waveguides. The total power handling of 150 mW in the unclad silicon waveguide was limited due to the ~ 100 mW power handling of the input mode multiplexer. However, designs with higher power tolerances should be possible. Importantly, the limiting factor is not the multimode silicon waveguide itself, indicating that further energy transfer is possible even with the same waveguide design; for comparison, longer propagation lengths (~ 7 cm) with similar gain and loss coefficients to this integrated silicon waveguide could theoretically permit $>90\%$ energy transfer efficiency.

These results, showing strong energy transfer over short propagation lengths, compare well with energy transfer experiments in fiber optic waveguides, and may form a basis for new nonlinear and nonreciprocal processes. Ref [187] demonstrated 97% energy transfer using 300 mW total powers in a 15 meter long highly-nonlinear photonic crystal fiber with a Brillouin gain coefficient $G_B \approx 1 \text{ W}^{-1}\text{m}^{-1}$. With further work, similar efficiencies should be possible in integrated waveguides [280, 281].

5.6.1 SIMS vs. FSBS Cascading and Phonon Dynamics

Single-sideband energy transfer through inter-modal forward scattering exhibits very different dynamics from the intra-modal FSBS studied in Section 3.7.1. While SIMS couples only two optical fields, the latter permits stimulated energy transfer to multiple successive orders, limiting the strength of power conversion from pump to signal waves to around 50%. These results are contrasted in Fig. 5.10a-d, which plot energy transfer stem plots for SIMS (a) and FSBS (b) at roughly equal gain-power-length ($G_B PL$) products. Because the phonon that mediates SIMS phase matches unidirectionally from one optical mode to

another, cascading is forbidden—in principle this removes the $\sim 50\%$ limit on Stokes energy transfer set by FSBS cascading (see Section 3.7.1). On-chip inter-modal scattering also provides a powerful means to control the dynamics of traditional nonlinear couplings such as four-wave mixing [282].

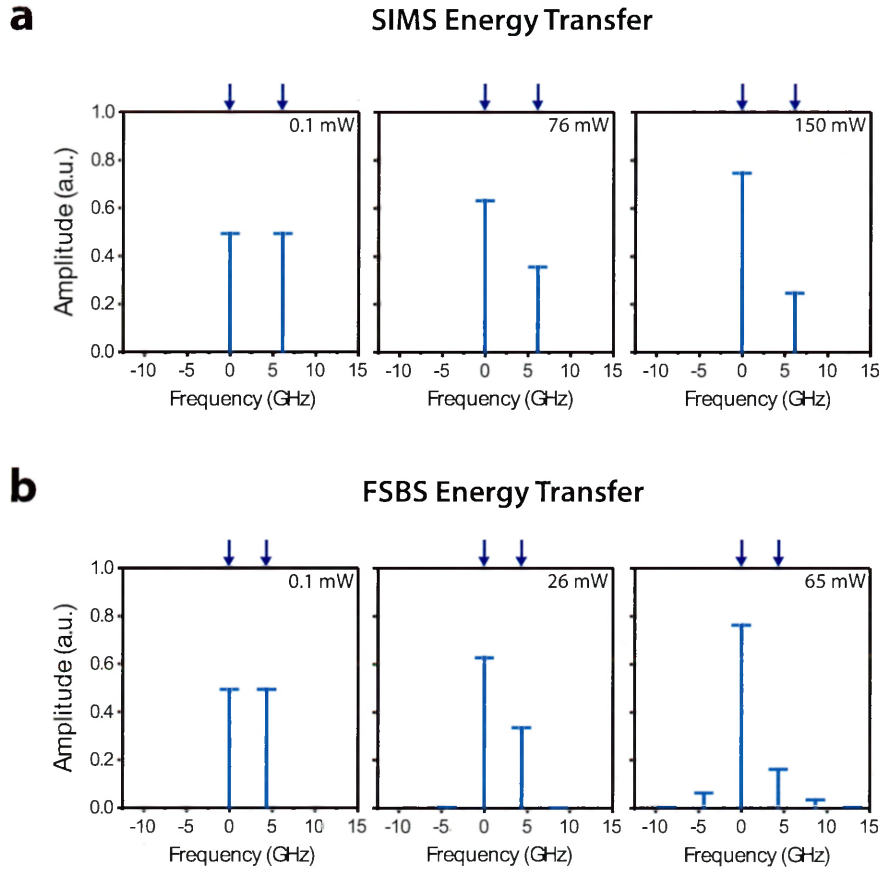


Figure 5.10: **Comparison of SIMS and FSBS energy transfer dynamics.** Stem plots showing normalized output power spectra under two-tone driving for a FSBS-active waveguide (a) and a SIMS-active waveguide (b). For both experiments, the total incident power is equally divided by two incident waves separated by the Brillouin frequency of the device (denoted by dark blue arrows). While SIMS produces energy transfer only between fields at the incident optical frequencies, FSBS leads to cascaded energy transfer to additional frequency lines. Adapted from Ref. [221].

It is worth pointing out one final difference between FSBS and SIMS dynamics which is important for certain applications. Specifically, while FSBS drives a phonon field whose amplitude is uniform in space (at least in the absence of optical loss), SIMS does not. This can be understood from the power transfer dynamics of these processes: for FSBS, the rates

of anti-Stokes (phonon annihilation) and Stokes (phonon generation) processes are balanced [233], so the phonon amplitude will not vary in space under almost all circumstances. In the limit of large spatial phonon dissipation, the total phonon field amplitude in a FSBS-active waveguide can be expressed as a coherent sum of the optical field amplitudes:

$$b = \sum_n a_n^* a_{n+1} \quad (5.7)$$

where n indexes over the participating optical lines which differ in frequency from their neighbors by the Brillouin frequency, and a_n is the amplitude of the n^{th} comb line. This constant phonon field (and hence constant photoelastic modulation amplitude) leads to the phase-modulation-like response of cascaded FSBS, and also makes FSBS an ideal candidate for applications where long-range driven phonon fields are useful—one such example is studied in Chapter 4 and in Refs. [165, 220].

By contrast, SIMS produces stimulated phonon emission, which strongly modifies the spatial dynamics of the phonon field. In the case where SIMS energy transfer is very strong over length scales smaller than the phonon decay length, stimulated phonon emission leads to Rabi flopping between the photon and phonon fields [283]—in this situation, the phonon field, whose intensity rapidly increases in time, enhances the pump-Stokes scattering rate until complete energy transfer is achieved. Thereafter, the back-action of this phonon field, which has not yet decayed, leads to anti-Stokes scattering (and phonon annihilation) until energy is transferred back to the pump field. These dynamics require extremely strong light-sound coupling, and is yet to be experimentally observed in linear Brillouin-active waveguides.

Under more typical circumstances, where the spatial phonon decay rate is larger than the Brillouin coupling length, the phonon field intensity follows the pump-Stokes beat note:

$$b = a_s^* a_p \quad (5.8)$$

where a_s and a_p are the amplitudes of the Stokes and pump waves.

This results in a driven phonon intensity whose field is growing in space when the probe wave is smaller than the pump wave, and decreases at longer propagation lengths where the

strength of the probe wave overtakes that of the pump wave. These dynamics produce the self-limiting pump-Stokes energy transfer observed in Fig. 5.9 and Refs. [187,188]. However, this process also intrinsically localizes the phonon field driven by SIMS to the spatial domain where strong energy transfer occurs. This driven phonon localization poses a potential difficulty to high-efficiency optical isolator and circulator designs based on acousto-optic light scattering from phonons driven via SIMS [258].

5.7 Design Considerations and Tailorable SIMS Interactions

We have shown that the multimode optomechanical silicon waveguide permits single-sideband optical amplification and energy transfer through SIMS. In this section, we briefly discuss some of the design considerations behind the SIMS-active waveguide. We begin with a discussion of the elastic modes guided in the membrane structure and those which couple strongly through inter-modal SBS. We then comment briefly on the wavevector and frequency tunability of the SIMS process, and study a related topic, the robustness of the device’s Brillouin response to fabrication-induced dimensional variations.

5.7.1 Guided Elastic Waves in the Membrane Waveguide and Phonon Wavevector Tunability

Brillouin coupling is observed when an elastic mode couples to the optical force distribution generated by the optical modes, and phase-matching is satisfied. The latter requires that the phonon wavevector $q_m(\Omega)$ of the m^{th} Brillouin-active elastic mode matches the optical wavevector mismatch, $\Delta k(\Omega) = k_1(\omega_p) - k_2(\omega_p - \Omega)$, where k_1 and k_2 are the optical dispersion relations for the pump and signal waves, respectively. In the case of inter-modal interactions, this optical wavevector mismatch is practically independent of Ω , since the wavevector mismatch between distinct transverse optical modes varies very little over \sim GHz frequency ranges. At the same time, since ω_p can vary within the transparency window of silicon (or at least over the range where low-loss multimode waveguiding is supported), by changing the optical pump wavelength strong tunability of the acoustic wavevector is supported:

$$q = \Delta k \approx k_1(\omega_p) - k_2(\omega_p). \quad (5.9)$$

As a result, SIMS is potentially useful for wavevector-tunable phonon generation—we harness this capability to produce wavelength-tunable optical nonreciprocity in Section 6.

The corresponding phonon frequencies which satisfy the phase-matching condition for optical wavelengths around 1550 nm in the SIMS-active membrane waveguide are identified by the purple circles in in Fig. 5.11a; these points correspond to the intersection between the simulated phonon dispersion curves and the nearly-vertical gray line indicating computed $\Delta k(\Omega) \sim 4.5 \cdot 10^5 \text{ m}^{-1}$. The primary displacement profiles of the three dominant modes B1, B3, and B6 are plotted alongside their highlighted dispersion curves. Note that while B3 and B6 couple through transverse motion, B1 experiences its primary displacement in the longitudinal (z) direction—this represents a rare example of efficient Brillouin coupling in silicon through the p_{12} photoelastic tensor component. In material systems where $p_{12} > p_{11}$ (the latter of which is dominant in silicon), this low-frequency mode may support very strong inter-modal Brillouin couplings.

In addition to the Brillouin-active modes which are experimentally observed, the silicon membrane supports guidance of many elastic waves which do not couple appreciably through SIMS. The complete simulated dispersion relations for this structure are plotted in Fig. 5.11b for frequencies $\Omega/2\pi < 10 \text{ GHz}$ and acoustic wavevector $q < 10^6 \text{ m}^{-1}$. These elastic modes may be classified according to their primary displacement profiles. The first type experiences compression and rarefaction in the transverse x -direction (red lines in Fig. 5.11b). The 3- and 6-GHz phonon modes which experience the strongest inter-modal Brillouin coupling in the silicon waveguide belong to this family. Another example mode at around 4.3 GHz is plotted in Fig. 5.11b.i.

The second family of modes are asymmetric Lamb wave-like modes with sinusoidal displacement in the x - and y -directions (green lines). These elastic waves are similar to the transverse waves excited in a string or thin membrane. While several modes which belong to this family experience Brillouin coupling, this is typically a result of these modes being partially hybridized with the x -type modes due to the ridge structure. An example

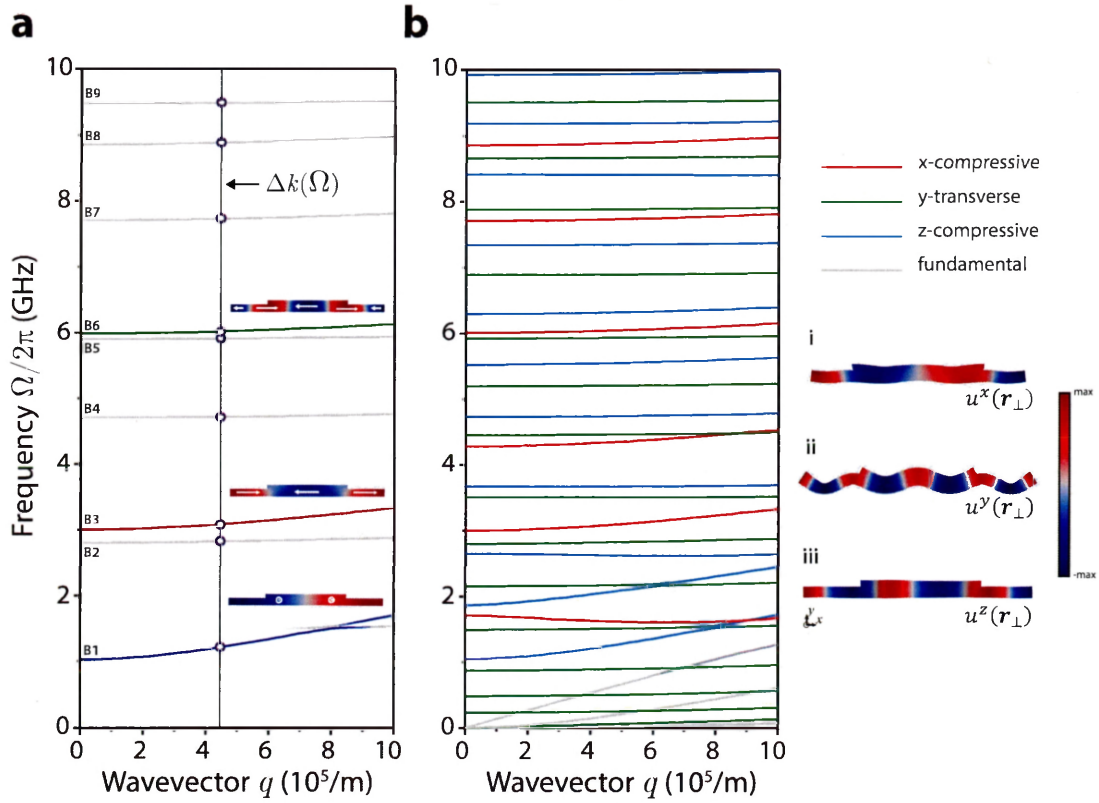


Figure 5.11: **Elastic modes of the SIMS-active silicon membrane waveguide.** (a) Simulated dispersion curves for the observed Brillouin-active elastic modes, with the dominant modes B1, B3, and B6 highlighted and with their displacement profiles plotted alongside. The vertical line labeled $\Delta k(\Omega)$ corresponds to the phonon wavevector determined through optical phase matching for the Brillouin process. (b) Dispersion relations for all elastic modes over this frequency/wavevector window. These modes are categorized according to their dominant displacement profiles. Examples showing three different categories of motion are plotted in subpanels (i)-(iii). Adapted from Ref. [221].

mode around 3.5 GHz is plotted in Fig. 5.11b.ii. The third family of elastic modes are the longitudinal (z -) compressive modes (blue lines), such as the mode B1 at around 1 GHz. Another example mode around 4.7 GHz is plotted in Fig. 5.11b.iii. Finally, three fundamental modes with linear dispersion (grey lines) correspond to motion in the two transverse and single longitudinal directions. The mode profiles and their dispersion curves are computed from elastic wave simulations using the commercially-available finite element method software COMSOL.

5.7.2 Dimensional Tunability of Brillouin Frequency

As has previously been studied in FSBS-active waveguides [196], the frequencies of the cutoff elastic modes which mediate forward Brillouin scattering interactions depend strongly on transverse device geometry. This contrasts with prior demonstrations of BSBS, where the Brillouin frequency is basically a wavelength-dependent material parameter which is influenced only weakly by geometry and mode order. Because SIMS utilizes the same types of cutoff modes as FSBS, in principle its interaction frequency should also be tailorable simply by changing device geometry.

To investigate the lithographic tunability of the SIMS frequency, we fabricated Brillouin-active waveguides of various widths and measured the frequencies of the two strongest Brillouin resonances (B3 and B6 in the notation used here) through direct Brillouin gain measurements. The resulting Brillouin frequencies are plotted as the green circles in Fig. 5.12. By varying the total membrane width from $w = 2.33 \mu\text{m}$ to $w = 2.85 \mu\text{m}$, the Brillouin frequency of the highest-gain mode is decreased from 7.06 GHz to 6.03 GHz. These measurements are corroborated with a numerical trend (black) calculated from finite-element simulations for these structures. The ability to control the SIMS frequency by changing device dimension allows tailoring of the Brillouin frequency shift for applications where a specific or lithographically-tunable operation frequency is desirable.

5.7.3 Sensitivity of SIMS to Dimensional Broadening

As discussed in Section 5.7.1, the wavevector of the phonons which mediate SIMS coupling is set directly through optical dispersion—in other words through optical wavelength and the

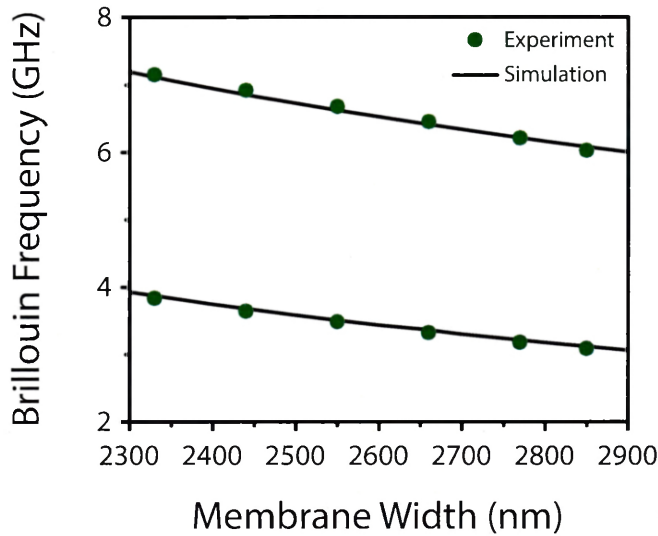


Figure 5.12: **Lithographic tunability of the SIMS frequency.** Measured (green) and simulated (black line) Brillouin frequencies for the two elastic modes with the largest Brillouin gain as device width is varied. Adapted from Ref. [221].

optical waveguide dimensions. Since, in contrast to FSBS, these modes have an appreciable wavevector, their dispersion bands are not flat, and their frequencies depend on the phase-matched wavevector. This leads to an additional mechanism for dimensional broadening (Section 3.8.4) beyond direct modification to the phonon frequency through mechanical design (Sections 3.8.4,5.7.2); now, due to changes in the optical ridge waveguide width, the Brillouin-active phonon may have a completely different wavevector and frequency at different positions along the waveguide length. This effect may lead to degradation of the effective phonon linewidth (and hence Brillouin gain) at long device lengths. Fortunately, the studied devices have quality factors in the range $Q \sim 400$ -500, which compare reasonably well with existing FSBS-active devices, indicating that this effect is not particularly strong in the studied devices.

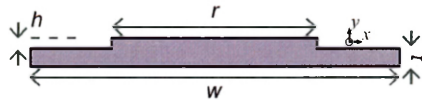


Figure 5.13: **Dimension-induced broadening for SIMS.** Diagram of the different device dimensions which may vary due to fabrication variations. The effect of each on the Brillouin frequency shift is tabulated in Table 5.1. Adapted from Ref. [221].

Table 5.1: Simulated Changes in Brillouin Frequency Due to Dimensional Variations for the SIMS-active Waveguide

Dimension	Description	Sensitivity to Dimension Error
w	Total membrane width	1.7×10^6 Hz/nm
t	Membrane Thickness	1.7×10^6 Hz/nm
r	Ridge waveguide width	9.2×10^5 Hz/nm
h	Ridge waveguide height	1.4×10^6 Hz/nm
	Ridge offset from center	$< 10^5$ Hz/nm

To characterize the sensitivity of the SIMS lineshape and compare to that of FSBS-active devices, we perform multi-physics simulations which take into account both sources of broadening. The results of these simulations, which tabulate the change in Brillouin resonance frequency with small changes from the desired design in various device dimensions (Fig. 5.13) are presented in Table 5.1. Due to the additional dispersive broadening mechanism, the Brillouin frequency is more sensitive to fabrication imperfections for SIMS than for FSBS. In particular, the Brillouin response is much more sensitive to changes in membrane thickness and etch depth, which may vary significantly along the device length.

5.8 Inter-modal Silicon Brillouin Laser

Stimulated inter-modal Brillouin amplification represents a significant step towards the creation of silicon-based Brillouin lasers, since its intrinsic dispersive symmetry breaking restores the single-sideband gain and stimulated phonon amplification necessary for Brillouin laser oscillation. This contrasts with intra-modal forward SBS, which requires some external mechanism (e.g. a nontrivial optical cavity design) to break the symmetry between Stokes and anti-Stokes processes [219, 233].

In this section, we briefly describe the creation of the first Brillouin laser in silicon through SIMS [222]. Laser oscillation is achieved within a multimode racetrack resonator where the two straight regions are SIMS-active waveguides identical in design to the multimode optomechanical waveguide studied earlier in this chapter. Interestingly, we find that due to the long temporal lifetimes of the phononic modes relative to the optical cavity modes, this Brillouin laser enters a regime of phonon linewidth narrowing, similar to

cavity-optomechanical oscillators (phonon lasers) [284–288]. Finally, we discuss some potential advantages of this multimode Brillouin laser design as compared to conventional lasers based on BSBS.

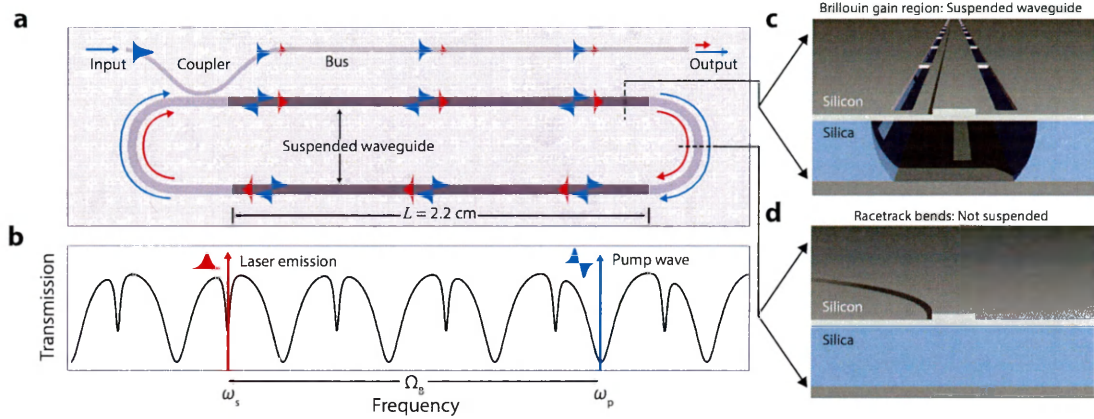


Figure 5.14: **SIMS silicon laser design.** (a) Depicts a top-down view of the laser design (not-to-scale). A racetrack resonator is composed of two cm-scale suspended Brillouin-active segments. The laser cavity is accessed via a mode-selective coupler which couples a bus waveguide strongly to the anti-symmetric spatial mode of the resonator and weakly to the symmetric mode. This results in the characteristic transmission spectrum of the multimode optical cavity plotted in (b), where the narrow features result from the symmetric mode and the broad features result from the strongly-coupled anti-symmetric mode. Note that the free spectral ranges of the two modes are not identical, making it relatively simple to find a wavelength where the pump-Stokes cavity mode separation is equal to the Brillouin frequency, a necessary condition for strong resonant enhancement. (c) and (d) plot diagrams of the device in the suspended gain region (c) and around the racetrack resonator bends (d), where no acoustic guidance is supported. Adapted from Ref. [222].

5.8.1 Silicon Brillouin Laser Design

The cavity modes are accessed via a spatial coupler similar in design to the mode multiplexers of Section 5.2; this coupler couples light between a bus waveguide and the symmetric and anti-symmetric spatial modes of the cavity—strongly to the anti-symmetric mode, but only weakly to the symmetric mode. This coupling results in the characteristic transmission spectrum illustrated in Ref. 5.14, where two distinct sets of cavity modes with different free spectral ranges (FSRs) are visible. The first set, due to the weakly-coupled symmetric mode, has a loaded quality factor $Q \approx 2.4 \times 10^6$ and FSR ≈ 1.614 GHz, while the second, due to the strongly-coupled anti-symmetric mode, has a lower quality factor $Q \approx 4 \times 10^5$

and a smaller FSR ≈ 1.570 GHz.

For Brillouin lasing to occur, cavity modes must be available at the pump and laser frequencies, ω_p and ω_s , respectively, which are separated by the Brillouin resonance frequency $\Omega_B = \omega_p - \omega_s$. Here, pump light is injected into the anti-symmetric cavity mode to produce Brillouin gain necessary for laser oscillation in the lower-loss symmetric cavity mode. Due to the different FSRs of the two sets of cavity modes, this condition is satisfied for a variety of pump wavelengths, with symmetric/anti-symmetric mode pairs which satisfy the frequency-matching condition spaced approximately every 0.4 nm across the C band. In this way, the inter-modal Brillouin laser design relaxes the constraint that the FSR must be an integer divisor of the Brillouin frequency, as is required for integrated lasers based on BSBS.

5.8.2 Observation of Laser Oscillation

To investigate the Brillouin lasing dynamics as a function of pump power, we use heterodyne spectral analysis with the experimental diagram in Fig. 5.15a. Pump light at frequency ω_p is amplified and split into two paths—one is coupled on-chip to pump Brillouin laser oscillation, while the other is frequency-shifted using an acousto-optic modulator to frequency $\omega_p + 2\pi \times 44$ MHz to serve as a local oscillator for heterodyne detection. The output light from the chip is combined with this reference field and is incident on a fast photoreceiver, where laser oscillation around frequency $\omega_s - \Omega_B$ is identified as a unique RF beat-note at a microwave frequency of $\Omega_B + 2\pi \times 44$ MHz.

Brillouin lasing occurs when the round-trip Brillouin gain exceeds the symmetric-mode optical loss within the racetrack resonator. From the characterization of SIMS amplification in these structures in Section 5.5.4, this threshold is expected to be around 18 mW. Experimentally, we find that when the intracavity pump power exceeds 19 mW (10.6 mW incident on-chip pump light), a significant increase in output power at the Stokes frequency is observed, representing the onset of Brillouin laser oscillation from thermal noise. As the pump power is increased beyond threshold, the output power at ω_s increases, corresponding to an external slope efficiency of 3%. This relatively low slope efficiency results from the weak output coupling for the symmetric mode. A detailed model of the laser system reveals

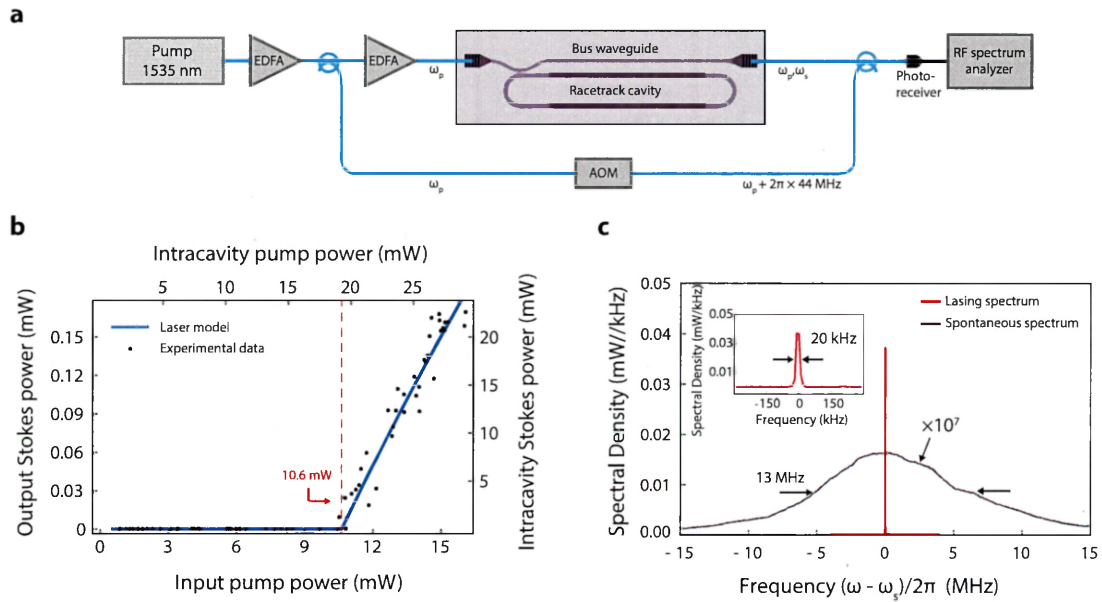


Figure 5.15: **Observation of Brillouin laser oscillation.** (a) depicts the experimental apparatus used to measure Brillouin lasing. A continuous-wave pump laser at frequency ω_p is split into two paths; the first is amplified and coupled on-chip, while the second is frequency-shifted using an acousto-optic modulator to $\omega_p + 2\pi \times 44$ MHz. The pump and Stokes signal (Brillouin laser) light at frequency ω_s are coupled off-chip and combined with the frequency-shifted reference tone which acts as a local oscillator for heterodyne detection. The combined waves are incident on a fast photo-receiver and the resulting spectrum analyzed using a RF spectrum analyzer. (b) plots theoretical and experimental output laser power vs. incident on-chip pump power, showing a clear threshold around 11 mW. Intracavity powers are determined by using the measured cavity spectra and measured input and output powers. (c) plots heterodyne spectra comparing the measured bandwidths of spontaneously-scattered Stokes light from a linear waveguide and the output beat-note between reference and silicon Brillouin laser light above threshold. Adapted from Ref. [222].

that the intracavity Stokes power in fact rapidly approaches the magnitude of the pump power, suggesting that the output efficiency may be improved through the use of couplers that more strongly address the symmetric mode, with relatively little increase to the lasing threshold.

5.8.3 Linewidth-narrowing Dynamics

We further explore the dynamics of this Brillouin laser through two separate heterodyne measurements which probe its linewidth-narrowing characteristics below and above threshold. These two experiments, diagrammed in Fig. 5.16a-b, use either a balanced (a) or sub-coherence delayed (b) heterodyne interferometer to study the laser coherence.

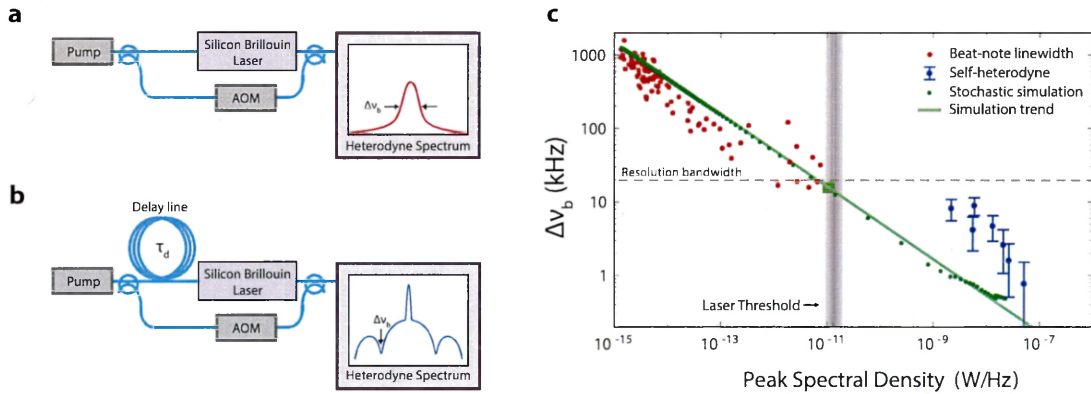


Figure 5.16: **Linewidth measurements of the silicon Brillouin laser.** (a) depicts a simplified version of the standard heterodyne spectroscopy apparatus used to measure the pump-Stokes excess phase noise—equivalent to the phonon linewidth $\delta\nu_b$ below the lasing threshold. In this situation, the phonon linewidth is given by the FWHM of the measured spectrum. (b) depicts a modified sub-coherence heterodyne measurement used to probe the phonon dynamics above threshold. In this experiment, an additional delay τ_d is added in one arm of the unbalanced interferometer, leading to the characteristic spectral shape shown in blue. Here the phonon linewidth is determined by measuring the contrast of interference fringes in the sub-coherence spectrum. (c) plots experimental measurements and theoretical calculations of the phonon linewidth as a function of peak spectral density. Below threshold, the standard heterodyne experiment is used (red dots), while above threshold the sub-coherence measurement technique is used (blue dots). The error bars on the blue dots represent 95% confidence intervals of fits to measured spectra. Adapted from Ref. [222].

Below threshold, the linewidth of the spontaneously-scattered Stokes spectrum is much greater than that of the pump laser, which has a linewidth of around 13 kHz. In this case,

the microwave spectrum from the balanced heterodyne measurement provides an excellent means of quantifying the Stokes linewidth, which is plotted as a function of power as the red circles in 5.16c. As the incident pump power approaches the laser threshold, the pump-Stokes beat-note narrows to a resolution-bandwidth limited value of 20 kHz, indicating significant spectral compression from its 13 MHz spontaneous bandwidth.

Above threshold, we use a sub-coherence length delayed interferometer design, which allows measurement of the Brillouin laser coherence with respect to the pump linewidth. Interestingly, we find that above threshold the Stokes output becomes coherent with the incident pump laser, with an excess phase noise $\delta\nu_b < 800$ Hz at the highest tested input powers. This phase noise corresponds directly through the phonon linewidth in this system since the phonon, which is heavily spatially damped, adiabatically follows the dynamics of the pump-Stokes beat note. These results differ from those found in typical glass-based Brillouin lasers, where the phonon linewidth narrows only to that of the pump laser field. In such systems, the phonon field is commonly understood to act as a “noise-eater” that facilitates optical linewidth narrowing of the Stokes output to far below that of the incident pump laser [289]. By contrast, these measurements demonstrate that the silicon Brillouin laser produces a form of phonon linewidth narrowing.

These dynamics are understood as resulting from the relative lifetimes of the photonic and phononic modes within the racetrack resonator. In traditional fiber optic [98] or glass-based [199, 200] Brillouin lasers, operation occurs in a dissipation hierarchy where the lifetime of the Stokes cavity mode γ is much longer than that of the phonon mode Γ . In this regime of Brillouin laser operation, the Stokes linewidth narrows dramatically below the pump linewidth, while the phonon linewidth narrows until it reaches that of the pump laser. By contrast, the silicon Brillouin laser operates in an inverted dissipation hierarchy, where $\Gamma < \gamma$. In this regime, the Stokes linewidth narrows until it nears that of the pump, whereas the phonon linewidth narrows below that of the pump laser. These dynamics are studied through a mean field model and numerical simulations plotted as the green dots in

Fig. 5.16c. Far above threshold, the excess phase noise is given to first order by [222, 290]

$$\delta\nu_b = \frac{\Gamma}{4\pi n_b^c} (n_b^{\text{th}} + n_s^{\text{th}} + 1). \quad (5.10)$$

where n_b^c is the coherently-driven phonon occupation number, n_b^{th} and n_s^{th} are the average thermal occupation numbers of the phonon and Stokes modes (at room temperature $n_b^{\text{th}} \approx 10^3$ and $n_s^{\text{th}} \approx 0$) and the +1 is due to vacuum fluctuations.

The observed phonon linewidth narrowing is reminiscent of that produced by self-oscillation in optomechanical resonators. However, in contrast to optomechanical oscillators, which generally possess both acoustic and optical cavities, the silicon Brillouin laser does not possess either an acoustic cavity or direct acoustic feedback around the ring, due to the short phonon decay length and phonon losses around the racetrack bends. Furthermore, this macroscopic system possesses strong spatial dynamics in which the optical and phonon intensities change considerably as they propagate around the resonator. As a result, this laser operates in a regime where the spatial phonon decay length ($\approx 60 \mu\text{m}$) is much smaller than the optical decay lengths ($\approx 10 \text{ cm}$), whereas the intrinsic phonon lifetime (77 ns) exceeds that of the optical fields (several ns). Therefore while the spatial dynamics are analogous to those exhibited by all prior Brillouin lasers (due to the disparate velocities of light and sound waves), this silicon laser accesses a distinct regime of temporal dynamics. These dynamics can be understood as a limiting case of singly-resonant optical parametric oscillator physics, with a slow but long-lived idler wave (for further discussion see the supplementary information to Ref. [222]). Interestingly, this analogy for parametric Brillouin interactions (though not the linewidth-narrowing dynamics) was understood in the 1960s [36, 291, 292]. It is also possible that other Brillouin lasers have operated in or near the inverted dissipation hierarchy [293–295], including the first fiber Brillouin ring laser [293]. The observation of these dynamics was possible due to the stability of the monolithic silicon Brillouin laser and the resolution of the heterodyne measurement technique and microwave spectral analysis.

5.8.4 Summary and Future Directions

The demonstration of Brillouin lasing in silicon represents a culmination of years of work towards creating strong SBS on-chip and in silicon. The silicon Brillouin laser represents only the second continuous-wave laser technology demonstrated in pure silicon—after the silicon Raman laser [236]—and with further work may prove useful for a variety of chip-based signal processing applications.

More generally, SIMS provides a flexible platform for integrated Brillouin lasers while providing many potential benefits over traditional BSBS lasers. Importantly, this laser based on forward-SIMS yields laser emission in the forward direction, eliminating the need for on-chip circulators as would be necessary for practical implementation of backward-SBS lasers in complex integrated photonic circuits. Furthermore, since pump and Stokes waves are guided in distinct optical modes, they can be simply de-multiplexed into different channels without the use of narrowband filtering.

The distinct FSRs of the two spatial optical modes ensure that there will always be a pair of cavity modes at some wavelength that satisfy the frequency-matching condition $\omega_s = \omega_p - \Omega_B$. This allows Brillouin racetrack cavities of arbitrary dimension, removing the size constraints on integrated Brillouin laser dimensions. This technology may enable Brillouin microcavity lasers with greatly reduced thresholds. Beyond relaxing these design constraints, the multimode cavity design also allows unprecedented control over the laser cascading dynamics. In typical BSBS lasers, evenly-spaced cavity modes permit cascaded lasing to many successive Stokes orders. This behavior is often undesirable since it produces additional bidirectional light emission, and limits the output power and linewidth narrowing of any one spectral order [290]. By contrast, the inter-modal laser design allows precise control over the degree to which cascading can or cannot occur. For example, by tailoring the relative Q -factors of the two cavity modes, it is possible to precisely engineer the threshold required for cascaded energy transfer. Alternatively, cascading can be completely suppressed by ensuring that no cavity mode is frequency-matched to this process, as has been done in the implementation presented here.

Due to the tailorability of SIMS, many parameters of the laser, such as the Brillouin

frequency shift, can likewise be tailored to the desired application. In its current form, this Brillouin laser may be used as a “passive” acousto-optic frequency shifter², or as a source for coherent phonon generation for sensing and signal processing applications. By increasing the acoustic dissipation rate (for example by adding more frequent tether structures) while reducing the optical losses (or through the use of a low loss delay line [296]), the standard dissipation hierarchy may also be within reach as a basis for narrow optical-linewidth waveguide-integrated silicon laser oscillators.

5.9 Spontaneous Brillouin Cooling through SIMS

Inter-modal Brillouin scattering breaks the symmetry between Stokes and anti-Stokes processes by requiring that they couple to distinct phonons. Because of this intrinsic symmetry breaking, inter-modal scattering is amenable to new forms of thermodynamic control of traveling elastic waves. In this section, we use the multimode Brillouin-active membrane waveguide to demonstrate a new form of non-resonant (cavity-less) optomechanical cooling within a continuous, linear system. Specifically, due to the strength of inter-modal Brillouin coupling, this process allows the cooling of a continuously-tunable band of phonon wavevectors through spontaneous Brillouin scattering.

Through experimental measurements, we use this interaction to produce 30 degrees of cooling relative to room temperature. These results contrast with prototypical cavity-optomechanical cooling, which utilizes resonator systems to couple and cool discrete photonic and phononic cavity modes [217, 297–301]. Within such systems, an optical cavity is used to favor the anti-Stokes process over the Stokes process, yielding a net damping of the mechanical motion within the phononic resonator. These techniques provide a potential path toward ground-state cooling of mechanical degrees of freedom for applications including precision measurement [299, 300], generation of non-classical mechanical states [302–304], studies of quantum decoherence of macroscopic objects [305], and quantum information processing and storage [306] (to name a few).

Beyond single-mode cavity optomechanical systems, there has been a growing interest

2. Meaning that it would not require an external microwave drive.

in extended optomechanical systems with many motional or optical degrees of freedom including multimode systems [307–310], optomechanical arrays [311–315], coupled resonator-waveguide systems [316–319], and optical cavity-less systems [320]. Such systems may offer new techniques for applications from on-chip quantum networking [309, 316–319] to intriguing reservoir engineering operations [315, 321, 322].

Because Brillouin interactions provide distributed optomechanical coupling, they represent a natural path to extend the regime of optomechanics to the continuum limit, where optical fields may be used to control mechanical motion within continuous, translationally-invariant systems [283, 323]. Such extended systems permit interactions between continua of optical and acoustic states [224, 324] with unprecedented bandwidth and tailorability, and may enable quantum optomechanical networks [317, 325, 326], and new forms of quantum nonlinear optics [327] and squeezing [309]. The potential of inter-modal Brillouin coupling to produce significant optomechanical cooling provides a first step toward quantum control within these systems [328].

5.9.1 Operation Scheme of Spontaneous Inter-modal Brillouin Scattering

Spontaneous inter-modal Brillouin scattering experiments are carried out in the same optomechanical waveguide system studied throughout this chapter. To perform spontaneous scattering measurements, pump light at frequency ω_p is injected into port 1 of the input mode multiplexer (labeled M1 in Fig. 5.17) and coupled into the symmetric optical mode. As this light traverses the Brillouin-active region, it interacts with thermal phonons through spontaneous inter-modal Brillouin scattering to produce red- (Stokes) and blue-shifted (anti-Stokes) sidebands in the anti-symmetric mode at frequencies $\omega_p \pm \Omega_b$, where Ω_b is the frequency of the Brillouin-active phonons with which the pump light interacts. These signals are demultiplexed through an output mode multiplexer (M2 in Fig. 5.17) and coupled off-chip.

Through inter-modal Brillouin scattering, Stokes and anti-Stokes processes are mediated by phonons traveling in opposite directions. As diagrammed in Fig. 5.17b, the Stokes process is mediated by a forward-moving phonon, whereas the anti-Stokes process is mediated by a backward-moving phonon. Note that the lifetime of each phonon mode can be

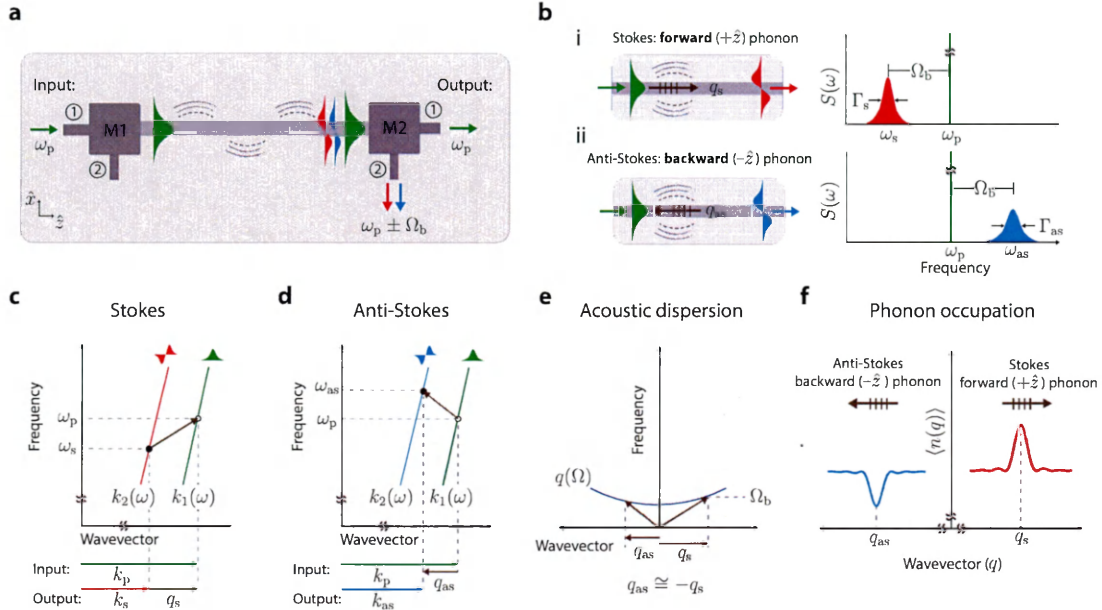


Figure 5.17: **Spontaneous inter-modal Brillouin scattering.** (a) Schematic depicting spontaneous Brillouin scattering on-chip. Pump light (green) at frequency ω_p is coupled through a mode multiplexer (M1) into the symmetric waveguide mode. Through interactions with thermal phonons (gray) as it propagates through the waveguide, light is scattered to anti-Stokes (blue) and Stokes (red) sidebands guided in the anti-symmetric mode at frequencies $\omega_p \pm \Omega_b$, where Ω_b is the Brillouin-active phonon frequency of the device. These waves are de-multiplexed into the two ports of an output mode multiplexer (M2). (b) (i) Through this process, the Stokes scattering process is mediated by a forward-moving phonon, resulting in light scattering to a red-detuned sideband at frequency $\omega_s = \omega_p - \Omega_b$. The lifetime of these phonons can be determined by measuring the spectral bandwidth of the scattered Stokes light. (ii) (b) The anti-Stokes scattering process is mediated by a backward-moving phonon, resulting in light scattering to a blue-detuned sideband at frequency $\omega_{as} = \omega_p + \Omega_b$. The lifetime of these backward-propagating phonons can be determined by measuring the spectral bandwidth of the scattered anti-Stokes light. (c) and (d) depict phase-matching and energy conservation requirements for Stokes and anti-Stokes scattering processes, which separately determine the wavevectors q_s and q_{as} of phonons that mediate Stokes and anti-Stokes processes. In these diagrams, these phonons produce scattering between initial (open circle) and final (closed circle) optical states through these processes. As plotted on the acoustic dispersion relation (e), these phonons are nearly equal in frequency, and have wavevectors that are nearly opposite in sign. (f) Because the anti-Stokes process annihilates thermal phonons, it increases the effective damping rate of the phonons with which the pump light interacts, resulting in a decrease in the phonon population $\langle n(q) \rangle$ (cooling) for a narrow wavevector band around q_{as} . By contrast, the Stokes process leads to phonon generation, resulting in effective heating of a narrow wavevector band around q_s . In this way, the incident laser field drives the thermal phonon bath out of equilibrium, producing a net phonon flux. Adapted from Ref. [223].

determined by measuring the spectral width of the corresponding scattered sideband, as plotted in the right side of Fig. 5.17b. These interactions with distinct phonons can be understood by the separate phase-matching and energy conservation conditions for Stokes and anti-Stokes processes, plotted in 5.17c-d. These conditions result in coupling to phonons whose frequencies are nearly identical, and whose wavevectors are nearly opposite in sign.

Each anti-Stokes scattering process annihilates a phonon, resulting in an effective increase to the damping rate for phonons around the anti-Stokes wavevector q_{as} . By contrast, the Stokes process leads to phonon generation, resulting an increase to the phonon population in a narrow wavevector band around q_{s} . The net change to the phonon occupation as a function of wavevector is illustrated in Fig. 5.17f, depicting modulation of the phonon wavevector with a sinc-squared-like response set by the optical phase-matching uncertainty bandwidth $2\pi/L$, where L is the device length.

5.9.2 Observation of Brillouin Cooling within a Linear Waveguide

When the rate of anti-Stokes scattering is high enough, it can significantly alter the phonon occupation from room temperature. This occurs since, through anti-Stokes scattering, thermal energy is transferred from a phonon to an anti-Stokes photon, which rapidly leaves the system before this phonon can be replenished from thermal noise. As a result, anti-Stokes scattering reduces both the average lifetime and occupation of this phonon field, which can be observed experimentally as both a reduction in the effective phonon lifetime (seen as broadening of the linewidth Γ_{as} of the spontaneously-scattered light spectrum) and a reduction in the total scattering efficiency e_{as} . By contrast, the same pump field which drives optomechanical cooling yields narrowing of the Stokes sideband linewidth Γ_{s} and an increase in the total Stokes scattering efficiency e_{s} . These two decoupled processes occur simultaneously through spontaneous Brillouin scattering; the forward-propagating phonons experience heating, and backward-propagating phonons are cooled within the linear membrane waveguide. As a result, the forward- and backward-propagating phonon fluxes are no longer equal, producing a net phonon flux (see Fig. 5.17f).

We explore these dynamics within the silicon membrane waveguide using the experimental apparatus diagrammed in Fig. 5.18a. Pump light at frequency ω_{p} (with a vacuum

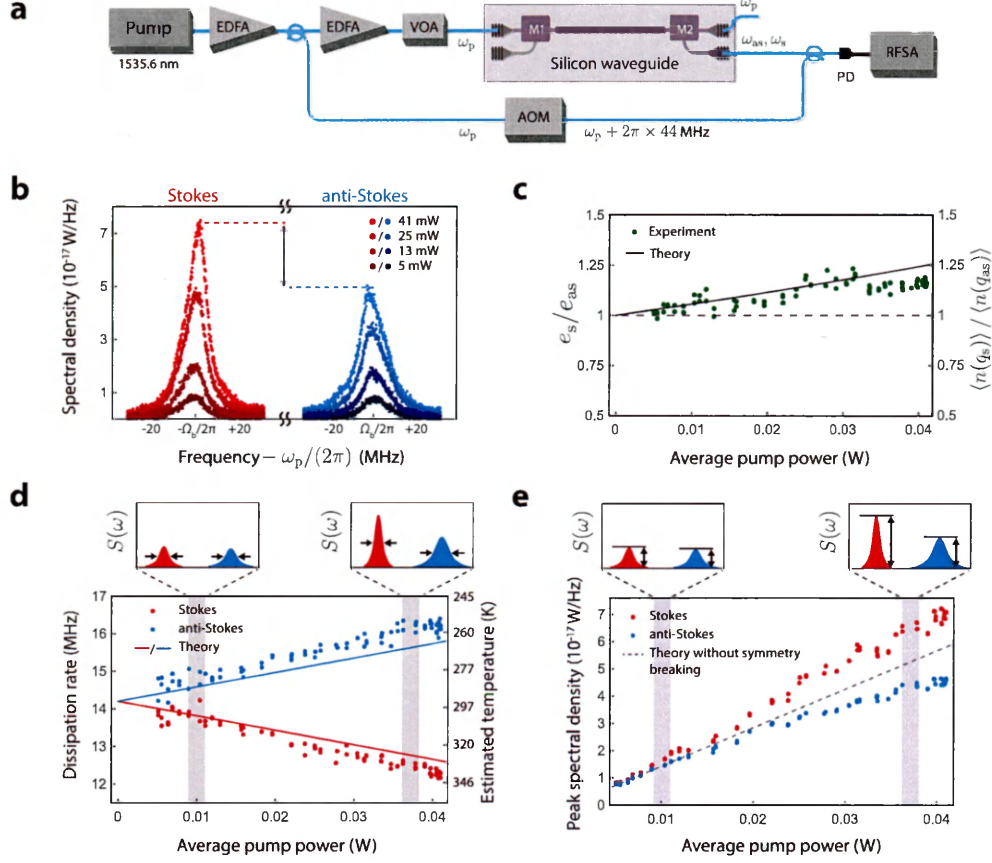


Figure 5.18: **Experimental observation of spontaneous Brillouin cooling.** (a) Experimental diagram used to observe spontaneous Brillouin scattering. Pump light at frequency ω_p is amplified and split into two paths; the bottom path frequency-shifts the light using an acousto-optic modulator (AOM) to a reference frequency $\omega_p + 2\pi \times 44$ MHz to act as a local oscillator for heterodyne detection. In the top path, the intensity of pump light is controlled by an erbium-doped fiber amplifier (EDFA) and variable attenuator (VOA) before being coupled on-chip. As it propagates through the Brillouin-active waveguide, light scatters to anti-Stokes and Stokes sidebands at frequencies ω_{as} and ω_s , respectively, which are coupled off-chip and combined with the reference path for heterodyne detection in the microwave domain. (b) plots measured Stokes and anti-Stokes spectra for several input pump powers. As the pump power increases, the total scattering amplitude increases for both sidebands, but clear asymmetries in height and linewidth are visible. (c) plots the total integrated scattering efficiency ratio between Stokes and anti-Stokes sidebands as a function of pump power in the waveguide. This corresponds to the ratio in phonon occupation numbers (right side). (d) plots the measured dissipation rates as a function of average pump power, showing good agreement with theory. At the highest pump powers of 40 mW, the temperature of the anti-Stokes phonon is cooled over 30 K below room temperature (right y-axis). (e) plots the peak spectral density of the scattered light for both sidebands as a function of pump power. As the pump powers increase, the measured spectral densities deviate from the values expected in the absence of symmetry-breaking between the two processes typical to intra-modal forward-SBS (Ref. [233]). Adapted from Ref. [223].

wavelength around 1535 nm) is amplified and split into two paths. In the top path, the intensity of this pump wave is controlled with an erbium-doped fiber amplifier and variable optical attenuator and is coupled on-chip using an integrated grating coupler, and into the symmetric waveguide mode using an integrated mode multiplexer. As it traverses the device, light scatters through spontaneous inter-modal Brillouin scattering into the anti-symmetric mode, producing frequency-detuned anti-Stokes and Stokes sidebands at frequencies $\omega_{\text{as}} = \omega_{\text{p}} + \Omega_{\text{b}}$ and $\omega_{\text{s}} = \omega_{\text{p}} - \Omega_{\text{b}}$, respectively. These waves are de-multiplexed and coupled off-chip, after which they are combined with a frequency-shifted local oscillator at frequency $\omega_{\text{p}} + 2\pi \times 44$ MHz and incident on a fast photodiode. The scattered sidebands are identified as unique spectral signatures around microwave frequencies of $\Omega_{\text{b}} \pm 2\pi \times 44$ MHz for the Stokes (+) and anti-Stokes (-) waves using a microwave spectrum analyzer. This technique permits high-resolution and high-sensitivity detection of both sidebands simultaneously.

As the pump power is turned up, an increase in the total scattered light is observed for both Stokes and anti-Stokes sidebands, as plotted in Fig. 5.18b. At the same time, these sidebands exhibit an asymmetry in both peak power and linewidth that grows with increasing pump powers; while at the lowest powers these sidebands are practically identical, at higher powers the Stokes scattering efficiency is enhanced and its spectral linewidth narrows. Simultaneously, the anti-Stokes scattering efficiency is diminished and its spectral linewidth broadens. These trends, indicative of cooling for the anti-Stokes phonon and heating for the Stokes-mediating phonon, are illustrated through the integrated scattering efficiency asymmetry $e_{\text{s}}/e_{\text{as}}$ (Fig. 5.18c), the dissipation rates for the two phonons Γ_{as} and Γ_{s} (Fig. 5.18d), and the peak power spectral densities of the two sidebands (Fig. 5.18e). The measured increase in the anti-Stokes linewidth in Fig. 5.18d corresponds to an effective cooling of 32 K relative to room temperature.

5.9.3 Wavevector-selective Phonon Spectroscopy

Thus far, we have observed a pump power-dependent linewidth and scattering rate for spontaneous anti-Stokes scattering, interpreted as a decrease in phonon lifetime and population through interactions with a strong optical pump. As discussed earlier, this cooling takes

place over a wavevector band set through optical phase-matching. An intriguing consequence of this is the ability to target different sets of phonon wavevectors simply through tuning of the optical wavelength, which “selects” the acoustic wavevectors which can produce inter-modal Brillouin scattering.

These dynamics also permit a useful form of phononic pump-probe spectroscopy, wherein a strong pump is used to cool a phonon band, and a weaker probe beam is then tuned to interrogate the phonon occupation as a function of wavevector. We demonstrate this experimentally by introducing a pump laser fixed at a frequency of $\omega_p^{(2)}$ to produce strong cooling at a fixed wavevector band, and by using a tunable probe laser as a weak phonon probe at a tunable frequency $\omega_p^{(1)}$. This configuration is diagrammed in Fig. 5.19a. Both lasers interact with phonons through inter-modal Brillouin scattering to produce scattered Stokes and anti-Stokes sidebands. However, through heterodyne detection with a frequency-shifted local oscillator (produced by passing probe light through an acousto-optic modulator in Fig. 5.19a) the scattered sidebands from the probe laser appear as tones with unique microwave frequencies.

When the probe wavelength is far away from the pump wavelength, no asymmetry is observed between Stokes and anti-Stokes sidebands scattered from the probe laser light, even as the pump power is increased to ~ 40 mW levels. However, when the probe wavelength is very close to that of the pump, pump-power dependent asymmetries in the Stokes and anti-Stokes linewidths and scattering rates are observed. These results are summarized in the right side of 5.19b. To study these contrasting effects, we systematically vary the probe frequency $\omega_p^{(1)}$, and hence the wavevector of interrogated phonons. The interpolated Stokes/anti-Stokes phonon dissipation rate difference and the corresponding anti-Stokes phonon occupation is plotted as a function of phonon wavevector and probe wavelength in 5.19b, showing that the presence of the strong pump wave produces a cold phonon window in wavevector-space. This contrasts with the cold frequency windows typically produced in optomechanical resonators.

This phononic spectroscopy technique reveals the wavevector-selective dynamics of Brillouin cooling within the continuous optomechanical waveguide. These results demonstrate how the waveguide system allows access to a continuum of phonon modes which can be

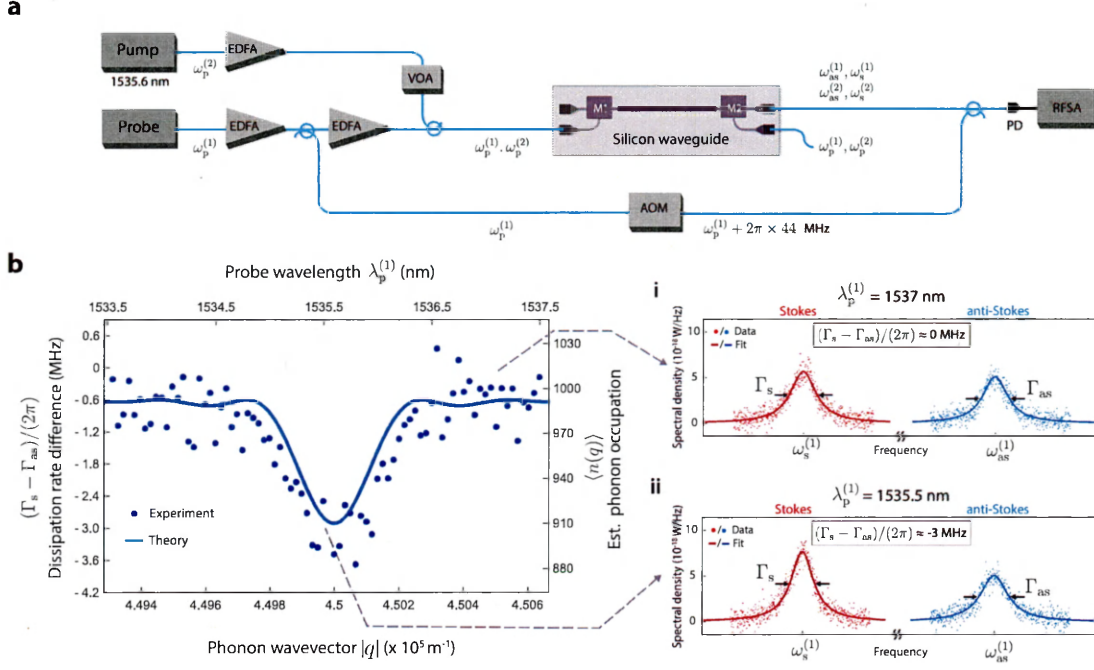


Figure 5.19: **Wavevector-selective phonon spectroscopy.** (a) diagrams the pump-probe experimental diagram. A strong pump laser (frequency $\omega_p^{(2)}$) and weak probe laser (frequency $\omega_p^{(1)}$) are both incident within the optomechanical silicon waveguide. Both pump and probe lasers scatter light through spontaneous inter-modal Brillouin scattering. The pump laser cools a band of phonon wavevectors, while the tunable probe laser has only a small effect on the thermodynamic properties of the system and is used to probe the phonon population as a function of phonon wavevector. The scattered sidebands from the probe laser are analyzed through heterodyne detection referenced by frequency-shifted probe light at frequency $\omega_p^{(2)} + 2\pi \times 44$ MHz. The left panel of (b) shows the measured dissipation rate difference between Stokes and anti-Stokes processes as a function of phonon wavevector, which is selected by the probe wavelength. Each data point represents this dissipation rate asymmetry normalized to a pump power of 30 mW, as determined by measurements of the dissipation rate over a series of ten different pump powers. The theoretical trend from Eq. 5.12 (solid line) shows good agreement with the measured data. Sub-panels (i)-(ii) on the right show sample spectra corresponding to situations where the pump and probe waves are phase-matched to scattering from the same phonon (i) and different phonon bands (ii). Adapted from Ref. [223].

selectively controlled and cooled.

5.9.4 Cooling Dynamics

The spatiotemporal dynamics of Brillouin cooling are studied in detail in Ref. [223]. Assuming that the dissipation rate for the acoustic field Γ is much less than that for the optical field γ , separation of time scales allows the temporal dynamics of the anti-Stokes light to approximately follow those of the thermally-driven phonon field with which it interacts. Within the continuous waveguide of length L , pump light interacts with phonons with a wavevector q around $\Delta k_{\text{as}} \equiv k_{\text{as}} - k_{\text{p}}$, where k_{p} and k_{as} are the (optical frequency-dependent) wavevectors of the pump light and the anti-Stokes light to which it scatters. The occupation of the thermal phonon field around this wavevector $\langle n(\Delta k_{\text{as}}) \rangle$ relative to its equilibrium value $\langle n_{\text{th}}(\Delta k_{\text{as}}) \rangle$ is approximated by

$$\frac{\langle n(\Delta k_{\text{as}}) \rangle}{\langle n_{\text{th}}(\Delta k_{\text{as}}) \rangle} \approx 1 - \frac{G_{\text{B}} P_{\text{p}} L}{4}, \quad (5.11)$$

where G_{B} is the Brillouin gain coefficient and P_{p} is the pump power. This approximation is valid when $\frac{G_{\text{B}} P_{\text{p}} L}{4} \ll 1$, which is well-satisfied in these experiments. Similarly, the effective phonon dissipation rate is $\Gamma_{\text{as,eff}} \approx \Gamma(1 + G_{\text{B}} P_{\text{p}} L/4)$. These results are plotted in Fig. 5.19c-d, showing good agreement with the measured data.

The corresponding expression for the pump-probe experiment, given the same condition that the modification on the phonon field is relatively small to first order, is

$$\frac{\langle n(\Delta k_{\text{as}}^{(1)}) \rangle}{\langle n_{\text{th}}(\Delta k_{\text{as}}^{(1)}) \rangle} \approx 1 - \frac{G_{\text{B}} P_{\text{p}}^{(2)} L}{4} \text{sinc}^2 \left[\frac{(\Delta k_{\text{as}}^{(2)} - \Delta k_{\text{as}}^{(1)}) L}{2} \right], \quad (5.12)$$

where the superscripts ⁽¹⁾ and ⁽²⁾ index quantities relating to the probe and pump waves, respectively. This relation is plotted in Fig 5.19b with no fit parameters, showing excellent agreement with the measured data.

This analysis shows that the optical fields couple to a phase-matched wavevector band with a narrow bandwidth (FWHM) determined by the length of the system $\delta q \equiv \Delta k_{\text{as}}^{(2)} - \Delta k_{\text{as}}^{(1)} = 2.78/L$. These results, corroborated by experimental measurements, show that the

cooling bandwidth is set through optical phase matching as opposed to acoustic propagation (the phonons themselves have a very short propagation length $< 100 \mu\text{m}$).

According to these dynamics, the degree of cooling of these relatively localized traveling-wave phonons counter-intuitively depends directly on the device length. Note however that as the device length increases, this cooling occurs over a narrower bandwidth. One way of thinking of this phenomenon is that cooling is optically-driven at a perfectly well-defined point in wavevector space. However, due to the finite device length, this delta-function cooling window is under-sampled, resulting in the observed sinc-squared-like response. As device length increases, the infinitesimal cooling window is better resolved, resulting in stronger observed cooling over a narrower bandwidth.

Moreover, cooling depends critically on separation of time scales ($\gamma \gg \Gamma$). If this condition is not satisfied, then energy transferred from thermal phonons to the optical field can return to the acoustic field before it leaves the system, preventing appreciable phonon cooling. This sets a length limit on the system since the optical dissipation rate, which is set by the optical transit time through the device, cannot be smaller than the acoustic dissipation rate. As a result, appreciable cooling requires that $L \ll v_g/\Gamma$, which is of the order of meters, and that $G_B P_p L$ be reasonably large. This condition may explain why Brillouin cooling has not previously been observed in fiber optic waveguides, which have comparatively small Brillouin coupling strengths for short fiber lengths.

The realization of controllable optomechanical cooling within a continuous waveguide provides an important step towards flexible continuum optomechanical operations not possible in zero-dimensional cavity-optomechanical systems. In particular, such continuous systems have arbitrarily large optical and acoustic bandwidths, potentially enabling greater degrees of flexibility for traveling-wave quantum optical and optomechanical operations. Further work may enable ground-state optomechanical cooling of continuously-tunable wavevectors, control of noise in practical continuum optomechanical systems, flexible forms of reservoir engineering [329], and non-classical operations within continuous waveguides.

5.10 Conclusions and Outlook

In this chapter, we adapted recently-demonstrated strong forward Brillouin couplings in silicon membrane waveguides to inter-modal interactions. Efficient SIMS produces single-sideband coupling, permitting single-sideband optical gain necessary for robust Brillouin laser designs. More generally, mode multiplexing within multimode nonlinear optics allows for flexible access to pump and signal waves, an important boon for integration within complex integrated photonic circuits. The forward-scattering dynamics of this process eliminate the need for circulators or isolators as are required for BSBS-based signal processing. The SIMS-active waveguide was used to produce net optical amplification and $> 50\%$ optical energy transfer between two strong fields with dynamics very different from the cascaded energy transfer of FSBS.

This same waveguide was used to demonstrate Brillouin cooling within a continuous waveguide. This scientific advance was made possible due to the large Brillouin coupling of the silicon membrane waveguide and the intrinsic dispersive symmetry breaking of inter-modal Brillouin scattering. The continuously-tunable optical phase-matching condition of SIMS also enabled a unique form of phonon spectroscopy which allows the probing of phonon population and lifetime as a function of wavevector. This work provides an entry-point toward nonlocal continuum optomechanical engineering for classical and quantum control of extended, traveling-wave phonons and photons.

This flexible form of Brillouin coupling was also used to create the first Brillouin laser in silicon, a potentially significant advance toward the creation of versatile and customizable silicon-photonic light sources. The robustness of the silicon membrane waveguide and stability of this monolithically-fabricated system allowed the probing of the linewidth-narrowing dynamics of this laser, revealing a new phonon line-narrowing regime which is general to Brillouin lasers that do not exploit ultrahigh- Q optical resonators. The use of a multimode racetrack resonator with inter-modal amplification allows remarkable flexibility in terms of resonator dimensions, resonance frequency-matching, and laser cascading behavior.

Beyond these advances, SIMS may have numerous applications for classical and quantum signal processing. For example, the emit-receive operations discussed in Chapter 4 may be

extended to inter-modal interactions to offer unprecedented tunability for RF-photonic and optical filtering and spectral analysis, as well as additional degrees of control enabled by on-chip inter-modal couplings.

In Chapter 6, we will demonstrate such a structure, but use it for a quite different application; by utilizing SIMS to drive wavevector-tunable traveling acoustic phonons, the intrinsic nonreciprocity of inter-modal Brillouin scattering is harnessed to create wideband, wavelength tunable nonreciprocal light scattering, with bandwidths orders of magnitude greater than prior optomechanical approaches to nonreciprocity. These results represent the first experimental demonstration of processes proposed years earlier [239, 258], and are a step toward the creation of broadband, non-magnetic integrated isolators and circulators.

These example applications are certainly only a small subset of what is possible with on-chip inter-modal Brillouin couplings. It will therefore be exciting to see what techniques are enabled by these processes with future progress.

Chapter 6

Nonreciprocal, Nonlocal Inter-band Brillouin Modulation

6.1 Introduction

Thus far, we have explored light-sound interactions as a tool to permit new degrees of control over optical waves within integrated photonic circuits. In such integrated-waveguide systems, an important area of current research is the creation of microscale devices that produce nonreciprocal light propagation. Through a variety of approaches and experimental systems, this field seeks to address the lack of mature technologies for chip-based optical isolators and circulators. In this chapter, we build on the results of Chapters 4-5 to demonstrate a new optomechanical device design that produces broadband nonreciprocal light propagation in a silicon photonic waveguide.

A variety of different approaches have been explored to create waveguide-integrated nonreciprocal devices. Traditionally, benchtop optical isolators and circulators are based on magneto-optic effects that produce a nonreciprocal polarization shift in the presence of magnetic field. Despite great efforts to adapt these technologies to integrated systems [330–334], it is difficult to implement these same techniques in microscale waveguides because materials which possess a strong magneto-optic response are intrinsically lossy and not complementary metal-oxide-semiconductor (CMOS)-compatible [330–335]. Another approach which

has gained a significant attention is based on the strong nonlinear effect of nanophotonic waveguides [336–339]. While it is possible to make devices that produce nonreciprocal transmission of a strong optical wave, it has been shown that any such device is reciprocal with regard to additional optical waves (e.g. optical backscatter) [339]. Thus, nonreciprocal devices based on Kerr-type nonlinearities cannot simultaneously transmit light in the forward direction and reject it in the backward direction, limiting practical applications. Systems designs based on optical phase modulation may demonstrate nonreciprocity for narrowband signals through the use of coherent effects, though these techniques typically shift light to nearby frequencies and require careful electro-optic design [340–342].

Common to any technique that produces nonreciprocal light propagation is some mechanism to break the symmetry between forward- and backward-propagating waves. In the case of magneto-optic isolators, this is the presence of an external magnetic field. For phase-modulator isolators, this effect results from phase-coherent electro-optic modulation of an optical signal at two time-delayed points. Regardless of the symmetry-breaking mechanism, any such process should ideally create linear nonreciprocity in a device that has low optical insertion loss, operates over a wide optical bandwidth, and provides a strong nonreciprocal response.

Optomechanical interactions provide a natural path to create nonreciprocal devices since mechanical degrees of freedom may act as an intrinsic symmetry-breaking mechanism [343]. For example, the SIMS-active waveguide of Chapter 5 produces unidirectional amplification or attenuation in the presence of a strong pump wave, since the elastic wave mediates gain or loss of a second optical probe only when it is co-propagating with the pump. As such, the Brillouin loss data in Fig. 5.8 can be seen as an optical isolator with 3 dB of rejection. Using this same approach in a 15-meter-long photonic crystal fiber, Ref. [188] demonstrated 20 dB of optical isolation. In contrast to fiber-based experiments, microscale cavity-optomechanical resonators permit enhancement of light-sound coupling to produce efficient optical nonreciprocity with low optical loss [207–211, 344–346]. However, a common limitation of these approaches is that their operating bandwidth is limited to just kHz-MHz by the lifetimes of resonant acoustic or optical modes.

Alternately, traveling-wave interactions can be used to create broadband nonreciprocal

light scattering in the presence of an external time-harmonic perturbation of the material dielectric tensor [239, 258, 344, 347–350]. This approach is based on spatiotemporal optical modulation that drives a transition between distinct dispersion bands with a non-reciprocal phase-matching condition. Nonreciprocal modulation of this type can be achieved using direct electro- or acousto-optic driving, allowing external control and dynamic reconfigurability. Electro-optic demonstrations of traveling-wave nonreciprocal modulation have demonstrated nanometer-operating bandwidths, but absorption resulting from the co-location of electrical and electro-optic components with optical waveguides produce excessive loss that has hindered performance [348].

The essential challenge to achieving nonreciprocal inter-band modulation is that a robust nonreciprocal response requires long interaction lengths (related to the wavevector uncertainty of propagating modes), as well as a refractive index modulation with the correct spatial character to permit the inter-band transition. A recent paper by Sohn et al. [351] demonstrated an alternate to the difficulties of the electro-optic approach by using acousto-optic modulation of a multimode optical ring resonator. While the active modulation region was only ~ 200 μm in length, the use of a ring resonator permitted effective propagation lengths sufficient to achieve reasonable nonreciprocity between forward- and backward-propagating light waves. However, the operation bandwidth was limited to the GHz-wide bandwidths of the resonator modes. Nonetheless, this work demonstrated that elastic waves provide a method to induce robust nonreciprocal behavior in nanophotonic waveguides. Furthermore, because the acoustic emitter is spatially separated from the optical waveguide, acousto-optic modulation does not induce excess propagation loss.

In this section, we demonstrate an alternate method to induce robust traveling-wave nonreciprocal modulation based on a non-local inter-band Brillouin scattering (NIBS) process. This technique utilizes a dual-core multimode optomechanical waveguide, where optically-driven elastic waves created in one optical waveguide produce spatiotemporal acousto-optic modulation of light guided in the second waveguide over centimeter length scales. This distributed process permits nonreciprocal single-sideband modulation and mode conversion over nanometer (>125 GHz) bandwidths, with up to 38 dB of contrast between forward- and backward-propagating light waves.

Through the traveling-wave NIBS interaction, the operation bandwidth is set only through optical dispersion, and is not limited by the lifetimes of resonant optical or elastic modes as in nonreciprocal cavity-optomechanical structures, enabling a full-width at half-maximum (FWHM) modulation bandwidth four orders of magnitude greater than that of the device’s intrinsic acoustic response. Furthermore, the wavevector of the driven elastic wave can be directly tuned through changing the wavelength of a pump laser, allowing direct translation of the device’s modulation response across a 35-nm wavelength band. The NIBS modulator is designed and fabricated from low-loss silicon ridge waveguides to permit excess insertion losses <1 dB, demonstrating a promising step toward the creation of low-loss and broadband waveguide-integrated circulators and isolators.

6.2 NIBS Modulator Device Concept

The device design and basic concept of operation of the NIBS modulator is shown in Fig. 6.1. A 2.39-cm-long optomechanical waveguide (Fig. 6.1a) is fabricated from a single-crystal silicon layer, and consists of two multimode optical ridge waveguides atop a silicon membrane, with cross-sectional dimensions shown in Fig. 6.1b. The two optical waveguide cores are designed to be different in width by an asymmetry δ to prevent optical crosstalk due to evanescent coupling. Each optical waveguide supports fundamental (symmetric) and higher-order (anti-symmetric) optical modes around $\lambda = 1550$ nm, with field profiles plotted in Fig. 6.1c. Elastic waves are confined throughout the membrane structure, permitting light-sound couplings to optical fields within both waveguide cores. One such acoustic phonon mode which mediates strong inter-modal Brillouin scattering around a frequency of $\Omega_B = 5.7$ GHz, is shown in Fig. 6.1g.

The basic operation of the NIBS process is depicted in Fig. 6.1h-i. Two strong optical waves at pump frequency $\omega_p^{(1)}$ and Stokes frequency $\omega_s^{(1)}$ are launched into the first ‘drive’ waveguide. These waves drive a coherent elastic wave at their difference frequency $\Omega = \omega_p^{(1)} - \omega_s^{(1)}$ via electrostrictive forces. Probe light at frequency $\omega_p^{(2)}$ is injected into the second ‘modulator’ waveguide, where it is mode-converted and frequency-shifted to $\omega_s^{(2)} = \omega_p^{(2)} - \Omega$ by the incident elastic wave through acousto-optic scattering. This process is a form of non-

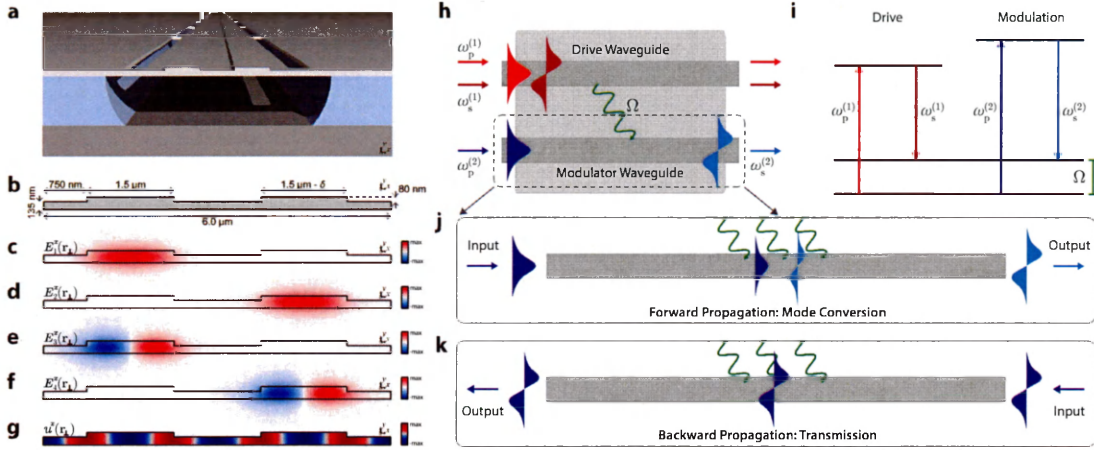


Figure 6.1: **Optomechanical silicon inter-band modulator.** (a) plots an artistic representation of the dual-core suspended waveguide, with the cross sectional dimensions diagrammed in (b) The two optical waveguide cores are designed to be different in width by δ to inhibit optical crosstalk. Each waveguide guides fundamental (symmetric) and higher-order (anti-symmetric) optical spatial modes, with E_x field distributions plotted in (c-f). The entire membrane structure confines elastic waves due to the impedance mismatch between silicon and air. The x -displacement field of one such mode that mediates inter-band Brillouin coupling around a frequency of ~ 5.7 GHz is plotted in (g). (h) diagrams the basic operation of the NIBS process. Two optical waves at frequencies $\omega_p^{(1)}$ and $\omega_s^{(1)}$ guided in separate optical modes of the first ‘drive’ waveguide coherently excite an acoustic phonon at their difference frequency Ω through optical forces. Light injected into a second ‘modulator’ waveguide at frequency $\omega_p^{(2)}$ is frequency-shifted to $\omega_s^{(2)} = \omega_p^{(2)} - \Omega$ and mode-converted by this elastic wave through photoelastic coupling. The energy level diagram for this process is shown in (i). (j-k) depict the propagation of light within the modulator waveguide. In the forward direction, light is mode-converted and frequency-shifted through NIBS. In the backward direction, light passes through the device unaffected. Adapted from Ref. [224].

local coherent Stokes Brillouin scattering (CSBS), with the energy level diagram plotted in Fig. 6.1i. (This can be understood in direct analogy to coherent Stokes Raman scattering. Similarly, a coherent anti-Stokes Brillouin scattering process can be created in analogy to coherent anti-Stokes Raman scattering, as we will demonstrate later in Section 6.4.1.) Note that we use the superscripts ⁽¹⁾ and ⁽²⁾ to denote fields within the drive and modulator waveguide, respectively.

The nonreciprocal operation of the NIBS modulator is diagrammed in Fig. 6.1j-k. When probe light is launched in the forward direction within the modulator waveguide, it experiences acousto-optic mode conversion and frequency-shifting. However, when probe light is launched in the backward direction within the same waveguide (Fig. 6.1k), it propagates through the device unaffected by the elastic wave.

6.3 Light-Sound Phase-matching and Modulator Operation Scheme

The non-reciprocal behavior of the NIBS process originates from the distinct phase-matching requirements for inter-band light scattering in the forward and backward directions. The specific behavior is directly determined by the dispersion of the participating optical waves [188, 221, 239, 347]. In this section, we theoretically investigate this process and derive the relationship between device parameters, operation bandwidth, and nonreciprocity.

To separately address the symmetric and anti-symmetric optical modes of each optical waveguide, we use integrated mode multiplexers of the design studied in Section 5.2. These mode multiplexers are represented by the diagrams in Fig. 6.2a; light injected into port p1 of a mode multiplexer is coupled into the symmetric mode, while light injected into port p2 is coupled into the anti-symmetric mode. Similarly, these mode multiplexers de-multiplex the two modes into their respective ports. We label the four mode multiplexers used to (de)multiplex the waves in the drive and modulator waveguides with the indices M1-M4 in Fig. 6.2c,e,g.

The acoustic phonon which mediates inter-band coupling is optically-driven as depicted in Fig. 6.2c. Light at pump frequency $\omega_p^{(1)}$ is coupled into the symmetric mode of the drive

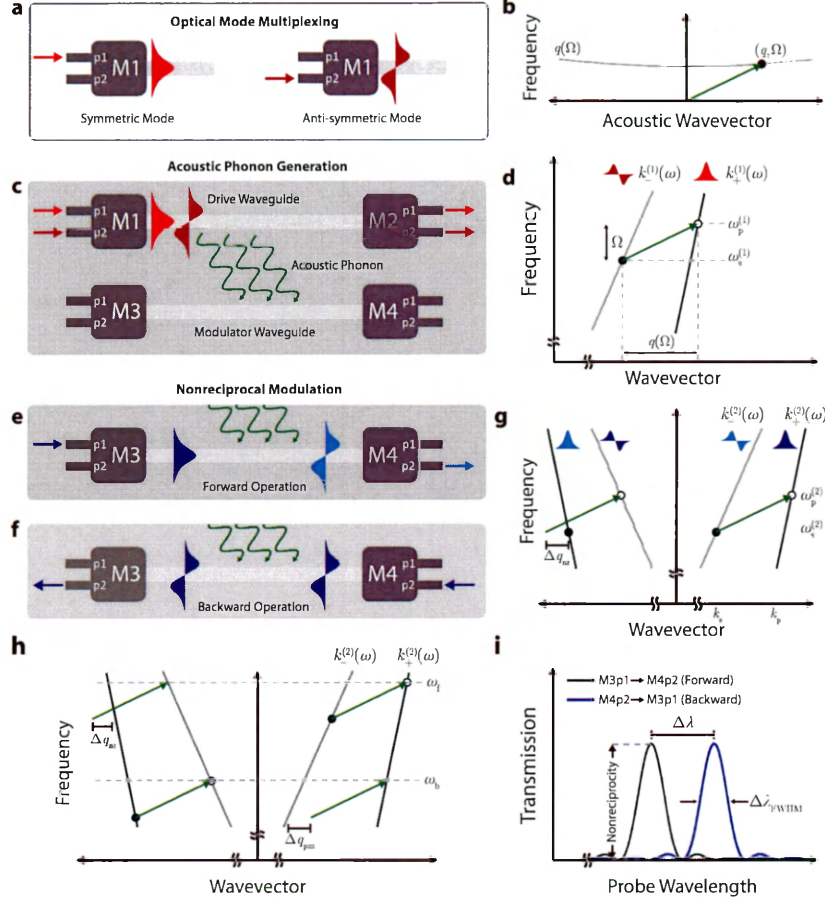


Figure 6.2: **Phase-matching and operation scheme of the NIBS modulator.** (a) shows the operation of two-port mode multiplexers which couple to the symmetric and anti-symmetric optical waveguide modes. (b) plots the dispersion relation of the NIBS-active acoustic phonon. (c) Two strong optical waves in the drive waveguide generate an acoustic phonon through SIMS. (d) plots phase-matching and energy conservation for this process, where the phonon (green) couples light between initial (open circle) and final (filled circle) states. (e-f) depict the propagation of light in the modulator waveguide. In forward operation, light injected into port p1 of M3 (shorthand M3p1) experiences acousto-optic modulation and mode conversion, exiting through port p2 of M4 (M4p2). Light injected in the backward direction through M4p2 passes through the device unaffected and exits through M3p2. (g) shows the phase-matching diagrams for forward (right) and backward propagation (left). In the forward direction, the phonon is phase-matched to an inter-band photonic transition. However, in the backward direction a nonreciprocal wavevector mismatch Δq_{nr} prohibits inter-band coupling. (h) depicts the effects of optical dispersion. In the forward direction, detuning the probe frequency from its phase-matched value ω_f results in a wavevector walkoff Δq_{pm} due to the differing group velocities of the optical modes, leading to a finite operation bandwidth. However, this effect may also cancel Δq_{nr} to produce phase-matched NIBS in the backward direction at ω_b . The resulting transmission spectra are plotted in (i). Adapted from Ref. [224].

waveguide through port p1 of M1, and a second optical wave at Stokes frequency $\omega_s^{(1)}$ is injected into the anti-symmetric mode through port p2 of M1. Within the drive waveguide, these fields couple through stimulated inter-modal Brillouin scattering (SIMS) to produce optical energy transfer and coherent emission of an acoustic phonon corresponding to a point on the elastic-wave dispersion diagram plotted in Fig. 6.2b. In this drive configuration, these waves excite a forward-moving phonon with frequency and wavevector $(\Omega, q(\Omega))$. The phonon frequency is set through the energy conservation condition $\Omega = \omega_p^{(1)} - \omega_s^{(1)}$, while wavevector conservation (phase-matching) for SIMS requires that

$$q(\Omega) = k_+^{(1)}(\omega_p^{(1)}) - k_-^{(1)}(\omega_p^{(1)} - \Omega), \quad (6.1)$$

where $k_+^{(1)}$ and $k_-^{(1)}$ are the dispersion relations for the symmetric and anti-symmetric optical modes in the drive waveguide. These optical dispersion relations are plotted in Fig. 6.2d,g,h as gray (symmetric) and black (anti-symmetric) lines. The energy conservation and phase-matching conditions for SIMS can be represented diagrammatically by Fig. 6.2d, where the acoustic phonon (green arrow) scatters light between initial (open circle) and final (closed circle) optical states.

This optically-driven acoustic phonon may then mediate linear inter-band scattering through NIBS, as diagrammed in Fig. 6.2e-g. In the forward direction, light at probe frequency $\omega_p^{(2)}$ is injected into port p1 of M3, and is mode-converted and frequency-shifted to $\omega_s^{(2)} = \omega_p^{(2)} - \Omega$ through acousto-optic modulation. This light is then exits the device through port p2 of M4, while any residual un-modulated light in the symmetric mode is demultiplexed through port p1 of M4. An inter-band photonic transition within the modulator waveguide must satisfy the phase-matching condition

$$q(\Omega) = k_+^{(2)}(\omega_p^{(2)}) - k_-^{(2)}(\omega_p^{(2)} - \Omega) \quad (6.2)$$

as plotted in the right side of Fig. 6.2g. Here $k_+^{(2)}(\omega)$ and $k_-^{(2)}(\omega)$ are the (positive-valued) wavenumbers of the symmetric and anti-symmetric optical modes in the modulator waveguide.

6.3.1 Relationship between Drive and Modulation Wavelengths

Note that the optical frequencies within the modulator waveguide need not be the same as the frequency as the drive waves, provided that the scattering process couples through the same phonon. Within the device diagrammed in Fig. 6.1, there is a designed width asymmetry δ between the two waveguides. As a result, the acoustic phonon driven by optical waves around free-space wavelength λ_d permits NIBS interactions with light in the modulator waveguide at a different wavelength λ_m . We can calculate the relationship between these two wavelengths by requiring that the two processes couple to phonons with the same wavevector, i.e. equating Eqs. 6.1-6.2:

$$\frac{2\pi}{\lambda_d} \left(n_{p,+}^{(1)}(\lambda_d) - n_{p,-}^{(1)}(\lambda_d) \right) = \frac{2\pi}{\lambda_m} \left(n_{p,+}^{(2)}(\lambda_m) - n_{p,-}^{(2)}(\lambda_m) \right). \quad (6.3)$$

In this equation, $n_{p,+}^{(1)}$ and $n_{p,+}^{(2)}$ are the optical phase indices for the symmetric modes of the drive and modulator waveguides, respectively, and $n_{p,-}^{(1)}$ and $n_{p,-}^{(2)}$ are the phase indices for the anti-symmetric modes. For the sake of simplicity, we have neglected a correction in the phase indices of the anti-symmetric modes resulting from the modulation frequency shift. The resulting relationship between drive and modulation wavelengths can be expressed as:

$$\frac{\lambda_m}{\lambda_d} = \frac{n_{p,+}^{(2)}(\lambda_m) - n_{p,-}^{(2)}(\lambda_m)}{n_{p,+}^{(1)}(\lambda_d) - n_{p,-}^{(1)}(\lambda_d)}. \quad (6.4)$$

Equation 6.4 shows that, with proper optical mode engineering, drive and modulation processes can operate within disparate wavelength bands. As an example, a dual-core NIBS modulator with drive waveguide core width $w = 1.5 \mu\text{m}$ ($n_{p,+}^{(1)} - n_{p,-}^{(1)} = 0.112$ at $\lambda = 1550$ nm) and modulator core width $w = 2.18 \mu\text{m}$ ($n_{p,+}^{(2)} - n_{p,-}^{(2)} = 0.112$ at $\lambda = 2100$ nm), can be used to produce modulation of optical waves >500 nm away from the drive wavelength, provided that the strength of the acousto-optic coupling is maintained for both waveguides.

6.3.2 Origin of Nonreciprocal Response

The traveling elastic wave produces direction-dependent light propagation when there are different phase-matching conditions for inter-band scattering in the forward and backward

directions. This behavior, diagrammed in Fig. 6.2g, results from the finite group velocities of the optical modes. While the condition for NIBS modulation in the forward direction is given by Eq. 6.2, in the backward direction phase-matching dictates that:

$$-q(\Omega) + \Delta q_{\text{nr}} = -k_+^{(2)}(\omega_p^{(2)} - \Omega) + k_-^{(2)}(\omega_p^{(2)}). \quad (6.5)$$

An additional term q_{nr} results in a phase mismatch accumulation $\Delta q_{\text{nr}}L$ for the scattering process in the backward direction within a device of length L . Comparing Eqs. 6.2 and 6.5, we find

$$\Delta q_{\text{nr}} = k_+^{(2)}(\omega_p^{(2)}) - k_+^{(2)}(\omega_p^{(2)} - \Omega) + k_-^{(2)}(\omega_p^{(2)}) - k_-^{(2)}(\omega_p^{(2)} - \Omega). \quad (6.6)$$

Assuming linear dispersion in the vicinity of the operation wavelength, we can approximate this expression as

$$\Delta q_{\text{nr}} = \Omega \frac{\partial k_+^{(2)}}{\partial \omega} (\omega_p^{(2)}) + \Omega \frac{\partial k_-^{(2)}}{\partial \omega} (\omega_p^{(2)}) = \frac{n_{g,+}^{(2)} + n_{g,-}^{(2)}}{c} \Omega. \quad (6.7)$$

Here $n_{g,+}^{(2)}$ and $n_{g,-}^{(2)}$ are the optical group velocities of the two modes around $\omega_p^{(2)}$. When $\Delta q_{\text{nr}}L \gg 1$, a phonon that produces phase-matched inter-band coupling for light in one propagation direction does not produce scattering in the reverse direction. This represents a necessary condition for nonreciprocal operation.

6.3.3 Modulator Operation Bandwidth

The NIBS process is perfectly phase-matched at an optical frequency $\omega_p^{(2)} = \omega_f$ where Eq. 6.2 is satisfied. However, as the probe wavelength $\omega_p^{(2)}$ is changed from this frequency, the differing slopes of the optical dispersion curves results in an optical wavevector mismatch Δq_{pm} given by

$$\begin{aligned} \Delta q_{\text{pm}} = k_+^{(2)}(\omega_p^{(2)}) - k_-^{(2)}(\omega_p^{(2)} - \Omega) - q(\Omega) = \\ \left(k_+^{(2)}(\omega_p^{(2)}) - k_+^{(2)}(\omega_f) \right) - \left(k_-^{(2)}(\omega_p^{(2)} - \Omega) - k_-^{(2)}(\omega_f - \Omega) \right) \end{aligned} \quad (6.8)$$

Assuming linear dispersion (i.e. constant optical group velocities) over the phase-matching bandwidth, a reasonable approximation for typical integrated systems, we can expand Eq. 6.8 to first order about $\omega_p^{(2)}$:

$$\Delta q_{\text{pm}} = \frac{\partial k_+^{(2)}}{\partial \omega} (\omega_p^{(2)} - \omega_f) - \frac{\partial k_-^{(2)}}{\partial \omega} (\omega_p^{(2)} - \omega_f) = \frac{n_{\text{g},+}^{(2)} - n_{\text{g},-}^{(2)}}{c} \Delta \omega, \quad (6.9)$$

where $\Delta \omega = (\omega_p^{(2)} - \omega_f)$ is the frequency detuning of the experimental probe frequency from the modulation center frequency ω_f . This expression results in a finite operating bandwidth over which the inter-band modulation process occurs, with a full-width at half-maximum given by

$$\Delta \omega_{\text{FWHM}} = \frac{4 \cdot 1.39c}{L} \frac{1}{|n_{\text{g},+}^{(2)} - n_{\text{g},-}^{(2)}|}. \quad (6.10)$$

Equation 6.10 shows that the operation wavelength range of the NIBS modulator is set by the difference in group velocities of the participating optical modes. Therefore, with optical dispersion engineering, this bandwidth can potentially be extremely wide (10-100s of nm).

6.3.4 Forward/Backward Operation and Essential Condition for Robust Nonreciprocity

In the previous sections, we have shown how a nonreciprocal wavevector mismatch Δq_{nr} leads to unidirectional light scattering, and how a wavevector walkoff Δq_{pm} leads to a finite operating bandwidth of the modulation process. Interestingly, these two wavevector mismatch terms may exactly cancel, leading to phase-matched NIBS in the backward direction at a frequency $\omega_p^{(2)} = \omega_b$. This situation is illustrated in Fig. 6.2h. The resulting two-way transmission spectrum is sketched in Fig. 6.2i. Each direction experiences a sinc-squared-like response $\propto \text{sinc}^2(\Delta q_{\text{pm}}L/2)$, with center wavelengths determined through the phase-matching conditions. We can calculate the frequency difference between ω_f and ω_b by setting $\Delta q_{\text{nr}} = \Delta q_{\text{pm}}$:

$$\frac{n_{\text{g},+}^{(2)} - n_{\text{g},-}^{(2)}}{c} (\omega_f - \omega_b) = \frac{n_{\text{g},+}^{(2)} + n_{\text{g},-}^{(2)}}{c} \Omega, \quad (6.11)$$

which simplifies to

$$\omega_f - \omega_b = \frac{n_{g,+}^{(2)} + n_{g,-}^{(2)}}{n_{g,+}^{(2)} - n_{g,-}^{(2)}} \Omega. \quad (6.12)$$

As stated above, significant nonreciprocity occurs when the peak modulation response in one direction corresponds to no modulation response in the reverse direction. Under ideal circumstances, this means that the separation $\Delta\lambda$ between forward and backward transmission in Fig. 6.2i (related to Eq. 6.12) is much larger than the half-width at half-maximum (HWHM) operating bandwidth of the modulator $\Delta\lambda_{\text{FWHM}}/2$, i.e. $\omega_f - \omega_b \gg \Delta\omega_{\text{FWHM}}/2$. From Eqs. 6.10 and 6.12, we find that

$$\frac{2 \cdot 1.39c}{L} \frac{1}{|n_{g,+}^{(2)} - n_{g,-}^{(2)}|} \ll \frac{n_{g,+}^{(2)} + n_{g,-}^{(2)}}{|n_{g,+}^{(2)} - n_{g,-}^{(2)}|} \Omega, \quad (6.13)$$

which leads to the fundamental length constraint for nonreciprocal operation

$$L \gg \frac{2.78c}{\Omega (n_{g,+}^{(2)} + n_{g,-}^{(2)})}. \quad (6.14)$$

For the silicon NIBS modulator devices with $\Omega \approx 5.7$ GHz, and group indices $n_{g,+}^{(2)} = 4.0595$ and $n_{g,-}^{(2)} = 4.1853$ [222], this length is 2.8 mm. Therefore the fabricated devices with designed $L = 23.9$ mm are expected to produce a strong nonreciprocal response. From Eq. 6.10, the expected bandwidth of these devices is $\Delta\omega_{\text{FWHM}} \approx 2\pi \times 88$ GHz, and from Eq. 6.12 the expected forward-backward splitting is $\Delta\omega \approx 2\pi \times 374$ GHz.

In the next section, we experimentally characterize the response of the silicon NIBS modulator. Thereafter, we will develop models that describe the dynamics of NIBS coupling and the nonreciprocal input/output behavior of this eight-port device.

6.4 Experimental Characterization of the NIBS Modulator

We experimentally characterize the behavior of the silicon NIBS modulator diagrammed in Fig. 6.1 using the apparatus diagrammed in Fig. 6.3a. In the top path, the two strong drive waves at frequencies $\omega_p^{(1)}$ and $\omega_s^{(1)} = \omega_p^{(1)} - \Omega$ are synthesized from the same laser

split into two branches. The tone at $\omega_s^{(1)}$ is created using a null-biased intensity modulator (IM) and fiber Bragg grating filter (FBG), and its detuning Ω controlled via a microwave frequency synthesizer. Both waves are amplified through erbium doped fiber amplifiers (EDFAs) before being coupled on-chip and into the drive waveguide using grating couplers and integrated mode multiplexers. The total on-chip power in the drive waveguide is set to around 90 mW.

Light from a separate probe laser at frequency $\omega_s^{(1)}$ is then injected into the modulator waveguide in either the forward or backward direction. In forward operation for a Stokes NIBS process, light is coupled into the symmetric mode through port p1 of M3, and frequency-shifted light is collected from port p2 of M4. In the backward direction, light is injected into the anti-symmetric mode through port p2 of M4, and the output signal is measured at port p1 of M3. In either direction, the output light is combined with a frequency-shifted local oscillator at frequency $\omega_s^{(1)} + \Delta$ produced using an acousto-optic modulator (AOM) driven by a microwave source. The combined signal is incident on a photodiode (PD) and detected in the microwave domain using a radiofrequency spectrum analyzer (RFSAs). Using this heterodyne configuration, Stokes-shifted probe light at $\omega_p^{(2)} - \Omega$ appears as a unique microwave beat-note at $\Omega + \Delta$, while anti-Stokes light at $\omega_p^{(2)} + \Omega$ corresponds to a microwave tone at $\Omega - \Delta$.

The response of one device is plotted as a function of modulation frequency Ω in Fig. 6.3b, revealing a narrowband resonant response around a frequency of $\Omega = \Omega_B = 2\pi \times 5.7$ GHz, corresponding to the acoustic phonon mode plotted in Fig. 6.1g. The FWHM bandwidth of $\Gamma/2\pi = 17$ MHz corresponds to the acoustic decay rate, and sets the theoretical on/off switching time for the modulator to $\tau = 2/\Gamma \approx 19$ ns [188].

We now fix the modulation frequency to $\Omega = \Omega_B$ and investigate the dependence of the inter-band modulation efficiency as a function of probe wavelength $\lambda_p^{(2)} = 2\pi c/\omega_p^{(2)}$. The resulting two-way transmission spectrum is plotted for one device in Fig. 6.3c, showing the characteristic nonreciprocal response diagrammed earlier in Fig. 6.2i. A FWHM modulation bandwidth of around 1 nm (125 GHz) is observed for both forward and backward propagation at wavelengths of 1545.3 nm and 1548.5 nm, respectively, with a peak on-chip modulation efficiency relative to the input probe power of $\eta^2 \equiv P(\text{M3p1})/P(\text{M4p2}) \approx 1\%$ (-20

dB). The maximum nonreciprocal contrast between forward- and backward-propagating optical waves is achieved around $\lambda_b = 1548.5$ nm, where efficient NIBS modulation is observed only for backward-traveling light. At this wavelength, the spectral content of the output light is plotted in Fig. 6.3e. These data show that light is single-sideband frequency-shifted by $-\Omega$, with 37 dB suppression of spurious tones. The residual anti-Stokes scattered light at $+\Omega$ results from a small amount of light being coupled into the incorrect spatial mode in M4.

Zoomed-in data for three different devices are depicted in Fig. 6.3d.i-iii, showing up to 38 dB of nonreciprocal contrast in Fig. 6.3d.i, and more than 19 dB of contrast over the entire FWHM bandwidth of 1.18 nm (150 GHz) in the device of Fig. 6.3d.iii. Note that as the waveguide width asymmetry δ is increased between these devices, the center modulation frequency λ_b is decreased to satisfy phase-matching (Eq. 6.4).

In addition to geometric wavelength tuning, the modulation response may be directly tuned by changing the wavelength of the optical drive waves, and hence the driven phonon wavevector (Eq. 6.1). This technique is used in Fig. 6.3, where tuning the wavelength of the drive from 1530 nm to 1565 nm translates the probe modulation response by a corresponding amount without changing the overall shape. Through this process, the modulator center wavelength may be continuously tuned across the entire C band. Within this device, this range was limited only by the tunability of the drive laser.

6.4.1 Anti-Stokes Modulation Data

Through these experiments, we have utilized inter-band modulation through a Stokes scattering process. All of the same operations and nonreciprocal behavior are also available through anti-Stokes NIBS, a form of coherent anti-Stokes Brillouin scattering (CABS). This process is plotted in Fig. 6.4a-b. The basic operation scheme for the anti-Stokes process (Fig. 6.4a) is identical to that of the Stokes process (Fig. 6.4h), except the opposite mode is injected in the modulator waveguide. In the forward direction, the elastic wave produced through SIMS mediates anti-Stokes scattering from light in the anti-symmetric mode to light in the symmetric mode. The energy level diagram for anti-Stokes NIBS is depicted in Fig. 6.4b. The interaction of two optical waves in the drive waveguide moves the system

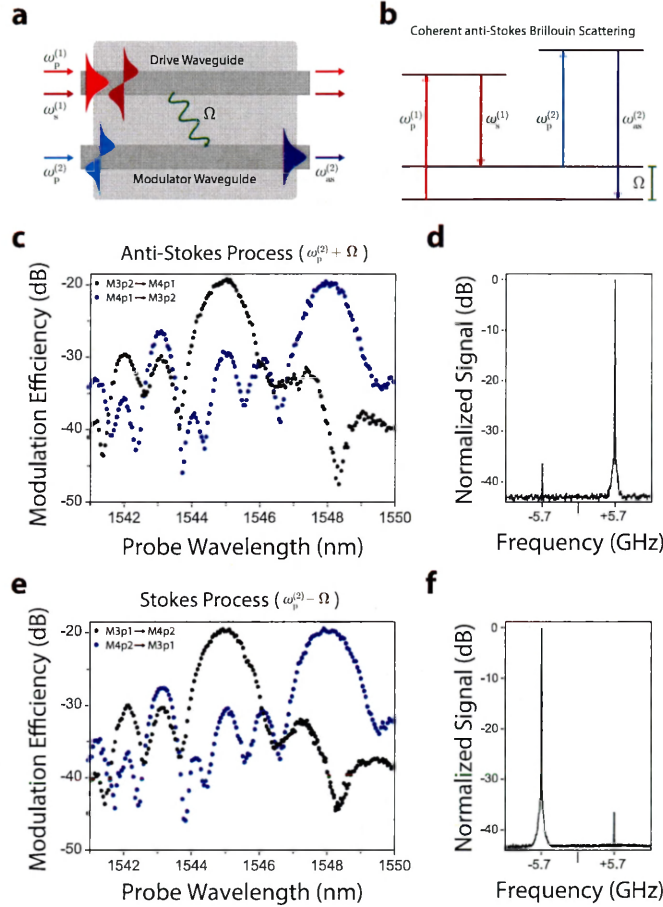


Figure 6.4: **Anti-Stokes NIBS modulation.** (a-b) depict the device operation scheme and energy level diagram in analogy to Fig. 1 of the main article. (a) shows an illustration of nonlocal interband Brillouin scattering for the anti-Stokes process. While the phonon emission is unchanged from the text, light is incident in the anti-symmetric mode of the modulator waveguide. The phonon blue-shifts and mode converts this light as it traverses the device. (b) plots the energy level diagram for this nonlocal coherent anti-Stokes Brillouin scattering process. (c) shows the anti-Stokes modulation response for light propagating in both directions through the modulator waveguide as a function of probe wavelength. (d) plots the corresponding output spectrum relative to a single optical incident field for a wavelength of 1548.3 nm. (e-f) plot data for the Stokes process in the same device for comparison. (e) plots the forward-backward Stokes modulation response, while (f) plots the output spectrum at a probe wavelength of 1548.3 nm. Adapted from Ref. [224].

into an excited vibrational state (drives a phonon), and this phonon is then annihilated through linear anti-Stokes scattering to produce a blue-shifted probe photon.

As show in Fig. 6.4c-f, the experimental modulation response (Fig. 6.4c,e) and single-sideband suppression (Fig. 6.4d,f) are identical for anti-Stokes (middle panels) and Stokes processes (bottom panels) within the same waveguide. Therefore, either process may be used for nonreciprocal operation ¹. The insensitivity of the modulation response to the type of process used means that the data plotted in Fig. 6.3 essentially represent the forward- and backward-modulation response for both Stokes and anti-Stokes processes. So, regardless of the input modal content, through nonreciprocal operation light propagating in one direction experiences mode conversion, whereas light propagating in the reverse direction does not.

6.4.2 Phase-mismatched Lineshape

When the NIBS process is phase-matched, (i.e. $\lambda_p^{(2)} = \lambda_f$ or λ_b), the frequency-response of the modulation efficiency follows a Lorentzian response, as in Fig. 6.3b. However, when the probe is detuned from this wavelength, the inter-band scattering process accumulates a relative phase $\Delta q_{\text{pm}}z$ as it propagates along the device, resulting in phase-mismatched coupling, where Δq_{pm} is given by Eq. 6.8. When this is the case, the experimentally-observed modulation frequency response takes on different and interesting shapes, characterized by features such as asymmetric lineshapes, very sharp frequency rolloffs, and notch-type features indicative of interference effects. Several characteristic lineshapes are plotted as a function of probe wavelength, and hence wavevector mismatch, in Fig. 6.5.

These lineshapes can be understood as resulting from a combination of a position dependent phase-mismatch, and changes in the resonant Brillouin frequency and optical wavevectors along the device length. The latter two of these mechanisms are discussed in detail in Ref. [242]. To understand the source of the various frequency response shapes, we construct a simple model that includes a constant wavevector mismatch Δq_{pm} within the device that is set by Eq. 6.8, and variations in the Brillouin frequency and gain coefficient along the device. We represent the power amplitudes of the drive-waveguide optical fields as $a_p^{(1)}$

1. Note that, if large probe powers are used, the CSBS process can nonlinearly enhance the phonon field, and hence modulation efficiency, while CABS, through a conjugate process, annihilates phonons.

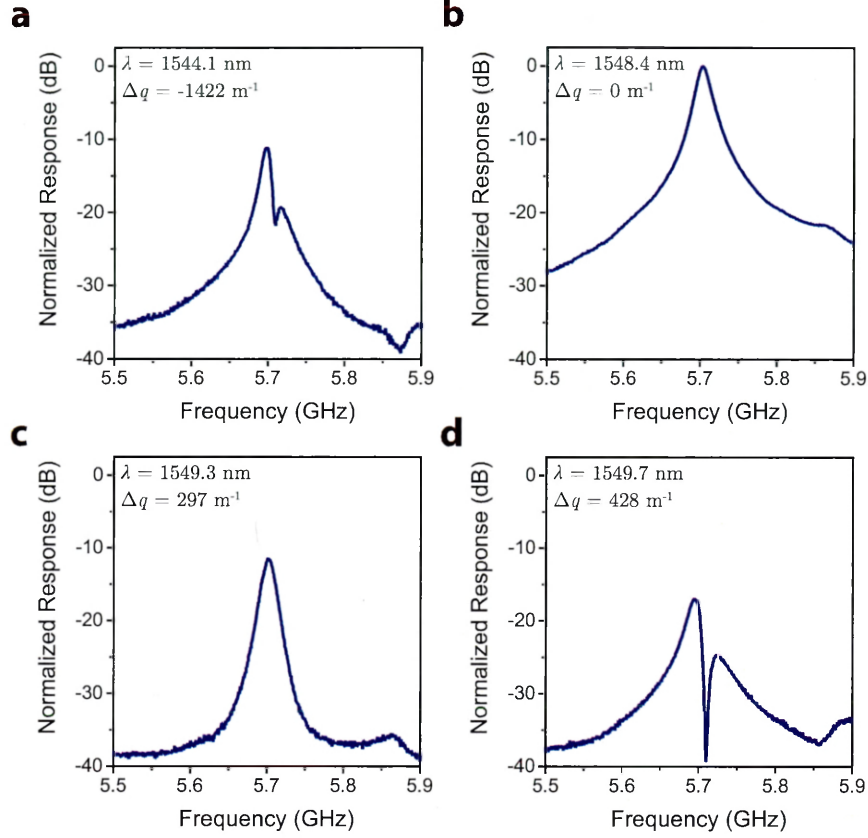


Figure 6.5: **Phase-mismatched NIBS response.** Frequency response of one silicon NIBS modulator device four different probe wavelengths, and hence wavevector mismatches. (a) $\lambda_p = 1544.1$ nm, $\Delta q = -1422$ m $^{-1}$ (b) $\lambda_p = 1548.4$ nm, $\Delta q = 0$ m $^{-1}$ (“phase-matched”) (c) $\lambda_p = 1549.3$ nm, $\Delta q = 297$ m $^{-1}$ (d) $\lambda_p = 1549.7$ nm, $\Delta q = 428$ m $^{-1}$. These different lineshape behaviors result from position-dependent changes in device dimensions, and hence optical and acoustic propagation. Adapted from Ref. [224].

and $a_s^{(1)}$, and the amplitude of the probe wave in the modulator waveguide as $a_p^{(2)}$. The accumulation of the scattered Stokes wave $a_s^{(2)}$ can be described according to the equation

$$\frac{\partial a_s^{(2)}}{\partial z} = e^{i\Delta q_{pm}z} a_p^{(1)}(z) a_s^{(1)*}(z) a_p^{(2)}(z) \frac{\gamma_B(z) \Gamma/2}{\Omega_B(z) - \Omega - i\Gamma/2}, \quad (6.15)$$

where $\gamma_B(z) = G_B(z)/2$ is the nonlinear coupling coefficient and $\Omega_B(z)$ is the phonon resonance frequency as a function of position z along the device length, and Γ is the intrinsic phonon decay rate. The effect of waveguide core size variations on the optical propagation constants for the two modes may also be included by letting Δq_{pm} also depend on z , though

we neglect this here for simplicity. Depending on the chosen forms of $\gamma_B(z)$ and $\Omega_B(z)$, Eq. 6.15 produces all of the behaviors observed in Fig. 6.5, and many others.

If we take all parameters to be constant with respect to z and assume undepleted drive fields, Eq. 6.15 leads to the expected sinc-like modulation response as wavevector detuning is varied:

$$\begin{aligned} a_s^{(2)}(L) &= a_p^{(1)} a_s^{(1)*} a_p^{(2)} \frac{\gamma_B \Gamma / 2}{\Omega_B - \Omega - i\Gamma / 2} \int_0^L e^{i\Delta q_{pm} z} dz \\ &= a_p^{(1)} a_s^{(1)*} a_p^{(2)} \frac{\gamma_B \Gamma / 2}{\Omega_B - \Omega - i\Gamma / 2} L e^{i\Delta q_{pm} L / 2} \text{sinc} \left(\frac{\Delta q_{pm} L}{2} \right), \end{aligned} \quad (6.16)$$

so that the output scattered light power is

$$P_s^{(2)}(L) = a_s^{(2)}(L) a_s^{(2)*}(L) = P_p^{(1)} P_s^{(1)} P_p^{(2)} L^2 \frac{|\gamma_B|^2 \Gamma^2 / 4}{(\Omega_B - \Omega)^2 + \Gamma^2 / 4} \text{sinc}^2 \left(\frac{\Delta q_{pm} L}{2} \right). \quad (6.17)$$

6.4.3 Experimental Modulation Efficiency and Device Parameters

For each of the devices studied in Fig. 6.3, the maximum modulation efficiency $\eta^2 = P_s^{(2)}(L) / P_p^{(2)}(0)$ was around 0.01 (1%). Here, we briefly study the dependence of η^2 on the incident drive-waveguide powers $P_p^{(1)}$ and $P_s^{(1)}$. Fig. 6.6 shows the experimentally-measured modulation (mode-conversion) efficiency for one NIBS modulator device as a function of the total drive waveguide power, up to a maximum incident power of $P = 104$ mW. The pump- and Stokes- waves powers are scaled by the same amount so that, throughout these measurements, the relative input ratio is $P_s^{(1)}(0) = 0.65 P_p^{(1)}(0)$.

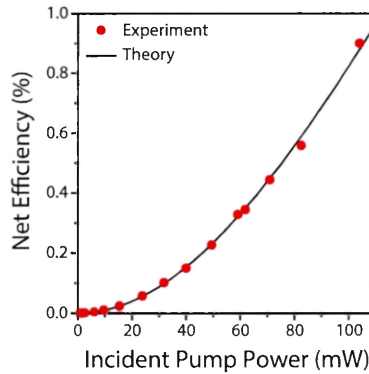


Figure 6.6: **Experimental modulation efficiency.** NIBS modulation efficiency for one device as a function of incident drive-waveguide power. Adapted from Ref. [224].

At low powers, the modulation efficiency follows the expected power-squared trend according to Eq. 6.17. However, this trend deviates somewhat due to nonlinear absorption in the drive waveguide at high powers (see Section 5.4 for more details). At the highest tested total power, the observed efficiency relative to the incident probe power is about 0.9%, including ~ 1 dB of linear loss through the modulator waveguide. In principle, improved efficiency should be possible with increased pump powers.

A theory curve (black) is plotted atop the data in Fig. 6.6, corresponding to a numerical fit to the full dynamics of the system (studied later in Section 6.6). This curve agrees well with the measured efficiency trend for a Brillouin gain coefficient in each waveguide of $G_B = G^{(1)} = G^{(2)} = 195 \pm 10 \text{ W}^{-1}\text{m}^{-1}$. The other device parameters used in this fit are summarized in Table 6.1. The linear and nonlinear loss coefficients are determined according to the methods of Section 5.4, and the acoustic wavevector q and group and phase velocities $v_{b,g}$ and $v_{b,p}$ are determined from finite-element simulations. The loss coefficients are indexed according to the participation of the symmetric (+) and anti-symmetric (-) optical modes.

6.5 Scattering Matrix Model of NIBS

We have seen how NIBS can produce nonreciprocal mode conversion through both Stokes and anti-Stokes scattering, and can produce modulation for either forward- or backward-propagating light depending on the optical wavelength. In this section, we develop a simple, phenomenological scattering matrix model that describes the various processes produced through NIBS, and show how this model can be used to explore the behavior of cascaded operation through multiple NIBS-active devices.

Each NIBS modulator waveguide has four ports corresponding to each end and optical mode. We represent these four ports, as diagrammed in Fig. 6.7, as an element of a column

Table 6.1: Measured and Calculated Device Parameters

Linear optical parameters	value
L	2.387 cm
$\alpha_+^{(1,2)}$	4.6 m^{-1}
$\alpha_-^{(1,2)}$	9.2 m^{-1}
Nonlinear optical parameters	value
Brillouin Gain G	$195 \text{ W}^{-1}\text{m}^{-1}$
TPA coefficients	
$\beta_{++}^{(1,2)}$	$34 \pm 10 \text{ m}^{-1}\text{W}^{-1}$
$\beta_{--}^{(1,2)}$	$30 \pm 9 \text{ m}^{-1}\text{W}^{-1}$
$\beta_{+-}^{(1,2)} = \beta^{21}$	$20 \pm 6 \text{ m}^{-1}\text{W}^{-1}$
FCA coefficients	
$\gamma_{+++}^{(1,2)}$	$1000 \pm 400 \text{ m}^{-1}\text{W}^{-2}$
$\gamma_{---}^{(1,2)}$	$790 \pm 430 \text{ m}^{-1}\text{W}^{-2}$
$\gamma_{+--}^{(1,2)} \approx \gamma_{-++}^{122}$	$340 \pm 200 \text{ m}^{-1}\text{W}^{-2}$
Acoustic parameters	value
Ω_B	$2\pi \times 5.70 \text{ GHz}$
Γ	$2\pi \times 17.0 \text{ MHz}$
$Q = \Omega_B/\Gamma$	335
q	$4.5 \times 10^5 \text{ m}^{-1}$
$v_{b,g}$	830 m/s
$v_{b,p}$	$8.4 \times 10^4 \text{ m/s}$

vector \mathbf{A} . An optical signal at a single port i is represented by a single nonzero entry:

$$\mathbf{A}_i = \begin{pmatrix} \delta_{1i} \\ \delta_{2i} \\ \delta_{3i} \\ \delta_{4i} \end{pmatrix}, \quad (6.18)$$

where we have normalized the total power amplitude to a value of 1. In this model, we can write the scattering matrix for the NIBS modulator on an input signal as:

$$\mathbf{A}_{\text{out}} = \mathbf{B} \cdot \mathbf{A}_{\text{in}}, \quad (6.19)$$

where \mathbf{A}_{in} and \mathbf{A}_{out} are the column vectors representing the respective input and output fields. Assuming ideal mode multiplexers so that there is no cross-talk between channels, then \mathbf{B} is given by

$$\mathbf{B} = \begin{pmatrix} 0 & 0 & \sqrt{1 - \eta_f^2} & \eta_b e^{\pm i(\phi_b + \Omega t)} \\ 0 & 0 & \eta_b e^{\mp i(\phi_b + \Omega t)} & \sqrt{1 - \eta_f^2} \\ \sqrt{1 - \eta_f^2} & \eta_f e^{\mp i(\phi_f + \Omega t)} & 0 & 0 \\ \eta_f e^{\pm i(\phi_f + \Omega t)} & \sqrt{1 - \eta_f^2} & 0 & 0 \end{pmatrix}. \quad (6.20)$$

In this scattering matrix, η_f^2 and η_b^2 are the modulation efficiencies for forward- and backward-propagating light, respectively. ϕ_f (ϕ_b) is the phase shift associated with inter-band scattering in the forward (backward) direction, and Ω is the frequency shift imparted by NIBS. The upper or lower symbol of \pm and \mp represents the case of a forward- or backward-propagating acoustic field. The anti-diagonal terms of the scattering matrix represent NIBS, with the sign of the frequency shift corresponding to Stokes or anti-Stokes scattering. This matrix is asymmetric when $\eta_f \neq \eta_b$, representing a linear, nonreciprocal mode conversion process.

Through typical operation, strong nonreciprocity is achieved when the forward- and backward- modulation efficiencies are different by orders of magnitude. For example, we consider the case where $\eta_f^2 \gg \eta_b^2 \approx 0$, in other words that the device is operating around an optical frequency ω_f where strong modulation occurs only for forward-propagating light.

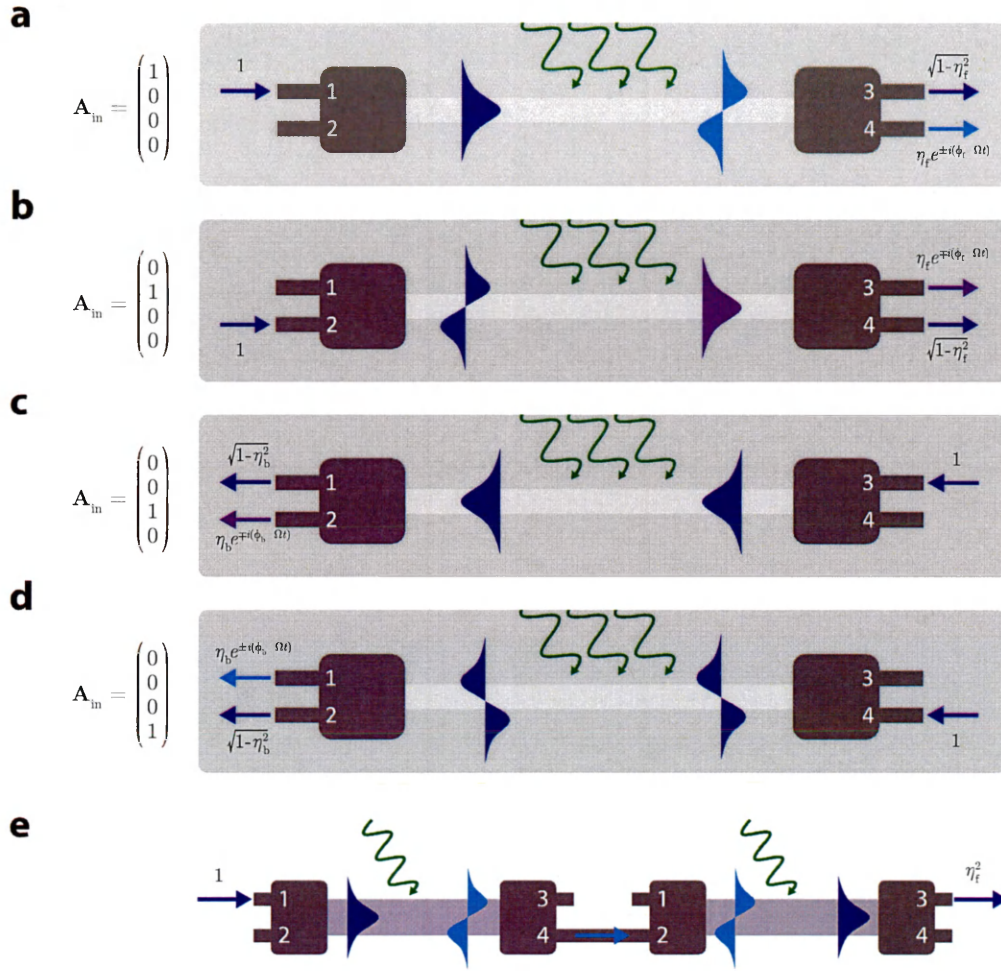


Figure 6.7: **NIBS modulation within the scattering matrix formulation.** (a-d) show the output wave amplitudes at each port corresponding to light incident in each port of the four-port modulator waveguide. In (a-b), significant mode conversion is achieved in the forward direction ($\eta_f^2 \approx 1$), while in the backward direction light propagates through the device with only a small amount being mode-converted ($\eta_b^2 \ll 1$). (e) shows one potential approach to construct a frequency-neutral acousto-optic isolator based on serial cascading of two NIBS modulators. Adapted from Ref. [224].

(Alternately we could consider backward-propagating light around a frequency ω_b where $\eta_b^2 \gg \eta_f^2 \approx 0$.) In this case, we can represent the operation of \mathbf{B} for four different input cases using the diagrams in Fig. 6.7. The input and output amplitudes at each port are labeled next to their corresponding position in space.

When the interband conversion efficiency approaches unity $\eta_f^2 \approx 1$, the scattering matrix becomes:

$$\mathbf{B}_{\eta_f^2=1} = \begin{pmatrix} 0 & 0 & 1 & 0 \\ 0 & 0 & 0 & 1 \\ 0 & e^{\mp i(\phi_f + \Omega t)} & 0 & 0 \\ e^{\pm i(\phi_f + \Omega t)} & 0 & 0 & 0 \end{pmatrix}. \quad (6.21)$$

In this form, NIBS is represented by the antidiagonal terms in the first two columns, while the next two columns represent transmission of backward-injected light through the device. This scattering matrix represents a frequency-shifting four-port circulator: Light incident in port 1 scatters to port 4, port 4 transmits light to port 2, port 2 scatters light to port 3, and port 3 transmits light back to port 1. We can see these behaviors explicitly through the scattering matrix equations:

$$\mathbf{B}_{\eta_f^2=1} \cdot \mathbf{A}_1 = e^{\pm i(\phi_f + \Omega t)} \mathbf{A}_4, \quad (6.22)$$

$$\mathbf{B}_{\eta_f^2=1} \cdot \mathbf{A}_4 = \mathbf{A}_2, \quad (6.23)$$

$$\mathbf{B}_{\eta_f^2=1} \cdot \mathbf{A}_2 = e^{\mp i(\phi_f + \Omega t)} \mathbf{A}_3, \quad (6.24)$$

$$\mathbf{B}_{\eta_f^2=1} \cdot \mathbf{A}_3 = \mathbf{A}_1. \quad (6.25)$$

We now extend this model to include the potential for cascaded operation of multiple NIBS modulator devices. To enable port-connecting operations, we introduce an auxiliary matrix \mathbf{T}_{ij} defined by

$$\mathbf{T}_{ij} = \begin{pmatrix} \delta_{1i}\delta_{1j} & \delta_{1i}\delta_{2j} & \delta_{1i}\delta_{3j} & \delta_{1i}\delta_{4j} \\ \delta_{2i}\delta_{1j} & \delta_{2i}\delta_{2j} & \delta_{2i}\delta_{3j} & \delta_{2i}\delta_{4j} \\ \delta_{3i}\delta_{1j} & \delta_{3i}\delta_{2j} & \delta_{3i}\delta_{3j} & \delta_{3i}\delta_{4j} \\ \delta_{4i}\delta_{1j} & \delta_{4i}\delta_{2j} & \delta_{4i}\delta_{3j} & \delta_{4i}\delta_{4j} \end{pmatrix}. \quad (6.26)$$

For a series of two NIBS modulators, \mathbf{T}_{ij} represents connecting port i of the first device

to port j of the second device. Through the use of a repeated index, i.e. \mathbf{T}_{ii} , we can also represent back-reflecting light at port i .

To illustrate an application of this mode, we consider a simple design for a frequency-neutral isolator consisting of two NIBS modulators connected in series through the configuration in Fig. 6.7e. In this design, port 4 of the first modulator is connected to port 2 of the second. In the forward direction, light incident in port 1 is mode-converted and red-shifted through a Stokes process in the first modulator, before being transmitted into port 2 of the second modulator. This signal is then blue-shifted back to its initial frequency and converted to the fundamental mode through an anti-Stokes process. The net forward transmission is:

$$\begin{aligned} \mathbf{A}_f &= \mathbf{B} \cdot \mathbf{T}_{42} \cdot \mathbf{B} \cdot \mathbf{A}_1 \\ &= \begin{pmatrix} 0 \\ 0 \\ \eta_f^2 \\ \eta_f \sqrt{1 - \eta_f^2} e^{\pm i(\phi_f + \Omega t)} \end{pmatrix}. \end{aligned} \quad (6.27)$$

Light injected in the backward direction through port 3 of the second modulator does not experience strong mode conversion since $\eta_b \ll 1$. As a result only a small amount of light is transmitted through through the system:

$$\begin{aligned} \mathbf{A}_b &= \mathbf{B} \cdot \mathbf{T}_{24} \cdot \mathbf{B} \cdot \mathbf{A}_3 \\ &= \begin{pmatrix} \eta_b^2 \\ \eta_b \sqrt{1 - \eta_b^2} e^{\mp i(\phi_b + \Omega t)} \\ 0 \\ 0 \end{pmatrix}. \end{aligned} \quad (6.28)$$

The nonreciprocal power transmission ratio between forward and backward directions is $T_{\text{nr}} \equiv P_{1 \rightarrow 3} / P_{3 \rightarrow 1} = \eta_f^4 / \eta_b^4$. The effective insertion loss for forward transmission is η_f^4 , the square of the modulation efficiency for a single device.

6.6 Coupled Amplitude Equations and Dynamics of NIBS Couplings

In the previous sections, we have studied the behavior of NIBS in terms of nonreciprocal transmission and traveling-wave phase-matching. Here, we write down the coupled amplitude equations which describe the spatial evolution of the optical and acoustic fields participating in the NIBS process. We consider a system which separately couples two pairs of optical waves through a common phonon mode, as in the dual-waveguide membrane structure of Fig. 6.1. This treatment may be generalized to devices which couple additional sets of optical waves, or be readily adapted to systems which produce similar traveling-wave couplings, including general classes of polarization-multiplexed or multi-core optical fibers and integrated waveguides.

6.6.1 General Coupling Equations Including Nonlinear Loss

We assume that the NIBS interaction is driven on-resonance ($\Omega = \Omega_B$), phase-matching is satisfied, and that the system is in the steady-state so that all time derivatives go to zero, following the approach of Chapter 2. In the drive waveguide, we consider two guided optical waves at frequencies $\omega_p^{(1)}$ and $\omega_s^{(1)} = \omega_p^{(1)} - \Omega$ with amplitudes $a_p^{(1)}$ and $a_s^{(1)}$. When these waves are coupled through a common phonon field with amplitude b , their coupled-amplitude equations of motion are those for SIMS (Section 2.2.3) in the presence of nonlinear loss.

$$\frac{\partial a_p^{(1)}}{\partial z} = -\frac{G^{(1)}}{2} a_s^{(1)} b - \frac{1}{2} \left(\alpha_p^{(1)} + \beta_{pp}^{(1)} |a_p^{(1)}|^2 + \gamma_{ppp}^{(1)} |a_p^{(1)}|^4 \right) a_p^{(1)} - \frac{1}{2} \left(2\beta_{ps}^{(1)} + 4\gamma_{pps}^{(1)} |a_p^{(1)}|^2 + \gamma_{pss}^{(1)} |a_s^{(1)}|^2 \right) |a_s^{(1)}|^2 a_p^{(1)}, \quad (6.29)$$

$$\begin{aligned} \frac{\partial a_s^{(1)}}{\partial z} = & \frac{G^{(1)}}{2} a_p^{(1)} b^* - \frac{1}{2} \left(\alpha_s^{(1)} + \beta_{ss}^{(1)} |a_s^{(1)}|^2 + \gamma_{sss}^{(1)} |a_s^{(1)}|^4 \right) a_s^{(1)} - \\ & \frac{1}{2} \left(2\beta_{sp}^{(1)} + 4\gamma_{ssp}^{(1)} |a_s^{(1)}|^2 + \gamma_{spp}^{(1)} |a_p^{(1)}|^2 \right) |a_p^{(1)}|^2 a_s^{(1)}. \end{aligned} \quad (6.30)$$

As in prior chapters, we have assumed that the phonon field is heavily spatially damped compared to the distance over which significant optical energy transfer occurs, so that the phonon field adiabatically follows the spatial evolution of the optical field product:

$$b = a_s^{(1)*} a_p^{(1)}. \quad (6.31)$$

In these equations, $G^{(1)}$ represents the real-valued Brillouin gain coefficient in the drive waveguide, α_i is the linear power loss coefficient for mode i , β_{ii} and β_{ij} are the intra- and inter-modal loss coefficients due to two-photon absorption (TPA). γ_{iii} is the intra-modal loss coefficient for TPA-induced free carrier absorption (FCA), while γ_{ijj} and γ_{iij} are the inter-modal FCA loss coefficients. Here i and j are indices which refer to either optical field (mode). The optical amplitudes are normalized with the condition $P_p^{(1)}(z) = |a_p^{(1)}|^2$ and $P_s^{(1)}(z) = |a_s^{(1)}|^2$ and the phonon field is normalized such that $P_b = \frac{\Omega_B}{\omega_s^{(1)}} \frac{v_{b,g}}{\Gamma_B} G^{(1)} |b|^2$, where $v_{b,g}$ is the acoustic group velocity and Γ_B is the acoustic decay rate. This particular normalization allows the equations of motion for the field amplitudes to be written in terms of the usual Brillouin gain coefficient, for simplicity. Equations 6.29-6.31 describe SIMS in the presence of nonlinear loss.

To describe NIBS couplings, we introduce two additional optical waves (guided in a separate waveguide) which couple through the same acoustic phonon mode. These fields have power amplitudes $a_p^{(2)}$ and $a_s^{(2)}$, at distinct optical frequencies separated by the modulation frequency $\omega_s^{(2)} = \omega_p^{(2)} - \Omega$. In general, the spatial evolution of these fields is governed by equations corresponding to Eqs. 6.29-6.30:

$$\begin{aligned} \frac{\partial a_p^{(2)}}{\partial z} = & -\frac{G^{(2)}}{2} a_s^{(2)} b - \frac{1}{2} \left(\alpha_p^{(2)} + \beta_{pp}^{(2)} |a_p^{(2)}|^2 + \gamma_{ppp}^{(2)} |a_p^{(2)}|^4 \right) a_p^{(2)} - \\ & \frac{1}{2} \left(2\beta_{ps}^{(2)} + 4\gamma_{pps}^{(2)} |a_p^{(2)}|^2 + \gamma_{pss}^{(2)} |a_s^{(2)}|^2 \right) |a_s^{(2)}|^2 a_p^{(2)}, \quad (6.32) \end{aligned}$$

$$\begin{aligned} \frac{\partial a_s^{(2)}}{\partial z} = & \frac{G^{(2)}}{2} a_p^{(2)} b^* - \frac{1}{2} \left(\alpha_s^{(2)} + \beta_{ss}^{(2)} |a_s^{(2)}|^2 + \gamma_{sss}^{(2)} |a_s^{(2)}|^4 \right) a_s^{(2)} - \\ & \frac{1}{2} \left(2\beta_{sp}^{(2)} + 4\gamma_{ssp}^{(2)} |a_s^{(2)}|^2 + \gamma_{spp}^{(2)} |a_p^{(2)}|^2 \right) |a_p^{(2)}|^2 a_s^{(2)}, \quad (6.33) \end{aligned}$$

where we must also modify the phonon field (Eq. 6.31) to include drive terms from both sets of optical waves:

$$b = a_s^{(1)*} a_p^{(1)} + a_s^{(2)*} a_p^{(2)}. \quad (6.34)$$

Note that this modification opens the door to new types of couplings. In contrast to SIMS, which always mediates energy transfer from red to blue tones, NIBS can produce anti-Stokes couplings, and back-action on the phonon field with behavior dependent on the relative coupling phase.

Depending on the specific drive and modulator waveguide geometries, the linear and nonlinear coupling and loss coefficients can be very different for each set of optical waves. However, in the silicon NIBS modulator, drive and modulator waveguides are almost identical, so $G^{(1)} \approx G^{(2)}$, $\alpha_i^{(1)} \approx \alpha_i^{(2)}$, $\beta_{ij}^{(1)} \approx \beta_{ij}^{(2)}$, and $\gamma_{ijk}^{(1)} \approx \gamma_{ijk}^{(2)}$. In the equations of motion, we have also neglected the potential for inter-core nonlinear loss arising from diffusion of optically-driven free carriers from one core to the other. We do not experimentally observe excess inter-core loss even at the highest tested powers, so this simplification seems justified.

Together, Eqs. 6.29-6.30 and 6.32-6.34 describe the general spatial evolution of the coupled waves within the NIBS modulator, and are used to calculate the theoretical trend in Fig. 6.6.

6.6.2 Approximate Analytic Solution to Coupling Equations

To understand the limiting behavior of energy transfer through NIBS, we seek a closed-form solution to these coupling equations. In order to make this problem tractable, we neglect nonlinear loss, which we can later re-introduce in an approximate form, and consider only a single linear loss parameter $\alpha_s^{(1)} = \alpha_p^{(1)} \equiv \alpha^{(1)}$. We also assume that the optical powers in the modulator waveguide are relatively small, so that we can neglect the action of the modulator waveguide optical fields on the phonon amplitude $|a_s^{(1)} a_p^{(1)}| \gg |a_s^{(2)} a_p^{(2)}|$. In this case, the equations of motion for the five field amplitudes become:

$$\frac{\partial a_p^{(1)}}{\partial z} = -\frac{G^{(1)}}{2} a_s^{(1)} b - \frac{1}{2} \alpha^{(1)} a_p^{(1)}, \quad (6.35)$$

$$\frac{\partial a_s^{(1)}}{\partial z} = \frac{G^{(1)}}{2} a_p^{(1)} b^* - \frac{1}{2} \alpha^{(1)} a_s^{(1)}, \quad (6.36)$$

$$\frac{\partial a_p^{(2)}}{\partial z} = -\frac{G^{(2)}}{2} a_s^{(2)} b - \frac{1}{2} \alpha^{(2)} a_p^{(2)}, \quad (6.37)$$

$$\frac{\partial a_s^{(2)}}{\partial z} = \frac{G^{(2)}}{2} a_p^{(2)} b^* - \frac{1}{2} \alpha^{(2)} a_s^{(2)}, \quad (6.38)$$

$$b = a_s^{(1)*} a_p^{(1)}. \quad (6.39)$$

Substituting Eq. 6.39 into Eqs. 6.35-6.36 simplifies the equations for the fields in the drive waveguide to the form:

$$\frac{\partial a_p^{(1)}}{\partial z} = -\frac{G^{(1)}}{2} |a_s^{(1)}|^2 a_p^{(1)} - \frac{\alpha^{(1)}}{2} a_p^{(1)}, \quad (6.40)$$

$$\frac{\partial a_s^{(1)}}{\partial z} = \frac{G^{(1)}}{2} |a_p^{(1)}|^2 a_s^{(1)} - \frac{\alpha^{(1)}}{2} a_s^{(1)}. \quad (6.41)$$

Since we assumed that the phonon field is only strongly-driven by the waves within the drive waveguide, these equations are decoupled from those representing the modulator wave. We first seek the general solution to this pair, which will let us write down the spatial evolution of the phonon field b .

To simplify these equations, we make the change of variables $a_p^{(1)} = e^{-\alpha^{(1)}z/2}q_p^{(1)}$, $a_s^{(1)} = e^{-\alpha^{(1)}z/2}q_s^{(1)}$. The resulting equations read

$$\frac{\partial q_p^{(1)}}{\partial z} = -\frac{G^{(1)}}{2} |q_s^{(1)}|^2 e^{-\alpha^{(1)}z} q_p^{(1)}, \quad (6.42)$$

$$\frac{\partial q_s^{(1)}}{\partial z} = \frac{G^{(1)}}{2} |q_p^{(1)}|^2 e^{-\alpha^{(1)}z} q_s^{(1)}. \quad (6.43)$$

Note that these transformed equations satisfy the conservation relation $\frac{\partial}{\partial z} \left(q_p^{(1)*} q_p^{(1)} + q_s^{(1)*} q_s^{(1)} \right) = 0$. As a result, $|q_p^{(1)}|^2 + |q_s^{(1)}|^2$ is a constant exactly equal to the total input power $P_{\text{in}}^{(1)}$. This power conservation relation lets us decouple Eqs. 6.42-6.43:

$$\frac{\partial q_p^{(1)}}{\partial z} = -\frac{G^{(1)}}{2} \left(P_{\text{in}}^{(1)} - |q_p^{(1)}|^2 \right) e^{-\alpha^{(1)}z} q_p^{(1)}, \quad (6.44)$$

$$\frac{\partial q_s^{(1)}}{\partial z} = \frac{G^{(1)}}{2} \left(P_{\text{in}}^{(1)} - |q_s^{(1)}|^2 \right) e^{-\alpha^{(1)}z} q_s^{(1)}. \quad (6.45)$$

Finally, we seek a solution of these decoupled equations through direct integration. This is possible because, although $q_p^{(1)}$ and $q_s^{(1)}$ are complex numbers, their complex phase is unchanged with propagation. Therefore, we can make another set of substitutions $r_p^{(1)} = e^{-i\phi_p^{(1)}} q_p^{(1)}$ and $r_s^{(1)} = e^{-i\phi_s^{(1)}} q_s^{(1)}$, where $r_p^{(1)}$ and $r_s^{(1)}$ are real and $e^{i\phi_p^{(1)}}$ and $e^{i\phi_s^{(1)}}$ are the phase factors of the pump and Stokes waves, respectively. The equations governing the spatial evolution of these real variables are

$$\frac{\partial r_p^{(1)}}{\partial z} = -\frac{G^{(1)}}{2} \left(P_{\text{in}}^{(1)} - \left(r_p^{(1)} \right)^2 \right) e^{-\alpha^{(1)}z} r_p^{(1)}, \quad (6.46)$$

$$\frac{\partial r_s^{(1)}}{\partial z} = \frac{G^{(1)}}{2} \left(P_{\text{in}}^{(1)} - \left(r_s^{(1)} \right)^2 \right) e^{-\alpha^{(1)}z} r_s^{(1)}. \quad (6.47)$$

Each of these is now separable with the respective solutions

$$r_p^{(1)2}(z) = \frac{P_{\text{in}}^{(1)} e^{\frac{G^{(1)} P_{\text{in}}^{(1)}}{\alpha^{(1)}} (e^{-\alpha^{(1)} z} - 1)}}{k + e^{\frac{G^{(1)} P_{\text{in}}^{(1)}}{\alpha^{(1)}} (e^{-\alpha^{(1)} z} - 1)}}, \quad (6.48)$$

$$r_s^{(1)2}(z) = \frac{P_{\text{in}}^{(1)} k}{k + e^{\frac{G^{(1)} P_{\text{in}}^{(1)}}{\alpha^{(1)}} (e^{-\alpha^{(1)} z} - 1)}}, \quad (6.49)$$

where $k \equiv P_s^{(1)}(z=0)/P_p^{(1)}(z=0)$ is the ratio of input Stokes-wave to pump-wave power. Since the exponential terms in each solution, as well as k and $P_{\text{in}}^{(1)}$, are all positive, we take the positive square root of each side and transform back to field amplitudes using $a_p^{(1)} = e^{i\phi_p^{(1)}} e^{-\alpha^{(1)} z/2} r_p^{(1)}$, $a_s^{(1)} = e^{i\phi_s^{(1)}} e^{-\alpha^{(1)} z/2} r_s^{(1)}$:

$$a_p^{(1)}(z) = \frac{e^{i\phi_p^{(1)}} \sqrt{P_{\text{in}}^{(1)}} e^{-\alpha^{(1)} z/2} e^{\frac{G^{(1)} P_{\text{in}}^{(1)}}{2\alpha^{(1)}} (e^{-\alpha^{(1)} z} - 1)}}{\sqrt{k + e^{\frac{G^{(1)} P_{\text{in}}^{(1)}}{\alpha^{(1)}} (e^{-\alpha^{(1)} z} - 1)}}}, \quad (6.50)$$

$$a_s^{(1)}(z) = \frac{e^{i\phi_s^{(1)}} e^{-\alpha^{(1)} z/2} \sqrt{P_{\text{in}}^{(1)} k}}{\sqrt{k + e^{\frac{G^{(1)} P_{\text{in}}^{(1)}}{\alpha^{(1)}} (e^{-\alpha^{(1)} z} - 1)}}}. \quad (6.51)$$

The resulting driven phonon amplitude is directly calculated as

$$b(z) = a_s^{(1)*}(z) a_p^{(1)}(z) = \frac{e^{i(\phi_p^{(1)} - \phi_s^{(1)})} e^{-\alpha^{(1)} z} P_{\text{in}}^{(1)} \sqrt{k} e^{\frac{G^{(1)} P_{\text{in}}^{(1)}}{2\alpha^{(1)}} (e^{-\alpha^{(1)} z} - 1)}}{k + e^{\frac{G^{(1)} P_{\text{in}}^{(1)}}{\alpha^{(1)}} (e^{-\alpha^{(1)} z} - 1)}} \equiv e^{i\phi_b} |b(z)|, \quad (6.52)$$

where we have also rewritten the phonon amplitude as a product of a complex phase $e^{i\phi_b} = e^{i(\phi_p^{(1)} - \phi_s^{(1)})}$ and a real amplitude, $|b(z)|$.

We now return to the Eqs. 6.37-6.38 for the modulator-waveguide optical field amplitudes. Note that energy transfer may occur in either direction between these two fields. In particular, if we inject light into one of the two modes (fields), it is initially coupled to the other via either Stokes or anti-Stokes scattering. Through this analysis, we will focus on the Stokes scattering process, i.e. we inject probe light into the higher-frequency field. We

begin with the same change of variables $a_p^{(2)} = e^{-\alpha^{(2)}z/2}q_p^{(2)}$, $a_s^{(2)} = e^{-\alpha^{(2)}z/2}q_s^{(2)}$ to eliminate the optical loss term:

$$\frac{\partial q_p^{(2)}}{\partial z} = -\frac{G^{(2)}}{2}q_s^{(2)}b = -\frac{G^{(2)}}{2}q_s^{(2)}e^{i\phi_b}|b(z)|, \quad (6.53)$$

$$\frac{\partial q_s^{(2)}}{\partial z} = \frac{G^{(2)}}{2}q_p^{(2)}b^* = \frac{G^{(2)}}{2}q_p^{(2)}e^{-i\phi_b}|b(z)|. \quad (6.54)$$

As before, we would like to transform these complex differential equations to terms involving real variables with a complex overall phase. We use the substitutions $r_p^{(2)} = e^{-i\phi_p^{(2)}}q_p^{(2)}$ and $r_s^{(2)} = e^{-i(\phi_b+\phi_p^{(2)})}q_s^{(2)}$, where $e^{i\phi_p^{(2)}}$ is the input phase of the probe wave in the modulator waveguide. This transformation eliminates the phase of the phonon field which we introduced earlier, to yield the coupled equations

$$\frac{\partial r_p^{(2)}}{\partial z} = -\frac{G^{(2)}}{2}r_s^{(2)}|b(z)|, \quad (6.55)$$

$$\frac{\partial r_s^{(2)}}{\partial z} = \frac{G^{(2)}}{2}r_p^{(2)}|b(z)|. \quad (6.56)$$

In contrast to the equations for the drive waveguide, here we can only assume a single arbitrary phase factor $e^{i\phi_p^{(2)}}$ for the pump wave, while the scattered Stokes wave is constrained to phase $\phi_b + \phi_p^{(2)}$. If some amount of light in the Stokes wave were incident at a different phase, then the dynamics of this problem become more complicated. Instead, we assume that there is no incident Stokes signal, as is typically the case. In this situation we let $r_p^{(2)}$ be real since we have already factored out an arbitrary phase, and hence $r_s^{(2)}$ will also be real.

These equations satisfy the power conservation relation $\frac{\partial}{\partial z} \left((r_p^{(2)})^2 + (r_s^{(2)})^2 \right) = 0$, so as before we can write $(r_p^{(2)})^2 + (r_s^{(2)})^2 = P_{\text{in}}^{(2)}$, where $P_{\text{in}}^{(2)}$ is the total incident power in the modulator waveguide and is assumed to be incident entirely in the blue-detuned probe wave, i.e. $P_{\text{in}}^{(2)} = (r_p^{(2)})^2 (z=0)$. The spatial evolution of the probe wave then obeys the

equation:

$$\frac{\partial r_s^{(2)}}{\partial z} = \frac{G^{(2)}}{2} \sqrt{P_{\text{in}}^{(2)} - \left(r_s^{(2)}\right)^2} |b(z)|. \quad (6.57)$$

Regardless of the form of the phonon field $|b(z)|$, this equation is separable:

$$\frac{\partial r_s^{(2)}}{\sqrt{P_{\text{in}}^{(2)} - \left(r_s^{(2)}\right)^2}} = \frac{G^{(2)}}{2} |b(z)| \partial z \quad (6.58)$$

In other words, provided that we can integrate the driven phonon field over space, we can find an exact expression for the Stokes signal power. When the phonon amplitude is given by Eq. 6.52, this equation becomes

$$\int \frac{\partial r_s^{(2)}}{\sqrt{P_{\text{in}}^{(2)} - \left(r_s^{(2)}\right)^2}} = \int \frac{G^{(2)} e^{-\alpha^{(1)}z} P_{\text{in}}^{(1)} \sqrt{k} e^{\frac{G^{(1)} P_{\text{in}}^{(1)}}{2\alpha^{(1)}} (e^{-\alpha^{(1)}z} - 1)}}{k + e^{\frac{G^{(1)} P_{\text{in}}^{(1)}}{\alpha^{(1)}} (e^{-\alpha^{(1)}z} - 1)}} \partial z. \quad (6.59)$$

The lefthand side may be integrated with a trigonometric substitution, and the righthand side is integrable with the substitution $u = e^{-\alpha^{(1)}z}$.

$$\tan^{-1} \left(\frac{r_s^{(2)}}{\sqrt{P_{\text{in}}^{(2)} - \left(r_s^{(2)}\right)^2}} \right) = \frac{G^{(2)}}{G^{(1)}} \left(\tan^{-1} \left(\frac{1}{\sqrt{k}} \right) - \tan^{-1} \left(\frac{e^{\frac{G^{(1)} P_{\text{in}}^{(1)}}{2\alpha^{(1)}} (e^{-\alpha^{(1)}z} - 1)}}{\sqrt{k}} \right) \right), \quad (6.60)$$

which leads to

$$r_s^{(2)} = \sqrt{P_{\text{in}}^{(2)}} \sin \left(\frac{G^{(2)}}{G^{(1)}} \left(\tan^{-1} \left(\frac{1}{\sqrt{k}} \right) - \tan^{-1} \left(\frac{e^{\frac{G^{(1)} P_{\text{in}}^{(1)}}{2\alpha^{(1)}} (e^{-\alpha^{(1)}z} - 1)}}{\sqrt{k}} \right) \right) \right). \quad (6.61)$$

Substituting back to find the original complex field amplitude using $a_s^{(2)} = e^{i(\phi_p^{(1)} - \phi_s^{(1)} + \phi_p^{(2)})} e^{-\alpha^{(2)}z/2} r_s^{(2)}$

we have

$$a_s^{(2)} = \sqrt{P_{\text{in}}^{(2)}} e^{i(\phi_p^{(1)} - \phi_s^{(1)} + \phi_p^{(2)})} e^{-\alpha^{(2)}z/2} \sin \left(\frac{G^{(2)}}{G^{(1)}} \left(\tan^{-1} \left(\frac{1}{\sqrt{k}} \right) - \tan^{-1} \left(\frac{e^{\frac{G^{(1)} P_{\text{in}}^{(1)}}{2\alpha^{(1)}} (e^{-\alpha^{(1)}z} - 1)}}{\sqrt{k}} \right) \right) \right). \quad (6.62)$$

This equation gives the amplitude of the Stokes-scattered signal in the modulator waveguide for any combination of input drive and probe powers, or Brillouin couplings. We can also calculate the modulation efficiency η^2 , which we defined earlier as the ratio of the output scattered power relative to the incident optical power in the modulator waveguide:

$$\begin{aligned} \eta^2 &\equiv \frac{P_s^{(2)}(L)}{P_{\text{in}}^{(2)}} = \frac{a_s^{(2)*}(L) a_s^{(2)}(L)}{P_{\text{in}}^{(2)}} \\ &= e^{-\alpha^{(2)}L} \sin^2 \left(\frac{G^{(2)}}{G^{(1)}} \left(\tan^{-1} \left(\frac{1}{\sqrt{k}} \right) - \tan^{-1} \left(\frac{e^{\frac{G^{(1)} P_{\text{in}}^{(1)}}{2\alpha_1} (e^{-\alpha^{(1)}L} - 1)}}{\sqrt{k}} \right) \right) \right). \end{aligned} \quad (6.63)$$

Here $z = L$ is the total device length. To reach the maximum efficiency, the expression inside the sine-squared term should be equal to $\pi/2$. Of course, it is not always possible to increase the drive power or Brillouin coupling strength at will. For fixed values of $G^{(1)}$ and $P_{\text{in}}^{(1)}$, (i.e. given a device design and power budget), this expression is maximized when

$$k = e^{\frac{G^{(1)} P_{\text{in}}^{(1)}}{2\alpha^{(1)}} (e^{-\alpha^{(1)}L} - 1)}. \quad (6.64)$$

This condition describes an optimal way to bias the relative input powers of the two optical waves in the drive waveguide. Assuming that we can reach this optimal power biasing, the minimum drive power to reach unity efficiency (complete power conversion, neglecting linear insertion loss, in the modulator waveguide) is:

$$P_{\text{in}}^{(1)} = \frac{2\alpha^{(1)}}{G^{(1)} (e^{-\alpha^{(1)}L} - 1)} \log \left(\tan^2 \left(\frac{\pi}{4} \left(1 - \frac{G^{(1)}}{G^{(2)}} \right) \right) \right). \quad (6.65)$$

Special Case: $G^{(1)} = G^{(2)}$

Eq. 6.65 describes the minimum drive power to reach unity conversion within a system where the drive- and modulator-waveguide Brillouin gain coefficients are unequal. It turns out that this configuration may actually be beneficial to achieving large NIBS energy transfer.

By contrast, in symmetrical systems the Brillouin coupling coefficients for each waveguide are nearly identical, as is the case for the silicon NIBS modulator where the drive

and modulator waveguide core sizes and wavelengths are different by less than 2%. In this situation, the equations governing the energy transfer dynamics simplify considerably. In the case where $G^{(1)} = G^{(2)} \equiv G$, Eq. 6.63 becomes

$$\eta^2 = e^{-\alpha^{(2)}L} \frac{k}{k+1} \frac{\left(\frac{GP_{\text{in}}^{(1)}}{e^{2\alpha^{(1)}}} (1 - e^{-\alpha^{(1)}L}) - 1 \right)^2}{\left(k e^{\frac{GP_{\text{in}}^{(1)}}{\alpha^{(1)}}} (1 - e^{-\alpha^{(1)}L}) + 1 \right)}. \quad (6.66)$$

In this case, it is impossible to exactly reach 100% energy transfer. An absolute upper bound on η^2 is defined by the relative ratio of input pump to Stokes powers in the modulator waveguide.

$$\lim_{GP_{\text{in}}^{(1)} \rightarrow \infty} \eta^2 = e^{-\alpha^{(2)}L} \frac{1}{k+1} \quad (6.67)$$

In other words, in the case of equal couplings, the fractional power transfer in the modulator waveguide is bounded by the fractional power transfer in the drive waveguide. This limit results from pump depletion, and hence phonon field attenuation, in the drive waveguide.

In practical experimental systems, there is an upper limit on optical power, Brillouin coupling, and device length. When these are fixed, the maximum energy transfer is achieved when the input power ratio k satisfies Eq. 6.64. In this case, the maximum efficiency is given by:

$$\eta_{\text{max}}^2 = e^{-\alpha^{(2)}L} \tanh^2 \left(\frac{GP_{\text{in}}^{(1)} (1 - e^{-\alpha^{(1)}L})}{4\alpha^{(1)}} \right). \quad (6.68)$$

If drive-waveguide propagation losses are small ($\alpha^{(1)}L \ll 1$), then this expression simplifies further

$$\eta_{\text{max}}^2 = e^{-\alpha^{(2)}L} \tanh^2 \left(\frac{GP_{\text{in}}^{(1)}L}{4} \right). \quad (6.69)$$

6.6.3 Externally-driven Phonon Field

In the previous sections, we have derived expressions governing NIBS energy transfer in the case of distributed driving of the elastic field by a pair of coupled optical drive waves. In order to achieve maximum energy transfer within a reasonable device footprint, other driving schemes would likely be preferable, e.g. re-injection of drive light along device length,

or electromechanical driving of the phonon mode [351,352]. To evaluate these possibilities, we briefly consider the case of an arbitrary phonon amplitude profile.

From Eq. 6.58, we derive an analogous result to Eq. 6.63 for an arbitrary external phonon field:

$$\eta^2 \equiv \frac{P_s^{(2)}(L)}{P_{\text{in}}^{(2)}} = e^{-\alpha^{(2)}L} \sin^2 \left(\int_0^L \frac{G^{(2)} |b(z)| dz}{2} \right). \quad (6.70)$$

For a phonon field $b(z) = b_0$ whose power amplitude is constant in space, this expression becomes:

$$\eta^2 = e^{-\alpha^{(2)}L} \sin^2 \left(\frac{G^{(2)} b_0 L}{2} \right). \quad (6.71)$$

This efficiency is maximized when $G^{(2)} b_0 L = \pi$ or an odd multiple of π .

Note that for an optically-driven acoustic phonon $b_0 \propto \sqrt{P_p^{(1)} P_s^{(1)}}$, so we can actually find a minimum bound on the optical power necessary to achieve unity modulation efficiency. This could be the case if we utilize re-injection of drive light along the waveguide, or an alternate phonon emission scheme which does not produce phonon depletion (for example using intra-mode FSBS). Alternately, resonant designs for the drive waveguide could achieve similar benefits at lower input powers. Regardless of the drive scheme, assuming $P_p^{(1)} = P_s^{(1)} = P_{\text{in}}^{(1)}/2$, which locally maximizes the driven phonon amplitude, then $G^{(2)} P_{\text{in}}^{(1)} L > 2\pi$. By contrast, in the case of a linear NIBS modulator, Eq. 6.66 gives a condition $G^{(2)} P_{\text{in}}^{(1)} L = 12$ for 99% modulation efficiency in a linear device.

We can calculate the corresponding z -directed acoustic power necessary for unity efficiency by invoking the normalization condition $P_b = \frac{\Omega_B v_{b,g}}{\omega_s \Gamma_B} G |b_0|^2$ where we assume a single Brillouin coupling coefficient G and optical Stokes frequency ω_s . In this case, the approximate acoustic power required for complete energy transfer from pump to Stokes waves is

$$P_b = \frac{\Omega_B v_{b,g}}{\omega_s \Gamma_B} \frac{\pi^2}{GL^2}, \quad (6.72)$$

which can also be expressed in terms of the distributed optomechanical coupling strength g_0 as [233]

$$P_b = \hbar \Omega_B \frac{v_{b,g} v_s v_p}{4 |g_0|^2} \frac{\pi^2}{L^2}, \quad (6.73)$$

where v_s and v_p are the optical group velocities of the pump and Stokes waves. For a Brillouin-active silicon waveguide with identical parameters to those studied here, this threshold acoustic power is:

$$P_b = \frac{2\pi \cdot 5.7 \text{ GHz}}{2\pi \cdot 194 \text{ THz}} \cdot \frac{826 \text{ m s}^{-1}}{2\pi \cdot 17 \text{ MHz}} \cdot \frac{\pi^2}{(0.024 \text{ m})^2} \cdot \frac{1}{195 \text{ W}^{-1} \text{ m}^{-1}} = 20 \text{ nW}. \quad (6.74)$$

Traveling-wave acoustic powers of this magnitude could easily be achieved through electromechanical driving, or by SIMS-mediated phonon emission in silicon at mid-IR wavelengths, where two-photon absorption vanishes, permitting order-of-magnitude increases in optical power handling.

6.7 Improving Modulation Bandwidth with Waveguide Dispersion Engineering

The phase-matching bandwidth $\Delta\omega_{\text{FWHM}}$ of the NIBS process is determined by the group velocities of the participating optical modes according to Eq. 6.10. Specifically, this bandwidth is inversely proportional to the difference in group indexes of the modulator-waveguide waves $\Delta n_g = |n_{g,+}^{(2)} - n_{g,-}^{(2)}|$. Reducing the difference in group indexes between these fields therefore provides a means to directly enhance the bandwidth of the NIBS modulator. Note also that this increase in modulation bandwidth preserves the nonreciprocal performance, since the frequency splitting between ω_f and ω_b also scales inversely with Δn_g as seen in Eq. 6.12.

The optical group velocities of the modes are determined by the cross-section refractive index profile of the modulator waveguide. Therefore, minimizing Δn_g can be achieved through careful choice of the waveguide design and material system [258, 353–357] as a means to maximize the NIBS modulator bandwidth.

As an example, we compare the phase-matching bandwidth of the silicon NIBS modulator and an alternate design based on a modified waveguide geometry. Fig. 6.8a shows the cross-sectional geometry used for each waveguide core of the NIBS modulator, and the symmetric and anti-symmetric optical mode profiles. For this design, the simulated difference of

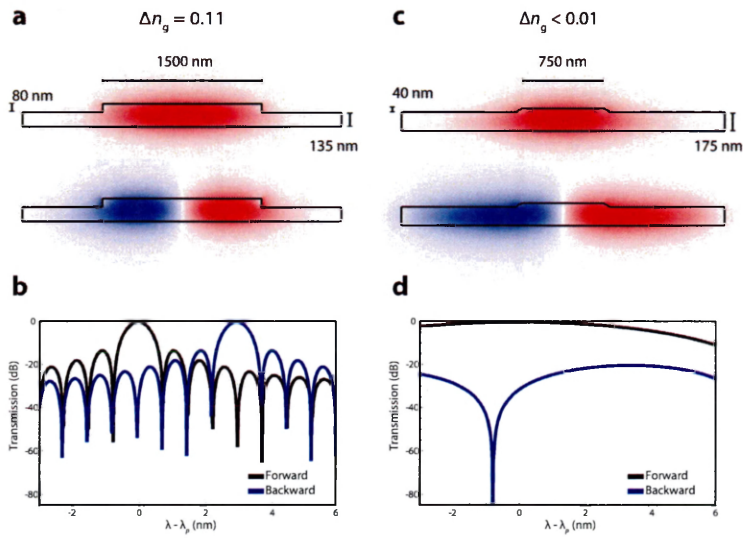


Figure 6.8: **Dispersion engineering and the phase-matching bandwidth.** (a) shows the relevant cross-sectional dimensions of a ridge waveguide used to construct the silicon NIBS modulator, and the simulated x -component of the electric field for the symmetric and anti-symmetric optical modes. (b) Calculated normalized transmission as a function of wavelength shows the expected sinc-squared response in the forward and backward directions. (c) An alternative ridge waveguide design with reduced ridge dimensions and angled sidewalls, resulting in a tenfold reduction in the difference of group indexes. (d) Calculated normalized transmission of a NIBS process using waveguides shown in (c). The reduction of Δn_g increases the bandwidth by a factor of ten. Adapted from Ref. [224].

group indexes $\Delta n_g = 0.11$. The expected forward- and backward-transmission response of a NIBS modulator based on this waveguide design is illustrated in Fig. 6.8b. An alternate, weakly-guiding waveguide design is illustrated in Fig. 6.8c, where the dimensions of the guiding ridge are half of those in 6.8a and the sidewalls are at a 65° angle. The difference in optical group indices for the two modes in this design is calculated to be $\Delta n_g = 0.01$. The calculated transmission response of the modified device is illustrated in Fig. 6.8d, showing a >10 -fold increase in modulation bandwidth. Similar decreases in Δn_g can be achieved by a variety of different design strategies to enable ultra-broadband nonreciprocal devices in silicon photonic circuits.

6.8 Discussion and Summary

In this chapter, we have proposed and demonstrated an intriguing form of traveling-wave Brillouin-based nonreciprocal modulation in an optomechanical silicon waveguide. Through this process, we have demonstrated high-fidelity nonreciprocal couplings over large (>125 GHz) operation bandwidths in an ultralow-loss integrated waveguide for the first time. Furthermore, through optical tuning of a driven phonon wavevector, we have shown tunability of this process over a 4 THz (35 nm) frequency window. Because the bandwidth of the NIBS modulator is directly set by the dispersion of the participating optical modes ($\propto |n_{g,-}^{(1)} - n_{g,+}^{(2)}|^{-1}$), nonreciprocal devices with operation bandwidths greater than 10-100 nm may be possible through such interactions [239, 258]. These results point to inter-band acousto-optic scattering as a promising method to create high-performance non-magnetic isolators and circulators within integrated photonic circuits.

The use of a nonlocal traveling-wave acoustic emitter to drive inter-band transitions permits low-loss nonreciprocal modulation. This approach avoids a difficulty of early electro-optic implementations where designing structures to induce an asymmetric index modulation over cm-scales led to prohibitively high (70 dB/cm) propagation losses [348]. By contrast, the silicon NIBS modulator permits linear propagation losses as low as 0.2 dB/cm and 0.4 dB/cm for the symmetric and anti-symmetric optical modes, respectively. The traveling-wave NIBS modulator extends narrowband schemes for nonreciprocity based on

resonant optomechanical [188, 207–211, 221, 344–346] or acousto-optic structures [351] to broadband operation; because NIBS uses no optical resonances, and a steady-state driven elastic wave, it permits reconfigurable nonreciprocal operation over a bandwidth 7000 times greater than that of its intrinsic resonant elastic response.

To ultimately adapt the inter-band modulator to low-loss isolator and circulator designs, it is necessary to achieve internal efficiencies close to unity. Through the experiments of this chapter, we have demonstrated scattering efficiency $\eta^2 \approx 1\%$ using an average drive-waveguide power $P \approx 90$ mW. While this efficiency scales $\propto P^2$, power handling within these types of waveguide structures is limited to ~ 200 mW without improved thermal anchoring or surface passivation steps. Alternately, optical power handling could be improved through electrical extraction of optically-produced free carriers [236], or by designing the drive waveguide to operate at wavelengths above $\lambda = 2.1$ μm , where two-photon absorption vanishes in silicon.

An alternate approach to realize near-unity coupling is by utilizing piezoelectric phonon generation, as in Ref. [351], to drive the inter-band transition. While this approach is not generally wavevector-tunable, it should permit efficient conversion of electro energy into elastic waves. While optical driving produced phonon powers on the sub-nW level within the silicon NIBS modulator, piezoelectric transduction is routinely used to produce acoustic powers $\gg 1$ mW [352, 358–361], and can be engineered to provide the necessary elastic wave shape and wavevector for efficient inter-band coupling. In the future, electromechanical transducer designs which produce distributed phonon emission similar to the electrostrictive drive in the NIBS modulator could offer an energy-efficient path toward high-performance, waveguide-integrated acousto-optic isolators.

In summary, in this chapter we have demonstrated a new form of nonlocal, inter-modal Brillouin coupling drawing heavily on the advances of the previous chapters to demonstrate broadband nonreciprocal acousto-optic modulation. This work represents the fruition of a collection of prior theoretical [239, 258, 347] and experimental works [188, 221] toward the creation of novel (and hopefully useful) functionalities within integrated photonic systems.

Chapter 7

Conclusion

Through the work documented in this dissertation, we have developed a variety of devices which harness light-sound couplings within integrated waveguides. This research has been extremely exciting, not only because of the fascinating physics underpinning these various optomechanical systems, but also since it has brought new functionalities to the toolkit of silicon photonics, a field which at this point seems comparatively mature.

Retrospectively, the output of this research may be grouped according to several overarching themes: First, although the development of FSBS- and SIMS-based optical amplifiers led to an array of interesting phonon physics, these studies were grounded in the field of integrated nonlinear optics. In particular, the use of multimode interactions enabled powerful control over the dynamics of nonlinear energy transfer in guided-wave systems. Beyond integrated devices, this paradigm seems to simultaneously be of growing interest to the study of more traditional optical platforms, such as with Kerr and Raman interactions in optical fiber.

Second, all of the devices presented here harness interactions between traveling-wave photons and phonons. In contrast to cavity-optomechanical systems, which can be thought of as zero-dimensional, traveling-wave systems allow for broadband interactions, as well as tailorable spatial dynamics. These degrees of control enable a wide array of behaviors ranging from intrinsic decoupling of Stokes and anti-Stokes scattering in inter-modal SBS, to broadband optomechanical modulation achieved through the PPER and NIBS modulator devices. These types of traveling-wave interactions provide a path to new flexible and

tunable signal-processing operations in guided-wave systems.

Finally, all of these operations (Brillouin amplification, lasers, filtering, modulation, etc.) were realized within integrated silicon waveguides, opening the door to incorporating photon-phonon couplings within silicon photonics. However, since SBS interactions occur in practically every material, these concepts may be readily adapted to other platforms, including both fiber- and microchip-based devices.

The ultimate impact of these, and many other Brillouin-based technologies, depends on the feasibility of their integration within complex integrated photonic circuits. In this sense, the demonstration of flexible techniques for Brillouin-based signal processing in silicon is particularly important, especially for Brillouin amplifiers and lasers. We hope that, in the coming years, these new advances will lead to further innovation in Brillouin photonics, and inspire new useful photonic-phononic devices within a variety of optical systems.

Appendix A

Methods: Fabrication

The fabrication of the devices presented in this dissertation were performed at Yale University in the Applied Physics Cleanroom and at the Yale Institute for Nanoscience and Quantum Engineering (YINQE). In this appendix, we outline the fabrication process common to these different devices.

Fabrication begins with commercial 6" silicon-on-insulator (SOI) wafers produced by Soitec. For the devices presented in this dissertation, these wafers had a top crystalline silicon layer with a thickness around 215 nm and a buried SiO₂ layer 3 μm thick on top of a Si carrier.

A.1 Preparation of Alignment Markers and SOI Chips

Square alignment markers 40 × 40 μm in dimension are patterned across the wafer using a Cr/Au deposition and liftoff process on a photoresist bi-layer consisting of P(MMA-MAA) underneath PMMA (poly-methylmethacrylate-methacrylic acid copolymer layer underneath poly-methylmethacrylate resist). When patterning these markers using electron-beam (e-beam) lithography, the more sensitive copolymer becomes overexposed, creating an undercut during development. For developing PMMA, we use isopropyl alcohol (IPA):water [362]. Liftoff is performed in room-temperature N-Methylpyrrolidone (NMP), with an NMP squeeze bottle used to remove any remaining metal flecks from the surface.

Once alignment markers have been successfully patterned on the wafer, we cover the

surface with a protective PMMA layer and dice the wafer into rectangular chips 35x22 mm in dimension using an ADT proVectus wafer saw.

A.2 Ridge Waveguide Fabrication

Next, we write the ridge waveguide and input coupler structures. This process begins with a standard solvent cleaning step—we place the chip in an ultrasonic cleaner for 2 minutes each in acetone (which removes the PMMA layer), isopropyl alcohol, and water. Afterward, we rinse the chip again with water until no droplets are observed sticking to dirt on the surface.

For writing the silicon waveguides we use Dow Corning[®] XR-1541 hydrogen silsesquioxane (HSQ) negative-tone photoresist, which provides high resolution and good etch resistance. To preserve the quality of this relatively unstable resist (which degrades over months even when kept in a freezer), we store it in liquid nitrogen and thaw before use [363]. The waveguide structure designs are written using electron beam lithography and developed using Microposit[™]MF[™]-312 developer (0.54 M tetramethylammonium hydroxide with surfactant). During development, a large amount of unexposed resist is removed, causing bubbles to form on the surface of the chip—these are removed by repeatedly removing and dipping the chip in the developer.

After development, the waveguide structures are dry-etched using reactive ion etching (RIE) in Cl₂ plasma using an Oxford Instruments PlasmaPro 100 system. Prior to etching, good quality of the gas plasma is ensured by a chamber conditioning step where a stable plasma is achieved on a silica carrier wafer and a light blue color of the chlorine plasma is observed. Etch rates are calibrated by using a test chip with a fixed etch time and a thin film interferometer to measure thickness before and after etching. After calibration of the etch rate, we etch 80 nm through the top silicon wafer to define the silicon waveguides.

A.3 Membrane and Slot Fabrication

Prior to patterning the slots which act as phononic mirrors, another ultrasonic solvent cleaning step is performed. Note that the exposed HSQ photoresist on top of the waveguide

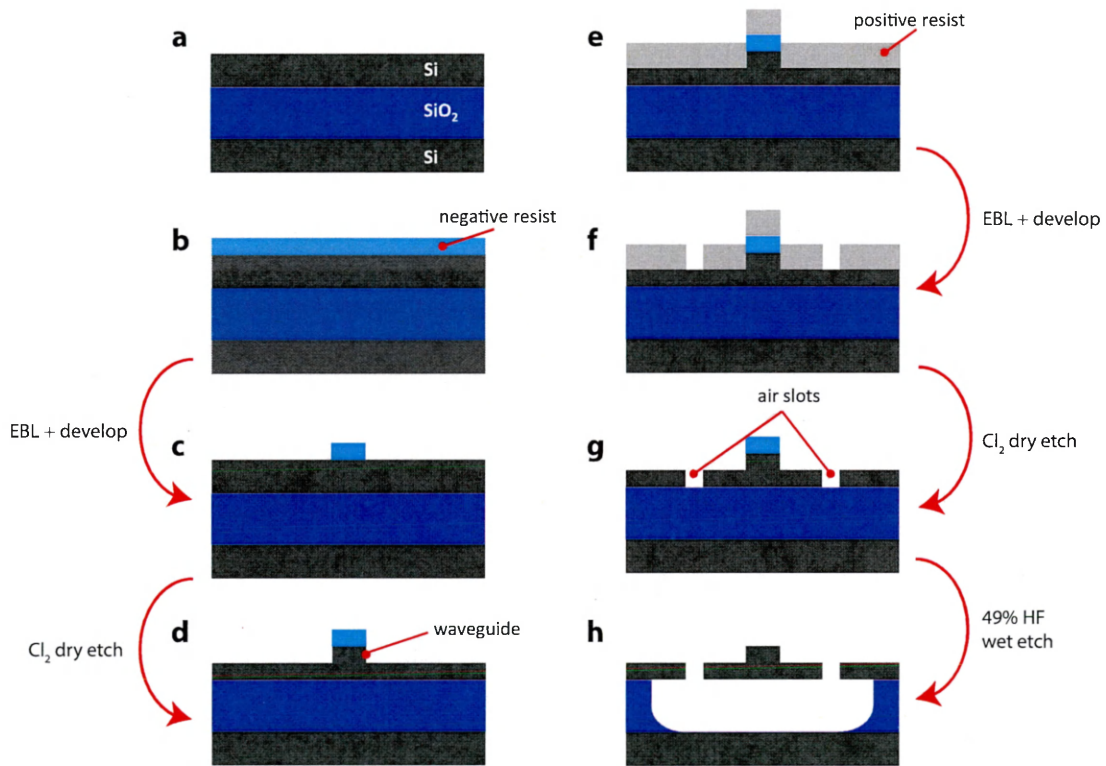


Figure A.1: **Suspended silicon membrane waveguide fabrication.** (a) Diagram of the SOI wafer cross-section as-received. (b) depicts the wafer after HSQ resist is spun on the surface. (c) e-beam lithography defines the waveguide pattern layer. After development of the exposed layer and etching, these patterns are transferred to the silicon layer through Cl₂ reactive ion etching, shown in (d). (e) shows the cross-section when a second positive resist is spun on top of the processed wafer. (f) A second electron beam lithography and development step defines patterns for the slot features. (g) These features are etched through the silicon top layer through a second Cl₂ dry etch step. (h) depicts the final structure after wet-etching in HF. *Image credit: Heedeuk Shin and Eric Kittlaus.*

structure is still present at this point.

For writing the slots, we use a positive-tone photoresist, either Zeon ZEP 520A or Allresist CSAR 62. After spinning resist, a pre-exposure soft bake at 180° C is performed to remove residual solvent. Slot structures are written using electron beam lithography, with alignment to the waveguide structures facilitated by the gold alignment markers. The positive photoresist is developed using xylenes, after which alignment between waveguide and slot structures is verified using an optical microscope.

The slot patterns are etched using a second Cl₂ RIE step which removes the entire silicon top-layer where the photoresist is exposed. Thereafter, the photoresist is removed using NMP, and another ultrasonic cleaning step is performed to ensure that the chip is free of dirt.

Finally, the silica undercladding is removed underneath the waveguide-slot structures using wet etching in 49% hydrofluoric (HF) acid with a few drops of Sigma-Aldrich® Tergitol™ surfactant added to allow the acid solution to freely flow into the slots. Typically the etch rate is around 1-2 μm per minute, so this step lasts a few minutes to ensure that the membrane waveguide structure is fully suspended. This step also removes the exposed HSQ photoresist. Afterward, the chip is immediately transferred to a container containing deionized water with Tergitol™, and then to two successive beakers of IPA for rinsing. The chip is then allowed to air-dry.

Appendix B

Methods: Coupling to Integrated Waveguide Devices

In this section, we briefly describe the methods used to couple light to chip-based devices. One important complexity of many of the optomechanical waveguides studied in this dissertation is that they have several physical input and output ports. For example, the SIMS-active waveguide and IM-PPER devices have two inputs and two outputs for a total of four-ports. The NIBS modulator has a total of eight ports. While the specific experimental setups used to characterize these devices consist of commercially-available fiber-coupled active and passive components, free-space coupling to waveguide-integrated devices is facilitated by a combination of mechanical stages, precision-mounted fiber arrays, and on-chip diffractive components.

B.1 Integrated Grating Couplers

To couple light in and out of our integrated optical devices, we use grating couplers [364,365], with designs of the type shown in Fig. B.1a-b. The grating coupler, with a fixed pitch Λ , scatters light from a cleaved single-mode optical fiber into the planar silicon waveguide structure. These grating couplers are fabricated in the same step as silicon ridge waveguides, and thus share the same etch depth $d \approx 80$ nm. This process therefore allows simple fabrication of waveguide couplers at any location on the SOI chip. In contrast to end-firing

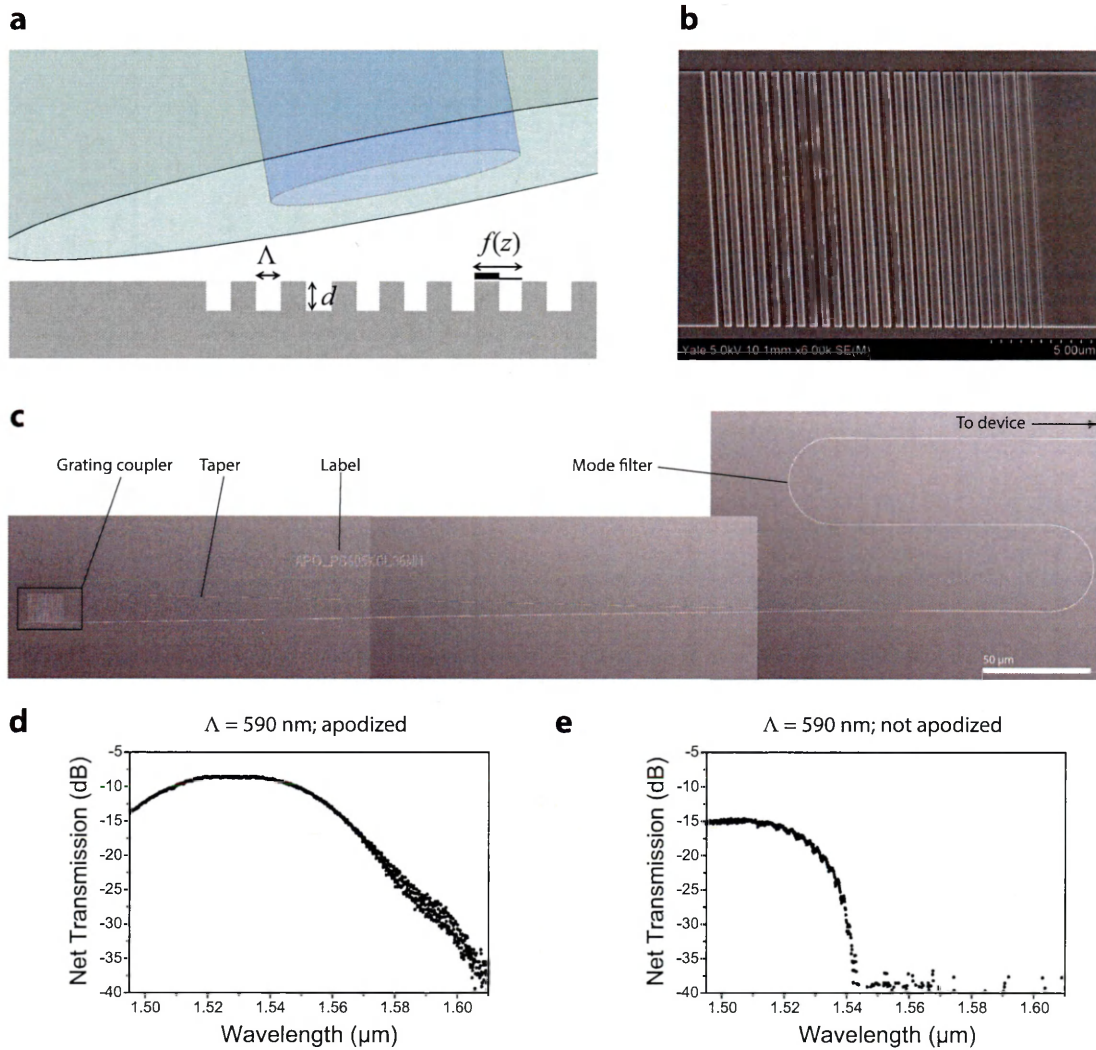


Figure B.1: **Input coupling for SOI waveguides using grating couplers.** (a) shows a schematic of an optical fiber aligned to an integrated grating coupler, with relevant grating dimensions: pitch Λ , etch depth d , and filling factor $f(z)$. (b) close-up SEM of a fabricated grating coupler, with an apodized filling factor (c) depicts stitched-together SEMs showing the entire input coupler region of a SOI ridge waveguide (d) and (e) show sample transmission data for waveguides interfaced with two apodized grating couplers (d) or two grating couplers with a constant fill factor (e).

with tapered structures, which have the advantage of low-loss and broadband coupling into integrated waveguides, grating couplers are simple to fabricate, allow flexible coupling from above the chip surface, offer high power-handling, and are mechanically robust. They have the drawbacks of being relatively narrowband (our designs typically efficiently couple light over ~ 50 nm FWHM bandwidths), and comparatively inefficient without the use of optimized and/or multi-layer fabrication [364, 366, 367].

To optimize the performance of our grating couplers, we vary the filling-factor (or duty cycle) $f(z)$ of our gratings as a function of position. These apodized designs modulate the grating reflectivity as a function of tooth number to mode-match to the Gaussian-like field distribution of the optical fiber mode [364, 367]. This behavior can be understood from the fact that a grating with equal teeth matches to a scattered field profile that is exponentially decaying in space. Therefore an optimized grating should scatter light more strongly when it is far away from the waveguide input. One such apodized grating is depicted in the SEM in Fig. B.1b. A comparison between the transmission spectra of fabricated apodized and non-apodized gratings is shown in Fig. B.1d-e. Each figure shows the net transmission through a silicon waveguide interfaced with two identical grating couplers. The device with apodized gratings displays higher peak transmission (-4.25 dB/facet vs -7.5 dB/facet), and better out-of band transmission than the non-apodized device, as well as a red-shifted center band. These grating couplers are designed to couple to optical fibers at an angle 8° from normal to the chip surface.

After light is routed into the silicon layer by a grating coupler, the $13\text{-}\mu\text{m}$ -wide silicon ridge waveguide is tapered down to a single-mode width of 450 nm, and wrapped in an s-bend. This design, shown in the top-down SEMs in Fig. B.1c, acts as a mode filter that radiates any higher-order modal content. Thereafter, light is routed into the active device region.

B.2 Coupling to On-chip Devices using Fiber Arrays

To address integrated waveguides on the SOI chip, we align cleaved single-mode optical fibers to grating couplers using an experimental setup of the type diagrammed in Fig.

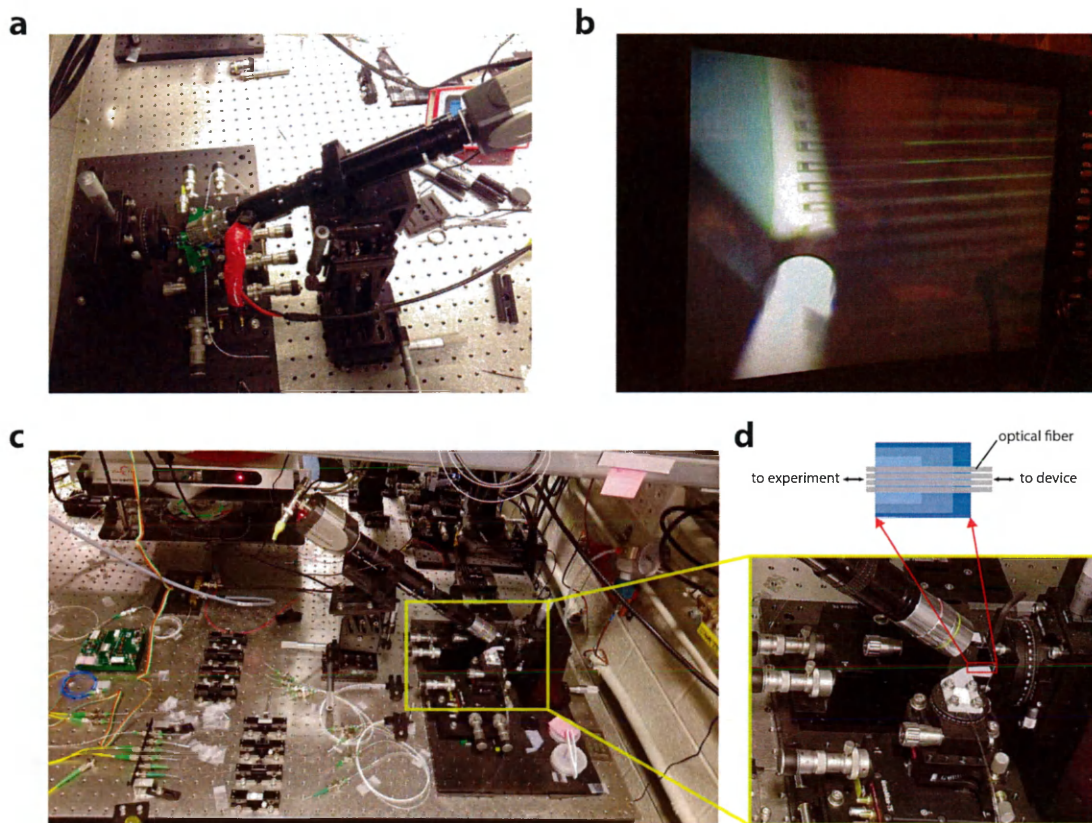


Figure B.2: **Experimental setup for coupling light into integrated optical waveguides.** (a) shows an early two-port setup where optical fibers are aligned to the surface of an SOI chip using mechanical translation and rotation stages. An optical imaging system allows alignment of the fibers to integrated grating couplers with micron-scale position, as shown in (b). (c) pictures an alignment setup for characterizing devices with eight total ports. An inset is expanded in (d), showing the region where light is coupled on- and off-chip using optical fiber arrays.

B.2a. Throughout these experiments, the fiber axis is tilted 8° relative to the chip normal to maximize coupling and mitigate back-reflections. Two precision three-axis linear stages are used to couple light on- and off-chip, respectively, and are interfaced with additional mechanical stages which allow rotational degrees of freedom as necessary. Additional linear stages provide long-distance translation of the three-axis stages in one direction parallel to the chip surface, while the chip itself is connected to linear stages which provide long travel in the other two dimensions. Finally, the chip is mounted on top of a 360° rotation stage to ensure that waveguides are aligned parallel to the optical table. An imaging microscope system facilitates alignment of the optical fibers to the chip-based grating couplers (Fig. B.2b).

For the multiport devices studied in Chapters 4-6, we use fiber arrays based on v-groove assemblies, which house precisely-spaced optical fibers with a pitch matching the designed separation between adjacent grating couplers on-chip. We fabricated two-port fiber arrays in-house, where the fibers were designed to extend several millimeters out from the end of the fiber array, allowing easy imaging and alignment of the fiber tips, as depicted in Fig. B.2b. To address the eight-port NIBS modulator devices of Chapter 6, we used commercial v-groove fiber arrays produced by OZ Optics Ltd., which contain fibers flush with the edge of the fiber array assembly. For this experiment, alignment was facilitated by visible-wavelength alignment lasers.

The eight-port setup is pictured in Fig. B.2c-d. The polarization state at each of the four inputs and outputs is controlled by the eight fiber polarization controllers on the optical table. Fiber arrays are mounted on 3D-printed adapters designed to position the fiber array housing normal to the chip.

Bibliography

- [1] J. W. Strutt. On the light from the sky, its polarization and colour. *Philos. Mag.*, 41(271):107–120, 1871.
- [2] J. W. Strutt. On the scattering of light by small particles. *Philos. Mag.*, 41(275):447–454, 1871.
- [3] Lord Rayleigh. On the transmission of light through an atmosphere containing small particles in suspension, and on the origin of the blue of the sky. *Philos. Mag.*, 47(287):375–384, 1899.
- [4] M. E. Lines. Scattering losses in optic fiber materials. i. a new parametrization. *J. of Appl. Phys.*, 55(11):4052–4057, 1984.
- [5] M. Ohashi, K. Shiraki, and K. Tajima. Optical loss property of silica-based single-mode fibers. *J. Lightwave Technol.*, 10(5):539–543, 1992.
- [6] J. Larmor. The principle of molecular scattering of radiation. *Philos. Mag.*, 37(217):161–163, 1919.
- [7] C. V. Raman. The Doppler effect in the molecular scattering of radiation. *Nature*, 103(2583):165, 1919.
- [8] J. Larmor. The Doppler effect in the molecular scattering of radiation. *Nature*, 103(2583):165–166, 1919.
- [9] C. V. Raman. Optical observation of the thermal agitation of the atoms in crystals. *Nature*, 109(2724):42, 1922.

- [10] R. J. Strutt. Scattering of light by solid substances. *Proc. R. Soc. Lond. A*, 95(672):476–479, 1919.
- [11] C. V. Raman. A new radiation. *Indian J. Phys.*, 2:387–398, 1928.
- [12] C. V. Raman and K. S. Krishnan. A new type of secondary radiation. *Nature*, 121(3048):501, 1928.
- [13] C. V. Raman and K. S. Krishnan. The optical analogue of the compton effect. *Nature*, 121(3053):711, 1928.
- [14] G. Landsberg and L. Mandelstam. Eine neue erscheinung bei der lichtzerstreuung in krystallen. *Naturwissenschaften*, 16(28):557–558, Jul 1928.
- [15] N. J. Rud. The Raman effect. *Sch. Sci. Math.*, 29(6):581–589, 1929.
- [16] A. C. Menzies. The Raman effect. *Nature*, 125:205, 1930.
- [17] L. Brillouin. Diffusion de lumière par un corps transparent homogène. *Ann. Phys*, 17:88–122, 1922.
- [18] L. I. Mandelstam. Light scattering by inhomogeneous media. *Zh. Russ. Fiz-Khim. Ova*, 58:381, 1926.
- [19] P. Debye and F. W. Sears. On the scattering of light by supersonic waves. *Proc. Natl. Acad. Sci.*, 18(6):409–414, 1932.
- [20] E. F. Gross. Change of wave-length of light due to elastic heat waves at scattering in liquids. *Nature*, 126(3171):201, 1930.
- [21] E. H. L. Meyer and W. Ramm. Die struktur der Rayleigh-strahlung. *Phys. Zeitschr.*, 33:270, 1932.
- [22] C. V. Raman and C. S. Venkateswaran. Optical observation of the Debye heat waves in crystals. *Nature*, 142(3588):250, 1938.
- [23] B. V. Raghavendra Rao. Examination of molecularly scattered light with a Fabry-Perot etalon. *Proc. Indian Acad. Sci. - Sect. A*, 1(5):261–268, 1934.

- [24] D. Rank, E. Shull, and D. Axford. Hypersonic velocity in acetone at low temperatures. *Nature*, 164(4158):67, 1949.
- [25] R. S. Krishnan. Elastic constants of crystals from light scattering measurements. *Proc. Indian Acad. Sci. - Sect. A*, 41(3):91–97, 1955.
- [26] J. P. Gordon, H. J. Zeiger, and C. H. Townes. Molecular microwave oscillator and new hyperfine structure in the microwave spectrum of NH_3 . *Phys. Rev.*, 95(1):282, 1954.
- [27] J. P. Gordon, H. J. Zeiger, and C. H. Townes. The maser—new type of microwave amplifier, frequency standard, and spectrometer. *Phys. Rev.*, 99:1264–1274, 1955.
- [28] T. H. Maiman. Stimulated optical radiation in ruby. *Nature*, 187:493, 1960.
- [29] R. N. Hall, G. E. Fenner, J. Kingsley, T. Soltys, and R. Carlson. Coherent light emission from GaAs junctions. *Phys. Rev. Lett.*, 9(9):366, 1962.
- [30] E. J. Woodbury and W. K. Ng. Ruby laser operation in near IR. *Proc. IRE*, 50(11):2367, 1962.
- [31] G. Eckhardt, R. W. Hellwarth, F. J. McClung, S. E. Schwarz, D. Weiner, and E. J. Woodbury. Stimulated Raman scattering from organic liquids. *Phys. Rev. Lett.*, 9:455–457, 1962.
- [32] R. W. Hellwarth. Theory of stimulated Raman scattering. *Phys. Rev.*, 130:1850–1852, 1963.
- [33] B. Stoicheff. Characteristics of stimulated Raman radiation generated by coherent light. *Phys. Lett.*, 7(3):186–188, 1963.
- [34] E. Garmire, F. Pandarese, and C. H. Townes. Coherently driven molecular vibrations and light modulation. *Phys. Rev. Lett.*, 11:160–163, 1963.
- [35] E. Garmire. Perspectives on stimulated Brillouin scattering. *New J. Phys.*, 19(1):011003, 2017.

- [36] R. Y. Chiao, C. H. Townes, and B. P. Stoicheff. Stimulated Brillouin scattering and coherent generation of intense hypersonic waves. *Phys. Rev. Lett.*, 12:592–595, 1964.
- [37] E. Garmire and C. H. Townes. Stimulated Brillouin scattering in liquids. *Appl. Phys. Lett.*, 5(4):84–86, 1964.
- [38] R. Y. Chiao and B. P. Stoicheff. Brillouin scattering in Liquids excited by the He–Ne maser. *J. Opt. Soc. Am.*, 54(10):1286–1287, 1964.
- [39] R. G. Brewer and K. E. Rieckhoff. Stimulated Brillouin scattering in liquids. *Phys. Rev. Lett.*, 13:334–336, 1964.
- [40] H. Takuma and D. A. Jennings. Stimulated Brillouin scattering in the off-axis resonator. *Appl. Phys. Lett.*, 5(12):239–241, 1964.
- [41] Y. R. Shen and N. Bloembergen. Theory of stimulated Brillouin and Raman scattering. *Phys. Rev.*, 137:A1787–A1805, 1965.
- [42] E. Hagenlocker and W. Rado. Stimulated Brillouin and Raman scattering in gases. *Appl. Phys. Lett.*, 7(9):236–238, 1965.
- [43] N. M. Kroll. Excitation of hypersonic vibrations by means of photoelastic coupling of high-intensity light waves to elastic waves. *J. Appl. Phys.*, 36(1):34–43, 1965.
- [44] R. G. Brewer. Growth of optical plane waves in stimulated Brillouin scattering. *Phys. Rev.*, 140:A800–A805, 1965.
- [45] C. L. Tang. Saturation and spectral characteristics of the Stokes emission in the stimulated Brillouin process. *J. Appl. Phys.*, 37(8):2945–2955, 1966.
- [46] S. Shapiro, J. Giordmaine, and K. Wecht. Stimulated Raman and Brillouin scattering with picosecond light pulses. *Phys. Rev. Lett.*, 19(19):1093, 1967.
- [47] W. Heinicke and G. Winterling. The temperature dependence of stimulated Brillouin scattering in quartz. *Appl. Phys. Lett.*, 11(7):231–233, 1967.
- [48] N. Goldblatt and T. Litovitz. Stimulated Brillouin scattering: measurement of hypersonic velocity in liquids. *J. Acoust. Soc. Am.*, 41(5):1301–1307, 1967.

- [49] M. Maier, W. Rother, and W. Kaiser. Time-resolved measurements of stimulated Brillouin scattering. *Appl. Phys. Lett.*, 10(3):80–82, 1967.
- [50] E. Hagenlocker, R. Minck, and W. Rado. Effects of phonon lifetime on stimulated optical scattering in gases. *Phys. Rev.*, 154(2):226, 1967.
- [51] J. Budin, A. Donzel, J. Ernest, and J. Raffy. Stimulated Brillouin scattering in glasses. *Electron. Lett.*, 3(1):31–33, 1967.
- [52] M. Maier. Quasisteady state in the stimulated Brillouin scattering of liquids. *Phys. Rev.*, 166:113–119, 1968.
- [53] D. Pohl, M. Maier, and W. Kaiser. Phonon lifetimes measured in amplifiers for Brillouin radiation. *Phys. Rev. Lett.*, 20(8):366, 1968.
- [54] A. S. Pine. Brillouin scattering study of acoustic attenuation in fused quartz. *Phys. Rev.*, 185(3):1187, 1969.
- [55] R. Vacher and L. Boyer. Brillouin scattering: A tool for the measurement of elastic and photoelastic constants. *Phys. Rev. B*, 6(2):639, 1972.
- [56] A. S. Pine. Stimulated Brillouin scattering in liquids. *Phys. Rev.*, 149(1):113, 1966.
- [57] E. Aleksandrov, A. Bonch-Bruevich, N. Kostin, and V. Khodovoi. Stimulated Raman and Brillouin scattering in selective resonators. *Sov. Phys. JETP*, 22:986, 1966.
- [58] T. Ito and H. Takuma. Near threshold behavior of stimulated Brillouin scattering in an off-axis resonator. *Jpn. J. Appl. Phys.*, 8(7):941, 1969.
- [59] V. Kovalev, V. Popovichev, V. Ragul'skii, and F. Faizullov. Single frequency Brillouin laser using methane. *JETP Lett.*, 14:344–347, 1971.
- [60] B. Y. Zel'dovich, V. I. Popovichev, V. V. Ragul'skii, and F. S. Faizullov. Connection between the wave fronts of the reflected and exciting light in stimulated Mandel'shtam-Brillouin scattering. *Sov. Phys. JETP*, 15:109–113, 1972.
- [61] B. Y. Zel'dovich, N. F. Pilipetskiĭ, and V. V. Shkunov. Phase conjugation in stimulated scattering. *Sov. Phys. Usp.*, 25(10):713–737, 1982.

- [62] P. Suni and J. Falk. Theory of phase conjugation by stimulated Brillouin scattering. *JOSA B*, 3(12):1681–1691, 1986.
- [63] V. Wang and C. R. Giuliano. Correction of phase aberrations via stimulated Brillouin scattering. *Opt. Lett.*, 2(1):4–6, 1978.
- [64] C. B. Dane, L. E. Zapata, W. A. Neuman, M. A. Norton, and L. A. Hackel. Design and operation of a 150 W near diffraction-limited laser amplifier with SBS wavefront correction. *IEEE J. Quantum Electron.*, 31(1):148–163, 1995.
- [65] A. Yariv. Phase conjugate optics and real-time holography. *IEEE J. Quantum Electron.*, 14(9):650–660, 1978.
- [66] M. C. Gower and R. G. Caro. KrF laser with a phase-conjugate Brillouin mirror. *Opt. Lett.*, 7(4):162–164, 1982.
- [67] H. Yoshida, V. Kmetik, H. Fujita, M. Nakatsuka, T. Yamanaka, and K. Yoshida. Heavy fluorocarbon liquids for a phase-conjugated stimulated Brillouin scattering mirror. *Appl. Opt.*, 36(16):3739–3744, 1997.
- [68] B. C. Rodgers, T. H. Russell, and W. B. Roh. Laser beam combining and cleanup by stimulated Brillouin scattering in a multimode optical fiber. *Opt. Lett.*, 24(16):1124–1126, 1999.
- [69] T. H. Russell, W. B. Roh, and J. R. Marciante. Incoherent beam combining using stimulated Brillouin scattering in multimode fibers. *Opt. Express*, 8(4):246–254, 2001.
- [70] R. Boyd. *Nonlinear Optics*. Elsevier Science, 2003.
- [71] K. Kao and G. Hockham. Dielectric-fibre surface waveguides for optical frequencies. *IEE Proceedings J (Optoelectronics)*, 133(3):191–198, 1966.
- [72] F. Kapron, D. B. Keck, and R. D. Maurer. Radiation losses in glass optical waveguides. *Appl. Phys. Lett.*, 17(10):423–425, 1970.
- [73] W. G. French, J. B. MacChesney, P. B. O’Connor, and G. W. Tasker. Optical waveguides with very low losses. *Bell Syst. Tech. J.*, 53(5):951–954, 1974.

- [74] T. Miya, Y. Terunuma, T. Hosaka, and T. Miyashita. Ultimate low-loss single-mode fibre at 1.55 μm . *Electron. Lett.*, 15(4):106–108, 1979.
- [75] G. P. Agrawal. *Nonlinear fiber optics*. Academic Press, 2007.
- [76] R. G. Smith. Optical power handling capacity of low loss optical fibers as determined by stimulated Raman and Brillouin scattering. *Appl. Opt.*, 11(11):2489–2494, 1972.
- [77] E. P. Ippen and R. H. Stolen. Stimulated Brillouin scattering in optical fibers. *Appl. Phys. Lett.*, 21(11):539–541, 1972.
- [78] D. Cotter. Observation of stimulated Brillouin scattering in low-loss silica fibre at 1.3 μm . *Electron. Lett.*, 18(12):495–496, 1982.
- [79] D. Cotter. Stimulated Brillouin scattering in monomode optical fiber. *J. Opt. Commun.*, 4(1):10–19, 1983.
- [80] D. Cotter. Suppression of stimulated Brillouin scattering during transmission of high-power narrowband laser light in monomode fibre. *Electron. Lett.*, 18(15):638–640, 1982.
- [81] Y. Aoki, K. Tajima, and I. Mito. Input power limits of single-mode optical fibers due to stimulated Brillouin scattering in optical communication systems. *J. Lightwave Technol.*, 6(5):710–719, 1988.
- [82] N. Yoshizawa and T. Imai. Stimulated Brillouin scattering suppression by means of applying strain distribution to fiber with cabling. *J. Lightwave Technol.*, 11(10):1518–1522, 1993.
- [83] K. Shiraki, M. Ohashi, and M. Tateda. Suppression of stimulated Brillouin scattering in a fibre by changing the core radius. *Electron. Lett.*, 31(8):668–669, 1995.
- [84] M. Ohashi and M. Tateda. Design of strain-free-fiber with nonuniform dopant concentration for stimulated Brillouin scattering suppression. *J. Lightwave Technol.*, 11(12):1941–1945, 1993.

- [85] Y. Takushima and T. Okoshi. Suppression of stimulated Brillouin scattering using optical isolators. *Electron. Lett.*, 28(12):1155–1157, 1992.
- [86] P. Weßels, P. Adel, M. Auerbach, D. Wandt, and C. Fallnich. Novel suppression scheme for brillouin scattering. *Opt. Express*, 12(19):4443–4448, 2004.
- [87] J. B. Coles, B.-P. Kuo, N. Alic, S. Moro, C.-S. Bres, J. M. C. Boggio, P. A. Andrekson, M. Karlsson, and S. Radic. Bandwidth-efficient phase modulation techniques for stimulated Brillouin scattering suppression in fiber optic parametric amplifiers. *Opt. Express*, 18(17):18138–18150, 2010.
- [88] I. Dajani, C. Zeringue, C. Lu, C. Vergien, L. Henry, and C. Robin. Stimulated Brillouin scattering suppression through laser gain competition: scalability to high power. *Opt. Lett.*, 35(18):3114–3116, 2010.
- [89] J. White, A. Vasilyev, J. Cahill, N. Satyan, O. Okusaga, G. Rakuljic, C. Mungan, and A. Yariv. Suppression of stimulated Brillouin scattering in optical fibers using a linearly chirped diode laser. *Opt. Express*, 20(14):15872–15881, 2012.
- [90] K. Abedin, R. Ahmad, K. Feder, and D. J. DiGiovanni. Suppression of stimulated Brillouin scattering using off-axis twisted core fiber. In *CLEO: Science and Innovations*, pages SM3K–6. Optical Society of America, 2018.
- [91] K. Hill, B. Kawasaki, and D. Johnson. Cw brillouin laser. *Appl. Phys. Lett.*, 28(10):608–609, 1976.
- [92] R. Bergh, G. Kotler, and H. Shaw. Single-mode fibre optic directional coupler. *Electron. Lett.*, 16(7):260–261, 1980.
- [93] M. J. Digonnet and H. J. Shaw. Analysis of a tunable single mode optical fiber coupler. *IEEE Trans. Microw. Theory Tech.*, 30(4):592–600, 1982.
- [94] L. F. Stokes, M. Chodorow, and H. J. Shaw. All-fiber stimulated Brillouin ring laser with submilliwatt pump threshold. *Opt. Lett.*, 7(10):509–511, 1982.

- [95] P. Thomas, H. van Driel, and G. Stegeman. Possibility of using an optical fiber Brillouin ring laser for inertial sensing. *Appl. Opt.*, 19(12):1906–1908, 1980.
- [96] F. Zarinetchi, S. Smith, and S. Ezekiel. Stimulated Brillouin fiber-optic laser gyroscope. *Opt. Lett.*, 16(4):229–231, 1991.
- [97] D. R. Ponikvar and S. Ezekiel. Stabilized single-frequency stimulated Brillouin fiber ring laser. *Opt. Lett.*, 6(8):398–400, 1981.
- [98] S. Smith, F. Zarinetchi, and S. Ezekiel. Narrow-linewidth stimulated Brillouin fiber laser and applications. *Opt. Lett.*, 16(6):393–395, 1991.
- [99] D. T. Hon. Pulse compression by stimulated Brillouin scattering. *Opt. Lett.*, 5(12):516–518, 1980.
- [100] R. Fedosejevs and A. Offenberger. Subnanosecond pulses from a KrF laser pumped SF6 Brillouin amplifier. *IEEE J. Quantum Electron.*, 21(10):1558–1562, 1985.
- [101] R. Fedosejevs, I. V. Tomov, D. C. D. McKen, and A. A. Offenberger. Experimental study of an SF6 Brillouin amplifier pumped by KrF laser radiation. *Appl. Phys. Lett.*, 45(4):340–342, 1984.
- [102] N. A. Olsson and J. P. Van der Ziel. Cancellation of fiber loss by semiconductor laser pumped Brillouin amplification at 1.5 μm . *Appl. Phys. Lett.*, 48(20):1329–1330, 1986.
- [103] N. A. Olsson and J. P. Van Der Ziel. Fibre Brillouin amplifier with electronically controlled bandwidth. *Electron. Lett.*, 22(9):488–490, 1986.
- [104] D. Culverhouse, F. Farahi, C. N. Pannell, and D. A. Jackson. Potential of stimulated Brillouin scattering as sensing mechanism for distributed temperature sensors. *Electron. Lett.*, 25(14):913–915, 1989.
- [105] T. Kurashima, T. Horiguchi, and M. Tateda. Distributed-temperature sensing using stimulated Brillouin scattering in optical silica fibers. *Opt. Lett.*, 15(18):1038–1040, 1990.

- [106] X. Bao, D. J. Webb, and D. A. Jackson. 32-km distributed temperature sensor based on Brillouin loss in an optical fiber. *Opt. Lett.*, 18(18):1561–1563, 1993.
- [107] X. Bao, D. J. Webb, and D. A. Jackson. Combined distributed temperature and strain sensor based on Brillouin loss in an optical fiber. *Opt. Lett.*, 19(2):141–143, 1994.
- [108] T. Horiguchi, K. Shimizu, T. Kurashima, M. Tateda, and Y. Koyamada. Development of a distributed sensing technique using Brillouin scattering. *J. Lightwave Technol.*, 13(7):1296–1302, 1995.
- [109] M. Nikles, L. Thévenaz, and P. A. Robert. Simple distributed fiber sensor based on Brillouin gain spectrum analysis. *Opt. Lett.*, 21(10):758–760, 1996.
- [110] D. Garus, K. Krebber, F. Schliep, and T. Gogolla. Distributed sensing technique based on Brillouin optical-fiber frequency-domain analysis. *Opt. Lett.*, 21(17):1402–1404, 1996.
- [111] D. Garcus, T. Gogolla, K. Krebber, and F. Schliep. Brillouin optical-fiber frequency-domain analysis for distributed temperature and strain measurements. *J. Lightwave Technol.*, 15(4):654–662, 1997.
- [112] A. Fellay, L. Thévenaz, M. Facchini, M. Nikles, and P. Robert. Distributed sensing using stimulated Brillouin scattering: towards ultimate resolution. In *Optical Fiber Sensors*, page OWD3. Optical Society of America, 1997.
- [113] T. Parker, M. Farhadiroushan, V. Handerek, and A. Roger. A fully distributed simultaneous strain and temperature sensor using spontaneous Brillouin backscatter. *IEEE Photon. Technol. Lett.*, 9(7):979–981, 1997.
- [114] T. Parker, M. Farhadiroushan, V. Handerek, and A. Rogers. Temperature and strain dependence of the power level and frequency of spontaneous Brillouin scattering in optical fibers. *Opt. Lett.*, 22(11):787–789, 1997.
- [115] L. Thévenaz, M. Niklès, A. Fellay, M. Facchini, and P. A. Robert. Applications of distributed Brillouin fiber sensing. In *International Conference on Applied Optical*

- Metrology*, volume 3407, pages 374–382. International Society for Optics and Photonics, 1998.
- [116] H. H. Kee, G. P. Lees, and T. P. Newson. All-fiber system for simultaneous interrogation of distributed strain and temperature sensing by spontaneous Brillouin scattering. *Opt. Lett.*, 25(10):695–697, 2000.
- [117] K. Hotate and T. Hasegawa. Measurement of Brillouin gain spectrum distribution along an optical fiber using a correlation-based technique—proposal, experiment and simulation. *IEICE Trans. Electron.*, 83(3):405–412, 2000.
- [118] X. Bao, M. DeMerchant, A. Brown, and T. Bremner. Tensile and compressive strain measurement in the lab and field with the distributed Brillouin scattering sensor. *J. Lightwave Technol.*, 19(11):1698, 2001.
- [119] H. Ohno, H. Naruse, M. Kihara, and A. Shimada. Industrial applications of the BOTDR optical fiber strain sensor. *Opt. Fiber Technol.*, 7(1):45–64, 2001.
- [120] K. Hotate and M. Tanaka. Distributed fiber Brillouin strain sensing with 1-cm spatial resolution by correlation-based continuous-wave technique. *IEEE Photon. Technol. Lett.*, 14(2):179–181, 2002.
- [121] K. Hotate and S. S. L. Ong. Distributed dynamic strain measurement using a correlation-based Brillouin sensing system. *IEEE Photon. Technol. Lett.*, 15(2):272–274, 2003.
- [122] M. N. Alahbabi, Y. T. Cho, and T. P. Newson. 150-km-range distributed temperature sensor based on coherent detection of spontaneous Brillouin backscatter and in-line Raman amplification. *JOSA B*, 22(6):1321–1324, 2005.
- [123] L. Zou, X. Bao, Y. Wan, and L. Chen. Coherent probe-pump-based Brillouin sensor for centimeter-crack detection. *Opt. Lett.*, 30(4):370–372, 2005.
- [124] K.-Y. Song, Z. He, and K. Hotate. Distributed strain measurement with millimeter-order spatial resolution based on Brillouin optical correlation domain analysis and

- beat lock-in detection scheme. In *Optical Fiber Sensors*, page ThC2. Optical Society of America, 2006.
- [125] J. Geng, S. Staines, M. Blake, and S. Jiang. Distributed fiber temperature and strain sensor using coherent radio-frequency detection of spontaneous Brillouin scattering. *Appl. Opt.*, 46(23):5928–5932, 2007.
- [126] L. Thévenaz and S. F. Mafang. Distributed fiber sensing using Brillouin echoes. In *19th International Conference on Optical Fibre Sensors*, volume 7004, page 70043N. International Society for Optics and Photonics, 2008.
- [127] W. Zou, Z. He, and K. Hotate. Complete discrimination of strain and temperature using Brillouin frequency shift and birefringence in a polarization-maintaining fiber. *Opt. Express*, 17(3):1248–1255, 2009.
- [128] R. Bernini, A. Minardo, and L. Zeni. Dynamic strain measurement in optical fibers by stimulated Brillouin scattering. *Opt. Lett.*, 34(17):2613–2615, 2009.
- [129] Y. Peled, A. Motil, L. Yaron, and M. Tur. Slope-assisted fast distributed sensing in optical fibers with arbitrary Brillouin profile. *Opt. Express*, 19(21):19845–19854, 2011.
- [130] X. Bao and L. Chen. Recent progress in distributed fiber optic sensors. *Sensors*, 12(7):8601–8639, 2012.
- [131] Y. Dong, H. Zhang, L. Chen, and X. Bao. 2 cm spatial-resolution and 2 km range Brillouin optical fiber sensor using a transient differential pulse pair. *Appl. Opt.*, 51(9):1229–1235, 2012.
- [132] S. Chin, N. Primerov, L. Thévenaz, et al. Sub-centimeter spatial resolution in distributed fiber sensing based on dynamic Brillouin grating in optical fibers. *IEEE Sensors Journal*, 12(1):189–194, 2012.
- [133] A. Zadok, Y. Antman, N. Primerov, A. Denisov, J. Sancho, and L. Thevenaz. Random-access distributed fiber sensing. *Laser Photon. Rev.*, 6(5):L1–L5, 2012.

- [134] R. Cohen, Y. London, Y. Antman, and A. Zadok. Brillouin optical correlation domain analysis with 4 millimeter resolution based on amplified spontaneous emission. *Opt. Express*, 22(10):12070–12078, 2014.
- [135] Y. London, Y. Antman, R. Cohen, N. Kimelfeld, N. Levanon, and A. Zadok. High-resolution long-range distributed Brillouin analysis using dual-layer phase and amplitude coding. *Opt. Express*, 22(22):27144–27158, 2014.
- [136] D. Elooz, Y. Antman, N. Levanon, and A. Zadok. High-resolution long-reach distributed Brillouin sensing based on combined time-domain and correlation-domain analysis. *Opt. Express*, 22(6):6453–6463, 2014.
- [137] A. Motil, A. Bergman, and M. Tur. State of the art of Brillouin fiber-optic distributed sensing. *Opt. Laser Technol.*, 78:81–103, 2016.
- [138] K. Y. Song, W. Zou, Z. He, and K. Hotate. All-optical dynamic grating generation based on Brillouin scattering in polarization-maintaining fiber. *Opt. Lett.*, 33(9):926–928, 2008.
- [139] A. Bergman and M. Tur. Brillouin dynamic gratings—a practical form of Brillouin enhanced four wave mixing in waveguides: The first decade and beyond. *Sensors*, 18(9):2863, 2018.
- [140] J. Sancho, N. Primerov, S. Chin, Y. Antman, A. Zadok, S. Sales, and L. Thévenaz. Tunable and reconfigurable multi-tap microwave photonic filter based on dynamic Brillouin gratings in fibers. *Opt. Express*, 20(6):6157–6162, 2012.
- [141] Y. Dong, T. Jiang, L. Teng, H. Zhang, L. Chen, X. Bao, and Z. Lu. Sub-MHz ultrahigh-resolution optical spectrometry based on Brillouin dynamic gratings. *Opt. Lett.*, 39(10):2967–2970, 2014.
- [142] K. Y. Song, S. Chin, N. Primerov, and L. Thévenaz. Time-domain distributed fiber sensor with 1 cm spatial resolution based on Brillouin dynamic grating. *J. Lightwave Technol.*, 28(14):2062–2067, 2010.

- [143] Y. Antman, N. Primerov, J. Sancho, L. Thevenaz, and A. Zadok. Localized and stationary dynamic gratings via stimulated Brillouin scattering with phase modulated pumps. *Opt. Express*, 20(7):7807–7821, 2012.
- [144] M. Santagiustina, S. Chin, N. Primerov, L. Ursini, and L. Thévenaz. All-optical signal processing using dynamic Brillouin gratings. *Scientific reports*, 3:1594, 2013.
- [145] H. G. Winful. Chirped Brillouin dynamic gratings for storing and compressing light. *Opt. Express*, 21(8):10039–10047, 2013.
- [146] K. Y. Song. Operation of Brillouin dynamic grating in single-mode optical fibers. *Opt. Lett.*, 36(23):4686–4688, 2011.
- [147] R. Pant, E. Li, C. G. Poulton, D.-Y. Choi, S. Madden, B. Luther-Davies, and B. J. Eggleton. Observation of Brillouin dynamic grating in a photonic chip. *Opt. Lett.*, 38(3):305–307, 2013.
- [148] D. Culverhouse, K. Kalli, and D. A. Jackson. Stimulated Brillouin scattering ring resonator laser for SBS gain studies and microwave generation. *Electron. Lett.*, 27(22):2033–2035, Oct 1991.
- [149] K. J. Williams and R. D. Esman. Stimulated Brillouin scattering for improvement of microwave fibre-optic link efficiency. *Electron. Lett.*, 30(23):1965–1966, 1994.
- [150] X. Yao. Brillouin selective sideband amplification of microwave photonic signals. *IEEE Photon. Technol. Lett.*, 10(1):138–140, 1998.
- [151] A. Loayssa, D. Benito, and M. J. Garde. Optical carrier Brillouin processing of microwave photonic signals. *Opt. Lett.*, 25(17):1234–1236, 2000.
- [152] X. S. Yao. High-quality microwave signal generation by use of Brillouin scattering in optical fibers. *Opt. Lett.*, 22(17):1329–1331, 1997.
- [153] X. S. Yao. Brillouin opto-electronic oscillators, June 1999. US Patent 5,917,179.

- [154] T. Schneider, M. Junker, and K.-U. Lauterbach. Theoretical and experimental investigation of Brillouin scattering for the generation of millimeter waves. *J. Opt. Soc. Am. B*, 23(6):1012–1019, 2006.
- [155] J. Geng, S. Staines, and S. Jiang. Dual-frequency Brillouin fiber laser for optical generation of tunable low-noise radio frequency/microwave frequency. *Opt. Lett.*, 33(1):16–18, 2008.
- [156] M. C. Gross, P. T. Callahan, T. R. Clark, D. Novak, R. B. Waterhouse, and M. L. Dennis. Tunable millimeter-wave frequency synthesis up to 100 GHz by dual-wavelength Brillouin fiber laser. *Opt. Express*, 18(13):13321–13330, 2010.
- [157] J. Li, H. Lee, and K. J. Vahala. Microwave synthesizer using an on-chip Brillouin oscillator. *Nat. Commun.*, 4:2097, 2013.
- [158] M. Merklein, B. Stiller, I. V. Kabakova, U. S. Mutugala, K. Vu, S. J. Madden, B. J. Eggleton, and R. Slavík. Widely tunable, low phase noise microwave source based on a photonic chip. *Opt. Lett.*, 41(20):4633–4636, 2016.
- [159] T. Tanemura, Y. Takushima, and K. Kikuchi. Narrowband optical filter, with a variable transmission spectrum, using stimulated Brillouin scattering in optical fiber. *Opt. Lett.*, 27(17):1552–1554, 2002.
- [160] A. Zadok, A. Eyal, and M. Tur. Gigahertz-wide optically reconfigurable filters using stimulated Brillouin scattering. *J. Lightwave Technol.*, 25(8):2168–2174, 2007.
- [161] B. Vidal, M. A. Piqueras, and J. Martí. Tunable and reconfigurable photonic microwave filter based on stimulated Brillouin scattering. *Opt. Lett.*, 32(1):23–25, 2007.
- [162] Y. M. Chang and J. H. Lee. High-Q, tunable, photonic microwave single passband filter based on stimulated Brillouin scattering and fiber Bragg grating filtering. *Optics Communications*, 281(20):5146–5150, 2008.
- [163] W. Zhang and R. Minasian. Ultrawide tunable microwave photonic notch filter based on stimulated Brillouin scattering. *IEEE Photon. Technol. Lett.*, 24(14):1182–1184, 2012.

- [164] D. Marpaung, B. Morrison, M. Pagani, R. Pant, D.-Y. Choi, B. Luther-Davies, S. J. Madden, and B. J. Eggleton. Low-power, chip-based stimulated Brillouin scattering microwave photonic filter with ultrahigh selectivity. *Optica*, 2(2):76–83, 2015.
- [165] H. Shin, J. A. Cox, R. Jarecki, A. Starbuck, Z. Wang, and P. T. Rakich. Control of coherent information via on-chip photonic-phononic emitter-receivers. *Nat. Commun.*, 6:6427, 2015.
- [166] Y. Liu, D. Marpaung, B. J. Eggleton, and A. Choudhary. High-performance chip-assisted microwave photonic functionalities. *IEEE Photon. Technol. Lett.*, 2018.
- [167] Y. Okawachi, M. S. Bigelow, J. E. Sharping, Z. Zhu, A. Schweinsberg, D. J. Gauthier, R. W. Boyd, and A. L. Gaeta. Tunable all-optical delays via Brillouin slow light in an optical fiber. *Phys. Rev. Lett.*, 94:153902, 2005.
- [168] L. V. Hau, S. E. Harris, Z. Dutton, and C. H. Behroozi. Light speed reduction to 17 metres per second in an ultracold atomic gas. *Nature*, 397(6720):594, 1999.
- [169] M. S. Bigelow, N. N. Lepeshkin, and R. W. Boyd. Superluminal and slow light propagation in a room-temperature solid. *Science*, 301(5630):200–202, 2003.
- [170] M. S. Bigelow, N. N. Lepeshkin, and R. W. Boyd. Observation of ultraslow light propagation in a ruby crystal at room temperature. *Phys. Rev. Lett.*, 90(11):113903, 2003.
- [171] M. G. Herráez, K. Y. Song, and L. Thévenaz. Arbitrary-bandwidth Brillouin slow light in optical fibers. *Opt. Express*, 14(4):1395–1400, 2006.
- [172] L. Thévenaz. Slow and fast light in optical fibres. *Nat. Photonics*, 2(8):474, 2008.
- [173] A. Zadok, A. Eyal, and M. Tur. Stimulated Brillouin scattering slow light in optical fibers. *Appl. Opt.*, 50(25):E38–E49, 2011.
- [174] Z. Zhu, D. J. Gauthier, and R. W. Boyd. Stored light in an optical fiber via stimulated Brillouin scattering. *Science*, 318(5857):1748–1750, 2007.

- [175] R. Shelby, M. Levenson, and P. Bayer. Resolved forward Brillouin scattering in optical fibers. *Phys. Rev. Lett.*, 54(9):939, 1985.
- [176] R. M. Shelby, M. D. Levenson, and P. W. Bayer. Guided acoustic-wave Brillouin scattering. *Phys. Rev. B*, 31:5244–5252, Apr 1985.
- [177] R. N. Thurston. Elastic waves in rods and optical fibers. *J. Sound Vib.*, 159(3):441–467, 1992.
- [178] R. M. Shelby, M. D. Levenson, S. H. Perlmuter, R. G. DeVoe, and D. F. Walls. Broad-band parametric deamplification of quantum noise in an optical fiber. *Phys. Rev. Lett.*, 57:691–694, 1986.
- [179] P. St. J. Russell, D. Culverhouse, and F. Farahi. Experimental observation of forward stimulated Brillouin scattering in dual-mode single-core fibre. *Electron. Lett.*, 26(15):1195–1196, 1990.
- [180] P. St. J. Russell, D. Culverhouse, and F. Farahi. Theory of forward stimulated Brillouin scattering in dual-mode single-core fibers. *IEEE J. Quant. Electron.*, 27(3):836–842, 1991.
- [181] J. Knight, T. Birks, P. S. J. Russell, and D. Atkin. All-silica single-mode optical fiber with photonic crystal cladding. *Opt. Lett.*, 21(19):1547–1549, 1996.
- [182] T. A. Birks, J. C. Knight, and P. S. J. Russell. Endlessly single-mode photonic crystal fiber. *Opt. Lett.*, 22(13):961–963, 1997.
- [183] P. Dainese, P. S. J. Russell, N. Joly, J. Knight, G. Wiederhecker, H. L. Fragnito, V. Laude, and A. Khelif. Stimulated Brillouin scattering from multi-GHz-guided acoustic phonons in nanostructured photonic crystal fibres. *Nat. Phys.*, 2(6):388, 2006.
- [184] N. Shibata, A. Nakazono, N. Taguchi, and S. Tanaka. Forward Brillouin scattering in holey fibers. *IEEE Photon. Technol. Lett.*, 18(2):412–414, 2006.

- [185] J.-C. Beugnot, T. Sylvestre, H. Maillotte, G. Mélin, and V. Laude. Guided acoustic wave Brillouin scattering in photonic crystal fibers. *Opt. Lett.*, 32(1):17–19, 2007.
- [186] M. S. Kang, A. Nazarkin, A. Brenn, and P. St. J. Russell. Tightly trapped acoustic phonons in photonic crystal fibres as highly nonlinear artificial Raman oscillators. *Nat. Phys.*, 5(4):276–280, 2009.
- [187] M. S. Kang, A. Brenn, and P. St. J. Russell. All-optical control of gigahertz acoustic resonances by forward stimulated interpolarization scattering in a photonic crystal fiber. *Phys. Rev. Lett.*, 105:153901, 2010.
- [188] M. S. Kang, A. Butsch, and P. St. J. Russell. Reconfigurable light-driven opto-acoustic isolators in photonic crystal fibre. *Nat. Photonics*, 5(9):549–553, 2011.
- [189] I. S. Grudin, A. B. Matsko, and L. Maleki. Brillouin lasing with a CaF₂ whispering gallery mode resonator. *Phys. Rev. Lett.*, 102(4):043902, 2009.
- [190] M. Tomes and T. Carmon. Photonic micro-electromechanical systems vibrating at x-band (11-GHz) rates. *Phys. Rev. Lett.*, 102(11):113601, 2009.
- [191] H. Lee, T. Chen, J. Li, K. Y. Yang, S. Jeon, O. Painter, and K. J. Vahala. Chemically etched ultrahigh-Q wedge-resonator on a silicon chip. *Nat. Photonics*, 6(6):369, 2012.
- [192] K. H. Tow, Y. Léguillon, P. Besnard, L. Brilland, J. Troles, P. Toupin, D. Méchin, D. Trégoat, and S. Molin. Relative intensity noise and frequency noise of a compact brillouin laser made of As₃₈Se₆₂ suspended-core chalcogenide fiber. *Opt. Lett.*, 37(7):1157–1159, 2012.
- [193] A. Butsch, M. S. Kang, T. Euser, J. Koehler, S. Rammler, R. Keding, and P. S. J. Russell. Optomechanical nonlinearity in dual-nanoweb structure suspended inside capillary fiber. *Phys. Rev. Lett.*, 109(18):183904, 2012.
- [194] R. Pant, C. G. Poulton, D.-Y. Choi, H. Mcfarlane, S. Hile, E. Li, L. Thevenaz, B. Luther-Davies, S. J. Madden, and B. J. Eggleton. On-chip stimulated Brillouin scattering. *Opt. Express*, 19(9):8285–8290, 2011.

- [195] P. T. Rakich, C. Reinke, R. Camacho, P. Davids, and Z. Wang. Giant enhancement of stimulated Brillouin scattering in the subwavelength limit. *Phys. Rev. X*, 2:011008, 2012.
- [196] H. Shin, W. Qiu, R. Jarecki, J. A. Cox, R. H. Olsson, A. Starbuck, Z. Wang, and P. T. Rakich. Tailorable stimulated Brillouin scattering in nanoscale silicon waveguides. *Nat. Commun.*, 4:1944, 2013.
- [197] R. Van Laer, B. Kuyken, D. Van Thourhout, and R. Baets. Interaction between light and highly confined hypersound in a silicon photonic nanowire. *Nat. Photon.*, 9(3):199–203, 2015.
- [198] O. Florez, P. F. Jarschel, Y. A. Espinel, C. Cordeiro, T. M. Alegre, G. S. Wiederhecker, and P. Dainese. Brillouin scattering self-cancellation. *Nat. Commun.*, 7:11759, 2016.
- [199] J. Li, H. Lee, T. Chen, and K. J. Vahala. Characterization of a high coherence, Brillouin microcavity laser on silicon. *Opt. Express*, 20(18):20170–20180, 2012.
- [200] J. Li, H. Lee, and K. J. Vahala. Low-noise brillouin laser on a chip at 1064 nm. *Opt. Lett.*, 39(2):287–290, 2014.
- [201] R. Pant, D. Marpaung, I. V. Kabakova, B. Morrison, C. G. Poulton, and B. J. Eggleton. On-chip stimulated Brillouin scattering for microwave signal processing and generation. *Laser Photon. Rev.*, 8(5):653–666, 2014.
- [202] A. Casas-Bedoya, B. Morrison, M. Pagani, D. Marpaung, and B. J. Eggleton. Tunable narrowband microwave photonic filter created by stimulated Brillouin scattering from a silicon nanowire. *Opt. Lett.*, 40(17):4154–4157, 2015.
- [203] A. Choudhary, B. Morrison, I. Aryanfar, S. Shahnia, M. Pagani, Y. Liu, K. Vu, S. Madden, D. Marpaung, and B. J. Eggleton. Advanced integrated microwave signal processing with giant on-chip Brillouin gain. *J. Lightwave Technol.*, 35(4):846–854, 2017.
- [204] G. Bahl, J. Zehnpfennig, M. Tomes, and T. Carmon. Stimulated optomechanical excitation of surface acoustic waves in a microdevice. *Nat. Commun.*, 2:403, 2011.

- [205] G. Bahl, M. Tomes, F. Marquardt, and T. Carmon. Observation of spontaneous Brillouin cooling. *Nat. Phys.*, 8(3):203–207, 2012.
- [206] G. Bahl, K. H. Kim, W. Lee, J. Liu, X. Fan, and T. Carmon. Brillouin cavity optomechanics with microfluidic devices. *Nat. Commun.*, 4:1994, 2013.
- [207] J. Kim, M. C. Kuzyk, K. Han, H. Wang, and G. Bahl. Non-reciprocal Brillouin scattering induced transparency. *Nat. Phys.*, 11(3):275–280, 2015.
- [208] C. Dong, Z. Shen, C. Zou, Y. Zhang, W. Fu, and G. Guo. Brillouin-scattering-induced transparency and non-reciprocal light storage. *Nat. Commun.*, 6:6193, 2015.
- [209] Z. Shen, Y.-L. Zhang, Y. Chen, C.-L. Zou, Y.-F. Xiao, X.-B. Zou, F.-W. Sun, G.-C. Guo, and C.-H. Dong. Experimental realization of optomechanically induced non-reciprocity. *Nat. Photonics*, 10:657, 2016.
- [210] F. Ruesink, M.-A. Miri, A. Alù, and E. Verhagen. Nonreciprocity and magnetic-free isolation based on optomechanical interactions. *Nat. Commun.*, 7:13662, 2016.
- [211] J. Kim, S. Kim, and G. Bahl. Complete linear optical isolation at the microscale with ultralow loss. *Sci. Rep.*, 7(1):1647, 2017.
- [212] K. J. Vahala. Optical microcavities. *Nature*, 424(6950):839, 2003.
- [213] W. Loh, A. A. S. Green, F. N. Baynes, D. C. Cole, F. J. Quinlan, H. Lee, K. J. Vahala, S. B. Papp, and S. A. Diddams. Dual-microcavity narrow-linewidth Brillouin laser. *Optica*, 2(3):225–232, 2015.
- [214] W. Loh, J. Becker, D. C. Cole, A. Coillet, F. N. Baynes, S. B. Papp, and S. A. Diddams. A microrod-resonator Brillouin laser with 240 Hz absolute linewidth. *New J. Phys.*, 18(4):045001, 2016.
- [215] J. Li, M.-G. Suh, and K. Vahala. Microresonator Brillouin gyroscope. *Optica*, 4(3):346–348, 2017.
- [216] K. Y. Yang, D. Y. Oh, S. H. Lee, Q.-F. Yang, X. Yi, B. Shen, H. Wang, and K. Vahala. Bridging ultrahigh-Q devices and photonic circuits. *Nat. Photonics*, 12(5):297, 2018.

- [217] M. Aspelmeyer, T. J. Kippenberg, and F. Marquardt. Cavity optomechanics. *Rev. Mod. Phys.*, 86:1391–1452, 2014.
- [218] R. Van Laer, A. Bazin, B. Kuyken, R. Baets, and D. V. Thourhout. Net on-chip Brillouin gain based on suspended silicon nanowires. *New J. Phys.*, 17(11):115005, 2015.
- [219] E. A. Kittlaus, H. Shin, and P. T. Rakich. Large Brillouin amplification in silicon. *Nat. Photon.*, 10(7):463–467, 2016.
- [220] E. A. Kittlaus, P. Kharel, N. T. Otterstrom, Z. Wang, and P. T. Rakich. RF-photonic filters via on-chip photonic-phononic emit-receive operations. *J. Lightwave Technol.*, 36(13):2803–2809, 2018.
- [221] E. A. Kittlaus, N. T. Otterstrom, and P. T. Rakich. On-chip inter-modal Brillouin scattering. *Nat. Commun.*, 8:15819, Jul 2017.
- [222] N. T. Otterstrom, R. O. Behunin, E. A. Kittlaus, Z. Wang, and P. T. Rakich. A silicon brillouin laser. *Science*, 360(6393):1113–1116, 2018.
- [223] N. T. Otterstrom, R. O. Behunin, E. A. Kittlaus, and P. T. Rakich. Optomechanical cooling in a continuous system. *Phys. Rev. X*, 8:041034, 2018.
- [224] E. A. Kittlaus, N. T. Otterstrom, P. Kharel, S. Gertler, and P. Rakich. Nonreciprocal inter-band Brillouin modulation. *Nat. Photonics*, 12(10):613, 2018.
- [225] R. Lucas and P. Biquard. Propriétés optiques des milieux solides et liquides soumis aux vibrations élastiques ultra sonores. *Journal de Physique et le Radium*, 3(10):464–477, 1932.
- [226] D. Royer and E. Dieulesaint. *Elastic Waves in Solids II: Generation, Acousto-optic Interaction, Applications*. Advanced Texts in Physics. Springer-Verlag, Berlin, 2010.
- [227] D. K. Biegelsen. Photoelastic tensor of silicon and the volume dependence of the average gap. *Phys. Rev. Lett.*, 32:1196–1199, 1974.

- [228] A. Maradudin and E. Burstein. Relation between photoelasticity, electrostriction, and first-order Raman effect in crystals of the diamond structure. *Phys. Rev.*, 164(3):1081, 1967.
- [229] A. Feldman. Relations between electrostriction and the stress-optical effect. *Phys. Rev. B*, 11(12):5112, 1975.
- [230] P. T. Rakich, P. Davids, and Z. Wang. Tailoring optical forces in waveguides through radiation pressure and electrostrictive forces. *Opt. Express*, 18(14):14439–14453, 2010.
- [231] W. Qiu, P. T. Rakich, H. Shin, H. Dong, M. Soljačić, and Z. Wang. Stimulated Brillouin scattering in nanoscale silicon step-index waveguides: a general framework of selection rules and calculating SBS gain. *Opt. Express*, 21(25):31402–31419, 2013.
- [232] C. Wolff, M. J. Steel, B. J. Eggleton, and C. G. Poulton. Stimulated Brillouin scattering in integrated photonic waveguides: Forces, scattering mechanisms, and coupled-mode analysis. *Phys. Rev. A*, 92(1):013836, 2015.
- [233] P. Kharel, R. O. Behunin, W. H. Renninger, and P. T. Rakich. Noise and dynamics in forward Brillouin interactions. *Phys. Rev. A*, 93:063806, 2016.
- [234] D. Royer, , and E. Dieulesaint. *Elastic Waves in Solids I: Free and Guided Propagation*. Advanced Texts in Physics. Springer-Verlag, Berlin, 2010.
- [235] Simply silicon. *Nat. Photonics*, 4:491, Aug 2010. Editorial.
- [236] H. Rong, R. Jones, A. Liu, O. Cohen, D. Hak, A. Fang, and M. Paniccia. A continuous-wave Raman silicon laser. *Nature*, 433(7027):725–728, 2005.
- [237] N. Olsson and J. van der Ziel. Fibre Brillouin amplifier with electronically controlled bandwidth. *Electron. Lett.*, 22(9):488–490, 1986.
- [238] A. Wise, M. Tur, and A. Zadok. Sharp tunable optical filters based on the polarization attributes of stimulated Brillouin scattering. *Opt. Express*, 19(22):21945–21955, 2011.
- [239] X. Huang and S. Fan. Complete all-optical silica fiber isolator via stimulated Brillouin scattering. *J. Lightwave Technol.*, 29(15):2267–2275, 2011.

- [240] D. Braje, L. Hollberg, and S. Diddams. Brillouin-enhanced hyperparametric generation of an optical frequency comb in a monolithic highly nonlinear fiber cavity pumped by a CW laser. *Phys. Rev. Lett.*, 102:193902, 2009.
- [241] Q. Lin, O. J. Painter, and G. P. Agrawal. Nonlinear optical phenomena in silicon waveguides: Modeling and applications. *Opt. Express*, 15(25):16604–16644, 2007.
- [242] C. Wolff, R. V. Laer, M. J. Steel, B. J. Eggleton, and C. G. Poulton. Brillouin resonance broadening due to structural variations in nanoscale waveguides. *New J. Phys.*, 18(2):025006, 2016.
- [243] C. Wolff, P. Gutsche, M. J. Steel, B. J. Eggleton, and C. G. Poulton. Power limits and a figure of merit for stimulated Brillouin scattering in the presence of third and fifth order loss. *Opt. Express*, 23(20):26628–26638, 2015.
- [244] R. Jones, H. Rong, A. Liu, A. W. Fang, M. J. Paniccia, D. Hak, and O. Cohen. Net continuous wave optical gain in a low loss silicon-on-insulator waveguide by stimulated Raman scattering. *Opt. Express*, 13(2):519–525, 2005.
- [245] M. Dinu, F. Quochi, and H. Garcia. Third-order nonlinearities in silicon at telecom wavelengths. *Appl. Phys. Lett.*, 82(18):2954–2956, 2003.
- [246] A. D. Bristow, N. Rotenberg, and H. M. van Driel. Two-photon absorption and Kerr coefficients of silicon for 850-2200nm. *Appl. Phys. Lett.*, 90(19):191104, 2007.
- [247] S. A. V. and T. M. Monro. A full vectorial model for pulse propagation in emerging waveguides with subwavelength structures part I: Kerr nonlinearity. *Opt. Express*, 17(4):2298–2318, 2009.
- [248] R. Dekker, N. Usechak, M. Först, and A. Driessen. Ultrafast nonlinear all-optical processes in silicon-on-insulator waveguides. *J. Phys. D*, 40(14):R249, 2007.
- [249] R. Claps, V. Raghunathan, D. Dimitropoulos, and B. Jalali. Influence of nonlinear absorption on Raman amplification in silicon waveguides. *Opt. Express*, 12(12):2774–2780, 2004.

- [250] C. Wolff, P. Gutsche, M. J. Steel, B. J. Eggleton, and C. G. Poulton. Impact of nonlinear loss on stimulated Brillouin scattering. *J. Opt. Soc. Am. B*, 32(9):1968–1978, 2015.
- [251] T. Barwicz and H. A. Haus. Three-dimensional analysis of scattering losses due to sidewall roughness in microphotonic waveguides. *J. Lightwave Technol.*, 23(9):2719, 2005.
- [252] R. Soref and B. Bennett. Electrooptical effects in silicon. *IEEE J. Quantum Electron.*, 23(1):123–129, 1987.
- [253] D. Dimitropoulos, R. Jhaveri, R. Claps, J. C. S. Woo, and B. Jalali. Lifetime of photogenerated carriers in silicon-on-insulator rib waveguides. *Appl. Phys. Lett.*, 86(7):071115, 2005.
- [254] H. Rong, S. Xu, Y.-H. Kuo, V. Sih, O. Cohen, O. Raday, and M. Paniccia. Low-threshold continuous-wave Raman silicon laser. *Nat. Photonics*, 1:232, 2007. Article.
- [255] U. Fano. Effects of configuration interaction on intensities and phase shifts. *Phys. Rev.*, 124:1866–1878, 1961.
- [256] Y. Antman, A. Clain, Y. London, and A. Zadok. Optomechanical sensing of liquids outside standard fibers using forward stimulated Brillouin scattering. *Optica*, 3(5):510–516, 2016.
- [257] Y. A. V. Espinel, F. G. S. Santos, G. O. Luiz, T. P. M. Alegre, and G. S. Wiederhecker. Brillouin optomechanics in coupled silicon microcavities. *Scientific Reports*, 7:43423, 2017.
- [258] C. G. Poulton, R. Pant, A. Byrnes, S. Fan, M. J. Steel, and B. J. Eggleton. Design for broadband on-chip isolator using stimulated Brillouin scattering in dispersion-engineered chalcogenide waveguides. *Opt. Express*, 20(19):21235–21246, 2012.
- [259] D. Marpaung, C. Roeloffzen, R. Heideman, A. Leinse, S. Sales, and J. Capmany. Integrated microwave photonics. *Laser Photon. Rev.*, 7(4):506–538, 2013.

- [260] J. Capmany and D. Novak. Microwave photonics combines two worlds. *Nat. Photonics*, 1(6):319–330, 2007.
- [261] J. Capmany, B. Ortega, D. Pastor, and S. Sales. Discrete-time optical processing of microwave signals. *J. Lightwave Technol.*, 23(2):702–723, 2005.
- [262] V. Urick, J. McKinney, and K. Williams. *Fundamentals of Microwave Photonics*. Wiley series in microwave and optical engineering. John Wiley & Sons, Inc., 2015.
- [263] R. Van Laer, C. J. Sarabalis, R. Baets, D. Van Thourhout, and A. H. Safavi-Naeini. Thermal Brillouin noise observed in silicon optomechanical waveguide. *J. Opt.*, 19(4):044002, 2017.
- [264] J. Van Campenhout, W. M. J. Green, S. Assefa, and Y. A. Vlasov. Low-power, 2x2 silicon electro-optic switch with 110-nm bandwidth for broadband reconfigurable optical networks. *Opt. Express*, 17(26):24020–24029, 2009.
- [265] M. A. Van Camp, S. Assefa, D. M. Gill, T. Barwicz, S. M. Shank, P. M. Rice, T. Topuria, and W. M. J. Green. Demonstration of electrooptic modulation at 2165nm using a silicon mach-zehnder interferometer. *Opt. Express*, 20(27):28009–28016, 2012.
- [266] A. Ramaswamy, L. A. Johansson, J. Klamkin, H. F. Chou, C. Sheldon, M. J. Rodwell, L. A. Coldren, and J. E. Bowers. Integrated coherent receivers for high-linearity microwave photonic links. *J. Lightwave Technol.*, 26(1):209–216, 2008.
- [267] L. M. Johnson and H. V. Roussel. Reduction of intermodulation distortion in interferometric optical modulators. *Opt. Lett.*, 13(10):928–930, 1988.
- [268] G. E. Betts. Linearized modulator for suboctave-bandpass optical analog links. *IEEE Trans. Microw. Theory Tech.*, 42(12):2642–2649, 1994.
- [269] W. B. Bridges and J. H. Schaffner. Distortion in linearized electrooptic modulators. *IEEE Trans. Microw. Theory Tech.*, 43(9):2184–2197, 1995.
- [270] Q. Xu, B. Schmidt, S. Pradhan, and M. Lipson. Micrometre-scale silicon electro-optic modulator. *Nature*, 435(7040):325–327, 2005.

- [271] G. T. Reed, G. Mashanovich, F. Y. Gardes, and D. J. Thomson. Silicon optical modulators. *Nat. Photonics*, 4(8):518–526, 2010.
- [272] L. Chen, K. Preston, S. Manipatruni, and M. Lipson. Integrated GHz silicon photonic interconnect with micrometer-scale modulators and detectors. *Opt. Express*, 17(17):15248–15256, 2009.
- [273] T. Baehr-Jones, R. Ding, A. Ayazi, T. Pinguet, M. Streshinsky, N. Harris, J. Li, L. He, M. Gould, Y. Zhang, A. E.-J. Lim, T.-Y. Liow, S. H.-G. Teo, G.-Q. Lo, and M. Hochberg. A 25 Gb/s silicon photonics platform, 2012.
- [274] X. Xie, Q. Zhou, E. Norberg, M. Jacob-Mitos, Y. Chen, Z. Yang, A. Ramaswamy, G. Fish, J. C. Campbell, and A. Beling. High-power and high-speed heterogeneously integrated waveguide-coupled photodiodes on silicon-on-insulator. *J. Lightwave Technol.*, 34(1):73–78, 2016.
- [275] H. H. Diamandi, Y. London, and A. Zadok. Opto-mechanical inter-core cross-talk in multi-core fibers. *Optica*, 4(3):289–297, 2017.
- [276] J. R. Koehler, R. E. Noskov, A. A. Sukhorukov, A. Butsch, D. Novoa, and P. St. J. Russell. Resolving the mystery of milliwatt-threshold opto-mechanical self-oscillation in dual-nanoweb fiber. *APL Photonics*, 1(5):056101, 2016.
- [277] J. B. Driscoll, R. R. Grote, B. Souhan, J. I. Dadap, M. Lu, and R. M. Osgood. Asymmetric Y junctions in silicon waveguides for on-chip mode-division multiplexing. *Opt. Lett.*, 38(11):1854–1856, 2013.
- [278] D. Dai, J. Wang, and Y. Shi. Silicon mode (de)multiplexer enabling high capacity photonic networks-on-chip with a single-wavelength-carrier light. *Opt. Lett.*, 38(9):1422–1424, 2013.
- [279] L. Luo, N. Ophir, C. P. Chen, L. H. Gabrielli, C. B. Poitras, K. Bergmen, and M. Lipson. WDM-compatible mode-division multiplexing on a silicon chip. *Nat. Commun.*, 5:3069, 2014.

- [280] I. Aryanfar, C. Wolff, M. J. Steel, B. J. Eggleton, and C. G. Poulton. Mode conversion using stimulated Brillouin scattering in nanophotonic silicon waveguides. *Opt. Express*, 22(23):29270–29282, 2014.
- [281] G. Chen, R. Zhang, J. Sun, H. Xie, Y. Gao, D. Feng, and H. Xiong. Mode conversion based on forward stimulated Brillouin scattering in a hybrid phononic-photonic waveguide. *Opt. Express*, 22(26):32060–32070, 2014.
- [282] S. Signorini, M. Mancinelli, M. Borghi, M. Bernard, M. Ghulinyan, G. Pucker, and L. Pavesi. Intermodal four-wave mixing in silicon waveguides. *Photon. Res.*, 6(8):805–814, 2018.
- [283] R. Van Laer, R. Baets, and D. Van Thourhout. Unifying Brillouin scattering and cavity optomechanics. *Phys. Rev. A*, 93:053828, 2016.
- [284] M. Zalalutdinov, A. Zehnder, A. Olkhovets, S. Turner, L. Sekaric, B. Ilic, D. Czaplewski, J. M. Parpia, and H. G. Craighead. Autoparametric optical drive for micromechanical oscillators. *Appl. Phys. Lett*, 79(5):695–697, 2001.
- [285] T. Carmon, H. Rokhsari, L. Yang, T. J. Kippenberg, and K. J. Vahala. Temporal behavior of radiation-pressure-induced vibrations of an optical microcavity phonon mode. *Phys. Rev. Lett.*, 94:223902, 2005.
- [286] T. J. Kippenberg, H. Rokhsari, T. Carmon, A. Scherer, and K. J. Vahala. Analysis of radiation-pressure induced mechanical oscillation of an optical microcavity. *Phys. Rev. Lett.*, 95:033901, 2005.
- [287] H. Rokhsari, T. J. Kippenberg, T. Carmon, and K. J. Vahala. Radiation-pressure-driven micro-mechanical oscillator. *Opt. Express*, 13(14):5293–5301, 2005.
- [288] I. S. Grudin, H. Lee, O. Painter, and K. J. Vahala. Phonon laser action in a tunable two-level system. *Phys. Rev. Lett.*, 104:083901, 2010.
- [289] A. Debut, S. Randoux, and J. Zemmouri. Linewidth narrowing in Brillouin lasers: Theoretical analysis. *Phys. Rev. A*, 62:023803, 2000.

- [290] R. O. Behunin, N. T. Otterstrom, P. T. Rakich, S. Gundavarapu, and D. J. Blumenthal. Fundamental noise dynamics in cascaded-order brillouin lasers. *Phys. Rev. A*, 98:023832, 2018.
- [291] R. Y. Chiao. *Brillouin Scattering and Coherent Phonon Generation*. PhD thesis, Massachusetts Institute of Technology, 1965.
- [292] A. Yariv. Quantum theory for parametric interactions of light and hypersound. *IEEE J. Quantum Electron.*, 1(1):28–36, 1965.
- [293] K. O. Hill, B. S. Kawasaki, and D. C. Johnson. CW Brillouin laser. *Appl. Phys. Lett.*, 28(10):608–609, 1976.
- [294] K. S. Abedin. Single-frequency Brillouin lasing using single-mode As₂Se₃ chalcogenide fiber. *Opt. Express*, 14(9):4037–4042, 2006.
- [295] B. Morrison, A. Casas-Bedoya, G. Ren, K. Vu, Y. Liu, A. Zarifi, T. G. Nguyen, D.-Y. Choi, D. Marpaung, S. J. Madden, A. Mitchell, and B. J. Eggleton. Compact Brillouin devices through hybrid integration on silicon. *Optica*, 4(8):847–854, 2017.
- [296] I. V. Kabakova, R. Pant, D.-Y. Choi, S. Debbarma, B. Luther-Davies, S. J. Madden, and B. J. Eggleton. Narrow linewidth Brillouin laser based on chalcogenide photonic chip. *Opt. Lett.*, 38(17):3208–3211, 2013.
- [297] V. B. Braginskiĭ, A. B. Manukin, and M. Y. Tikhonov. Investigation of Dissipative Ponderomotive Effects of Electromagnetic Radiation. *Soviet JETP*, 31:829, 1970.
- [298] P. F. Cohadon, A. Heidmann, and M. Pinard. Cooling of a mirror by radiation pressure. *Phys. Rev. Lett.*, 83:3174–3177, 1999.
- [299] A. Schliesser, R. Rivière, G. Anetsberger, O. Arcizet, and T. J. Kippenberg. Resolved-sideband cooling of a micromechanical oscillator. *Nat. Phys.*, 4:415, 2008. Article.
- [300] J. D. Teufel, T. Donner, D. Li, J. W. Harlow, M. S. Allman, K. Cicak, A. J. Sirois, J. D. Whittaker, K. W. Lehnert, and R. W. Simmonds. Sideband cooling of micromechanical motion to the quantum ground state. *Nature*, 475:359, 2011.

- [301] J. Chan, T. P. M. Alegre, A. H. Safavi-Naeini, J. T. Hill, A. Krause, S. Gröblacher, M. Aspelmeyer, and O. Painter. Laser cooling of a nanomechanical oscillator into its quantum ground state. *Nature*, 478:89, 2011.
- [302] A. D. O’Connell, M. Hofheinz, M. Ansmann, R. C. Bialczak, M. Lenander, E. Lucero, M. Neeley, D. Sank, H. Wang, M. Weides, J. Wenner, J. M. Martinis, and A. N. Cleland. Quantum ground state and single-phonon control of a mechanical resonator. *Nature*, 464:697, 2010.
- [303] T. A. Palomaki, J. D. Teufel, R. W. Simmonds, and K. W. Lehnert. Entangling mechanical motion with microwave fields. *Science*, 342(6159):710–713, 2013.
- [304] E. Verhagen, S. Deléglise, S. Weis, A. Schliesser, and T. J. Kippenberg. Quantum-coherent coupling of a mechanical oscillator to an optical cavity mode. *Nature*, 482:63, 2012.
- [305] W. Marshall, C. Simon, R. Penrose, and D. Bouwmeester. Towards quantum superpositions of a mirror. *Phys. Rev. Lett.*, 91:130401, 2003.
- [306] Y. Chu, P. Kharel, W. H. Renninger, L. D. Burkhardt, L. Frunzio, P. T. Rakich, and R. J. Schoelkopf. Quantum acoustics with superconducting qubits. *Science*, 358(6360):199–202, 2017.
- [307] A. M. Jayich, J. C. Sankey, B. M. Zwickl, C. Yang, J. D. Thompson, S. M. Girvin, A. A. Clerk, F. Marquardt, and J. G. E. Harris. Dispersive optomechanics: a membrane inside a cavity. *New J. Phys.*, 10(9):095008, 2008.
- [308] M. Bhattacharya and P. Meystre. Multiple membrane cavity optomechanics. *Phys. Rev. A*, 78(4):041801, 2008.
- [309] M. Schmidt, M. Ludwig, and F. Marquardt. Optomechanical circuits for nanomechanical continuous variable quantum state processing. *New J. Phys.*, 14(12):125005, 2012.

- [310] D. Lee, M. Underwood, D. Mason, A. Shkarin, S. Hoch, and J. Harris. Multimode optomechanical dynamics in a cavity with avoided crossings. *Nat. Commun.*, 6:6232, 2015.
- [311] G. Heinrich, M. Ludwig, J. Qian, B. Kubala, and F. Marquardt. Collective dynamics in optomechanical arrays. *Phys. Rev. Lett.*, 107(4):043603, 2011.
- [312] M. Zhang, G. S. Wiederhecker, S. Manipatruni, A. Barnard, P. McEuen, and M. Lipson. Synchronization of micromechanical oscillators using light. *Phys. Rev. Lett.*, 109(23):233906, 2012.
- [313] A. Xuereb, C. Genes, and A. Dantan. Strong coupling and long-range collective interactions in optomechanical arrays. *Phys. Rev. Lett.*, 109(22):223601, 2012.
- [314] M. Schmidt, S. Kessler, V. Peano, O. Painter, and F. Marquardt. Optomechanical creation of magnetic fields for photons on a lattice. *Optica*, 2(7):635–641, 2015.
- [315] A. Tomadin, S. Diehl, M. D. Lukin, P. Rabl, and P. Zoller. Reservoir engineering and dynamical phase transitions in optomechanical arrays. *Phys. Rev. A*, 86(3):033821, 2012.
- [316] A. H. Safavi-Naeini and O. Painter. Proposal for an optomechanical traveling wave phonon–photon translator. *New J. Phys.*, 13(1):013017, 2011.
- [317] S. Habraken, K. Stannigel, M. D. Lukin, P. Zoller, and P. Rabl. Continuous mode cooling and phonon routers for phononic quantum networks. *New J. Phys.*, 14(11):115004, 2012.
- [318] K. Fang, M. H. Matheny, X. Luan, and O. Painter. Optical transduction and routing of microwave phonons in cavity-optomechanical circuits. *Nat. Photonics*, 10(7):489, 2016.
- [319] R. N. Patel, Z. Wang, W. Jiang, C. J. Sarabalis, J. T. Hill, and A. H. Safavi-Naeini. A single-mode phononic wire. *arXiv preprint arXiv:1711.00847*, 2017.

- [320] W. H. Renninger, P. Kharel, R. O. Behunin, and P. T. Rakich. Bulk crystalline optomechanics. *Nat. Phys.*, 14(6):601–607, 2018.
- [321] A. Metelmann and A. A. Clerk. Nonreciprocal photon transmission and amplification via reservoir engineering. *Phys. Rev. X*, 5(2):021025, 2015.
- [322] A. Seif, W. DeGottardi, K. Esfarjani, and M. Hafezi. Thermal management and non-reciprocal control of phonon flow via optomechanics. *Nat. Commun.*, 9(1):1207, 2018.
- [323] P. Rakich and F. Marquardt. Quantum theory of continuum optomechanics. *New J. Phys.*, 20(4):045005, 2018.
- [324] B. Stiller, M. Merklein, K. Vu, P. Ma, S. J. Madden, C. G. Poulton, and B. J. Eggleton. Crosstalk-free multi-wavelength coherent light storage via Brillouin interaction. *arXiv preprint arXiv:1803.08626*, 2018.
- [325] V. S. Shumeiko. Quantum acousto-optic transducer for superconducting qubits. *Phys. Rev. A*, 93(2):023838, 2016.
- [326] B. Vermersch, P.-O. Guimond, H. Pichler, and P. Zoller. Quantum state transfer via noisy photonic and phononic waveguides. *Phys. Rev. Lett.*, 118(13):133601, 2017.
- [327] H. Zoubi and K. Hammerer. Quantum nonlinear optics in optomechanical nanoscale waveguides. *Phys. Rev. Lett.*, 119(12):123602, 2017.
- [328] Y.-C. Chen, S. Kim, and G. Bahl. Brillouin cooling in a linear waveguide. *New J. Phys.*, 18(11):115004, 2016.
- [329] L. D. T’oth, N. R. Bernier, A. Nunnenkamp, A. Feofanov, and T. Kippenberg. A dissipative quantum reservoir for microwave light using a mechanical oscillator. *Nat. Phys.*, 13(8):787, 2017.
- [330] Y. Shoji, T. Mizumoto, H. Yokoi, I.-W. Hsieh, and R. M. O. Jr. Magneto-optical isolator with silicon waveguides fabricated by direct bonding. *Appl. Phys. Lett.*, 92(7):071117, 2008.

- [331] M.-C. Tien, T. Mizumoto, P. Pintus, H. Kromer, and J. E. Bowers. Silicon ring isolators with bonded nonreciprocal magneto-optic garnets. *Opt. Express*, 19(12):11740, 2011.
- [332] L. Bi, J. Hu, P. Jiang, D. H. Kim, G. F. Dionne, L. C. Kimerling, and C. A. Ross. On-chip optical isolation in monolithically integrated non-reciprocal optical resonators. *Nat. Photonics*, 5:758, 2011.
- [333] Y. Sobu, Y. Shoji, K. Sakurai, and T. Mizumoto. GaInAsP/InP MZI waveguide optical isolator integrated with spot size converter. *Opt. Express*, 21(13):15373, 2013.
- [334] D. Huang, P. Pintus, C. Zhang, Y. Shoji, T. Mizumoto, and J. E. Bowers. Electrically driven and thermally tunable integrated optical isolators for silicon photonics. *IEEE J. Sel. Top. Quantum Electron*, 22(6):271–278, 2016.
- [335] D. L. Sounas and A. Alù. Non-reciprocal photonics based on time modulation. *Nat. Photonics*, 11(12):774–783, 2017.
- [336] K. Gallo, G. Assanto, K. R. Parameswaran, and M. M. Fejer. All-optical diode in a periodically poled lithium niobate waveguide. *Appl. Phys. Lett.*, 79(3):314–316, 2001.
- [337] M. Soljačić, C. Luo, J. D. Joannopoulos, and S. Fan. Nonlinear photonic crystal microdevices for optical integration. *Opt. Lett.*, 28(8):637–639, Apr 2003.
- [338] L. Fan, J. Wang, L. T. Varghese, H. Shen, B. Niu, Y. Xuan, A. M. Weiner, and M. Qi. An all-silicon passive optical diode. *Science*, 335(6067):447–450, 2012.
- [339] Y. Shi, Z. Yu, and S. Fan. Limitations of nonlinear optical isolators due to dynamic reciprocity. *Nat. Photonics*, 9:388, 2015.
- [340] S. K. Ibrahim, S. Bhandare, D. Sandel, H. Zhang, and R. Noe. Non-magnetic 30 dB integrated optical isolator in III/V material. *Electron. Lett.*, 40(20):1293–1294, 2004.
- [341] C. R. Doerr, N. Dupuis, and L. Zhang. Optical isolator using two tandem phase modulators. *Opt. Lett.*, 36(21):4293–4295, 2011.

- [342] C. R. Doerr, L. Chen, and D. Vermeulen. Silicon photonics broadband modulation-based isolator. *Opt. Express*, 22(4):4493–4498, 2014.
- [343] E. Verhagen and A. Alu. Optomechanical nonreciprocity. *Nat. Phys.*, 13:922, 2017.
- [344] K. Fang, J. Luo, A. Metelmann, M. H. Matheny, F. Marquardt, A. A. Clerk, and O. Painter. Generalized non-reciprocity in an optomechanical circuit via synthetic magnetism and reservoir engineering. *Nat. Phys.*, 13:465, 2017.
- [345] Z. Shen, Y. Zhang, Y. Chen, F. Sun, X. Zou, G. Guo, C. Zou, and C. Dong. Reconfigurable optomechanical circulator and directional amplifier. *Nat. Commun.*, 9(1):1797, 2018.
- [346] F. Ruesink, J. P. Mathew, M.-A. Miri, A. Alù, and E. Verhagen. Optical circulation in a multimode optomechanical resonator. *Nat. Commun.*, 9(1):1798, 2018.
- [347] Z. Yu and S. Fan. Complete optical isolation created by indirect interband photonic transitions. *Nat. Photonics*, 3(2):91–94, 2009.
- [348] H. Lira, Z. Yu, S. Fan, and M. Lipson. Electrically driven nonreciprocity induced by interband photonic transition on a silicon chip. *Phys. Rev. Lett.*, 109:033901, 2012.
- [349] K. Fang, Z. Yu, and S. Fan. Photonic Aharonov-Bohm effect based on dynamic modulation. *Phys. Rev. Lett.*, 108:153901, 2012.
- [350] L. D. Tzuang, K. Fang, P. Nussenzveig, S. Fan, and M. Lipson. Non-reciprocal phase shift induced by an effective magnetic flux for light. *Nat. Photonics*, 8:701, 2014.
- [351] D. B. Sohn, S. Kim, and G. Bahl. Time-reversal symmetry breaking with acoustic pumping of nanophotonic circuits. *Nat. Photonics*, 12(2):91, 2018.
- [352] S. A. Tadesse and M. Li. Sub-optical wavelength acoustic wave modulation of integrated photonic resonators at microwave frequencies. *Nat. Commun.*, 5:5402, 2014.
- [353] L. Yin, Q. Lin, and G. P. Agrawal. Dispersion tailoring and soliton propagation in silicon waveguides. *Opt. Lett.*, 31(9):1295–1297, 2006.

- [354] X. Liu, W. M. J. Green, X. Chen, I.-W. Hsieh, J. I. Dadap, Y. A. Vlasov, and J. Richard M. Osgood. Conformal dielectric overlayers for engineering dispersion and effective nonlinearity of silicon nanophotonic wires. *Opt. Lett.*, 33(24):2889–2891, 2008.
- [355] L. Zhang, Y. Yue, R. G. Beausoleil, and A. E. Willner. Flattened dispersion in silicon slot waveguides. *Opt. Express*, 18(19):20529–20534, 2010.
- [356] L. Zhang, Q. Lin, Y. Yue, Y. Yan, R. G. Beausoleil, and A. E. Willner. Silicon waveguide with four zero-dispersion wavelengths and its application in on-chip octave-spanning supercontinuum generation. *Opt. Express*, 20(2):1685–1690, 2012.
- [357] H. Liang, Y. He, R. Luo, and Q. Lin. Ultra-broadband dispersion engineering of nanophotonic waveguides. *Opt. Express*, 24(26):29444–29451, 2016.
- [358] L. Kuhn, P. F. Heidrich, and E. G. Lean. Optical guided wave mode conversion by an acoustic surface wave. *Appl. Phys. Lett.*, 19(10):428, 1971.
- [359] H. Sasaki, J. Kushibiki, and N. Chubachi. Efficient acousto-optic TE=TM mode conversion in ZnO films. *Appl. Phys. Lett.*, 25(9):476–477, 1974.
- [360] A. Yariv. *Quantum Electronics*. John Wiley & Sons, Inc., 1975.
- [361] Y. Ohmachi and J. Noda. LiNbO₃ TE-TM mode converter using collinear acousto-optic interaction. *IEEE J. Quantum Electron.*, 13(2):43–46, 1977.
- [362] M. J. Rooks, E. Kratschmer, R. Viswanathan, J. Katine, R. E. Fontana, and S. A. MacDonald. Low stress development of poly(methylmethacrylate) for high aspect ratio structures. *Journal of Vacuum Science & Technology B: Microelectronics and Nanometer Structures Processing, Measurement, and Phenomena*, 20(6):2937–2941, 2002.
- [363] M. J. Rooks. Storing HSQ in liquid nitrogen. [https://nano.yale.edu/sites/default/files/files/hsq_frozen\(1\).pdf](https://nano.yale.edu/sites/default/files/files/hsq_frozen(1).pdf). Accessed: 2018-06-04.

- [364] D. Taillaert, P. Bienstman, and R. Baets. Compact efficient broadband grating coupler for silicon-on-insulator waveguides. *Opt. Lett.*, 29(23):2749–2751, 2004.
- [365] D. Taillaert, F. Van Laere, M. Ayre, W. Bogaerts, D. Van Thourhout, P. Bienstman, and R. Baets. Grating couplers for coupling between optical fibers and nanophotonic waveguides. *Japanese J. Appl. Phys.*, 45(8R):6071, 2006.
- [366] F. Van Laere, G. Roelkens, M. Ayre, J. Schrauwen, D. Taillaert, D. Van Thourhout, T. F. Krauss, and R. Baets. Compact and highly efficient grating couplers between optical fiber and nanophotonic waveguides. *J. Lightwave Technol.*, 25(1):151–156, 2007.
- [367] X. Chen, C. Li, C. K. Fung, S. M. Lo, and H. K. Tsang. Apodized waveguide grating couplers for efficient coupling to optical fibers. *IEEE Photon. Technol. Lett.*, 22(15):1156–1158, 2010.